Continuously monitored 1-dimensional dynamics with partial readouts

Chun Yin Leung,

Physics Department, Lancaster University

Supervisor: Dr. Alessandro Romito

Keywords: monitored systems, 1-dimensional systems, detector readouts

A thesis submitted for the degree of

Doctor of Philosophy

June, 2025

Abstract

The combined effect of unitary quantum dynamics and quantum measurement backaction leads to the emergence of unique phenomena, like the Quantum Zeno effect. Long limited to the case of single particles and few-body systems, the study of measurement-induced dynamics has recently come under much scrutiny for quantum-measured many-body systems, leading to the discovery of measurement-induced phase transitions (MiPTs). As a newly discovered out-of-equilibrium phase transition, it has drawn broad cross-disciplinary works, ranging from condensed matter physics and statistical mechanics to quantum information, quantum computation, and error correction, with several studies characterising its features in different models and scenarios. In this thesis, we address a general yet subtle feature of MiPTs: how does partial information, an incomplete set of measurement outcomes, affect the behaviours of these phase transitions? We address various facets of incomplete observer's information. We first consider the case of imperfect detection via a model of inefficient measurement, in which part of the information is lost, resulting in a density-matrix description of the system's state of knowledge. Inefficiency introduces different phase transitions characterised by entanglement or operator correlations. We move on to the case where the observer selects the information, introducing a novel continuous stochastic Schrodinger equation for partial post-selected (PPS) monitoring. We find that for a free fermion model, the degree of PPS introduces a new phase separation, with the phases of the post-selected dynamics remaining robust to a finite degree of PPS. Finally, we take advantage of the analytical tractability of non-Hermitian models to address the effect of initial conditions in a fully post-selected monitored free-fermionic model. The results in this thesis introduce new findings in MiPTs, along with new methods and techniques to overcome the hurdles in the field, both in the theoretical modelling and toward viable experimental protocols.

Acknowledgements

I want to acknowledge the immeasurable help from my supervisors, Dr. Alessandro Romito and Dr. Dganit Meidan, who have contributed substantially to the work developed. I would like to thank Dr. Amos Chan, Prof. Henning Schomerus, Prof. Edward McCann, and Dr. Neil Drummond for their invaluable comments during my PhD degree. I am indebted to Dr. Romito for his immense help in commenting on the texts and figures of this thesis. I would also like to thank my collaborators, Rafael Soares, Youenn Le Gal, and Dr. Marco Schirò, for allowing the inclusion of our work.

Finally, I would like to acknowledge my parents, Ka Wai Tang and Cho Fat Leung, who are integral to all my achievements.

Declaration

I, Chun Yin Leung, declare that the work presented in this thesis is, to the best of my knowledge and belief, original and my own work with my collaborators. I declare that a part of Ch. 5 consists of collaborative results provided by *Rafael Soares, Youenn Le Gal and Marco Schirò* from College de France. All the materials here have not been submitted for an equivalent degree of this or any other university. This thesis does not exceed the maximum permitted word length of 80,000 words, including appendices and footnotes, but excluding the bibliography. The following publications have been generated while developing this thesis, and, to an extent, have guided this thesis into what it has become.

Ch. 3 is based on the following work
C. Y. Leung and A. Romito, *"Entanglement and operator correlation signatures of many-body quantum Zeno phases in inefficiently monitored noisy systems"*,
under review in Physical Review A, arXiv preprint arXiv:2407.11723 (2024).

Ch. 4 is based on the following work
C. Y. Leung, D. Meidan and A. Romito, *"Theory of free fermions dynamics under partial post-selected monitoring"*,
under 2nd review in Physical Review X, arXiv preprint arXiv:2312.14022 (2023).

Ch. 5 is based on a manuscript in preparation from a collaborative work with Alessandro Romito, Dganit Meidan, Rafael Soares, Youenn Le Gal and Marco Schirò.

A rough estimate of the word count is: 34626

Chun Yin Leung

Contents

Nomenclature

Notation

$\mathcal{O}(a^n)$ order of a^n

$\{\dots\}$ a set

$\mathcal{H}$ Hilbert space

$\breve{\rho}_A \in \mathrm{L}[\mathcal{H}]$ **un**-normalised density matrix of region A

$\hat{\rho}_A \in \mathrm{L}[\mathcal{H}]$ normalised density matrix of region A

$|\psi\rangle \in \mathcal{H}$ a ket in $\mathcal{H}$

$\mathrm{L}[\mathcal{H}]$ set of linear operators in $\mathcal{H}$

$\hat{O} \in \mathrm{L}[\mathcal{H}]$ a linear operator $\hat{O}$

$\mathbb{I} \in \mathrm{L}[\mathcal{H}]$ Identity operator

$\big\| |\psi\rangle \big\| = \sqrt{\big|\langle\psi|\psi\rangle\big|}$ Norm of $|\psi\rangle$

$\langle \dots \rangle$ Expectation value with respect to some density matrix

$[\hat{A}, \hat{B}]$ commutator of $\hat{A}$ and $\hat{A}$, $\hat{A}\hat{B} - \hat{B}\hat{A}$.

$\{\hat{A}, \hat{B}\}$ anticommutator of $\hat{A}$ and $\hat{A}$, $\hat{A}\hat{B} + \hat{B}\hat{A}$.

$\forall$ for all

$\mathrm{Sign}(x)$ the sign of x

$\mathrm{Tr}[\ldots]$ trace over entire Hilbert space

$\mathrm{Tr}[\ldots]_A$ partial trace over subsystem A

Abbrevaition

w.r.t. with repeat to

Glossary

monitored system quantum system under continuous quantum measurement

quantum trajectory a sequence of quantum measurement outcomes

CFT Conformal field theory

Chapter 1

Introduction

A system under unitary[1] dynamics evolves coherently in the superposition of the Hamiltonian's eigenstates. In comparison, upon performing a projective measurement, according to the fundamental postulation of quantum mechanics, the state collapses into one of the eigenstates of the measurement operator. Suppose a measurement is compatible with the Hamiltonian (i.e. they commute and share the same eigenbasis), and we punctuate a unitary evolution by the Hamiltonian with a projective measurement. In that case, the post-measurement collapsed state is preserved in time and does not transition to other states; a second repeated projective measurement will yield the same outcome. However, if the measurement is incompatible with the Hamiltonian, the Hamiltonian does not maintain the post-measurement state and builds up over time finite amplitudes on other measurement eigenstates; a second repeated projective measurement can yield a different outcome. This simple thought scenario raises an intriguing question: what happens if the two incompatible dynamics coexist continuously, e.g. unitary Hamiltonian evolution punctuated by repeated measurement at repeated time intervals? Indeed, this question was addressed early on in research on quantum measurement, which led to the discovery of **quantum Zeno effect** [1, 2]: unlike in unitary dynamics where

[1]Throughout this thesis, the adjective 'unitary', if used alone, will be understood as the abbreviation of 'unitary operator', or 'unitary evolution/dynamics' depending on its context!

a system can explore the Hilbert space spanned by the Hamiltonian's eigenstates, under frequent measurements, the system's dynamics are mostly frozen in one of the measurement eigenstates. These hybrid unitary-measurement protocols hosting unique measurement-induced quantum effect have sparked much interest in the crossover between coherent evolution and quantum Zeno effect [3–26], and suggests novel ways to control quantum systems [14–21, 27–33]. The mainstream research on the quantum Zeno effect has generally been concerned with single/few-body systems. Recently, however, a new research direction emerged from the interplay of quantum Zeno effect and many-body quantum dynamics.

Out-of-equilibrium many-body systems emerge as a promising arena for exploring unique collective phenomena far from equilibrium, ranging from novel quantum phases and transitions, many-body localisation and thermalisation, to many-body chaos and entanglement dynamics [34–63]. Among many protocols, sitting at the intersection of condensed matter physics and quantum information, hybrid unitary-measurement dynamics has become an active field of research [64–116]. In particular, given the increasingly substantial role of many-body entanglement in characterising many-body quantum phases of matter during the past few decades [117, 118], it is of no surprise that the entanglement dynamics in these system is of tremendous interest. On the one hand, many-body unitary dynamics can spread information and build up entanglement, creating highly entangled dynamics [43, 44, 117–122]; in contrast, local measurement disentangles and localises information like the Zeno effect, lowering the many-body's entanglement. Putting together these two competing effects leads to measurement-induced phase transitions (MiPTs) between phases with different many-body entanglement properties, resembling in some way the entanglement transition in equilibrium system [117]: system-size-*dependent* entanglement for weak measurement influence and system-size-*independent* entanglement for strong measurement influence.

MiPTs were originally discovered in random quantum circuits [64–67], and were viewed as a many-body extension of the crossover between coherent unitary dynamics and frozen quantum Zeno regime. Therein, random unitary gates are punctuated by probabilistic measurement in spacetime, and increasing the probability (equivalent to more frequent measurements) suppresses the many-body entanglement, resulting in a MiPT. Even deeper, in Ref. [64], it was shown that the MiPT was connected to statistical mechanical models via a quantum-classical mapping. Fueled by these initial findings, the field has since established many novel connections with condensed matter physics, statistical mechanics, and quantum information [36], and correspondingly, initial extensions to non-projective measurements lead to new discoveries of MiPTs in a broader range of protocols [67, 123], creating both experimental and theoretical excitement. Since then, other dynamics with random Clifford gates have been analysed [99, 124–134], as well as replacing random unitary gates with Hamiltonians [71–94, 103, 104], revealing highly intricate MiPTs. Even more, a different kind of MiPT emerged from a unique setup: measurement-only dynamics. Here, the dynamics do not consist of any unitary operation, and the system is solely driven by the measurements. Notably, when there exist sets of non-commuting local measurement operations, they compete and contend to stabilise their respective eigenstates, resulting in a measurement-only MiPT from one short-range entanglement phase to another [75, 108–116]. Given MiPT's high-profile theoretical exposure, it is to no surprise that initial evidence of MiPTs were reported in recent experiments [68–70][1].

Analogues to (quantum) phase transitions characterised by (quantum) fluctuation-averaged thermodynamics observables, MiPTs are phase transitions in measurement-outcome-averaged observables. There is, however, a subtlety: linear average dynamics washes away measurement-induced effect, leaving in general a trivial steady state dynamics [135–138], and only non-linear averages can characterise MiPTs. Thus, this implies that in a MiPT, an observer needs vast knowledge of the density matrix to extract such non-linear averages. An immediate experimentally relevant consequence follows: to gain knowledge of the density matrix, one needs to

[1]Albeit with great experimental difficulties! One of them is discussed later.

prepare the same density matrix multiple times and perform various operations to characterise its matrix element. Yet, under many quantum measurements, as in the case of MiPT, the probability of obtaining a copy of the same density matrix, i.e. an identical sequence of outcomes, is exponentially small, making the preparation of multiple identical density matrices practically impossible. This monumental experimental challenge is known as the 'post-selection problem', a driving reason for the limited experimental realisations, and has been explored both theoretically and experimentally [69, 70, 139–145].

Moreover, other than experimental challenges, MiPTs raise new unanswered theoretical questions. To demonstrate one, contrary to conventional quantum phase transitions, where the quantum fluctuation is inaccessible to an observer, MiPT is a phase transition in the outcome-average dynamics. Since the outcomes are registered and known by the observer, does it imply that each outcome sequence contributes to a phase transition with features from distinct universality classes, and MiPT is an average of these phase transitions? Another closely related question concerns that MiPTs require the observer to have absolute knowledge of the outcomes; what happens when the observer has incomplete knowledge of the outcomes and introduces bias or classical uncertainty in the state of knowledge of the system? Furthermore, due to the complexity of the outcome-averaging scheme in MiPT, much literature has turned to studying the dynamics of MiPT in restricted deterministic measurement outcomes dynamics [75, 146–159]; yet, a connection between this dynamics and the fully random dynamics has not been seen. These emerging open theoretical questions pose significant challenges to the understanding of MiPTs, and a few works have addressed them very recently [73, 75, 87, 88, 159, 160].

The central theme of this thesis involves exploring some of the aforementioned unanswered questions in MiPTs through the lens of non-ideal detectors. A non-ideal detector's faults generally fall into two groups. In one case, the fault is associated with classical uncertainty, introducing a classical statistical mixture in the system [27]. In turn, the density matrix becomes mixed, potentially shadowing some features in MiPT. In the second case, the detector has an intrinsic quantum mechanical fault that handicaps the registration of a subset of measurement outcomes. This corresponds to retaining experiments for a subset of outcomes and is akin to outcome sequence selection; the fate of MiPT in this reduced measurement outcome subspace is unknown and is highly relevant to unveiling the role of measurement outcomes in MiPTs. Crucially, it has been shown that these faults can drastically alter the MiPTs' characteristics, whether it be the universality or the critical point [75, 88, 146, 159].

The thesis is organised as follows. Ch. 2 first introduces much of the background theory employed in this thesis. This section is intended to be self-contained with references for more extensive in-depth treatments.

Ch. 3 explores the effect of incomplete measurement readouts, also known as inefficient measurements, in MiPT. We study a model under the evolution of a nearest-neighbour hopping Hamiltonian, random local white noise and local continuous measurement. To elucidate the results, we first examine the effect of inefficiency in a simplified 2-qubit model and find that inefficiency can induce different effects that distinguish entanglement and operator correlation in the system. Motivated by this finding, we examine the spatially extended model and conclude that inefficiency can induce different MiPT in entanglement and operator correlation.

Ch. 4 explores the effect of selecting detectors' readout. We first develop a new microscopic theory interpolating between deterministic dissipative/enhancing non-Hermitian dynamics and fault-free continuous measurement dynamics. The two dynamics are related to a broadened class of stochastic dynamics, with a parameter controlling the degree of stochasticity. Next, we write down a new evolution equation, the partially post-selected stochastic Schrödinger equation for the time continuum description of this class of dynamics. After that, motivated by the numerical findings in Ref. [75], we consider this new class of dynamics in a model of measurement-only free fermion whose MiPT has been shown to display different universality in the non-Hermitian and continuously measurement limit. Here, we find the surprising robustness of the non-Hermitian universality against finite stochasticity from measurement. Furthermore, the universality changes as a function of stochasticity. Finally, with the incorporation of unitary dynamics, we find that the suppression of measurement stochasticity suppresses the establishment of long-range entanglement and gives way to a new phase with different entanglement scaling properties from the continuously measured phase.

Ch. 5 further explores an emergent non-Hermitian Hamiltonian from an extreme selection of measurement readouts to a single quantum trajectory. More specifically, we study a particular non-Hermitian Su–Schrieffer–Heeger (SSH) model, which supports real eigenvalues despite the non-Hermiticity ($\mathcal{PT}$-symmetric). To our surprise, the entanglement dynamics and scaling are initial-state-dependent, contrary to generic non-Hermitian dynamics, which 'forget' about the initial state over time. We find that the initial state can change the system from short-range entanglement to long-range entanglement. To gain more insight into this novel phenomenon, we combined analytics from large Toeplitz matrices and a field theoretical approach. We argue that an underlying CFT is responsible for this initial-state-dependent behaviour.

Chapter 2

Background theory

This section provides a self-contained overview of the various techniques and concepts employed in the thesis.

2.1 Quantum measurements

We consider the measurement process of a generic quantum system described by a density matrix.

Definition 2.1.1. density matrix— a density matrix $\hat{\rho}$ is a classical statistical mixture of different quantum states

$$\hat{\rho} = \sum_k p_k \left|\psi_k\right\rangle\!\left\langle\psi_k\right| . \tag{2.1}$$

Here, p_k is the classical probability for the system to be in a state $|\psi_k\rangle$, and $\mathrm{Tr}[\hat{\rho}] = 1$. A density matrix with only one p_k is called a pure state, and a density matrix proportional to an identity is called a totally mixed state, an infinite temperature state.

As a warm-up, let's start with the simplest case of quantum measurement: projective measurement, also known as von Neumann measurements [27]. For a quantum system with an N-dimensional Hilbert space, consider a measurement operator $\hat{O}$ of

$$\hat{O} = \sum_{m=0}^{N-1} \lambda_m \left|\lambda_m\right\rangle\!\left\langle\lambda_m\right| = \sum_m \lambda_m \hat{\Pi}_m, \tag{2.2}$$

where λ_m's are the possible measurement outcomes (eigenvalues) of $\hat{O}$ which, for simplicity, we assume to be non-degenerate for each eigenket, and their corresponding eigenkets are $|\lambda_m\rangle$'s. We represent the projector $|\lambda_m\rangle\!\langle\lambda_m| \equiv \hat{\Pi}_m$. By definition, a measurement operator is Hermitian, its span is complete $\sum_m \hat{\Pi}_m = \mathbb{I}$, and we can express a state $|\psi\rangle$ in the eigenbasis of $\hat{O}$

$$|\psi\rangle = \sum_m c_m |\lambda_m\rangle. \tag{2.3}$$

When performing a projective measurement of $\hat{O}$ on the state $|\psi\rangle$, the outcome is probabilistic: let p_m be the probability of outcome λ_m

$$p_m = |c_m|^2 = \mathrm{Tr}\left[\hat{\Pi}_m \left|\psi\right\rangle\!\left\langle\psi\right| \hat{\Pi}_m\right]. \tag{2.4}$$

The updated state after a projective measurement with outcome λ_m is collapsed

$$|\psi\rangle \xrightarrow[\text{with outcome } \lambda_m]{\text{measurement}} |\lambda_m\rangle = \frac{\hat{\Pi}_m|\psi\rangle}{\left\|\hat{\Pi}_m|\psi\rangle\right\|}. \tag{2.5}$$

The above discussion for the case of pure state (i.e. $\hat{\rho} = |\psi\rangle\!\langle\psi|$) can readily be extended to mixed state: given a density matrix $\hat{\rho}_0$, the probability and the updated density matrix are

$$p_m = \mathrm{Tr}\left[\hat{\Pi}_m \hat{\rho}_0 \hat{\Pi}_m\right],\ \hat{\rho}_0 \xrightarrow[\text{with outcome } \lambda_m]{\text{measurement}} \hat{\rho}_m = \frac{\hat{\Pi}_m \hat{\rho}_0 \hat{\Pi}_m}{\mathrm{Tr}\left[\hat{\Pi}_m \hat{\rho}_0 \hat{\Pi}_m\right]}, \tag{2.6}$$

where ρ_m is the resultant density matrix after the measurement. From this, we note that projective measurements are highly disruptive; any superposition in the measurement eigenbasis is collapsed onto a definite eigenstate of the measurement operator.

2.1.1 Generalised quantum measurement

Projective measurement does not provide an exhaustive framework for all measurement processes in the current quantum architectures [27, 161, 162]. Also, from a theoretical standpoint, protocols, where a detector is coupled to a system, are not projective measurements but lead to generalised quantum measurements in which one measures the system indirectly [27]. To elucidate this, consider a separable joint quantum state of the detector and system

$$\hat{\rho}_{\text{joint}} = \hat{\rho}_{\text{A}} \otimes \hat{\rho}_{\text{S}}, \tag{2.7}$$

where $\hat{\rho}_{\text{A}}$ ($\hat{\rho}_{\text{S}}$) denotes the detector (system) density matrix. For conventional reasons, we shall refer to the detector degree of freedom as **ancilla**. Without loss of generality and for simplicity, let's assume the ancilla is prepared in a definite eigenstate of an operator $\hat{O}$, i.e. $\hat{\rho}_{\text{A}} = |0\rangle\langle 0|$. Suppose there is a time (unitary) evolution on the joint system represented by the operator $\hat{U}_{\text{joint}}$, which we can express as

$$\hat{U}_{\text{joint}} = \sum_{\substack{n,n' \\ s_j,s'_j}} u_{n,s_j,n',s'_j} \left|n\middle\rangle\middle\langle n'\right| \otimes |s_j\rangle\langle s'_j|, \tag{2.8}$$

where $\{|n\rangle\}$, $n = 0 \ldots N-1$ is the eigenbasis of $\hat{O}$ (complete) and $\{|s_j\rangle\}$ is some complete basis we choose to represent the system. To further clarify the procedure, let's rewrite Eq.(2.8) as

$$\hat{U}_{\text{joint}} = \sum_{n,n'} \left|n\middle\rangle\middle\langle n'\right| \otimes \hat{K}_{n,n'}, \text{ where } \hat{K}_{n,n'} = \sum_{s_j,s'_j} u_{n,s_j,n',s'_j} |s_j\rangle\langle s'_j|, \tag{2.9}$$

and the operator $\hat{K}_{n,n'}$ acts on the system only: suppose $\{|s_j\rangle\}$, $\dim(\{|s_j\rangle\}) = q$ is finite-dimensional, in matrix-form we have

$$\hat{U}_{\text{joint}} = \begin{pmatrix} \hat{K}_{0,0} & \hat{K}_{0,1} & \ldots & \hat{K}_{0,N-1} \\ \hat{K}_{1,0} & \hat{K}_{1,1} & \ldots & \hat{K}_{1,N-1} \\ \vdots & \vdots & \ddots & \vdots \\ \hat{K}_{N-1,0} & \hat{K}_{N-1,1} & \ldots & \hat{K}_{N-1,N-1} \end{pmatrix}, \tag{2.10}$$

where $\hat{K}_{l,m}$ are matrices of dimension $q \times q$. As we prepared $\hat{\rho}_{\mathrm{A}} = |0\rangle\langle 0|$, only the first sub-block column is involved, the set of $\{\hat{K}_{l,0}\}$. Using the unitarity of $\hat{U}^{\dagger}_{\mathrm{joint}}\hat{U}_{\mathrm{joint}} = \mathbb{I}$, the set of $\{\hat{K}_{l,0}\}$ satisfy the following property

$$\sum_{n=1}^{N-1} \hat{K}^{\dagger}_{l,0}\hat{K}_{l,0} = \mathbb{I}_{q\times q}. \tag{2.11}$$

Note that the identity acts on the system.

If the ancilla is now projectively measured in the operator $\hat{O}$ after an evolution, given an outcome λ_m corresponding to the eigenstate $|m\rangle$, the resultant unnormalised joint density matrix is (cf Eq.(2.5))

$$\check{\rho}_1 = (|m\rangle\langle m| \otimes \mathbb{I})\hat{U}_{\mathrm{joint}}\left(|0\rangle\langle 0| \otimes \hat{\rho}_{\mathrm{S}}\right)\hat{U}^{\dagger}_{\mathrm{joint}}(|m\rangle\langle m| \otimes \mathbb{I}) = |m\rangle\langle m| \otimes \hat{K}_{m,0}\hat{\rho}_{\mathrm{S}}\hat{K}^{\dagger}_{m,0}. \tag{2.12}$$

The final state is simply $\hat{\rho}_1 = \check{\rho}_1/\operatorname{Tr}[\check{\rho}_1]$. Analogously, the probability of such an outcome is

$$p_m = \operatorname{Tr}\left[|m\rangle\langle m| \otimes \hat{K}_{m,0}\hat{\rho}_{\mathrm{S}}\hat{K}^{\dagger}_{m,0}\right] = \operatorname{Tr}\left[\hat{K}_{m,0}\hat{\rho}_{\mathrm{S}}\hat{K}^{\dagger}_{m,0}\right], \tag{2.13}$$

and can be checked that $\sum_m p_m = 1$ using Eq.(2.11). In the second equality, we used the fact that the trace of a tensor product is the product of individual traces. The above procedures can readily be generalised to an inseparable initial joint state, mixed initial ancilla states or degenerate measurement operators by summing over the indices of $\hat{K}_{m,0}$:

$$p_m = \sum_{j_m,l,k} \operatorname{Tr}\left[|j_m\rangle\langle j_m| \otimes \hat{K}_{j_m,l}\hat{\rho}_{\mathrm{S},k}\hat{K}^{\dagger}_{j_m,l}\right], \tag{2.14}$$

where j_m is the index of degenerate eigenket, l is the contribution from a mixed ancilla state, and k is the contribution from an inseparable state. Without loss of generality, a separable initial joint state is always assumed for the rest of the thesis.

We now have a full description of generalised/indirect quantum measurement through an ancilla-system interaction, which is entirely characterised by Eq.(2.11)-(2.13). The system is updated via backaction from the ancilla. Moreover, any set of operators $\{K_l\}$ with their sum satisfying the restriction Eq(2.11) automatically describes a valid indirect measurement process: one can write down a joint unitary with the first sub-block column made out of $\{K_l\}$, and the remaining columns can be filled using Gram–Schmidt process to ensure unitarity. With this, we can formulate a mathematical description of quantum measurements in the following.

Quantum measurements — a quantum measurement is a set of outcomes $\{\lambda_m\}$ and an associated set of linear maps $\{\varepsilon_m\}$ (also known as quantum channels) with the following properties.

Property 2.1.1. The probability p_m of an outcome λ_m is

$$p_m = \mathrm{Tr}\big[\varepsilon_m(\hat{\rho})\big], \text{ where } \varepsilon_m(\hat{\rho}) = \sum_{j_m,l} \hat{K}_{j_m,l}\hat{\rho}\hat{K}^{\dagger}_{j_m,l},$$

and the associated set of operators $\{\hat{K}_{j_m,l}\}$ are called **Kraus operator**. $\varepsilon_m(\hat{\rho})$ is the un-normalised post-measurement state, and the indices $\{j_m\}$ and $\{l\}$ account for the degeneracy of the outcomes and mixedness of the initial ancilla state.

Property 2.1.2. The set of $\{\varepsilon_m(\hat{\rho})\}$, equivalently the set of Kraus operators $\{\hat{K}_{j_m,l}\}$, satisfies the condition

$$\sum_m \mathrm{Tr}\big[\varepsilon_m(\hat{\rho})\big] = 1 \leftrightarrow \sum_m \sum_{j_m,l} \hat{K}^{\dagger}_{j_m,l}\hat{K}_{j_m,l} = \mathbb{I}$$

Property 2.1.3. The set of $\{\varepsilon_m(\hat{\rho})\}$ are *completely positive*: the set of Kraus operators $\{\hat{K}_{j_m,l}\}$ must be derivable from a joint unitary (cf Eq.(2.8)) of arbitrary ancilla dimension. In other words, they define positive-operator valued measure(POVM)[1] [27, 161].

[1] A measure is a map associating any subset of a set with a number. The term 'positive-operator' embodies the fact that any subset of the operators $\hat{K}^{\dagger}_{j_m,l}\hat{K}_{j_m,l}$ are 'positive': the resultant density matrix $\sum_{\mathcal{M}} \varepsilon_m(\hat{\rho})$ of any subset of outcome $\mathcal{M} \subseteq \{\lambda_m\}$ is always positive with $\mathrm{Tr}\big[\sum_{\mathcal{M}} \varepsilon_m(\hat{\rho})\big] = p_{\mathcal{M}} > 0$. Thus, POVM represents the measure induced by the set of Kraus operators, where a number 'probability' is associated with any subset of $\{\hat{K}^{\dagger}_{j_m,l}\hat{K}_{j_m,l}\}$, $m \in \mathcal{M}$.

It can be checked that the conventional projective measurements automatically satisfy these properties. More importantly, one can define a quantum measurement process that interacts with the system minimally: this is known as continuous measurement[1], which will be the subject in the following section.

2.1.2 Stochastic measurement-induced quantum evolution

With the formalism above, we are in a position to describe continuous measurement. There are two approaches to writing down the Kraus operators, and they can produce the same time-continuum evolution. I call the first approach 'one-dimensional pointer' and the second approach 'two-level ancilla'. Without loss of generality and unless specified, I consider only quantum measurements of a specific subset of two-level operators, which I term as *Gaussian-preserving measurement operators*.

Definition 2.1.2. Gaussian-preserving measurement operators—A measurement operator $\hat{O}$ is said to be *Gaussian-preserving* if it has the property

$$\hat{O}^2 \propto \mathbb{I},$$

which implies $\hat{O} \propto \hat{\Pi}_+ - \hat{\Pi}_-$, where $\hat{\Pi}_+$ ($\hat{\Pi}_-$) is the projector to $+1$ (-1) subspace[2].

I also refer to a sequence of measurement outcomes as *quantum trajectory*, and sometimes will be shorthanded as trajectory.

2.1.2.1 One dimensional pointer

[1]In literature, it is sometimes called 'weak measurement', but we reserve the term 'weak' for later purposes.

[2]This is because $\hat{O}^2 = A^2\mathbb{I}$ implies its eigenvalues must be $\pm A$, with each eigenvalue corresponding to a different projector in the spectral decomposition. It also means that there exists an operator $\hat{O}' = (\mathbb{I} - \hat{O}/A)/2$ that squares to itself, and is considered to be Gaussian-preserving as well.

Consider the following set of Kraus operators $\{\hat{K}_j(x_j)\}$ associated with the measurement of a Gaussian-preserving measurement operator $\hat{O}_j = \hat{\Pi}_{j,+} - \hat{\Pi}_{j,-}$

$$\hat{K}_j(x_j) \propto \sqrt{G(x_j - \lambda)}\hat{\Pi}_{j,+} + \sqrt{G(x_j + \lambda)}\hat{\Pi}_{j,-} = \sqrt{G(x_j - \lambda\hat{O}_j)}, \tag{2.15}$$

where $x_j \in \{-\infty, +\infty\}$ is the measurement outcome, and λ quantifies the strength of the measurement backaction from the ancilla. $G(y)$ is a Gaussian distribution

$$G(y) = \frac{1}{\sqrt{2\pi\Delta^2}} e^{-\frac{y^2}{2\Delta^2}}. \tag{2.16}$$

The role of the index j will become clear later, but it can be ignored for now, i.e. assume $j = 1$ only. It can be checked that Eq.(2.15) satisfies the properties 2.1.1-2.1.3 (integrate over all x_j), and thus represents a physical quantum measurement process; it represents a measurement operator coupled to a Gaussianly distributed one-dimensional particle (with coupling strength proportional to λ) whose position is projectively measured [27], see Fig. 2.1 for a schematic illustration.

Given a pure density matrix $\hat{\rho} = |\psi\rangle\langle\psi|$, the probability distribution of the continuous outcome x_j is

$$P(x_j) = \langle\psi|\hat{K}_j^\dagger(x_j)\hat{K}_j(x_j)|\psi\rangle = G(x_j - \lambda)\langle\hat{\Pi}_{j,+}\rangle + G(x_j + \lambda)\langle\hat{\Pi}_{j,-}\rangle, \tag{2.17}$$

and $\langle\dots\rangle$ represents the expectation value w.r.t. $|\psi\rangle$, see Fig.2.2 for a display. The update conditional to the outcome x_j follows

$$\check{\rho}(x_j) = \hat{K}_j(x_j)\,|\psi\rangle\langle\psi|\,\hat{K}_j^\dagger(x_j). \tag{2.18}$$

We will stay within the framework of pure state for now and consider only the update of the ket.

Two limits can be identified from Eq.(2.15) and (2.17):

1. $\lambda/\Delta \gg 1$— This is the projective limit, and the Kraus operator is effectively a projective measurement: the variance is sufficiently small (compared to the mean) such that most of the probability density concentrates at $\pm\lambda$. There is little to no overlap between the two Gaussians, and the outcomes are practically binary

$$x_j \simeq \{+\lambda, -\lambda\}, \text{ with } p_{\pm\lambda} \simeq \langle\hat{\Pi}_{j,\pm}\rangle. \tag{2.19}$$

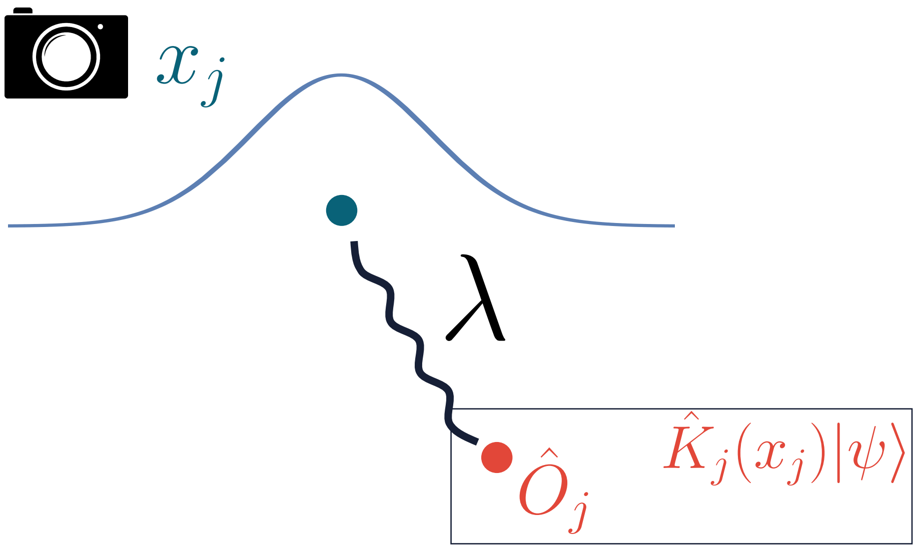

Figure 2.1: Schematic sketch for the physical setup of $\hat{K}_j(x_j)$ in Eq.(2.15). First, the one-dimensional pointer is projectively measured (camera), yielding a measurement result x_j, which is distributed according to a Gaussian distribution. Then, the system-ancilla Hamiltonian with strength λ (curly line) induces a change in the system. Upon tracing out the ancilla degree of freedom, the resultant measurement backaction on the system is described by $\hat{K}_j(x_j)$.

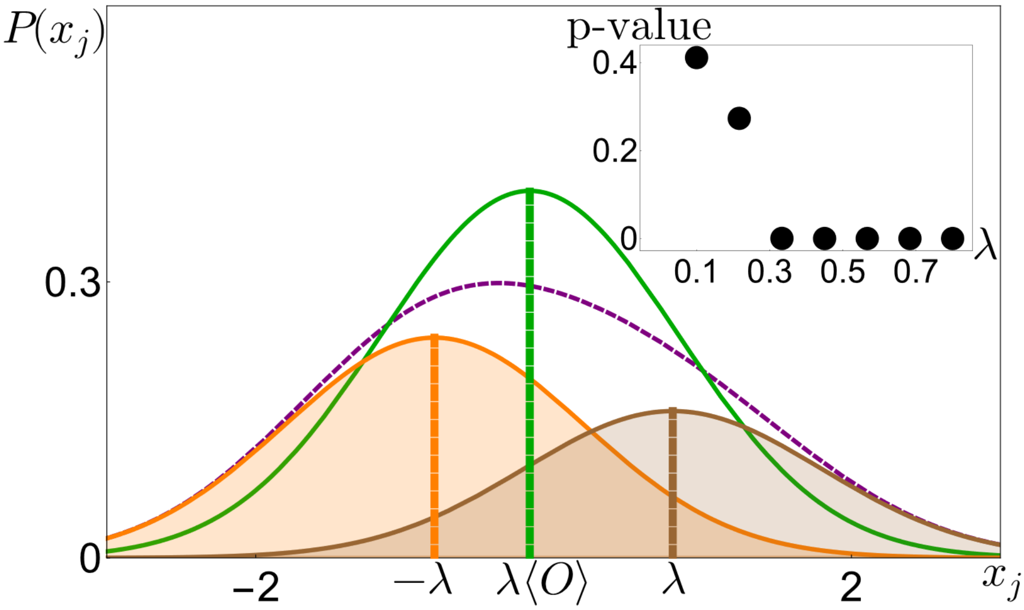

Figure 2.2: Probability distribution of continuous Gaussian measurement readouts Eq.(2.17). The readout distribution $P(x_j)$ (dashed purple) results from the sum of two overlapping Gaussians (brown and orange shaded), centred at positions λ and $-\lambda$ with different heights $\langle \Pi_{j,-} \rangle$ and $\langle \Pi_{j,+} \rangle$ respectively. The green curve shows the approximation of $P(x_j)$ by Eq.(2.20), which becomes exact in the limit of continuous measurements $\lambda/\Delta \to 0$ — cf. inset. Inset: Accuracy of the approximation in Eq.(4.3) quantified via a two-sample Kolmogorov-Smirnov test [163]. The accuracy (p-value) increases with decreasing λ and becomes exact in the case of continuous measurement $\lambda/\Delta \sim \sqrt{dt} \to 0$. The parameters are set as $\lambda = 0.8$, $\Delta = 1$, $\langle \Pi_{j,+} \rangle = 0.4$ and $\langle \Pi_{j,-} \rangle = 0.6$.

This is equivalent to the action of a projective measurement of the operator $\hat{O}_j = \hat{\Pi}_{j,+} - \hat{\Pi}_{j,-}$ (see the beginning of 2.1). The conditional update by the Kraus operator is virtually a projection.

2. $\lambda/\Delta \ll 1$— In this limit, the system-ancilla coupling is weak, and the two Gaussian distributions in the probability density $P(x_j)$ increasingly overlap. The measurements become continuous. Noting that the average of x_j is $\int_{-\infty}^{\infty} x_j P(x_j) dx_j = \lambda\langle\hat{O}_j\rangle$ and the variance is Δ^2, the two overlapping Gaussians may be approximated by a single Gaussian with the same average and variance

$$P(x_j) \approx \frac{1}{\sqrt{2\pi\Delta^2}} e^{-\frac{(x_j - \lambda\langle\hat{O}_j\rangle)^2}{2\Delta^2}}. \tag{2.20}$$

This becomes statistically indistinguishable in the limit $\lambda/\Delta \to 0$, as shown by the two-sample statistical test in Fig. 2.2. This approximation scheme is displayed in Fig. 2.2.

Hence, the Kraus operator $\hat{K}_j(x_j)$ interpolates between projective and continuous measurements as a function of λ/Δ. I will discuss only the continuous limit in the current topic of interest. In this limit, let's assign the following scaling to λ

$$\lambda = 2\Delta\sqrt{\gamma dt}, \tag{2.21}$$

where dt is an infinitesimal time increment — we measure the system via $\hat{K}_j(x_j)$ with infinitesimal duration. γ is the time-continuum measurement strength: the backaction λ and the duration dt simultaneously approaches to 0 but their ratio is fixed. Next, we define a new random variable ξ, related to x_j by

$$\xi_j = \frac{x_j - \lambda\langle\hat{O}_j\rangle}{\Delta} \Rightarrow \text{mean}(\xi_j) = 0 \text{ and } \text{var}(\xi_j) = 1. \tag{2.22}$$

Substituting ξ_j into Eq.(2.20), the action of $\hat{K}_j(x_j)$ on the $|\psi\rangle$ is

$$\begin{aligned}
\hat{K}_j(x_j)|\psi\rangle &= \frac{1}{(2\pi\Delta^2)^{1/4}} e^{-\frac{(\Delta\xi_j + \lambda\langle\hat{O}_j\rangle - \lambda\hat{O}_j)^2}{4\Delta^2}} |\psi\rangle \\
&= \frac{1}{\mathcal{N}_j} \exp\left[\frac{\xi_j\lambda(\hat{O}_j - \langle\hat{O}_j\rangle)}{2\Delta} - \frac{\lambda^2(\hat{O}_j - \langle\hat{O}_j\rangle)^2}{4\Delta^2}\right]|\psi\rangle \\
&= \frac{1}{\mathcal{N}_j} \exp\Big[\xi_j\sqrt{\gamma dt}(\hat{O}_j - \langle\hat{O}_j\rangle) - \gamma dt(\hat{O}_j - \langle\hat{O}_j\rangle)^2\Big]|\psi\rangle, \qquad (2.23)
\end{aligned}$$

and $\mathcal{N}$ is the normalisation. In the second equality, we absorb any operator-independent terms into $\mathcal{N}$. ξ_j is a Gaussian random variable with mean 0 and variance 1; we can recast this backaction as a Wiener process $dW_j^t \equiv \xi_j\sqrt{\gamma dt}$ with property

$$dW_j^t dW_j^{t'} = \gamma dt \delta_{t,t'}. \tag{2.24}$$

The superscript t keeps track of different time steps, and we will generally drop it. Thus, the evolution of $|\psi\rangle$ under continuous measurement is a stochastic differential equation

$$\begin{aligned}\hat{K}_j(x_j)|\psi\rangle \equiv |\psi_{dt}\rangle &= \frac{1}{\mathcal{N}_j}\exp\Big[dW_j(\hat{O}_j - \langle\hat{O}_j\rangle) - \gamma dt(\hat{O}_j - \langle\hat{O}_j\rangle)^2\Big]|\psi\rangle \\ |\psi_{dt}\rangle &= [1 + dW_j(\hat{O}_j - \langle\hat{O}_j\rangle) - \frac{\gamma}{2}dt(\hat{O}_j - \langle\hat{O}_j\rangle)^2 + \mathcal{O}(dt^{3/2})]|\psi\rangle,\end{aligned} \tag{2.25}$$

and the equation has been normalised. Anticipating unitary dynamics in the system, the combined evolution is

$$d|\psi\rangle = -i\hat{H}dt|\psi\rangle + dW_j(\hat{O}_j - \langle\hat{O}_j\rangle)|\psi\rangle - \frac{\gamma}{2}dt(\hat{O}_j - \langle\hat{O}_j\rangle)^2|\psi\rangle, \tag{2.26}$$

where H is the Hamiltonian generating the unitary component. Eq.(2.26) can readily be generalised to multiple simultaneous continuous measurements: upon measuring $\{\hat{O}_j\}$'s simultaneously, the joint action on the ket is given by the product

$$\prod_j \hat{K}_j(x_j)|\psi\rangle.$$

Each jth Kraus operator is uncorrelated with each other, giving rise to independent Wiener processes. We have as the final result

$$d|\psi\rangle = -iHdt|\psi\rangle + \sum_j dW_j(\hat{O}_j - \langle\hat{O}_j\rangle)|\psi\rangle - \frac{\gamma}{2}dt\sum_j(\hat{O}_j - \langle\hat{O}_j\rangle)^2|\psi\rangle, \tag{2.27}$$

where $dW_j dW_{j'} = \delta_{j,j'}\gamma dt$ and the expectation value $\langle\hat{O}\rangle$ is evaluated at time t w.r.t. $|\psi(t)\rangle$. This is known as the *quantum state diffusion equation*, a stochastic Schrödinger equation. I will return to this stochastic differential equation later on[1].

[1]See Ref. [164] for more on stochastic differential equations, also known as Itô calculus.

2.1.2.2 Two-level ancilla

In this protocol, we restrict to systems of two-level local degrees, e.g. qubits. The ancilla is a two-level system[1] that can perform any continuous Gaussian-preserving measurements. Furthermore, beside Eq.(2.27), a new stochastic Schrödinger equation, named *quantum jump equation*, emerges if the joint unitary is altered. We include the explicit form of the joint unitary corresponding to each set of Kraus operators in Appendix A's subsections. Without loss of generality, we consider continuous measurement of the operator $\hat{n} = |1\rangle\langle 1|$ in the system of interest[2].

Quantum state diffusion equation — consider the following set of Kraus operators on a two-level system obtained from the joint unitary Eq.(A.1)

$$\begin{aligned} \hat{K}_{+\epsilon} &= \sqrt{\frac{1}{2}}\,|0\rangle\langle 0| + \sqrt{\frac{1}{2}+\epsilon}\,|1\rangle\langle 1|\,, \\ \hat{K}_{-\epsilon} &= \sqrt{\frac{1}{2}}\,|0\rangle\langle 0| + \sqrt{\frac{1}{2}-\epsilon}\,|1\rangle\langle 1|\,. \end{aligned} \tag{2.28}$$

Their respective probabilities of happening follow from property 2.1.1. ϵ quantifies the backaction strength from the ancilla, similar to λ in Eq.(2.15).

An arbitrary state of the system is of the form $|\psi\rangle = \alpha|0\rangle + \beta|1\rangle$, $|\alpha|^2 + |\beta|^2 = 1$. When acted upon by the Kraus operators, the possible resultant state $|\psi'\rangle$ is binomially distributed

$$|\psi'\rangle = \begin{cases} \begin{array}{c} \alpha\left(-|\beta|^2\epsilon + \frac{3}{2}|\beta|^4\epsilon^2\right)|0\rangle \\ +\beta\left(\epsilon(|\beta|^2-1) + \frac{\epsilon^2}{2}(-1-2|\beta|^2+3|\beta|^4)\right)|1\rangle \end{array} & \text{with weight } p_+ \\ \begin{array}{c} \alpha\left(|\beta|^2\epsilon + \frac{3}{2}|\beta|^4\epsilon^2\right)|0\rangle \\ +\beta\left(\epsilon(1-|\beta|^2) + \frac{\epsilon^2}{2}(-1-2|\beta|^2+3|\beta|^4)\right)|1\rangle \end{array} & \text{with weight } p_- \end{cases}, \tag{2.29}$$

where $p_\pm = 1/2 \pm |\beta|^2\epsilon$ are the respective probabilities. We have expanded in ϵ and only retain terms up to $\mathcal{O}(\epsilon^2)$. This probabilistic update can be recast into a single

[1] Not to be confused with the actual system of interest!

[2] One can always rotate the basis to measure other Gaussian-preserving measurement operators.

stochastic differential equation by introducing the probabilistic binomial variable $d\xi = \mp\epsilon$, rewriting $|\beta|^2 = \langle\hat{n}\rangle$, and the measurement operator $\hat{n} = |1\rangle\langle 1|$

$$|\psi'\rangle - |\psi\rangle = d|\psi\rangle = \left[2\epsilon^2(\langle\hat{n}\rangle^2 - 2\langle\hat{n}\rangle\hat{n}) + d\xi(\hat{n} - \langle\hat{n}\rangle) - \frac{\epsilon^2}{2}(\hat{n} - \langle\hat{n}\rangle)^2\right]|\psi\rangle. \quad (2.30)$$

To further simplify this expression, we centre the random variable by defining $dW = d\xi - \overline{d\xi}$, where $\overline{d\xi} = 2|\beta|^2\epsilon^2 = 2\langle\hat{n}\rangle\epsilon^2$ is the average of $d\xi$. Under this centering, the variance (and the standard deviation) is unchanged: $\overline{d\xi^2} - \overline{d\xi}^2 = \epsilon^2 = \overline{dW^2} - \overline{dW}^2$. In terms of the variable dW, Eq.(2.30) becomes

$$d|\psi\rangle = \left[dW(\hat{n} - \langle\hat{n}\rangle) - \frac{\epsilon^2}{2}(\hat{n} - \langle\hat{n}\rangle)^2\right]|\psi\rangle. \quad (2.31)$$

By assigning the scaling $\epsilon = \sqrt{\gamma dt}$, we recognise that the binomial random variable dW, over a large sample, is simply a Gaussian random variable in time with mean 0 and variance γdt. This is a Wiener process, and we recover Eq.(2.26) where $\hat{O} = \hat{n} = |1\rangle\langle 1|$ and upon including the system's unitary. Extending to a system with multiple sites readily follows and gives Eq.(2.27) (Itô calculus applies).

Quantum jumps — now consider a different set of Kraus operators obtained from a different joint unitary Eq.(A.5)

$$\begin{aligned}\hat{K}_0 &= |0\rangle\langle 0| + \cos\epsilon\,|1\rangle\langle 1| = |0\rangle\langle 0| + (1 - \frac{1}{2}\epsilon^2)\,|1\rangle\langle 1| + \mathcal{O}(\epsilon^3)\\ \hat{K}_1 &= \sin\epsilon\,|1\rangle\langle 1| = \epsilon\,|1\rangle\langle 1| + \mathcal{O}(\epsilon^3).\end{aligned} \quad (2.32)$$

Only terms up to $\mathcal{O}(\epsilon^2)$ are considered. Given a state $|\psi\rangle = \alpha|0\rangle + \beta|0\rangle$ and measurement operator $\hat{n} = |1\rangle\langle 1|$, the possible resultant states are

$$|\psi'\rangle = \begin{cases}\left[1 - \frac{\epsilon^2}{2}(\hat{n} - |\beta|^2)\right]|\psi\rangle = \left[1 - \frac{\epsilon^2}{2}(\hat{n} - \langle\hat{n}\rangle)\right]|\psi\rangle & \text{with prob } p_0\\ |1\rangle = \frac{\hat{n}}{\sqrt{\langle\hat{n}\rangle}}|\psi\rangle & \text{with prob } p_1\end{cases}, \quad (2.33)$$

with probabilities $p_0 = 1 - |\beta|^2\epsilon^2 = 1 - \langle\hat{n}\rangle\epsilon^2$ and $p_1 = |\beta|^2\epsilon^2 = \langle\hat{n}\rangle\epsilon^2$ respectively. In a single stochastic differential equation, we have

$$d|\psi\rangle = \left[-\frac{\epsilon^2}{2}(\hat{n} - \langle\hat{n}\rangle) + \delta N\left(\frac{\hat{n}}{\sqrt{\langle\hat{n}\rangle}} - 1\right)\right]|\psi\rangle, \quad (2.34)$$

where δN is a Poisson process, $\delta N \in \{0, 1\}$ with probability p_0 and p_1 respectively. Note the mean and variance are both $\langle \hat{n} \rangle \epsilon^2$, as for a Poisson process. With the same time scaling assignment $\epsilon^2 = \gamma dt$ and including the effect of the system's unitary, we arrive at

$$d|\psi\rangle = \left[-idt\{H - i\frac{\gamma}{2}(\hat{n} - \langle \hat{n} \rangle)\} + \delta N \left(\frac{\hat{n}}{\sqrt{\langle \hat{n} \rangle}} - 1 \right) \right] |\psi\rangle, \tag{2.35}$$

which is known as *quantum jumps*, a different kind of stochastic Schrödinger equation. The generalisation to multiple sites is straightforward, with each Poisson process being independent.

The stochastic Schrödinger equations, Eq.(2.35) and (2.27), have been studied extensively [27, 161, 165]. Experimentally, they correspond to different protocols: prime examples include photon homodyne detection for quantum state diffusion, and photon counting for quantum jump. They can be implemented in cold atom systems [166], which has seen tremendous advances in recent years [167–169]. Indeed, experimental realisation of quantum jump has been achieved with excellent controllability [162].

2.1.3 Post-selection and non-Hermitian dynamics

An important observation with quantum jumps is that although the effect of $\delta N = 1$ is substantial and projects the system to $|1\rangle$, the probability of $\delta N = 1$ is infinitesimally small with $p_1 = \langle \hat{n} \rangle \gamma dt$. It is, therefore, natural to consider the quantum trajectory of $(\delta N) = (0, 0, 0, \dots)$ such that all the outcomes are 0. This trajectory is called the **no-click limit**, and the ancilla's backaction is now deterministic, leading to a non-Hermitian Hamiltonian; under the no-click limit, the system evolves according to an effective non-Hermitian Hamiltonian

$$H_{\text{eff}} = H - i \sum_j \frac{\gamma}{2} \hat{O}_j, \tag{2.36}$$

where $\hat{O}_j$'s are the measurement operators.

Similarly, in the quantum state diffusion equation Eq.(2.27), recall that the measurement outcome appearing in the Kraus operator is $x_j/\Delta = dW_j + 2\gamma dt\langle\hat{O}_j\rangle$ (cf Eq.(2.22) and (2.25)). The equivalent 'no-click limit' would be fixing x_j's to be some values such that the backaction from the ancilla is purely non-Hermitian. More precisely, post-selecting $x_j = \sqrt{2\Delta\gamma}dt$ or $x_j = 0\ \forall j$, the Kraus operators conditional to this trajectory are

$$\begin{aligned}\prod_j \hat{K}_j(x_j)|\psi\rangle &= \frac{1}{\mathcal{N}}\prod_j \exp\Big[2\gamma dt((1\pm 1)/2 - \langle\hat{O}_j\rangle)(\hat{O}_j - \langle\hat{O}_j\rangle) - \gamma dt(\hat{O}_j - \langle\hat{O}_j\rangle)^2\Big]|\psi\rangle \\ &\propto \prod_j \exp\Big[2\gamma dt((1\pm 1)/2 - \langle\hat{O}_j\rangle)\hat{O}_j - \gamma dt(\hat{O}_j - 2\langle\hat{O}_j\rangle)\Big]|\psi\rangle \\ &= \prod_j \propto \exp\Big[\pm\gamma dt\hat{O}_j\Big]|\psi\rangle, \end{aligned} \tag{2.37}$$

where $+$ $(-)$ corresponds to $x_j = 2\Delta\gamma dt$ $(x_j = 0)$. Together with the system Hamiltonian H, the dynamics follow the effective Hamiltonian

$$H_{\text{eff}} = H \pm i\gamma\sum_j \hat{O}_j, \tag{2.38}$$

which is a non-Hermitian Hamiltonian, equivalent to Eq.(2.36). A vital point: arbitrary post-selection of x_j results in a non-linear evolution in state and does not correspond to any non-Hermitian Hamiltonian.

This shows that continuous measurement and non-Hermitian dynamics are strongly interlinked; a substantial part of this thesis is devoted to studying this connection. From now on, I will mostly suppress the hat above the operator for notational convenience. I will also use the term '*monitoring*' for continuous quantum measurement; the two words are interchangeable. To fix some notation, throughout this thesis, I shall use the terms 'post-selected' and 'monitored' to indicate respectively the fully post-selected measurement dynamics and the fully stochastic continuous measurement where all readouts are retained.

2.1.4 Inefficient measurement

In Ch. 2.1.2, we outlined how quantum measurements influence a system, and we arrive at Eq.(2.27) and (2.35) describing the dynamics of the system. In deriving the dynamics, an underlying assumption implicitly used is that the observer has perfect knowledge of all measurement outcomes: the outcome from the microscopic part (ancilla) translates perfectly and correctly to the detector's readout. However, real physical processes/experiments are often imperfect, and a faulty detector fails to output correctly despite the underlying quantum process registering the correct outcome. When such imperfections happen, the quantum measurement is *inefficient*. The uncertainty that arises from inefficient measurement is purely *classical*, which introduces classical statistical mixedness in the system's dynamics. Below, we derive the dynamics of inefficient measurement in the context of the quantum state diffusion equation. Similar procedures apply to the quantum jump.

From the microscopic perspective, there are two scenarios in which a measurement is considered inefficient: 1. the detector only records a fraction of the readout, and 2. the readouts by the detector can be wrong. Case 1 arises naturally in a photon counting detector, and case 2 is a fault in the experimental apparatus [27, 165]. In both cases, a description based on the density matrix should be used in favour of a ket for the ease of introducing classical uncertainty. For clarity, the evolution of the density matrix by a quantum state diffusion equation reads

$$\partial_t \hat{\rho} = -idt[H, \hat{\rho}] + \sum_j dW_j (O_j - \langle O_j \rangle) - \frac{\gamma}{2} dt \sum_j [O_j, [O_j, \hat{\rho}]], \tag{2.39}$$

where Itô calculus, $dW_j dW_{j'} = \gamma dt \delta_{j,j'}$, applies.

Consider case 1, where one can view the actual physical detector as two imaginary sub-detectors: the first sub-detector with measurement strength γ_1 is a perfect detector where all readouts from the actual detector are recorded by it solely. In contrast, the second sub-detector with measurement strength γ_2 is ignorant of all its readouts, and the observer only has access to the average dynamics induced by it. To begin with, let's write down the evolution of the density matrix, assuming both detectors are efficient

$$
\begin{aligned}
d\rho_t = &\sum_j \{O_j - \langle O_j\rangle, \rho_t\} dW^t_{1,j} - \sum_j \frac{\gamma_1}{2} dt\left[O_j, [O_j, \rho_t]\right] \\
&+ \sum_j \{O_j - \langle O_j\rangle, \rho_t\} dW^t_{2,j} - \sum_j \frac{\gamma_2}{2} dt\left[O_j, [O_j, \rho_t]\right], \qquad (2.40)
\end{aligned}
$$

where $dW^t_{\alpha,k} dW^{t'}_{\beta,l} = \gamma_\alpha \delta_{\alpha,\beta}\delta_{k,l} dt \delta_{t,t'}$. In reality, since we are ignorant of the outcome of detector 2, we only have access to its average

$$
\begin{aligned}
d\rho_t &= \sum_j \{O_j - \langle O_j\rangle, \rho_t\} dW^t_{1,j} - \sum_j \frac{\gamma_1}{2} dt\left[O_j, [O_j, \rho_t]\right] - \sum_j \frac{\gamma_2}{2} dt\left[O_j, [O_j, \rho_t]\right] \\
&= \sum_j \{O_j - \langle O_j\rangle, \rho_t\} \sqrt{\frac{\gamma_1}{\gamma_1 + \gamma_2}} dW^t_j - \sum_j \frac{\gamma_1 + \gamma_2}{2} dt\left[O_j, [O_j, \rho_t]\right] \\
&\equiv \sum_j \{O_j - \langle O_j\rangle, \rho_t\} \sqrt{\eta} dW^t_j - \sum_j \frac{\gamma}{2} dt\left[O_j, [O_j, \rho_t]\right]. \qquad (2.41)
\end{aligned}
$$

We have defined a new Itô process $dW^t_j dW^{t'}_k = (\gamma_1 + \gamma_2) dt \delta_{t,t'} \delta_{j,k}$ and $\gamma_1 + \gamma_2$ is the true measurement strength of the actual detector. $\eta = \gamma_1/(\gamma_1 + \gamma_2)$ is the efficiency of the measurement with $\eta = 1$ for efficient measurement and $\eta = 0$ for inefficient measurement. This shows that inefficiency can be associated with incomplete knowledge.

We now demonstrate how case 2, wrong outputs by the detector, generate inefficiency. To proceed, we remind ourselves that continuous measurements are simply backactions from the projectively measured ancillae and appear as a quantum channel upon tracing out the ancillae's degree of freedom. With a slight modification of Eq.(2.28), the channel for quantum state diffusion equation can equivalently be represented by the following Kraus' operators:

$$
\begin{aligned}
K_u &= \frac{1}{\sqrt{2}}\left(\sqrt{1+\epsilon}\,|1\rangle\langle 1| + \sqrt{1-\epsilon}\,|0\rangle\langle 0|\right) \\
K_d &= \frac{1}{\sqrt{2}}\left(\sqrt{1-\epsilon}\,|1\rangle\langle 1| + \sqrt{1+\epsilon}\,|0\rangle\langle 0|\right), \qquad (2.42)
\end{aligned}
$$

and they satisfy the condition $K_u^\dagger K_u + K_d^\dagger K_d = \mathbb{I}$. ϵ is a small parameter, and we need only terms up to $\mathcal{O}(\epsilon^2)$. The two Kraus' operators in Eq.(2.42) correspond to the two possible readouts from the ancilla, and they update the state in the following way: given a readout $\mathrm{r} \in \{u, d\}$, the state after a measurement event is

$$\begin{aligned}\rho_{(u)} &= \frac{K_u \rho K_u^\dagger}{p_u} \text{ , if } \mathrm{r} = u \\ \rho_{(d)} &= \frac{K_d \rho K_d^\dagger}{p_d} \text{ , if } \mathrm{r} = d,\end{aligned} \tag{2.43}$$

with respective probability $p_u = \mathrm{Tr}\big[K_u \rho K_u^\dagger\big]$ and $p_d = \mathrm{Tr}\Big[K_d \rho K_d^\dagger\Big]$. ρ_u and ρ_d represents the post-measurement state corresponding to readout u and d. Eq.(2.43) assumes perfect detector: let $\Delta \in (0, 1)$ be the conditional probability of a detector readout to be u given that the actual readout is u, $\Delta = p(\mathrm{r} = u|u) = 1$ is unity for perfect measurement (respectively for d). Consider now systematic errors so that $\Delta = p(\mathrm{r} = u|u) < 1$ can be less than 1. The effect of this error on the density matrix modifies Eq.(2.43) to be

$$\begin{aligned}\rho_{(\mathrm{r}=u|u)} &= \frac{\Delta K_u \rho K_u^\dagger + (1-\Delta) K_d \rho K_d^\dagger}{p_{(u)}} \\ \rho_{(\mathrm{r}=d|d)} &= \frac{\Delta K_d \rho K_d^\dagger + (1-\Delta) K_u \rho K_u^\dagger}{p_{(d)}}.\end{aligned} \tag{2.44}$$

$p_{(u)} = \mathrm{Tr}\Big[\Delta K_u \rho K_u^\dagger + (1-\Delta) K_d \rho K_d^\dagger\Big]$ (and similarly $p_{(d)}$) now holds. $\Delta = 0.5$ corresponds to a completely inefficient detector whose readout is completely random, and $\Delta < 0.5$ is equivalent to exchanging $u \leftrightarrow d$ and a 'flipped' conditional probability $\Delta' = 1 - \Delta$ (a detector with $\Delta = 0$ has its readouts 'flipped', but working just fine). Expanding Eq.(2.44) up to $\mathcal{O}(\epsilon^2)$, we can combine both equations into a single differential equation:

$$\begin{aligned}d\rho = &\frac{dW}{2}(2\Delta - 1)\{\sigma^z, \rho\} - \frac{\epsilon^2}{8}\left[\sigma^z, [\sigma^z, \rho]\right] \\ &- dW(2\Delta - 1)\langle\sigma^z\rangle\rho - \frac{(2\Delta-1)^2}{2}\epsilon^2\langle\sigma^z\rangle\{\sigma^z, \rho\} \\ &+ (2\Delta - 1)^2\epsilon^2\rho\langle\sigma^z\rangle^2.\end{aligned} \tag{2.45}$$

$d\rho$ represents the change in ρ after a measurement event ($d\rho \equiv \rho_{(\mathrm{r}=k|k)} - \rho, k \in \{u, d\}$), and we introduce a binomial variable $dW = \pm\epsilon$ with probability distribution

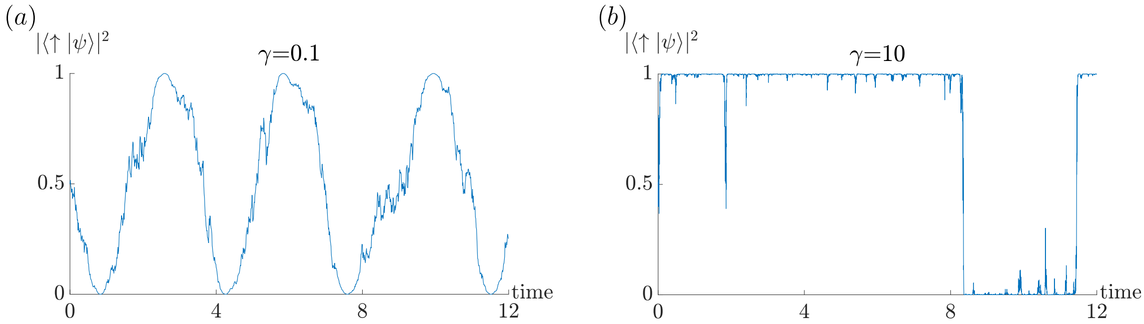

Figure 2.3: A spin-1/2 under the evolution of Eq.(2.47), and the figures show the probability of a spin-1/2 being in $|\uparrow\rangle$ in spin-z basis. The initial state was chosen to be $1/\sqrt{2}(|\uparrow\rangle+|\downarrow\rangle)$ so that the components stay real at all times, lowering the numerical cost. (a): plot for $\gamma=0.1$. (b): plot for $\gamma=10$

$p(\pm\epsilon)=1/2(1\pm(2\Delta-1)\epsilon\langle\sigma^z\rangle)$ and $\overline{dW}=\epsilon^2(2\Delta-1)\langle\sigma^z\rangle$. Constructing a new binomial variable $d\xi=dW-\overline{dW}$ (overline corresponds to average), the mean is now centred at zero $\overline{d\xi}=0$ and the variance $\overline{d\xi^2}=\epsilon^2+\mathcal{O}(\epsilon^4)=\overline{dW^2}$ is unchanged up $\mathcal{O}(\epsilon^2)$. Eq.(2.45) now becomes

$$d\rho=\frac{d\xi}{2}(2\Delta-1)\{\sigma^z-\langle\sigma^z\rangle,\rho\}-\frac{\epsilon^2}{8}\left[\sigma^z,[\sigma^z,\rho]\right]. \tag{2.46}$$

Setting the scaling $\epsilon=2\sqrt{\gamma dt}$, $d\xi$ is equivalent to a Wiener process (central limit theorem giving Gaussian distribution) with mean 0 and variance $4\gamma dt$ in the time continuum limit. With this, we recover Eq.(2.41) with $\eta=|2\Delta-1|^2$ (and appropriate rescaling).

2.1.5 Quantum Zeno effect

As demonstrated in previous sessions, quantum measurement tends to bring the system to one of the measurement operator's eigenstates. Combined with an 'incompatible' Hamiltonian, the two dynamics compete. It is natural to question what happens to the dynamics under the strong influence of measurement, i.e., frequent projective or strong continuous measurement. In this setting, the system's state is mostly frozen in one of the measurement operator's eigenstates, with occasional jumps between them induced by the unitary. This is known as the quantum Zeno effect [1, 2]. As an example, consider a single spin-1/2 model with the Hamiltonian $H = \sigma_y$ and measurement operator $O = \sigma_z$. Consider continuous measurement in the context of quantum state diffusion protocol; the spin-1/2 evolution follows

$$\begin{aligned} d|\psi\rangle &= \left[-i\sigma_y dt + dW(\sigma_z - \langle\sigma_z\rangle) - \frac{\gamma}{2}dt(\sigma_z - \langle\sigma_z\rangle)^2\right]|\psi\rangle \\ \rightarrow |\psi_{t+dt}\rangle &= e^{-i\sigma_y dt + dW(\sigma_z - \langle\sigma_z\rangle) - \gamma dt(\sigma_z - \langle\sigma_z\rangle)^2}|\psi\rangle, \end{aligned} \tag{2.47}$$

and since $[\sigma_y, \sigma_z] \neq 0$, there is a competition between the two. By numerically simulating the dynamics at a trajectory level[1], we can calculate the probability of the state $|\psi\rangle$ being in one of the eigenstates of the measurement (σ_z basis). The results are shown in Fig. 2.3 for two different measurement strengths, $\gamma = 0.1$ in Fig. 2.3(a) and $\gamma = 10$ in Fig. 2.3(b). For weak measurement influence $\gamma = 0.1$, the system mostly follows a coherent evolution, displaying oscillations between $|\uparrow\rangle$ and $|\downarrow\rangle$. For strong measurement, the system does not oscillate and instead is mostly pinned at $|\uparrow\rangle$ or $|\downarrow\rangle$ with occasional jumps between them; this is the quantum Zeno regime.

Since the initial theoretical proposal of quantum Zeno effect in the context of projective measurements [1, 2], many theoretical analyses have been done [6, 170–174], along with crucial experimental observations [23, 175–178]. Furthermore, theoretical analysis on continuous measurement has shown enriched dynamics in Zeno effect [10, 179–181], with promising experimental platform to test on [162].

Measurement-induced phase transition In simple terms, MiPT is a many-body phenomenon which arises when a many-body system is subject to incompatible quantum measurements. Unlike conventional quantum phase transition driven by quantum fluctuation, MiPT is a quantum phase transition driven by quantum measurement. In essence, when the measurement is weak, the system can build up

[1]The evolution is trotterized into a product of unitary and measurement parts, with the measurement part update given by the Kraus operator Eq.(2.25); in a finite time interval, Eq.(2.25) accounts all higher order expansion of the finite random Wiener process δW accurately.

long-range correlation induced by the coherent evolution of the unitary dynamics; when the measurement is strong, a many-body version of the quantum Zeno effect sets in, and the system is pinned in one of the eigenstates of the measurement, with short-range correlation. Remarkably, at the many-body level, the quantum Zeno effect becomes a phase transition [36, 64–67], and a critical measurement strength appears, separating these two distinct regimes; conventional scaling exponents apply, characterising the universality of the phase transition. In Ch. 2.4, I discuss various subtle non-trivial aspects in characterising MiPTs.

2.2 Methods for (1+1)d fermionic systems

All of the many-body quantum systems studied in this thesis are spatially and temporally one-dimensional: (1+1)d. This chapter provides most of the relevant techniques in 1D quantum systems for this thesis[1].

2.2.1 Bosonisation

Bosonisation is a powerful technique for analysing 1D fermionic many-body systems. At its core, it maps a fermionic system to a bosonic system. Other related systems, such as spin chain and hard-core bosons, can be analysed using bosonisation as well[2]. This chapter follows Ref. [182] loosely.

To begin with, consider an infinitely large periodic fermionic 1D system with the following linear spectrum Hamiltonian in momentum space

$$H = \sum_{\substack{k=-\infty \\ r=R,L}}^{\infty} v_{\mathrm{F}}(\epsilon_r k - k_{\mathrm{F}}) c_{k,r}^{\dagger} c_{k,r}, \qquad \{c_{k,r}^{\dagger}, c_{k',r'}\} = \delta_{k,k'}\delta_{r,r'}, \tag{2.48}$$

where $\epsilon_R = 1$ and $\epsilon_L = -1$, and from now we will abbreviate it by r. The quantities v_{F} and k_{F} are the Fermi velocity and Fermi wavevector, respectively. A schematic drawing of H and its ground state is shown in Fig. 2.4(b); H describes a 1D system

[1] We reserve upper case ‘D’ for spatial dimension and lower case ‘d’ for spacetime dimension

[2] In combination with Jordan-Wigner transformation

with infinitely many positive and negative energy states indexed by k, and its ground state has states filled up to $v_F k_F$:

$$|\mathrm{GS}\rangle \propto \prod_{k<k_\mathrm{F}} c^\dagger_{k,R} c^\dagger_{-k,L} |0\rangle, \tag{2.49}$$

where $c_{k,r}|0\rangle = 0 \ \forall \ k, r$. The presence of infinitely many negative states might appear arbitrary, but it is one of the prerequisites of bosonisation [183]. $c_{k,r}$ (positive slope) represents the right-moving fermions and $c_{k,l}$ (negative slope) represents the left-moving fermions. To proceed, let's introduce the following momentum density operator associated with the Fourier component of the real space density operator

$$\begin{aligned}
&\rho^\dagger_r(q) = \sum_k c^\dagger_{k+q,r} c_{k,r} \\
&\rho_r(x) = c^\dagger_r(x) c_r(x) = \frac{1}{L_0} \sum_{q,k} c^\dagger_{k+q,r} c_{k,r} e^{-iqx} = \frac{1}{L_0} \sum_q \rho^\dagger_r(q) e^{-iqx},
\end{aligned} \tag{2.50}$$

where L_0 is the length of the system and is taken to be infinite. As usual, $\rho_r(q) = \rho^\dagger_r(q)$. Since there are infinitely many occupied states, matrix elements of $\rho^\dagger$ can be infinite, i.e. the ground/vacuum state[1] expectation value of $\rho^\dagger(x)$ (and $\rho^\dagger(q=0)$) is, in fact, infinite. To avoid infinity, *normal ordering* must be introduced to keep all operators well-defined.

Definition 2.2.1. Fermionic normal ordering— The fermionic normal ordering of two operators, A and B, w.r.t to a ground/vacuum state is defined as

$$: AB := AB - \langle 0|AB|0\rangle, \tag{2.51}$$

where $|0\rangle$ is the ground/vacuum state. This is the same as ordering all the excitation creation (annihilation) operators on the left (right), w.r.t. the vacuum, such that $: AB : |0\rangle = 0$ annihilate the vacuum state. For occupied states, the creation (annihilation) operator is placed on the right (left) to destroy the vacuum state.

With the aid of normal ordering, consider the commutator between $\rho^\dagger_r(q)$ and

[1]We will call it the vacuum state as well, and the two terms are interchangeable for now.

$\rho_r^\dagger(-q')$

$$
\begin{aligned}
&[\rho_{r'}^\dagger(-q'), \rho_r^\dagger(q)] = \sum_{k_1,k_2} [c^\dagger_{k_2-q',r'} c_{k_2,r'}, c^\dagger_{k_1+q,r} c_{k_1,r}] \\
&= \delta_{r,r'} \sum_{k_1,k_2} -\delta_{k_1,k_2-q'} c^\dagger_{k_1+q,r} c_{k_2,r'} + \delta_{k_1+q,k_2} c^\dagger_{k_2-q',r'} c_{k_1,r} \\
&= \delta_{r,r'} \sum_{k_2} c^\dagger_{k_2-q',r'} c_{k_2-q,r} - c^\dagger_{k_2-q'+q,r} c_{k_2,r'} \\
&= \delta_{r,r'} \sum_{k_2} : c^\dagger_{k_2-q',r'} c_{k_2-q,r} : - : c^\dagger_{k_2-q'+q,r} c_{k_2,r'} : + \langle 0| c^\dagger_{k_2-q',r'} c_{k_2-q,r} |0\rangle - \langle 0| c^\dagger_{k_2-q'+q,r} c_{k_2,r'} |0\rangle \\
&= \delta_{r,r'} \delta_{q,q'} \sum_{k_2} \langle 0| c^\dagger_{k_2-q,r'} c_{k_2-q,r} |0\rangle - \langle 0| c^\dagger_{k_2,r} c_{k_2,r'} |0\rangle = \delta_{r,r'} \delta_{q,q'} rq = \delta_{r,r'} \delta_{q,q'} r \frac{L_0 n_q}{2\pi}.
\end{aligned}
\tag{2.52}
$$

The change of variable in the 4th line is allowed as it is performed in normal ordering. $\langle 0| c^\dagger_{k,r'} c_{k',r} |0\rangle = 1$ only if $k = k'$ and the state is occupied, i.e. $k < k_{\mathrm{F}}$ for right movers and $k > -k_{\mathrm{F}}$ for left movers. Periodic boundary condition is assumed, and the momentum index $q = 2\pi n_q / L_0$ can be labelled by an integer n_q. Most notably, Eq.(2.52) are bosonic commutation relations up to a normalisation. Thus, this prompts us to define the following bosonic operators

$$
\begin{aligned}
b_q^\dagger &= \sqrt{\frac{2\pi |n_q|}{L_0}} \sum_r \Theta_0(rq) \rho_r^\dagger(q) \\
b_q &= \sqrt{\frac{2\pi |n_q|}{L_0}} \sum_r \Theta_0(rq) \rho_r^\dagger(-q),
\end{aligned}
\tag{2.53}
$$

where $\Theta_0(x > 0) = 1$ and $\Theta_0(x < 0) = 0$, similar to a Heaviside function. Note that $b_{q=0}$ is not defined, and the commutator Eq.(2.52) vanishes. These operators are genuine bosonic creation/annihilation operators since the (fermionic) vacuum state has no bosonic excitation $b(q)|0\rangle = 0$, $\forall q$. Crucially, they are quadratic in fermion operators; quartic fermion terms may now be quadratic boson terms, which are straightforward to diagonalise.

With these bosonic operators, one can show that

$$
[b_q, H] = v_{\mathrm{F}} |q| b_q \text{ which implies } H \simeq v_{\mathrm{F}} \sum_{q \neq 0} |q| b_q^\dagger b_q. \tag{2.54}
$$

Furthermore, the following commutator between the real space fermion operator $\psi_r(x)$ and bosonic operator $\rho_r^\dagger(p)$

$$[\rho_r^\dagger(p), \psi_r(x)] = \frac{1}{\sqrt{L_0}} \sum_{k,k_1} [c_{k+q,r}^\dagger c_{k,r}, c_{k_1,r} e^{ik_1 x}] = -e^{iqx}\psi_r(x), \tag{2.55}$$

commutes with $\psi_r(x)$ itself. Thus, $\psi_r(x)$ must be of the form[1]

$$\psi_r(x) \simeq \exp\left[\sum_q e^{iqx}\rho_r^\dagger(-p)(\frac{2\pi r}{L_0 n_q})\right]. \tag{2.56}$$

We now appear to be able to bosonise a fermion operator! However, $\psi_r(x)$ is a fermion operator which must follow the usual anticommutation rules, whereas $\rho_r^\dagger(p)$ follows (up to normalisation) bosonic commutation rules, and it preserves the number of fermion quasi-excitations. An extra fermionic operator must be present to account for the fermion creation/annihilation and implement the necessary anticommutation rules. Such an operator is known as the Klein factor U_r [182], which satisfies the above requirements. The final bosonised expression for the fermion operator is

$$\psi_r(x) = U_r \exp\left[\sum_q e^{iqx}\rho_r^\dagger(-p)(\frac{2\pi r}{L_0 n_q})\right]. \tag{2.57}$$

Here, U_r, $r = R, L$ has no spatial dependence and commutes with all boson operators while following the usual anticommutation rules for fermions[2]. Thus far, L has been considered finite, introducing tedious finite-size contributions. Fortunately, universal behaviours are captured in the thermodynamic limit $L \to \infty$, greatly simplifying the analytics as the finite-size term vanishes. In the thermodynamic limit $L \to \infty$,

[1]Note $[A, f(B)] = [A, B]f'(B)$ if $[[A, B], B] = 0$.

[2]The explicit form of U_r is [182]

$$U_r^\dagger = \frac{1}{\sqrt{L}} \int_0^L dx\ e^{irk_F x} e^{-i\phi_r^\dagger(x)} \phi_r^\dagger(x) e^{-i\phi_r(x)},$$

where $\phi_r(x) = -\theta(x) + r\phi(x)$ with $\phi(x)$ and $\theta(x)$ defined in Eq.(2.58). The spatial dependence x is integrated out. It can be shown that $U_r^\dagger$ commutes with the boson operators, as well as adding a left/right fermion ($r = R/L$) to a fermionic state of given fermion number.

it is more convenient to introduce the following bosonic fields

$$
\begin{aligned}
\phi(x) &= -(N_R + N_L)\frac{\pi x}{L_0} - \frac{i\pi}{L_0}\sum_{q\neq 0}\sqrt{\frac{L_0 n_q}{2\pi}}\frac{1}{q}e^{-|\alpha|q/2 - iqx}(b_q^\dagger + b_{-q}), \\
\theta(x) &= (N_R - N_L)\frac{\pi x}{L_0} + \frac{i\pi}{L_0}\sum_{q\neq 0}\sqrt{\frac{L_0 n_q}{2\pi}}\frac{1}{|q|}e^{-|\alpha|q/2 - iqx}(b_q^\dagger - b_{-q}),
\end{aligned} \tag{2.58}
$$

where α is the cutoff of the theory[1] and N_r is the normally ordered total number operator

$$
N_r =: \sum_k c_k^\dagger c_k :, \tag{2.59}
$$

corresponding to the $q \to 0$ limit of the boson operator. Using these fields and accounting properly the $q = 0$ contribution [183], the linear Hamiltonian H and the fermion operator have the following exact expression

$$
\begin{aligned}
H &= \sum_{q\neq 0} v_{\mathrm{F}}|q|b_q^\dagger b_q + \frac{v_{\mathrm{F}}\pi}{L_0}\sum_r N_r^2 \\
\psi_r(x) &= U_r \lim_{\alpha\to 0}\frac{1}{\sqrt{2\pi\alpha}}e^{ir(k_{\mathrm{F}} - \pi/L)x}e^{-i(r\phi(x) - \theta(x))}.
\end{aligned} \tag{2.60}
$$

α, the ultraviolet cutoff, regularises the theory and prevents momentum from getting too large (a finite bandwidth)[2]. The boson fields $\phi(x)$ and $\theta(x)$ obey the following relations

$$
\begin{aligned}
[\phi(x), \theta(x')] &= i\frac{\pi}{2}\mathrm{Sign}(x' - x) \\
[\phi(x), \partial_x'\theta(x')] &= i\pi\delta(x - x'),
\end{aligned} \tag{2.61}
$$

and thus, $\phi(x)$ and $\Pi(x) \equiv \partial_x'\theta(x')$ are the conjugate density and momentum respectively. Eq.(2.60) and (2.61) are the core of bosonisation of 1D fermion systems with a linear spectrum.

Although our discussion so far applies only to a linear spectrum and might appear restricted, it is a potent tool for analysing the low-energy physics of 1D

[1] At the end of the day, we are dealing with a lattice system.

[2] Formally, $\alpha \to 0$ should be taken for the expression to be exact, which can lead to divergences. However, this problematic limit can be side-stepped for interaction with finite range [182].

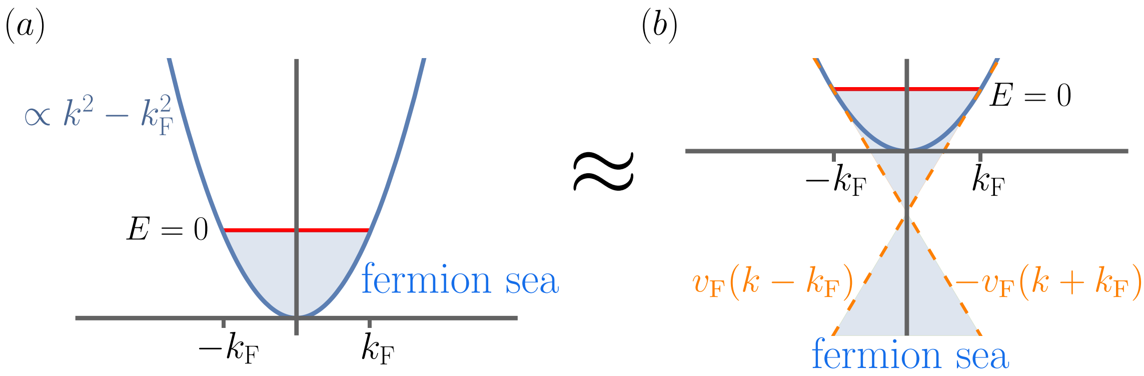

Figure 2.4: Schematic display of the linearising procedure in Eq.(2.63). (a): a quadratic momentum spectrum, typical of the free kinetic part of a many-body Hamiltonian. Its ground state is a fermion sea below $E = 0$, for momentum $|k| < k_F$ (b): linear spectrum by linearising the left spectrum around the Fermi point $\pm k_F$. This necessarily introduces left/right-moving fermions and spectrum, and the fermion sea of the ground state extends indefinitely to $-\infty$ (along with normal ordering for well-defined behaviour).

systems. More precisely, a typical many-body Hamiltonian's two-body kinetic part is quadratic in momentum space

$$H_{\text{free}} = \frac{k^2 - k_F^2}{2m}, \tag{2.62}$$

where m is the effective mass. Its ground state is a fermion sea occupying states below $|k| < k_F$. If we consider quasiparticle excitation close to the Fermi points $\pm k_F$, H_{free} can be linearised around the Fermi points[1]. This procedure is schematically shown in Fig. 2.4, and the linearised version of H_{free} is

$$H_{\text{free}} \approx v_F \sum_{\substack{k=-\infty \\ r=R,L}}^{k=\infty} (rk - k_F) c^\dagger_{k,r} c_{k,r}, \tag{2.63}$$

where $v_F = k_F/m$. In doing so, this forces us to necessarily introduce two species of fermions, the left ($c^\dagger_{k,L}$) and right ($c^\dagger_{k,R}$) movers, and extend the spectrum to include infinitely many negative states (and hence the ground state). H_{free} is now the same

[1] A non-trivial property of H_{free} is that its quasiparticle excitation has well-defined momentum q. Moreover, the quasiparticle dispersion approaches 0 faster than its average energy, implying that they can be treated as well-defined particles [182].

as the linear spectrum Hamiltonian in Eq.(2.48) and bosonisation readily follows. Note that in the current setting, bosonisation is only meaningful, provided that the excitation of interest is close to the Fermi point and the curvature of the band can be ignored. However, combined with renormalisation group analysis outlined below, much more can be obtained.

2.2.2 Renormalisation group

Renormalisaiton group (RG) is one of the most successful tools in modern physics. Since its interpretation and first application by Wilson in condensed matter physics [184], it has proven to be a powerful formalism in analysing (quantum) phase transitions [182, 185–187]. This section gives a brief outline of this formalism and its core spirit. More in-depth details about the mathematical implementation can be found in many texts [186–188] (see also Appendix B.7, a calculation relevant to later chapter).

One of the significant experimental findings leading to RG is *scale-invariance* at the critical point: the characteristic length scale of the system diverges. To explain this concept, we first note, and later in Ch. 2.3.2, that the (two-point) correlation generally decays exponentially $\sim \exp\bigl(-r/\xi\bigr)$, where r is the distance between the two regions in space, and ξ is the correlation length reflecting the characteristic length in the system. As we approach the critical point, ξ diverges to infinity; at the critical point, correlation decays with a power-law $|r|^{-\alpha}$ instead[1]. Suppose we now rescale the length of the system by a factor $b > 1$, hence $\xi \to \xi/b$. Away from the critical point, ξ decreases by a factor of $1/b$. In contrast, since ξ diverges at the critical point, any rescaling leaves ξ unchanged. When this length-rescaling procedure is repeatedly applied, one finds that finite ξ is connected to $\xi = 0$ and the point $\xi \to \infty$ is left unchanged. This leads to the conclusion that ξ finite belongs to one phase and $\xi \to \infty$ is a fixed point itself. This length-rescaling is the principal

[1]An argument for that is ξ is now much larger than the system size; hence there is literally not enough room for exponential decay.

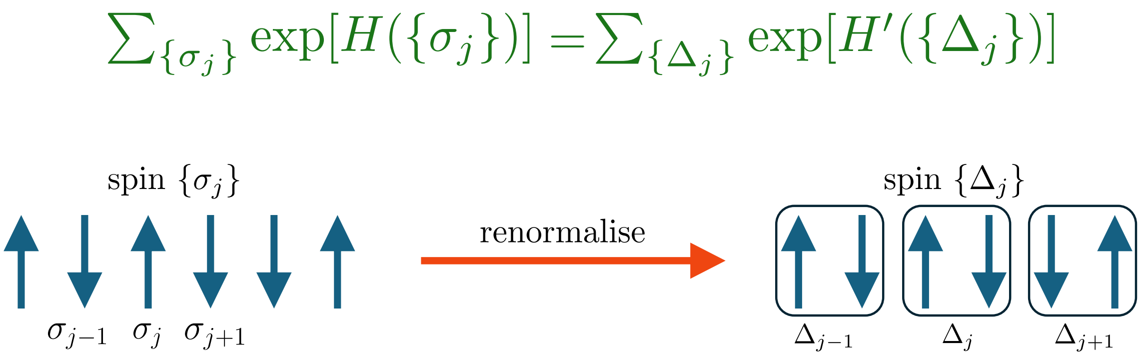

Figure 2.5: The spin blocking RG procedure. The original spin set $\{\sigma_j\}$ is replaced by a new set $\{\Delta_j\}$, formed by grouping two neighbouring spins. This grouping effectively rescales the system by a factor of $b = 2$. The Hamiltonian, and consequently the partition function, are expressed in $\{\Delta_j\}$, and the partition function in $\{\Delta_j\}$ must be identical to that in $\{\sigma_j\}$, as there are no external changes to the system. This forces the Hamiltonian to change from $H \to H'$, meaning that the couplings in the Hamiltonian would change along the RG procedure. This coupling change is known as the *RG flow*, where one can analyse the phase transition.

idea of RG, allowing one to identify the system's critical point. More precisely, it is implemented mathematically by integrating/decimating/blocking the smaller-scale degrees of freedom, grouping them into a new degree and expressing the system in this new degree. A famous example is the Kadanoff blocking in the Ising model, in which, during one iteration, the original set of spin degrees $\{\sigma_j\}$ is replaced by a new set of spin degrees $\{\Delta_j\}$ constructed by grouping two neighbouring spin degrees together [189]. This corresponds to changing the summation in the partition function and the Hamiltonian

$$\sum_{\{\sigma_j\}} \xrightarrow{RG} \sum_{\{\Delta_j\}}$$
$$H(\{\sigma_j\}) \to H'(\{\Delta_j\}), \tag{2.64}$$

while keeping the partition function identical. The next RG iteration follows by grouping the $\{\Delta_j\}$. This RG procedure is schematically displayed in Fig 2.5.

Moreover, by noting that smaller length scales correspond to shorter wavelengths of higher energy degrees of freedom, the RG integration/decimation/blocking procedure in real space can be extended further and applied equivalently with other quantities, e.g. momentum in Wilson RG approach [184, 190], as long as the higher energy degrees are repeatedly integrated out during each RG iteration. In this case, the RG goes from the ultraviolet (UV) limit of higher energy to the infrared (IR) limit of lower energy. By analysing the system under RG going from the UV to the IR, many universal properties of a critical point can be computed and characterised, despite the divergence of various thermodynamic statistical quantities.

To further demonstrate, consider a (1+1)d massless/gapless Gaussian model with the following action

$$\mathcal{S}[\phi] = -g \int dx d\tau \phi(\partial_x^2 + \partial_\tau^2)\phi, \tag{2.65}$$

where g is the coupling of the theory and τ is the imaginary time. The field ϕ is bounded over an (infinite) interval. Rescaling $x = x'/b$ and $\tau = \tau'/b$ by a factor b, the rescaled action is

$$\mathcal{S}[\phi] = -g \int \frac{dx' d\tau'}{b^2} \phi b^2(\partial_{x'}^2 + \partial_{\tau'}^2)\phi = -g \int dx' d\tau' \phi(\partial_{x'}^2 + \partial_{\tau'}^2)\phi = \mathcal{S}[\phi]. \tag{2.66}$$

Assuming the integration is over an infinite interval, i.e. infinite system size, $\mathcal{S}[\phi]$ is identical under RG transformation. Therefore, this model only has one phase which is massless/gapless.

2.3 Entanglement and correlations in 1D systems

In this chapter, I discuss the role of entanglement and correlation in characterising 1D systems. I will dedicate a part to discussing entanglement entropy, as it is relevant to much of this thesis. Other entanglement monotones are used in this thesis, but they will not be discussed here; they will be addressed in the appropriate chapter.

2.3.1 Entanglement entropy

To begin with, it is necessary to introduce the Von Neumann entropy of a density matrix $S_{\mathrm{vN}}(\rho)$. It is defined as

$$-\operatorname{Tr}[\rho \log \rho] = -\sum_j \lambda_j \log \lambda_j,$$

which extends the Gibbs entropy to quantum information and captures the entropy associated with the observer's incomplete knowledge. The entropy captured can be classical and quantum-mechanical, disqualifying it from being a genuine entanglement quantifier.

Nevertheless, restricting $S_{\mathrm{vN}}(\rho)$ to the set of reduced density matrices of a pure state leads to the characterisation of entanglement via *entanglement entropy*, which is an entanglement monotone. This means that no classical operation in the system can alter its value, and it only captures quantum mechanical entropy.

Definition 2.3.1. Entanglement entropy—Consider a system partitioned into region A and its complement $\not{A}$. Given that the joint density matrix $\rho_{A,\not{A}}$ is pure, so that $\operatorname{Tr}\left[\rho^2_{A,\not{A}}\right] = 1$, the *entanglement entropy* S_A between A and its complement $\not{A}$ is

$$S_A = -\operatorname{Tr}[\rho_A \log \rho_A] = -\operatorname{Tr}[\rho_{\not{A}} \log \rho_{\not{A}}], \tag{2.67}$$

where $\rho_A = \operatorname{Tr}\left[\rho_{A,\not{A}}\right]_{\not{A}}$ is the reduced density matrix of the subsystem A (similarly for $\rho_{\not{A}}$). Note that the entanglement entropy calculated for a non-pure system state is no longer an entanglement monotone, and is contaminated with classical contributions.

Unlike some entanglement monotones, entanglement entropy has a nice and intuitive interpretation. To see this, consider the state $|\psi_{A,\not{A}}\rangle$ of a system as a joint state of A and $\not{A}$, which can be decomposed as a linear combination of product states

$$|\psi_{A,\not{A}}\rangle = \sum_{i=0}^{d_A-1} \sum_{j=0}^{d_{\not{A}}-1} c_{i,j} |\Psi_{A,i}\rangle |\Psi_{\not{A},j}\rangle, \tag{2.68}$$

where d_A ($d_{\not{A}}$) is the dimension of A ($\not{A}$). $\{|\Psi_{A,i}\rangle\}$ and $\{|\Psi_{\not{A},i}\rangle\}$ are the sets of orthonormal bases in A and $\not{A}$. Each individual basis can be carefully chosen to give a Schmidt decomposition [117]:

$$|\psi_{A,\not{A}}\rangle = \sum_{i=0}^{n} \sqrt{\lambda_i} |\varphi_{A,i}\rangle |\varphi_{\not{A},i}\rangle, \tag{2.69}$$

where $n \leq \min(d_A, d_{\not{A}})$, λ_i's are known as the Schmidt values with $\sum_i \lambda_i = 1$[1], and $\{|\varphi_{A,i}\rangle|\varphi_{\not{A},i}\rangle\}$ is a complete orthonormal set. Written in Schmidt decomposition, the reduced density matrix of A is

$$\rho_A = \mathrm{Tr}\Big[|\psi_{A,\not{A}}\rangle\langle\psi_{A,\not{A}}|\Big]_{\not{A}} = \sum_{i=0}^{n} \lambda_i |\varphi_{A,i}\rangle\langle\varphi_{A,i}|. \tag{2.70}$$

From this, the entanglement entropy of A can be viewed as follows: suppose there is an observer in $\not{A}$ who has full knowledge of $\not{A}$, i.e. of its current state, but has no knowledge of A. From $\not{A}$'s observer perspective, A is a statistical mixture of states equivalent to its reduced density matrix. The Von Neumann (Gibbs) entropy $\not{A}$'s observer associated with A is the entanglement entropy between A and $\not{A}$; in other words, the quantum information $\not{A}$'s observer has on A.

As an additional note, analogously to mutual information in classical information theory, one can define the quantum mutual information of two subsystems A and B to be

$$I(A:B) = S_A + S_B - S_{AB}. \tag{2.71}$$

$I(A:B)$ indicates the amount of quantum information one can learn from A (B) by observing B (A). For example, if A and B are in product state $|\psi_A\rangle|\psi_B\rangle$, the mutual information

$$I(A:B) = 0;$$

learning A's state tells us nothing about B's state and vice versa. In contrast, if A and B are maximally entangled, e.g., a Bell pair in a two-qubit system

$$I(A:B) = 2\log 2;$$

A's information alone is enough to characterise B (or the reverse).

[1]It can be shown that Schmidt decomposition is equivalent to singular value decomposition.

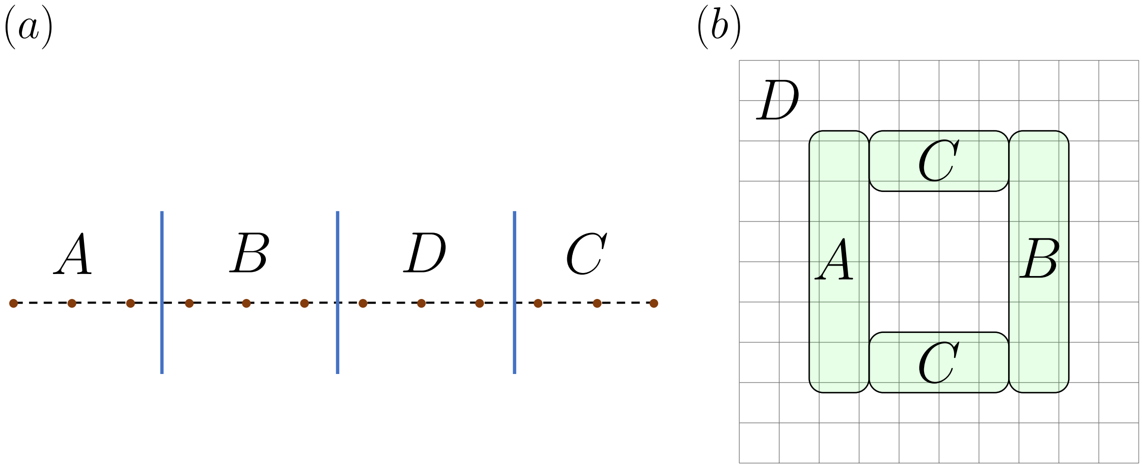

Figure 2.6: The partition of a system for the computation of S_{TEE}. (a): The partitioning of a 1D system; open boundary applies. Note that B and C are not connected. (b): The partitioning of a 2D system; picture from Ref. [117]. Unlike 1D, the boundary can be periodic. Note that in 2D, there are other equally valid partitions; see Ref. [117].

Topological entanglement entropy — An interesting extension to entanglement entropy is the topological entanglement entropy (S_{TEE}). In the most simplified terms, S_{TEE} is related to an underlying long-range entanglement across a many-body quantum system[1] [117], and is instrumental to distinguishing different phases of matter. This is discussed further in the next section.

For 1D systems, to compute S_{TEE}, one first sets open boundary condition on the system and partitions the system into four parts (A, B, C, and D) as shown in Fig. 2.6(a) [195]. Then, S_{TEE} is computed via

$$S_{TEE} = S_{AB} + S_{BC} - S_B - S_{ABC}, \tag{2.72}$$

where $S_{[\ldots]}$ is the entanglement entropy of region $[\ldots]$. The computation in higher dimensions follows a similar procedure; an example is shown in Fig. 2.6(b).

[1]In more technical terms, S_{TEE} measures the topological or symmetry-breaking orders in the system [191–195].

2.3.2 Scaling and phases of matter in 1D

Quantum phase transitions are characterised by a quantum critical point separating distinct quantum phases as one varies some parameters in the Hamiltonian. These different phases are distinguished by an order parameter, w.r.t. the ground state, which behaves differently in each of the phases; for example, spin-spin correlation in an Ising model that scales with power law decay at the critical point and exponential decay in the (anti-)ferromagnetic phase. Nonetheless, in the past decade, it became apparent that there are phases of matter that do not fit within this paradigm; for example, topological phases of matter [117, 191, 192], and their transition in out-of-equilibrium systems [75, 108, 109]. Motivated by the need to characterise these new phases, novel approaches relevant to this thesis are emerging: the use of *entanglement entropy* (and related quantities discussed above) as a quantum information-theoretical order parameter [117, 191, 192, 196].

The relevant concept in this quantum information-theoretical approach is the scaling of entanglement entropy against the subsystem's size: $S_A = f(|A|)$, where $|A|$ is A's region size. In 1D static steady-state, there are generally three different scalings:

$$\text{volume law } S_l \sim l, \text{area law } S_l \sim \text{constant, and critical scaling } S_l \sim \log l.$$

Volume law scalings are observed in the unitary evolution of a many-body wavefunction by quantum gates or Hamiltonians, without local constraints, to a steady-state of higher entanglement [43, 44, 64, 120, 121, 197–200]. These are out-of-equilibrium dynamical evolutions where the resultant steady-state entanglement in the long time limit is unbounded, only constrained by the system size[1]. In contrast, an area law entanglement steady-state is a noticeable signature of the ground state of a gapped Hamiltonian, indicating a suppression in entanglement spreading [117, 201, 202][2]. Finally, steady-state critical scaling is indicative of a critical quantum

[1]Dynamically, the entanglement spreads ballistically, forming a spacetime light cone.

[2]The terms volume (area) indicate that the entanglement entropy scales with the volume/size (boundary size) of the subsystem, i.e. in 1D, the boundary size is fixed.

phase, e.g. the critical point of a transverse-field Ising model, corresponding to a bounded entanglement spread dictated by the underlying conformal field theory [203, 204]. Given these distinct features, one can distinguish different phases by their entanglement scaling behaviour, gaining more insight from a quantum information perspective.

A subtlety in area law is that a universal constant can exist that distinguishes different area law phases [117, 191, 192]. In 1D, this universal constant (which does not depend on the specifics of the system) is hidden inside the constant term of the area law scaling, which contains some non-universal parts [117, 194, 195, 205]. The universal contribution is given by S_{TEE}, and the addition/subtraction of various terms in Eq.(2.72) cancel exactly the non-universal contribution. This non-trivial constant S_{TEE} indicates an underlying long-range entanglement arising from the (topological) degeneracy of the state. The simplest example is a p-wave Kitaev chain in the gapped phase with two 0-energy boundary states, where S_{TEE} is 1 in $\log_2$ base (indicating one qubit of information between the two boundary states) [75, 108, 206].

Another scaling feature closely related to entanglement scaling is the scaling of correlation: suppose there are two local operators O_1 and O_2, which act locally in two different regions of space and are separated by a distance r. The (connected) correlation between the two operators w.r.t. to a state is

$$C(r) = \langle O_1 O_2 \rangle - \langle O_1 \rangle \langle O_2 \rangle \,, \tag{2.73}$$

and the subtraction takes away the disconnected part. Generally, $C(r)$ decays w.r.t. r, and its form strongly depends on the entanglement scaling. For the ground state of a gapped Hamiltonian with area law entanglement, correlation decays exponentially [207–211]

$$C(r) \sim e^{-\frac{r}{\xi}},$$

where ξ is the correlation length. The relation with area law is intuitive in the following sense. Due to the exponential decay, only sites of distance $\sim \xi$ from the subsystem boundary are entangled with the outside; hence, entanglement can, at most, scale with the size of the boundary. For the ground state of a gapless system with critical scaling entanglement, $C(r)$ follows a power law decay [117, 182]

$$C(r) \sim \frac{1}{r^{\alpha}},$$

where the exponent α is a universal value[1]. The power-law decay indicates long-range correlations, hence the subsystem-size dependent entanglement[2]. Similarly, for volume law steady-state, long-range correlations exist, and $C(r)$ decays with a power law.

2.4 More on MiPTs

As mentioned briefly towards the end of Ch.2.1.5, the hallmark of MiPT (a quantum phase transition) is the drastic change in the system's intrinsic correlation, from extensive to quantum Zeno-like. Combining with the knowledge from Ch. 2.3, we can deduce that entanglement/correlation will play a significant role in MiPTs.

However, since the dynamics under quantum measurement are stochastic, the system never truly reaches a stationary state: even in the regime of the quantum Zeno effect, there is occasional stochasticity in time. As is typical for stochastic processes, the quantity that reaches a stationary state is the state's probability distribution. This prompts the idea of analysing the moments of the stochastic quantum trajectories. Indeed, in this distribution picture, MiPT emerges in the steady-state probability distribution. This chapter first deals with some of the subtleties in the averaging procedures and then introduces a powerful tool for dealing with quantum trajectory averaging.

[1]It depends on the universality of the critical point [186]

[2]The logarithmic dependence is a direct consequence of the power-law decay, which appears explicitly in the underlying conformal field theory calculation [203, 204].

2.4.1 Observables and entanglement in MiPT

Generally, to access information on an observable M, we may compute its expectation value $\mathrm{Tr}[\hat{\rho}M]$, which involves the density matrix. If we wish to compute the trajectory-averaged expectation value

$$\overline{\mathrm{Tr}[\hat{\rho}M]} = \mathrm{Tr}\left[\overline{\hat{\rho}}M\right],$$

where $\overline{\ldots}$ indicates average over quantum trajectories/outcomes.The averaging is entirely captured by $\overline{\hat{\rho}}$. Consequently, we need to average Eq.(2.39) over all outcomes to obtain a steady state solution for $\overline{\hat{\rho}}$. Averaging Eq.(2.39)

$$\partial_t\overline{\hat{\rho}} = -idt[H,\overline{\hat{\rho}}] - \frac{\gamma}{2}dt\sum_j[O_j,[O_j],\overline{\hat{\rho}}], \tag{2.74}$$

we arrive at the Lindblad master equation for the set of Hermitian operators $\{O_j\}$[1]. We have used $\overline{dW_j} = 0$ as they have a mean of 0. For $[O_j, H] \neq 0 \;\forall\; j$, this Lindblad master equation is known to support the following steady state solution

$$\overline{\hat{\rho}}(t \to \infty) \propto \mathbb{I},$$

a totally mixed state corresponding to an infinite temperature system[2]. This is an unpleasant issue: regardless of γ's value, provided it is non-zero, $\overline{\hat{\rho}}$ always heats up indefinitely to the identity. Indeed, any quantities linear in density matrix are insensitive to the measurement strength in the average dynamics. Consequently, there is no MiPT in the steady state of $\overline{\hat{\rho}}$ [3].

To account for measurement effects non-trivially, one must consider observables non-linear in the density matrix, i.e. $\mathrm{Tr}[\hat{\rho}M]^k$, $k \geq 2$ or $S_A = \mathrm{Tr}[\hat{\rho}_A \log\hat{\rho}_A]$. The average must be performed at a *trajectory level*, i.e.

$$\overline{\mathrm{Tr}[\hat{\rho}M]^k} = \mathrm{Tr}\left[\overline{\hat{\rho}^{\otimes k}}M^{\otimes k}\right] \neq \left(\overline{\mathrm{Tr}[\hat{\rho}M]}\right)^k.$$

[1] Generalisation to non-Hermitian operators exists using POVM [27, 161, 212].

[2] There can exist other solutions depending on H and $\{O_j\}$.

[3] It has been recently suggested that the early evolution of $\overline{\hat{\rho}}$ can reveal properties of MiPT [137, 138].

The fundamental objects of interest are now the average higher moment density matrix $\overline{\hat{\rho}^{\otimes k}}$, $k \geq 2$. Indeed, the steady state solution to $\partial_t \overline{\hat{\rho}^{\otimes k}}$ is no longer a totally mixed state, and it carries information about MiPTs.

In particular, the averaged entanglement entropy is a crucial indicator for most MiPTs and displays scaling behaviour similar to the ones observed in conventional phase transitions. For example, in Ref. [64], one of the first few works studying MiPT, increasing the probability of projective measurements (equivalent to increasing the strength of continuous measurement) changes the scaling of entanglement entropy on subsystem-size from volume law to area law, separated by a critical point with critical scaling. Moreover, in some cases, MiPTs can be identified from topological entanglement entropy, indicating a topological transition from quantum measurements [75, 108, 109]. It should be stressed again that all of these conclusions are in the average entanglement dynamics; the implication of MiPT for a single trajectory is still unclear.

Although the discussion above is set in the context of quantum state diffusion equation, it is also true for quantum jump and probabilistic projective measurements [64, 65, 76, 108, 109, 213]. Hence, the characterisation of MiPT boils down to studying the object $\overline{\hat{\rho}^{\otimes k}}$, and we will further elaborate on this in later sections.

The post-selection problem — Despite bearing desirable information about MiPT, measuring experimentally non-linear observables has been proven to be a tall task and poses a significant unresolved problem in modern physics, known as the **post-selection problem**. To elucidate this problem, consider characterising a MiPT via the entanglement entropy. It is required to first calculate the entanglement entropy along each trajectory, then average all the results. For such computation, complete knowledge of the density matrix, i.e. all the matrix elements, along each trajectory is needed. However, the only accessible information about each trajectory from quantum measurements is the measurement outcomes, which are insufficient to characterise the density matrix fully. To gain further knowledge, we must perform multiple different operations on an identical trajectory to characterise the matrix elements. This is where a fundamental experimental problem appears: when the space of possible outcomes is large, i.e. many local measurements or measurements over a long time, the probability of any trajectory becomes exponentially small; hence, it is experimentally unlikely to obtain the same trajectory more than once. However, we need many identical trajectories to characterise the density matrix and calculate the entanglement entropy. This significant experimental obstacle is the **post-selection problem**. Numerous proposals have been to resolve this problem [139–141, 214, 215]

2.4.2 Replica trick

As pointed out in the last section, MiPTs appear in non-linear averages involving $\overline{\rho^k}$. In this chapter, I outline a powerful mathematical approach to deal with these averages: the replica trick. The replica trick was originally developed in Hermitian disorder systems [182, 216, 217] but has since been extended to non-unitary systems [71, 77, 80, 92, 218–220].

For simplicity, let's omit the unitary process. To begin with, consider a system subject to quantum measurements represented by the set of Kraus operators $\{K_{x_t}\}$, where x_t is the outcome of a single measurement. The resultant *normalised* density matrix along a quantum trajectory with a certain set of measurement outcomes, $\{x_t\}$, at discrete times $t \in [1...M]$ is (we are suppressing the hat)

$$\rho_{\{x_t\}} = \frac{\check{\rho}_{\{x_t\}}}{\mathrm{Tr}\left[\check{\rho}_{\{x_t\}}\right]}, \tag{2.75}$$

where $\check{\rho}_{\{x_t\}} = K_{x_M} \dots K_{x_2} K_{x_1} \rho_0 K^{\dagger}_{x_1} K^{\dagger}_{x_2} \dots K^{\dagger}_{x_M}$ is the the *un-normalised* density matrix along the trajectory, and ρ_0 is the initial *normalised* density matrix[1]. The probability of this trajectory, labelled by $\{x_t\}$, is $P(\{x_t\}) = \mathrm{Tr}[\check{\rho}_{\{x_t\}}]$.

As mentioned in Ch. 2.4.1, to capture MiPTs, we must examine non-linear

[1]From here onward, we will specify an un-normalised density matrix by a caron above: $\rho = \check{\rho}/\,\mathrm{Tr}[\check{\rho}]$.

observables. The replica trick lies in the fact that there is an ingenious way to relate all non-linear observables to a single entity

$$\overline{\langle O\rangle^k} = \sum_{\{x_t\}} \left(\mathrm{Tr}[O\rho_{\{x_t\}}]\right)^k P(\{x_t\}) = \sum_{\{x_t\}} \mathrm{Tr}[O^{\otimes k}\check{\rho}^{\otimes k}_{\{x_t\}}](\mathrm{Tr}[\check{\rho}_{\{x_t\}}])^{1-k}$$
$$= \lim_{n\to 1}\sum_{\{x_t\}} \mathrm{Tr}\left[\left(O^{\otimes k}\otimes \mathbb{I}^{\otimes n-k}\right)\check{\rho}^{\otimes n}_{\{x_t\}}\right] = \lim_{n\to 1}\mathrm{Tr}\left[\left(O^{\otimes k}\otimes \mathbb{I}^{\otimes n-k}\right)\overline{\check{\rho}^{\otimes n}}\right]. \quad (2.76)$$

From Eq.(2.76), the fundamental object encoding all measurement averaging information is the trajectories averaged n-replicated *un-normalised* density matrix $\lim_{n\to 1}\overline{\check{\rho}^{\otimes n}}$, with the replica limit $n\to 1$. The replica limit $n\to 1$ is an analytical continuation for $k>1$[1].

2.4.2.1 Replica trick and entanglement

The calculation of entanglement entropy can be incorporated into the replica trick. To illustrate better, let's rewrite entanglement entropy $S_A = -\mathrm{Tr}[\rho_A\log\rho_A]$ as the following limit

$$S_A = -\mathrm{Tr}[\rho_A\log\rho_A] = \lim_{k\to 1}\frac{1}{1-k}\log\mathrm{Tr}\left[\rho_A^k\right] = \lim_{k\to 1} -\partial_k\,\mathrm{Tr}\left[\rho_A^k\right], \quad (2.77)$$

where the quantity

$$\frac{1}{1-k}\log\mathrm{Tr}\left[\rho_A^k\right] \equiv S_{A,k},\ \ \mu_{k,A}\equiv \mathrm{Tr}\left[\rho_A^k\right]$$

is the kth Renyi entropy and kth purity of subsystem A. Importantly, through the limit, the entanglement entropy is related to the traced matrix multiplication $\mathrm{Tr}\left[\rho_A^k\right]$. This traced matrix multiplication may be represented by a unitary operator in the k-replicated Hilbert space $\mathcal{H}^{\otimes k}$

$$\mathrm{Tr}\left[\rho_A^k\right] = \mathrm{Tr}\left[\mathcal{C}_{k,A}\rho^{\otimes k}\right],\ \ \mathcal{C}_{k,A} = \sum_{\{A_1\},\ldots,\{A_k\}}\bigotimes_{p=1}^{p=k}|A_p\rangle\langle A_{p+1}|. \quad (2.78)$$

[1]Notice that the replica limit $n\to 1$ is different from the replica limit for disordered systems $n\to 0$ [182, 216, 217].

$|A_p\rangle$ (p mod k) is a complete set of (orthonormal) basis in region A of replica index p [1], and the sum indicates summation over all of $|A_p\rangle$'s, the complete basis in A. ρ is the *normalised* system's density matrix. $\mathcal{C}_{k,A}$ acts as an identity outside of A while cyclically permuting kets across the replicas in region A by one replica index[2].

Written in Eq.(2.78), the computation of the average entanglement entropy in replica trick appears as

$$\overline{S_{A,k}} = \lim_{k\to 1} -\partial_k \operatorname{Tr}\left[\mathcal{C}_{k,A}\overline{\rho^{\otimes k}}\right] = \lim_{k\to 1}\lim_{n\to 1} -\partial_k \operatorname{Tr}\left[\left(\mathcal{C}_{k,A}\otimes \mathbb{I}^{\otimes n-k}\right)\overline{\tilde{\rho}^{\otimes n}}\right],$$

and the replica limit should be taken before the entanglement entropy limit.

[1]Not to be confused with its position in the tensor product. In a less formal wording, $|A_p\rangle\langle A_{p+1}|$ means taking an identity in A across all replicas and bringing the $p+1$ bra from replica $p+1$ to p replica.

[2]There is an implicit $\otimes|\not{A}_p\rangle\langle\not{A}_p|$ after the product

Chapter 3

Measurement-induced transitions in inefficiently monitored noisy systems

In this chapter, we explore the classical effects of inefficient quantum measurements on MiPTs. This chapter is based on the findings in Ref. [221].

3.1 Overview

The interplay between information-scrambling Hamiltonians and local monitoring hosts an ideal platform for exotic MiPTs in out-of-equilibrium steady states. At their heart, these systems feature a competition between quantum measurements by an active observer and coherent unitary dynamics [27, 161]. The simplest implementation of this competition is the quantum Zeno effect (c.f Ch. 2.1.5) in which sufficiently strong monitoring freezes the unitary dynamics, locking the system mostly in an eigenstate of the measured observable [1, 2, 8]. In this chapter, we address this interplay in stochastic Lindblad dynamics, from purity-preserving monitored systems to fully averaged deterministic Lindblad dynamics. We study specifically the dynamics of a spin-1/2 XX chain with nearest-neighbour interactions and additional incompatible stochastic contributions from (i) local continuous quantum measurement and (ii) random local unitary. We first address the dynamics in the simplest case of two qubits, revealing a non-trivial, non-monotonic behaviour in the entanglement and operator correlation dependence on the local unitary noise. With the introduction of inefficiency, this non-monotonicity in the entanglement disappears below a threshold efficiency value. On the contrary, it persists in the operator correlations (for any finite efficiency), indicating a breakdown in the correspondence between entanglement scaling and a quantum Zeno phase signalled by correlations. We explore the implication of this breakdown for MiPTs by extending the protocol to a finite-length chain. The system size dependence of both entanglement and operator correlations indicates that the correspondence between the two, valid for fully efficient measurement, is broken with the inclusion of inefficiency. This breakdown suggests a difference between the measurement-induced quantum Zeno phase and area-law entanglement phase, with different phase diagrams obtained from entanglement and operator correlations.

The rest of the chapter is structured as follows. In Ch. 3.2, we present the model of interest. In Ch. 3.3, we first outline the various entanglement monotone and operator correlation quantities relevant to this chapter. After discussing them, we numerically analyse the simplest version of the model, a 2-qubit system. We demonstrate here how operator correlations in this system are insensitive to measurement inefficiency contrary to the behaviour shown in entanglement monotone. In Ch. 3.4, we extend our analysis to a spin-1/2 XX chain, demonstrating that operator correlations and entanglement can lead to different measurement-induced phase transitions. We summarise our results and possible implications of our work in Ch. 3.6.

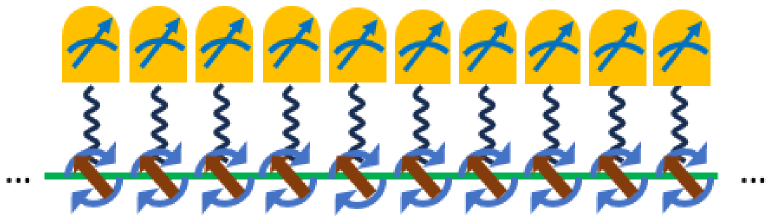

Figure 3.1: Sketch of the model under consideration. A spin 1/2 chain (red arrows) with nearest neighbour spin-flip is subjected to local continuous measurement of σ^z (yellow detectors). The spins are subject to random local magnetic fields in y-direction (blue arrow). The two stochastic dynamics are incompatible.

3.2 Model

We study an XX spin-1/2 chain of length L subject to local continuous measurements of the z-component of the spin and under the influence of a local random transverse magnetic field in the y direction. A sketch of the model is presented in Fig. 3.1. We model the local random magnetic field as local white noises statistically independent at different sites and the measurement backaction via quantum state diffusion equations (c.f Eq.(2.27)). A density matrix description is used instead of a ket, as we are incorporating measurement inefficiency in the dynamics (which introduces classical uncertainty). The term 'white noise' refers to a random Gaussian/Wiener process in time: formally, the unitary evolution with a set of white noise operators $\{M_j\}$ is

$$U = \exp\left\{-iHdt - i\sum_{j=1}^{j=L} d\xi_j M_j^y\right\} = 1 - iHdt - i\sum_{j=1}^{L} d\xi_j^t M_j^y - \frac{\Gamma}{2}dt\sum_{j=1}^{L}(M_j^y)^2 + \mathcal{O}(dt^{3/2}) \tag{3.1}$$

where H is the deterministic part of the Hamiltonian and $d\xi_j$'s are independent Weiner processes satisfying $d\xi_j^t d\xi_{j'}^{t'} = \delta_{t,t'}\delta_{j,j'}\Gamma dt$. Γ is the strength of the white noise. In the current model, the overall dynamics is written as [27]

$$
\begin{aligned}
d\rho_t = &-idt[H,\rho_t] - i\sum_{j=1,L}[\sigma_j^y,\rho_t]d\xi_j^t - \frac{\Gamma}{2}dt\sum_{j=1,L}\left[\sigma_j^y,[\sigma_j^y,\rho_t]\right] \\
&+\sum_{j=1,L}\{\sigma_z - \langle\sigma_j^z\rangle,\rho_t\}\sqrt{\eta}dW_j^t - \frac{\lambda}{2}dt\sum_{j=1,L}\left[\sigma_j^z,[\sigma_j^z,\rho_t]\right],
\end{aligned}
\tag{3.2}
$$

where

$$
H = \sum_j i\sigma_j^+\sigma_{j+1}^- + \ h.c.. \tag{3.3}
$$

In the current chapter, we set the notation so that we denote σ_j^α , $\alpha \in \{x,y,z,+,-\}$ as the α Pauli operator at site j and $\pm$ represents the raising and lowering ladder operators[1]. $0 \leq \eta \leq 1$ quantifies the efficiency of the measurements and λ is the measurement strength. dW_j^t is another Itô process independent of $d\xi_j^t$, with the property $dW_j^t dW_{j'}^{t'} = \lambda dt\delta_{t,t'}\delta_{j,j'}$. The strength of the Hamiltonian can be fixed as it merely appears as an overall energy scale that we set to be 1 hereafter.

The efficiency of the quantum diffusion process is controlled by η, which vanishes for completely inefficient measurements. The measurement contribution in Eq.(3.2) reduces to a Lindbladian master equation, and there is no stochasticity from measurement. As noted in Ch. 2.1.4, inefficient measurement arises from the observer's inability to register all measurement readouts — a common uncontrollable error in experiments [27, 161, 165]. This necessarily introduces statistical mixedness in the density matrix, which complicates the quantification of entanglement.

We denote the averages over all trajectories (all measurement outcomes and noise realisations) by an overline. It is important to stress again that detecting non-trivial Zeno regimes or capturing the entanglement dynamics requires computing the averages of non-linear observables of all quantum trajectories. The analysis of linear observables, e.g. $\overline{\mathrm{Tr}\left[\sigma_j^z\rho_t\right]} = \mathrm{Tr}\left[\sigma_j^z\overline{\rho}_t\right]$, reduces to the study of $\overline{\rho}_t$ which has a trivial steady state solution $\overline{\rho}_{t\to\infty} \sim \mathbb{I}$ (see Ch. 2.4.1). Instead, averages of non-linear

[1] The state's labelling follows the usual convention with $|0\rangle$ for spin-down states and $|1\rangle$ for spin-up states, e.g. $|01\rangle$ represents a state with spin-down on the first site and spin-up on the second site.

observables, e.g. $\overline{\mathrm{Tr}\left[\sigma_j^z \rho_t\right]^2}$, contain non-trivial statistical correlation terms leading to a non-trivial steady state value; this is analogous to deep thermalisation which is only detected by a higher moment of the density matrix along each quantum trajectory [222].

3.3 Two qubits

To elucidate our motivation and results, we begin by presenting the simplest scenario of the model: a 2-qubit system (c.f Eq.(3.2) with $j \in \{1, 2\}$). We use this system to introduce quantifiers for entanglement and operator correlations, as well as proxies for them, which will be used later in the extensive system. We are particularly interested in the case of inefficient measurements in which the state is generically non-pure, and entanglement quantifiers for pure states, like entanglement entropy, are no longer applicable.

3.3.1 Entanglement and operator correlation measures

Concurrence — There are several proposed estimators of entanglement in an overall mixed state; for two qubits, a natural choice is the Concurrence $\mathcal{C}$, which is a genuine entanglement monotone and remains valid for mixed states [223]. It is defined as follows: let ρ_t be the instantaneous 2-qubits density matrix at time t; define $\tilde{\rho}_t = \sigma^y \otimes \sigma^y \rho_t^* \sigma^y \otimes \sigma^y$ and and introduce the non-Hermitian matrix $\rho_t \tilde{\rho}_t$. The associated Concurrence $\mathcal{C}$ is

$$\mathcal{C} = \max\left(0, \sqrt{\lambda_1} - \sqrt{\lambda_2} - \sqrt{\lambda_3} - \sqrt{\lambda_4}\right), \tag{3.4}$$

where $\lambda_1 \ldots \lambda_4$ are the the eigenvalues of the matrix $\rho_t \tilde{\rho}_t$ in descending order. $\mathcal{C} = 0$ corresponds to no entanglement e.g. product states, while $\mathcal{C} = 1$ represents maximal entanglement e.g. Bell pairs.

Entanglement negativity — As $\mathcal{C}$ only applies to a 2-qubit system, other entanglement monotones should be considered for later extension to a chain.

A good candidate is the subsystem logarithmic negativity (an entanglement monotone [224]), which can readily be applied to larger systems. The subsystem logarithmic negativity is defined as:

$$\epsilon_A = \log ||\rho^{T_A}||, \tag{3.5}$$

where ρ^{T_A} denotes the partial transposition of the density matrix ρ concerning region A (transposing matrix element only for sites in A), and $||\rho^{T_A}|| = \mathrm{Tr}\left[\sqrt{\rho^{T_A\,\dagger}\rho^{T_A}}\right]$ is the sum of the singular values of ρ^{T_A}.

subsystem parity variance — Operator correlations are quantities closely related to entanglement [117], as detailed in Ch. 2.3.2, but they capture both classical and quantum correlations in the system. We are interested in operator correlations that signal a quantum Zeno regime in which the system is frozen in an eigenstate of the measured observable.

There are several candidates to be considered. Here, we choose the half-system parity variance, which quantifies how close a state is to a polarised spin up/down state [135, 144, 225]. It is defined as

$$P_{1/2} = \langle \prod_{j=1}^{L/2} \sigma_j^z \rangle^2, \tag{3.6}$$

and for a two qubits system, it is merely

$$P_{1/2} = \mathrm{Tr}[\sigma_1^z \rho_t]^2. \tag{3.7}$$

This measure serves as an indicator for the quantum Zeno effect: under frequent measurements (spin-z in our model), spin excitations are localised, becoming closer to a product state of spin-up/spin-down states. Therefore, a high half-system parity variance indicates a quantum Zeno regime.

subsystem purity — For completeness, we also compute the half-system purity. The half systems purity is defined as

$$\mu_{1/2} = \mathrm{Tr}\left[\rho_{1/2}^2\right], \tag{3.8}$$

where $\rho_{1/2}$ is the reduced density matrix of one part of the system.

$\mu_{1/2}$ is related to the quantum Zeno effect in the following way: if spin excitation is localised, the half-system reduced density matrix is highly pure with little correlation with the rest of the system and vice versa.

3.3.2 Results — efficient measurements

We compute the entanglement monotones and operator correlation functions introduced in Ch. 3.3.1 for the two-site model by numerical simulation of Eq. (3.2), following the procedures in Ref. [226]. We set $\delta t = \min(0.05, 0.05/\lambda, 0.05/\Gamma)$ across all simulations, which guarantees that the continuous limit is reached (tests with smaller time steps leave the results unaffected). For numerical convenience, we also restrict the initial state to be of the form

$$|\psi\rangle = \alpha|00\rangle + \beta|01\rangle + \gamma|10\rangle + \delta|11\rangle, \tag{3.9}$$

with $\alpha, \beta, \gamma, \delta \in \mathbb{R}$. This guarantees that the dynamics remain real at all times.

Before proceeding to the results, we shall discuss briefly some of the effects of various contributions. In a 2-qubit system, H with $j \in \{1, 2\}$ is the usual hopping term coupling the two qubits. In the absence of any randomness, starting from an initial state $|\psi\rangle = \alpha|00\rangle + \beta|01\rangle + \gamma|10\rangle + \delta|11\rangle$, the system displays periodicity in entanglement reflecting the unitarity of H[1]. With the addition of white noises and measurements, which do not commute with H, all three dynamics compete. Without measurement, finite local white noises scramble information within the system, suggesting a noise-strength independent entanglement in the long-time steady-state dynamics. With the addition of measurement (which tends to localise information), entanglement is expected to be suppressed as the measurement strength increases. The ultimate fate of entanglement and correlations with the interplay of all three dynamics depends non-trivially on their relative strength.

First, we present our main results for efficient measurement (pure state

[1]In fact, the system is equivalent to a single qubit with σ_y rotation.

dynamics) in Fig. 3.2. Panels (a) and (b) display the results of the average concurrence $\overline{\mathcal{C}}$ in the long-time steady-state as a function of the noise strength Γ, for various measurement strength λ. Without measurement ($\lambda = 0$), the average concurrence in the long-time steady-state $\overline{\mathcal{C}}$ converges to a value independent of the noise strength, $\overline{\mathcal{C}} = 0.5$. This is a direct consequence of the information scrambling by the local random unitary, which, in the steady state, leads to a flat probability distribution over all the allowed states. As a result, the noise strength merely affects how fast the information is scrambled (time required to saturate). At the same time, the steady-state value is uniquely determined by the subspace of available states. With the parametrization in Eq. (3.9), the average concurrence is given by

$$\overline{\mathcal{C}} = \int_{\Omega} dSP|\alpha\delta - \beta\gamma| = 0.5, \tag{3.10}$$

where Ω is the hyper-surface defined by $\alpha^2 + \beta^2 + \gamma^2 + \delta^2 = 1$ (a 3-sphere). $P = 1/(2\pi^2)$ is the normalised constant probability distribution and dS the infinitesimal surface element. With the inclusion of measurement, entanglement is overall suppressed, displaying a trend of reduction with increasing measurement strength λ, as indicated in Fig.3.2(a) (vertical slices) and (b). In particular, there is a non-monotonic behaviour in $\overline{\mathcal{C}}$ with increasing Γ, as a non-trivial result of the interplay between noise and measurement. The initial increase of average concurrence with Γ for weak noise can be understood heuristically as an information scrambling effect from the random local unitary. This scrambling competes with and reduces the localising effect from measurement. This simple argument, however, breaks down when the noise is increased further: $\overline{\mathcal{C}}$ first reaches a maximum as indicated by the blue dots, then decreases for larger Γ. This is one of our first findings: competing local noise and measurement can reduce entanglement for strong noise, contrary to enhancement for weak noise. The reduction in entanglement induced by measurement for strong noise can be reasoned as an effect of fast fluctuations of local energy levels, which hinder the ability of H_0 to entangle adjacent spins.

This non-monotonic behaviour is observed in the half-system parity variance as

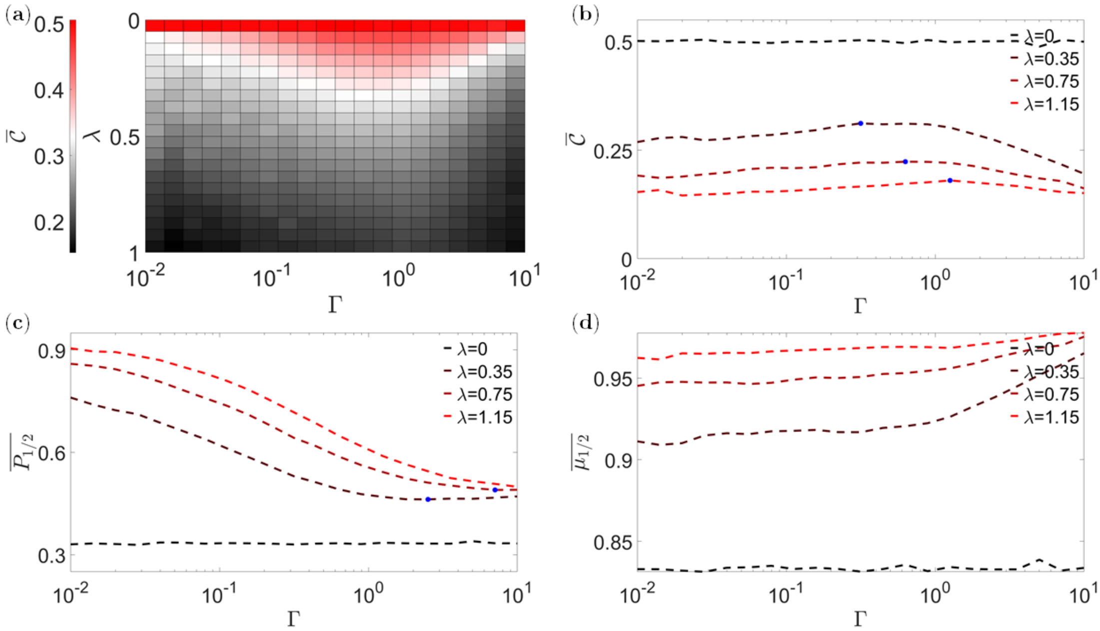

Figure 3.2: Average entanglement and half-system parity variance in the steady state of the two-qubit model (c.f Eq.(3.2)). (a): density plot of the average concurrence $\overline{\mathcal{C}}$ over an array of noise strengths Γ and measurement rates λ. A non-monotonic dependence on the noise strength Γ can be observed, as indicated by the color scheme. (b): horizontal cuts along the density plot Fig. 3.2(a) displaying the average $\overline{\mathcal{C}}$ as a function of Γ for various λ, see legend. The blue dots indicate the maximum of each curve. (c): average half system parity $\overline{P_{1/2}}$ as a function of Γ for various λ. The blue dots indicate the minimum of each curve, and for $\lambda = 1.15$ (red) the minimum lies outside of the plot (estimated to be $\Gamma \approx 20$). (d): average half system purity $\overline{\mu_{1/2}}$ as function of Γ for various λ. The curves are monotonic in the noise strength Γ.

well. In Fig. 3.2(c), we observe from the half-system parity that there is an initial decrease for small Γ, reaching a minimum (blue dots), followed by an increase for larger Γ. The overall values of $\overline{P_{1/2}}$ in the presence of measurement are higher than the noise-only scenario, revealing less correlation within the system and the dynamics resembling a quantum Zeno regime. The non-monotonic behaviour in $\overline{P_{1/2}}$ indicates various degrees of localised correlations, and it is qualitatively in agreement with the behaviour observed in $\overline{\mathcal{C}}$: high $\overline{\mathcal{C}} \leftrightarrow$ low $\overline{P_1}$ and vice versa. It is worth pointing out that the location of the minimum in $\overline{P_{1/2}}$ does not match exactly the location of the maximum in $\overline{\mathcal{C}}$. In both cases, the maximum/minimum of the non-monotonicity shifts to a larger value of Γ with increasing λ as indicated by the blue dots. In particular, the minimum of $\overline{P_{1/2}}$ shifts faster than the maximum of $\overline{\mathcal{C}}$ (the minimum for $\lambda = 1.15$ lies outside of the plot in Fig. 3.2(c), estimated to be $\Gamma \approx 20$).

In addition, for larger measurement strength λ, the non-monotonic behaviours in both $\overline{\mathcal{C}}$ and $\overline{P_{1/2}}$ are less noticeable; for $\lambda = 1.15$, the curve for $\overline{P_{1/2}}$ appears to be monotonic in the range of Γ shown, but further numerical simulation for larger Γ confirms its non-monotonicity. Whether the non-monotonic trend persists for arbitrarily large λ is not conclusive.

Interestingly, in Fig. 3.2(d), $\overline{\mu_{1/2}}$ does not show any non-monotonic behaviour in the set of λ's values presented here, but it is present for smaller λ as reported in Ch. 3.5. Although its overall increase with Γ qualitatively agrees with the overall trend observed in $\overline{\mathcal{C}}$ and $\overline{P_{1/2}}$, the disappearance of non-monotonicity for larger λ suggests that different indicators, may have quantitative differences in capturing the features of Zeno dynamics. In the following, we will drop $\overline{\mu_{1/2}}$ and retain only the half-system parity variance $P_{1/2}$ that more closely matches the entanglement dynamics.

3.3.3 Inefficient measurements

As presented above, for efficient measurements (pure state), both the entanglement and correlations capture, to some extent, the same non-monotonic feature in the dynamics, indicating some correspondence between correlations and entanglement in a similar fashion to equilibrium physics. In a many-body setting, this suggests that a quantum Zeno regime, in which the dynamics stabilize a short-range correlated state (local measurement operator eigenstate), is related to the low entanglement area law in the system [227, 228]. However, as demonstrated below, this relationship appears somewhat broken in inefficient measurements (mixed state).

In Fig.3.3, we display the results of the concurrence and the half-system parity variance for inefficient measurements. From the simulations of $\overline{\mathcal{C}}$ (Fig. 3.3(a)-(c)), we observe that the entanglement in the system generally decreases with decreasing efficiency of the measurements (lighter to darker blue). This is a direct consequence of inefficient measurements that make the density matrix increasingly mixed and closer to the fully mixed state as the inefficiency increases, diminishing entanglement in the system. An important feature is observed here: for any measurement strength, λ, the non-monotonicity of $\overline{\mathcal{C}}$ in Γ disappears below a threshold efficiency η^*, which depends on λ (disappearance of maxima indicated by black dots). We interpret this as a new regime in which the density matrix is highly mixed, and the scrambling from local random unitaries cannot out-compete entanglement loss from local measurements.

However, the operator correlations in the system tell a different story. In Fig.3.3(d)-(f), we display the results of the average half-system parity variance in the steady state as a function of Γ. Although the absolute values of $\overline{P_1}$ are lower for decreasing η, non-monotonic behaviour is present across all finite efficiency η. This behaviour is different from that of the entanglement: the average concurrence $\overline{\mathcal{C}}$ becomes monotonically decreasing for larger η, whilst the average half-system parity variance $\overline{P_1}$ remains non-monotonic. This comparison shows that entanglement and operator correlations may behave as two distinct system features. Therefore, it is natural to ask whether the phase transition captured by operator correlations is the same as that captured by entanglement. This will be the main theme of the next section, Ch.3.4

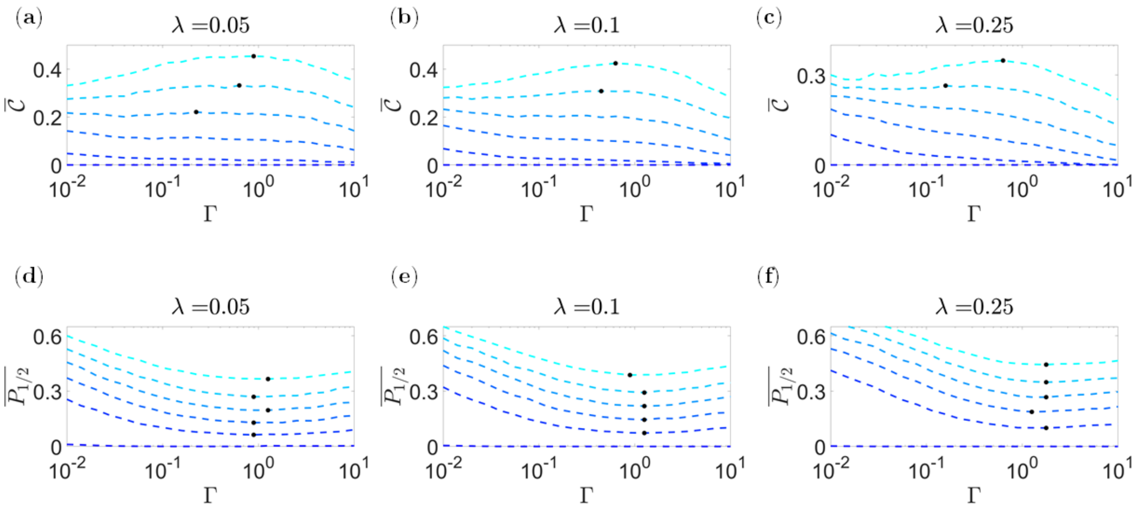

Figure 3.3: Trajectories averaged concurrence $\overline{\mathcal{C}}$ (top) and half-system parity $\overline{P_{1/2}}$ (bottom) as a function of local white noise strength Γ, for given measurement strength λ with increasing values from left to right panels, and various measurement efficiencies η. The values of η, from dark blue to light cyan, are $\{0, 0.2, 0.4, 0.6, 0.8, 1\}$. (a)-(c): the black dots indicate the maximum for each curve. The maximum drifts to lower Γ for smaller η. (d)-(f): the black dots indicate the minimum for each curve. The position of the black dots is essentially independent of η.

3.4 Spin chain

We now extend our investigation to a chain of more than two qubits (c.f eq.(3.2)). Given the qualitative differences of inefficiencies in entanglement and operator correlations highlighted in the last section, we focus specifically on whether the phase transitions (of a many-body system) indicated by the two separate measures are equivalent. We employ the half system logarithmic entanglement negativity labelled by $\epsilon_{L/2} \equiv \epsilon_{1/2}$ to quantify entanglement (c.f eq.(3.5)), and half system parity variance labelled by $P_{1/2} = \mathrm{Tr}\left[\prod_{j=1}^{L/2} \sigma_j^z \rho_t\right]^2$ for operator correlations in the spin chain dynamics (c.f Eq.(3.7)).

Note that although there exists a generalised many-body concurrence [229, 230], it only applies to pure states (efficient measurement), hence we employ the entanglement negativity as a proper entanglement estimator.

3.4.1 Efficient measurement

From Ch.3.3.2, entanglement and operator correlations generally agree with each other in capturing the same qualitative features for the case of two qubits for efficient measurement. We expect this to hold here as well. This implies that as the system's entanglement changes from extensive-entanglement scaling to area-law behaviour when λ increases, $\overline{P_{1/2}}$ changes from system-size dependent to system-size independent. The former indicates strong spin-spin correlations.

In Fig. 3.4, we display the scaling of $\overline{\epsilon_{1/2}}$ and $\overline{P_{1/2}}$ with respect to different system sizes L, for various λ at fixed Γ. Fig. 3.4(a) shows a qualitative change in entanglement scaling upon increasing measurement strength for a fixed $\Gamma = 0.1$. For small measurement strength $\lambda \leq 2.4$, $\overline{\epsilon_{1/2}}$ is L dependent with extensive entanglement scaling, as shown by the pale yellow line in Fig. 3.4(a); in contrast, the darker brown lines in Fig. 3.4(a) show that $\overline{\epsilon_{1/2}}$ becomes L independent for larger $\lambda > 2.4$, suggesting an area-law phase. When the noise strength is increased, the extensive entanglement phase sets on at increased values of $\lambda > 4$ as shown

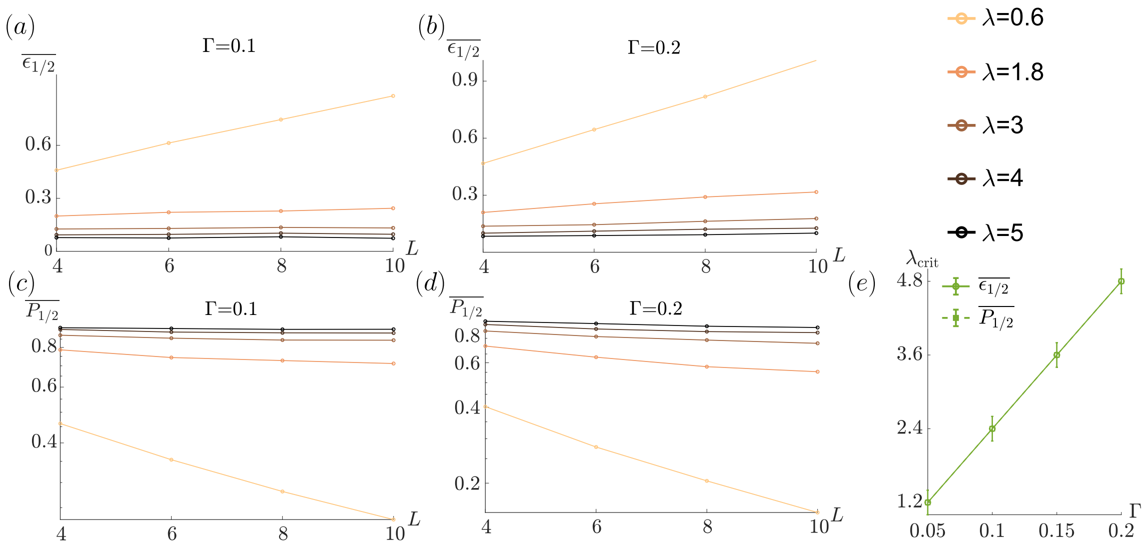

Figure 3.4: Scaling of the averaged entanglement negativity $\overline{\epsilon_{1/2}}$ (panels a,b) and half system parity (panels c,d) in the spin chain model under efficient continuous measurement $\eta = 1$ for different values of the measurement strength. The results are shown for two different values of noise strength, $\Gamma = 0.1$ in panels (a) and (d), and $\Gamma = 0.2$ in panels (b) and (c). (e): estimated critical measurement strength λ_{crit} as a function of Γ as estimated from $\overline{P_{1/2}}$ (square marker/dashed line) and $\overline{\epsilon_{1/2}}$ (triangle marker/solid line). The two lines are indistinguishable since they fully overlap.

in Fig. 3.4(b): the $\lambda = 3$ brown line is L-dependent in Fig 3.4(b), while it is L-independent in Fig. 3.4(a). Although the system sizes are limited and finite size effects are relevant, the results indicate noise strength-dependent MiPTs between an area-law phase and an extensive entanglement scaling phase. With the caveat of finite-size scaling, the latter appears to be a volume-law scaling phase. We also note that our results imply a measurement-induced phase transition induced by local unitary noise, which has recently been addressed in a different model [231].

Turning our attention to the results of half system parity in Fig. 3.4(c) and (b), their L-scaling is qualitatively consistent with that of entanglement: whenever $\overline{\epsilon_{1/2}}$ indicates an area law phase entanglement, $\overline{P_{1/2}}$ is L independent [pale colour lines in Fig. 3.4(c)], whereas it decreases with larger L in the extensive entanglement phase [dark colour lines Fig. 3.4(c) and all lines in Fig. 3.4(b)] [135, 225].

We can identify a critical measurement strength, which separates the two distinct phases from either the entanglement negativity or the half-system parity variance. In the former, $\overline{\epsilon_{1/2}}$, it separates the extensive entanglement phase from the area-law phase and in the latter, $\overline{P_{1/2}}$, it separates L-decreasing $\overline{P_{1/2}}$ from L-independent $\overline{P_{1/2}}$. We denote the respective critical measurement strengths by $\lambda_{c,\bar{\epsilon}}$ and $\lambda_{c,\overline{P}}$. Repeating the analysis in Fig. 3.4(a-d) for different values of Γ, we can estimate the Γ-dependence of $\lambda_{c,\bar{\epsilon}}$ and $\lambda_{c,\overline{P}}$. As shown in Fig.3.4(e), $\lambda_{c,\bar{\epsilon}}$ and $\lambda_{c,\overline{P}}$ approximately coincide with each other and increase monotonically for increasing Γ.

3.4.2 Inefficient measurements

We now discuss our results for inefficient measurements. As observed from the simple case of two qubits (c.f Eq. 3.3.3), correlations and entanglement under inefficient measurements may display different behaviours. Therefore, we are interested in the implications of this discrepancy on the measurement-induced entanglement transition, comparing it with the transition indicated by correlations.

In Fig. 3.5(a)-(d), we report the results for the scaling of the average half-system negativity $\overline{\epsilon_{1/2}}$ and the average half-system parity variance $\overline{P_{1/2}}$ for inefficient measurements at given noise strength and inefficiency, for different measurement strengths. For high efficiency, $\eta = 0.8$, we observe that the behaviours of entanglement and operator correlations remain qualitatively similar to the fully efficient case, i.e. both $\overline{P_{1/2}}$ and $\overline{\epsilon_{1/2}}$ undergo a transition from long-range to short-range upon increasing the measurement strength. As an example, this is shown in Fig. 3.5 panel (a) and (c) for $\Gamma = 0.15$. However, different from the fully monitored case, the estimated critical measurement strength from the two indicators is different, with $\lambda_{c,\overline{\epsilon}} \approx 3.6 < \lambda_{c,\overline{P}} \approx 4.4$. The critical points follow a dependence on the noise strength similar to that observed in the fully efficient case, with the critical measurement strength increasing with the noise strength, as shown in panel (e). Notably the difference between $\lambda_{c,\overline{\epsilon}}$ and $\lambda_{c,\overline{P}}$ is also reduced at smaller noise strength, and the two are no longer distinguishable at $\Gamma \approx 0.05$.

The different behaviours of the entanglement negativity and the half-system parity variance mirror the behaviours observed in the two-qubit system, in which for $\eta < \eta^*$, the non-monotonicity survives in half-system parity variance, but not in the entanglement negativity. The discrepancy between the two is further enhanced as we reduce the efficiency to $\eta = 0.4$ [panels (b) and (d)]. In fact, $\lambda_c(\epsilon)$ appears at a much lower value and is no longer λ dependent. This aligns with the known effect that highly inefficient measurement tends to thermalise the system with vanishing entanglement. This suggests a different kind of MiPT controlled by inefficiencies, which generates mixedness and suppresses entanglement differently from the localising effect of measurement [232]. Such transition to vanishing entanglement due to inefficiency was also found in other models, and in some cases, a critical inefficiency can be identified at which, below the critical efficiency, the system is generally in the mixed phase [135, 136]. This transition to a mixed phase can also be observed through the effect of noise. For small inefficiency, increasing Γ still has the effect of favouring the extensive entanglement phase, which increases $\lambda_{c,\overline{\epsilon}}$ as shown in Fig. 3.5(e) (solid purple line). However, as the inefficiency is increased further, this entanglement enhancing effect by noise is suppressed as

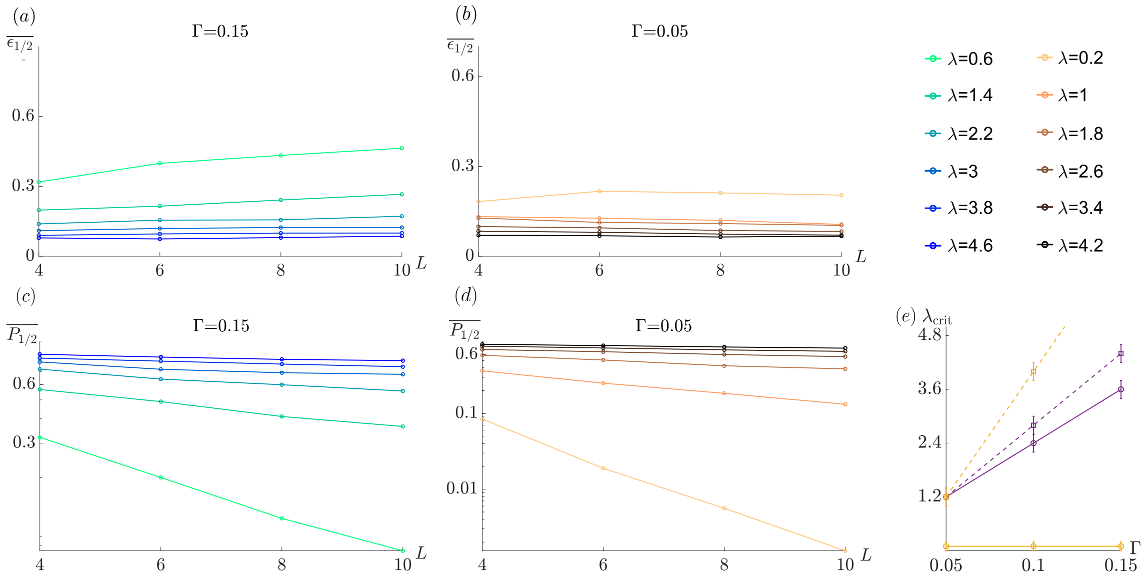

Figure 3.5: Scaling of the averaged entanglement negativity $\overline{\epsilon_{1/2}}$ (panels a,b) and half system parity (panels c,d) in the spin chain model under inefficient continuous measurement $\eta < 1$. The results are shown for two different values of noise strength and inefficiencies, $\Gamma = 0.15$ $\eta = 0.8$ in panels (a) and (c), and $\Gamma = 0.05$ $\eta = 0.4$ in panels (b) and (d). Legend of the lines appears at the top right corner. (e): estimated critical measurement strength λ_{crit} as a function of Γ for $\lambda_{c,\overline{P}}$ (square marker/dashed line) and $\lambda_{c,\overline{\epsilon}}$ (triangle marker/solid line). The colour scheme indicates different values of inefficiency with purple for $\eta = 0.8$ and yellow for $\eta = 0.4$.

displayed in Fig. 3.5(e) (solid yellow line), where $\lambda_{c,\bar{\epsilon}}$ is Γ-independent and possibly equal to 0 for any finite measurement strength. The absence of this enhancement by noise is in line with the discussion previously on entanglement suppression by inefficiency/thermalisation in Ch. 3.3.

It is important to note that the results presented here so far are heavily affected by finite-size effects. For example, the lightest green line in Fig. 3.5(a) appears to bend down for larger L, and it is not certain from the results presented whether it grows or saturates for larger L. While this implies that the critical points presented in Fig. 3.5(e) are far from their thermodynamic value, the main conclusion that $\lambda_{c,\bar{\epsilon}}$ and $\lambda_{c,\overline{P}}$ differ from each other in inefficient measurement should remain valid, as it is both demonstrated by the light brown lines in Fig. 3.5(b) and (d), and suggested by previous results in Ch. 3.3.3.

Finally, I note that the case $\eta = 0$ is trivial: any finite λ will induce trivial dynamics since the measurement part of the master equation Eq.(3.2) reduces down to a Lindbladian, and the density matrix at long times is merely proportional to identity.

3.5 Supplementary numerical simulations

In this chapter, we present more numerical results for entanglement negativity and purity for completeness. We also report simulations using the quantum jump equation, which shows identical average features.

Quantum jump —The procedure to simulate the quantum jump equation is slightly different from the one used in the main text: we modify the measurement operator σ^z to a jump operator $\hat{n}_j = 1/2(1+\sigma^z_j)$ which is a projector. The quantum jump equation can be derived using suitable Kraus operators, similar to Eq.(2.42):

$$\begin{aligned} K_u &= \sqrt{\epsilon}\,|1\rangle\langle 1| \\ K_d &= \sqrt{1-\epsilon}\,|1\rangle\langle 1| + |0\rangle\langle 0|\,. \end{aligned} \tag{3.11}$$

Here ϵ is a small number quantifying the strength of the measurement, and its temporal scaling should be set as $\epsilon \sim dt \equiv \gamma dt$ to derive the time continuum quantum jump equation [27, 146]. Measurement inefficiency is incorporated as outlined in Ch. 2.1.4: given a true measurement result u, the probability of the detector's output being u is not unity (c.f. Eq(2.42)).

In Fig. 3.6, we present the results for average concurrence squared $\overline{\mathcal{C}^2}$ using the quantum jump equation. Non-monotonicity is present for perfect measurement (Fig. 3.6(a)), and it disappears for sufficiently inefficient measurement (Fig. 3.6(a)).

Logarithmic negativity — In Fig. 3.7, we display the results of half system logarithmic negativity, obtained by simulating Eq.(3.2). Non-monotonicity is also present, which confirms that this is a general entanglement feature in this 2-qubit system, irrespective of the monotone used for entanglement.

3.6 Summary

In this chapter, we have numerically investigated the effect of local unitary noise in locally monitored systems. In a minimal 2-qubit setup, the interplay of these competing dynamics produces an intriguing non-monotonic behaviour in entanglement and operator correlations as a function of noise strength. This unique feature associated with quantum trajectory dynamics is most visible at small measurement strength, where the system displays higher entanglement/correlations for intermediate noise strength. With increasing measurement strength, the minimum/maximum of the non-monotonicity shifts to larger noise strength and the non-monotonicity becomes less prominent.

Interestingly, upon the inclusion of measurement inefficiency, the 2-qubit system signals non-trivial dynamics for the entanglement and operator correlations: entanglement gradually becomes monotonic, whereas correlations, specifically the hal-parity variance, remain non-monotonic for all finite measurement inefficiencies. This

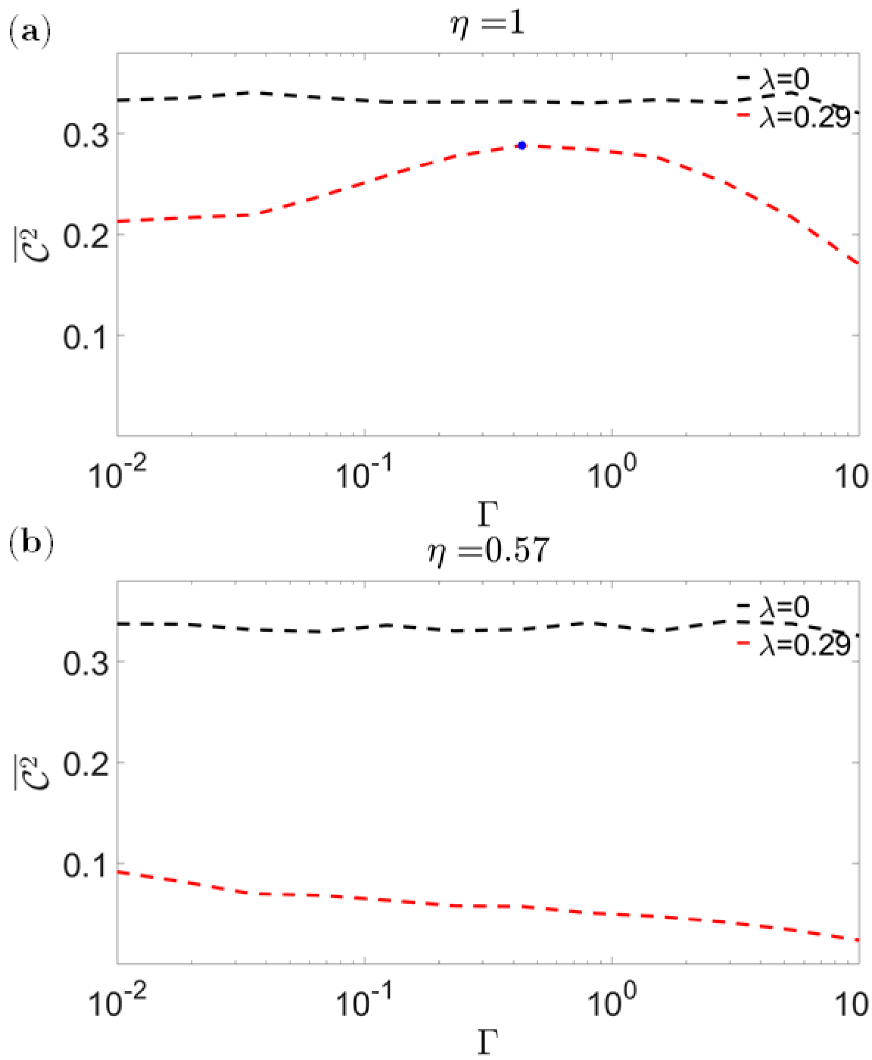

Figure 3.6: Average squared concurrence $\overline{\mathcal{C}^2}$ as a function of noise strength and for different values of the measurement strength for jump operator $\hat{n}_j = 1/2(1+\sigma_j^z)$, $j \in \{1, 2\}$. Results for two measurement inefficiencies are presented: (a) $\eta = 1$ and (b) $\eta = 0.57$.

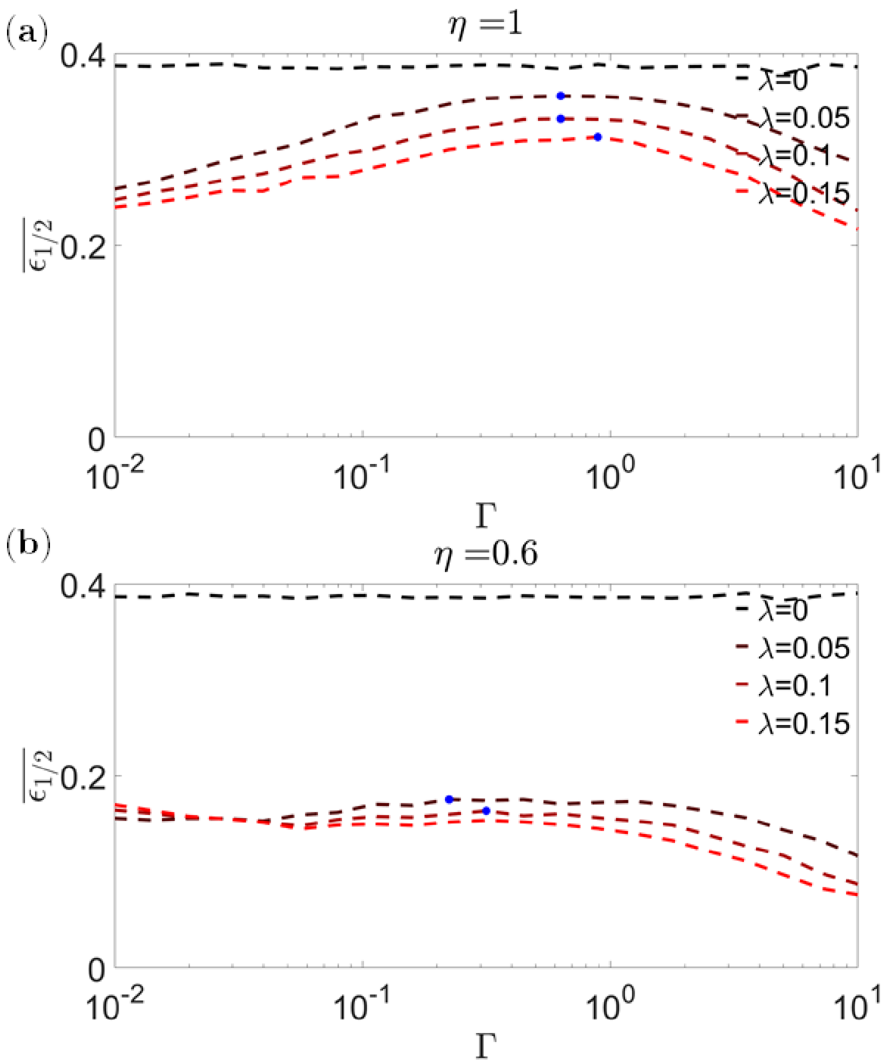

Figure 3.7: Average half system logarithmic negativity $\overline{\epsilon_{1/2}}$ as a function of noise strength for different values of the measurement strength, obtained by using identical time evolution as in the main text (c.f Eq.(3.2)). Results for two measurement inefficiencies are presented: (a) $\eta = 1$ and (b) $\eta = 0.6$. The presence (absence) of a blue dot indicates whether a non-monotonic behaviour is present(absence), and its location corresponds to the maximum.

suggests a breakdown of the conventional correspondence between entanglement and operator correlations present in equilibrium physics, and mixed dynamics could host correlations, which behave differently from entanglement. This can be heuristically understood because operator correlators generally capture both quantum and classical correlations, which might be responsible for the breakdown. Such behaviour was also hinted at in pure state unitary dynamics [233], where entanglement entropy scales differently from higher order Rényi entropy.

Motivated by this observation in mixed state dynamics (inefficient measurement), we study an extended spin 1/2 chain model and compute the system size scaling of entanglement and half-parity variance. For efficient measurements, the scaling of entanglement and operator correlations display the typical correspondence in behaviour so that the short-range (area-law) entanglement phase coincides with the short-range phase from operator correlations. For inefficient measurements, however, the breakdown of the relation is visible: short-range entanglement no longer corresponds to short-range correlations. The results suggest that entanglement and operator correlations can generically differ from each other in mixed-state dynamics, and the phase diagrams indicated by the two quantities are no longer equivalent.

Chapter 4

Theory of free fermions under partial post-selected monitoring

In the last chapter, we explored the effect of inefficiency (classical uncertainty) in MiPT. Therein, the microscopic ancilla still picks up all the available measurement results; we simply do not have access to all of them. This naturally leads to asking what happens when a pure quantum-mechanical fault in the ancilla causes it to only output a fraction of the results, i.e., only certain trajectories are selected. We know from the background section that this can lead to non-Hermitian dynamics, as discussed in Ch. 2.1.3. In this chapter, we analyse this problem further and formulate a new theory interpolating between deterministic non-Hermitian dynamics and stochastic measurement updates. This chapter is based on Ref. [234].

4.1 Overview

As mentioned many times throughout this chapter, MiPTs are fascinating phenomena in open quantum systems. However, due to the nonlinearity of Eq.(2.27), MiPTs are analytically demanding to analyse. To circumvent this, a common route to gain insight into MiPTs is to investigate its corresponding post-selected dynamics [75, 146–158], governed by a non-Hermitian Hamiltonian as pointed out in Ch. 2.1.3.

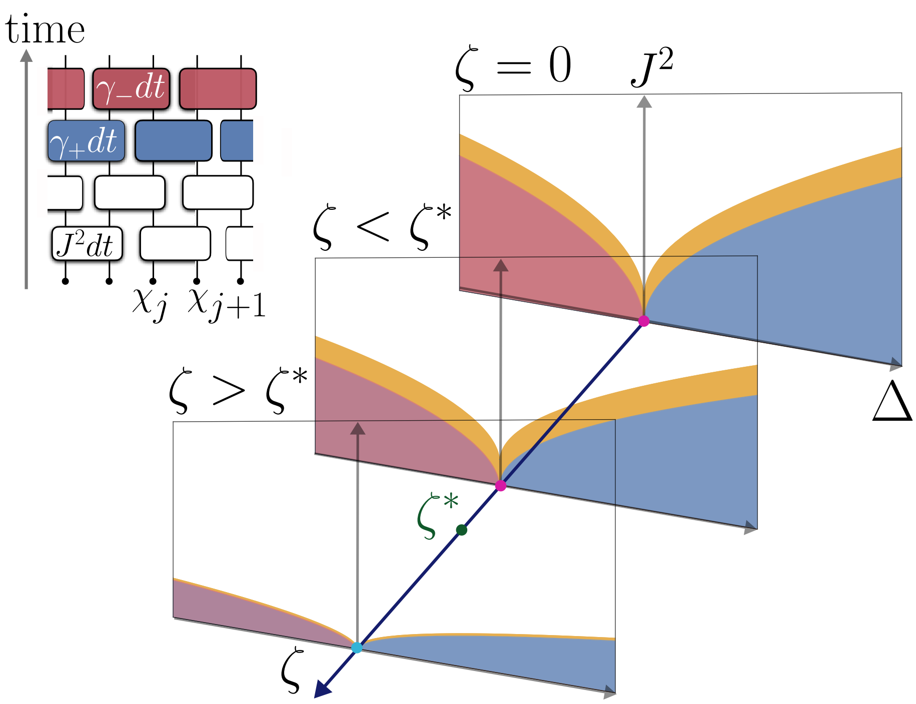

Figure 4.1: Schematic drawing of the phase diagram for the model in the inset under partial post-selection. The parameter $\zeta \in [0, 1]$ controls the degree of partial post-selection, with no post-selection for $\zeta = 1$ and complete post-selection for $\zeta = 0$. The system displays topological trivial (blue) and non-trivial (purple) entanglement area-law phases, as well as critical log-scaling (orange) and $\log^2$-scaling (white) phases. The measurement-only phase transition (at $\Delta = 0$ on the $J^2 = 0$ line) changes its universality class with the degree of post-selection from the post-selected one (red dot) for $\zeta < \zeta^*$ to the full monitored one (cyan dot) for $\zeta > \zeta^*$. Inset: quantum circuit representation of the model consisting of random unitary evolution (white) and competing sets of Majorana fermions' bond-parity measurements of strength $\gamma_+ = \gamma(1 + \Delta)$ (blue) and $\gamma_- = \gamma(1 - \Delta)$ (purple).

However, MiPTs in the post-selected limit of monitored dynamics exhibit **key differences** compared to their monitored counterparts. These differences extend from features of the phase diagram to the universality class of the transition [75, 146]. There have been some steps to incorporate sparse quantum jumps beyond the post-selected limit [149, 151], or to explore numerically the full crossover [75, 159]; nonetheless, a theory that captures a systematic way to include a fraction of trajectories and explains the change in MiPTs properties is generally lacking. This is the question we address in this chapter. We first summarise here our main findings.

First, we derive a *partial-post-selected* (PPS) *stochastic Schrödinger equation* (SSE) — cf. Eq.(4.9), with a continuous parameter ξ that controls the range of detector's outcomes that are retained. The PPS-SSE includes the fully monitored and fully post-selected dynamics as limiting cases and is valid for a generic quantum system with a continuously monitored Hermitian observable. Next, we apply our analytic PPS approach to study the MiPT driven by non-commuting sets of local parity measurements in a real free fermionic chain. In this model, the post-selected dynamics feature an area-to-area topological MiPT driven by the competing measurements, with a different critical exponent than its monitored analogue [75]. We use the PPS-SSE approach to calculate the conditional entanglement entropy across the transition (see Ch. 4.3.1 for details); this allows us to use a two-replica limit to obtain an effective description of the out-of-equilibrium steady-state phases in terms of an effective Hamiltonian—cf. Eqs. (4.33,4.42,4.39). From a renormalisation group (RG) flow analysis of the Hamiltonian, we find that the universal properties of the post-selected MiPT persist when one moves away from the post-selected limit by increasing the range of outcomes retained —cf. Ch. 4.7.1, Fig. 4.4.

Our calculation further shows that the Luttinger parameter of the effective bosonised theory for strong partial post-selection diverges at a finite value of partial post-selection strength, which may indicate a phase transition driven by the stochasticity from quantum trajectories. This result is supported by numerical calculations, which identify the non-monotonic behaviour of the critical exponent at similar partial post-selection strength —cf. Fig. 4.6.

In the presence of unitary dynamics, the partial post-selected model features two distinct area law phases separated by a sub-volume law phase. We find that the sub-volume phase becomes increasingly stable upon moving away from the post-selected limit, as shown in Fig. 4.1 (also Ch. 4.7.2, Fig. 4.8).

The rest of the chapter is structured as follows. We develop the formalism of partial post-selection in Ch. 4.2 and extend it to the replica formalism in Ch. 4.3. Ch. 4.5 presents the model of interest, with the corresponding effective 2-replica description in Ch. 4.5.1 and the effective theory for the strong-post-selection regime in Ch. 4.6. The results are presented in Ch. 4.7 with a final discussion and conclusions in Ch. 4.8.

4.2 Partial post-selection

We consider the dynamics of a continuously monitored quantum system whose evolution is described by the quantum state diffusion equation, a stochastic Schrödinger equation (SSE)

$$d|\psi_t\rangle = \left[-idtH - dt\frac{\gamma}{2}\sum_j \left(\hat{O}_j - \langle\hat{O}_j\rangle\right)^2 + \sum_j dW_j\left(\hat{O}_j - \langle\hat{O}_j\rangle\right)\right]|\psi_t\rangle, \tag{4.1}$$

where $|\psi_t\rangle$ is the system's state at time t, $\hat{O}_j$ the set of observables being measured, and H the system's Hamiltonian. To lighten the notation, we shall drop the hat above the measurement operator unless it is needed for clarity. Eq.(4.1) is the Ito formulation of stochastic dynamics with dW_j uncorrelated Gaussian-distributed stochastic increments with $\overline{dW_j dW_k} = \gamma dt\delta_{j,k}$, where γ is the inverse measurement time at which typical stochastic realizations of the quantum trajectories are close to the observable's eigenvalue.

To develop the idea of partial post-selection, let's begin with a brief reminder of the microscopic measurement model leading to the SSE, as detailed in Ch. 2.1.2.1. We consider the measurement process described by a positively valued measurement [27]. After coupling the detector to the system in a state $|\psi\rangle_t$, the process returns a readout x_j, drawn from a probability distribution $P(x_j) = \langle\psi_t|K_j(x_j)^\dagger K_j(x_j)|\psi_t\rangle$, and a conditional state update $|\psi_{t+dt}\rangle = K_j(x_j)|\psi_t\rangle/\sqrt{P(x_j)}$. The process is entirely dictated by the Kraus operators $K_j(x_j)$. As outlined in Ch. 2.1.2.1, a 2-dimensional measurement operator $O_j = \Pi_{j,+} - \Pi_{j,-}$ is coupled to a one-dimensional pointer; as a reminder, we are restricting to *a priori* the set of

Gaussian-preserving measurement operator, see Def. 2.1.2. The Kraus operator follows from Eq.(2.15), and for clarity, we repeat it here

$$K_j(x_j,\lambda) = \sqrt{G(x_j-\lambda)}\Pi_{j,+} + \sqrt{G(x_j+\lambda)}\Pi_{j,-}, \tag{4.2}$$

and the probability $P(x_j)$ is

$$P(x_j) = G(x-\lambda)\langle \Pi_{j,+}\rangle + G(x+\lambda)\langle \Pi_{j,-}\rangle, \tag{4.3}$$

where $G(x) = 1/\sqrt{2\pi\Delta^2}\exp\big(-x^2/2\Delta^2\big)$ is a Gaussian distribution. The continuous SSE in Eq.(4.1) is recovered by setting $\lambda^2 = \gamma dt$, $dt \to 0$ with γ finite. This guarantees $\lambda \ll 1$. In this limit,

$$\begin{aligned} P(x_j) &\approx \frac{1}{\sqrt{2\pi\Delta^2}}\exp\left(-\frac{(x_j-\lambda\langle O_j\rangle)^2}{2\Delta^2}\right), \\ K_j(x_j,\lambda) &\approx \frac{1}{(2\pi\Delta^2)^{1/4}}\exp\left(-\frac{(x_j-\lambda O_j)^2}{4\Delta^2}\right). \end{aligned} \tag{4.4}$$

The probability distribution is schematically shown in Fig. 2.2. Notably, in Eq.4.4, $\lambda^2 = \gamma dt \to 0$, $\Delta \sim \mathcal{O}(dt^0)$ in the continuum limit.

The scenario of multiple measurement events can be written down readily: if there are L lots of measurement operators $\hat{O}_j, j \in [1\ldots L]$, the final state after measurements across all operators is

$$|\psi_{t+dt}\rangle = \frac{1}{\mathcal{N}}\prod_{j=1}^{L} K_j(x_j,\lambda)|\psi_t\rangle, \tag{4.5}$$

where the results hold in the continuum limit $dt \to 0$ to order $\mathcal{O}(dt)$, even if some of the operators $\mathcal{O}_j$ do not commute. As a side note, (4.2) can also be generalised to measurement operators with arbitrary spectrum with the same procedure illustrated in Ch. 2.1.2.1 [27].

The process of post-selection amounts to choosing and retaining the quantum trajectories that correspond to a unique set of predetermined detector readouts $\{x_j\}$, while discarding the rest. We generalize this procedure to achieve **partial post-selection** (PPS) by retaining all quantum trajectories that correspond to a finite range of detector outcomes. A natural means to achieve PPS is to force some degree of bias in the measurement outcome retaining the detector's outcome only if they are larger than a given, preset value, r_c. This amounts to truncating the readout probability distribution function $P(x_j)$ to a modified one,

$$P_{r_c}(x_j) = P(x_j)\Theta(x_j - r_c) \approx e^{-\frac{(x_j - \lambda\langle O_j\rangle - \delta\lambda)^2}{2(\Delta+\delta)^2}} \equiv \underline{P}(x_j), \tag{4.6}$$

where $\Theta(x)$ is the Heaviside step function.

In the last step in Eq.(4.6), we have approximated the truncated distribution by a Gaussian distribution whose mean and variance, parametrised by $\delta\lambda$ and δ respectively, are determined by demanding that they coincide with those of $P_{r_c}(x_j)$, as illustrated in Fig. (4.2). While the distribution P_{r_c} and $\underline{P}$ are generically different, we demand a proper scaling of r_c with $dt \to 0$, so that the two distributions coincide in the continuum limit. This is achieved with the scaling

$$\delta\lambda = b\lambda = b\sqrt{\gamma dt}, \tag{4.7}$$

where b is kept constant in the limit $dt \to 0$ (see Appendix B.1). The relation between r_c and b is derived and discussed in Appendix B.1, and b captures the discrete-time process r_c in the time continuum limit, in analogy to γ capturing the discrete process λ in continuous measurement backaction. On the other hand, the correction in variance, δ, can be safely ignored (Appendix B.1). Importantly, at leading order in dt, the functional dependence of r_c on b is independent of the system's state, so that the continuum limit at constant b corresponds to an operationally well-defined truncation of the probability $P(x_j)$.

We show explicitly via a two-sample Kolmogorov-Smirnov (KS2) test from a numerical sampling of P_{r_c} and $\underline{P}$ [163], that the approximation by a Gaussian distribution in the time continuum analysis becomes exact in the continuum limit. The results are reported in figure 4.2, with the inset showing that the p-values (a statistical measure of overlap) of the two distributions are increasing with small time increments dt.

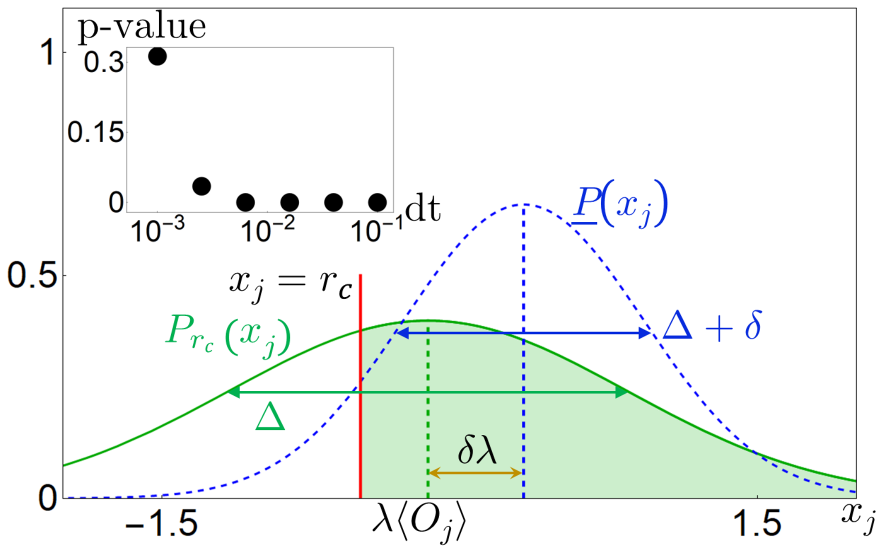

Figure 4.2: Partial-post selection procedure in (4.6). The measurement outcome Gaussian distribution (green) is truncated at $x_j = r_c$, resulting in a new distribution $P_{r_c}(x_j)$ (shaded) with shifted mean $\lambda \to \lambda + \delta\lambda$ and shifted variance $\Delta^2 \to (\Delta+\delta)^2$. P_{r_c} is approximated by a new Gaussian, $\underline{P}(x_j)$ (blue), with mean $\lambda + \delta\lambda$ and variance $(\Delta + \delta)^2$. The approximation is valid in the continuum limit as shown in the inset. Inset: p-value from a KS2 test for the two distributions P_{r_c} and $\underline{P}$ with various dt. The approximation is exact in the continuum limit $dt \to 0$ The parameters are set as $\langle O_j\rangle = 0.2$, $r_c = -0.5$ and $\lambda = 0.3$.

The continuum limit of $\underline{P}(x_j)$ in Eq.(4.6), allows us to obtain a corresponding PPS SSE. Specifically, we introduce a new random variable $\xi_j = x_j/\Delta - \lambda\langle O_j\rangle - b\lambda$, $\mathbf{mean}(\xi_j) = 0, \mathbf{Var}(\xi_j) = 1$. When expressed in terms of ξ, the update of the state by the Kraus operator in (4.5) becomes

$$|\psi_{t+dt}\rangle = \frac{1}{\mathcal{N}}\prod_j K_j(x_j,\lambda)|\psi_t\rangle = \frac{1}{\mathcal{N}_2}\prod_j e^{\left(\frac{\lambda^2(O_j-\langle O_j\rangle-b)^2}{4\Delta^2}+\xi_j\lambda\frac{O_j-\langle O_j\rangle-b}{2\Delta}\right)}|\psi_t\rangle, \tag{4.8}$$

where overall factors have been reabsorbed in the state-normalization $\mathcal{N}_2$. By setting $\Delta = 1/2$, $\lambda^2 = \gamma dt$ and noticing that the random variable $\xi_j\sqrt{\gamma dt} = dW_j$ fulfils $\overline{dW_j dW_k} = \gamma dt$, the state update in Eq.(4.8) defines a Wiener process to order dt and we arrive at the modified partial-post selected stochastic Schrödinger equation (PPS SSE)

$$\begin{aligned} d|\psi_t\rangle = -idtH|\psi_t\rangle - \frac{\zeta dt}{2}\sum_j\left(\hat{O}_j - \langle\hat{O}_j\rangle\right)^2|\psi_t\rangle + (1-\zeta)dt\sum_j\left(\hat{O}_j - \langle\hat{O}_j\rangle\right)|\psi_t\rangle \\ + \sum_j dW_j\left(\hat{O}_j - \langle\hat{O}_j\rangle\right)|\psi_t\rangle, \end{aligned} \tag{4.9}$$

where $dW_j dW_k = \zeta dt\delta_{j,k}$. Going from Eq.(4.8) to Eq.(4.9), we use $\gamma + b\gamma > 0$ as an overall energy scale which we then set to $\gamma + b\gamma = 1$, and introduced a dimensionless parameter

$$\zeta = \frac{\gamma}{\gamma + b\gamma} = \frac{1}{1+b} \in [0,1], \tag{4.10}$$

controlling the degree of partial post-selection.

Eq.(4.9) is the first main result of our work. It generalises the SSE for observables of a 2-dimensional Hilbert space to account for a partial selection of trajectories defined in an operationally meaningful procedure. From, Eq.(4.9), we can identify two limits: for $\zeta = 1$, we recover the standards SSE for monitored dynamics, while for $\zeta = 0$ we are in the post-selected limit governed by a non-Hermitian Hamiltonian $H_{\text{eff}} = H + idt\sum_j \hat{O}_j$[1]. It is worth noting that the above procedures can be generalised readily to observables of a higher-dimensional Hilbert space, in which one of the eigenvalues is biased.

[1]The expectation value has been omitted as it is an operator independent term, which can be absorbed into the normalisation.

4.3 Measurement induced transition and replicated dynamics

As discussed in Ch. 2.4.2, the replica trick is a powerful tool for analysing random dynamics. In this chapter, we take the replica limit $n \to 2$ in Eq.(2.76) and develop an effective theory based on it. Although this is not the true replica limit and has been shown to lead to non-exact results [80], we combine this with other analyses to support our findings.

4.3.1 Conditional purity

The remainder of the chapter focuses on the analytical investigation of **conditional purity**, one of the simplest non-linear physical indicators of MiPTs in the density matrix. This quantity, which we denote by a double over line above, $\overline{\overline{\mu}}_{2,\mathbf{A}}$, was introduced in Ref. [219, 225] and is associated with the conditional 2-nd Rényi entropy $S^{(\mathrm{cond})}_{2,\mathbf{A}}$ as

$$\begin{aligned}
\overline{\overline{\mu}}_{k,\mathbf{A}}\Big|_{k=2} &\equiv e^{-S^{(\mathrm{cond})}_{k,\mathbf{A}}}\Big|_{k=2} \\
&= \left(\frac{\mathrm{Tr}\left[\mathcal{C}_{2,\mathbf{A}}\sum_{\{x_t\}}\check{\rho}^{\otimes 2}_{\{x_t\}}\right]}{\mathrm{Tr}\left[\sum_{\{x_t\}}\check{\rho}^{\otimes 2}_{\{x_t\}}\right]}\right)\Bigg|_{k=2} \\
&= \left(\frac{\sum_{\{x_t\}}P(\{x_t\})^k\,\mathrm{Tr}\left[\rho^k_{\mathbf{A},\{x_t\}}\right]}{\sum_{\{x_t\}}P(\{x_t\})^k}\right)\Bigg|_{k=2} = \frac{\mathrm{Tr}\,\rho^2_{\mathbf{A},M}}{\mathrm{Tr}\,\rho^2_M}.
\end{aligned} \tag{4.11}$$

Here, ρ_M is the reduced density matrix of the measurement devices (the ancillae) and $\rho_{\mathbf{A},M}$ is the reduced density of the subsystem $\mathbf{A}$ along with the ancillae. The trajectory-averaging is now included in the trace operation, which is explained below.

In the measurement outcome basis, ρ_M and $\rho_{\mathbf{A},M}$ are

$$\begin{aligned}\rho_M &= \sum_{\{x_t\}} \mathrm{Tr}\big[\check{\rho}_{M,\{x_t\}}\big]|\{x_t\}\rangle\langle\{x_t\}| \\ \rho_{\mathbf{A},M} &= \sum_{\{x_t\}} \mathrm{Tr}\big[\check{\rho}_{\mathbf{A},M,\{x_t\}}\big]_M|\{x_t\}\rangle\langle\{x_t\}|,\end{aligned} \tag{4.12}$$

where the trace $\mathrm{Tr}[\ldots]_M$ denotes the partial trace w.r.t. the measurement devices. $\check{\rho}_{M,\{x_t\}}$ is the un-normalised density matrix of the measurement devices conditional on the readouts $\{x_t\}$ (c.f. Eq.(2.75)). These expressions come from the fact that along each trajectory $\{x_t\}$, the density matrix of the ancillae is pure, and therefore, it is simply $|\{x_t\}\rangle\langle\{x_t\}|$ in the measurement basis with weighting $P(\{x_t\}) = \mathrm{Tr}\big[\check{\rho}_{M,\{x_t\}}\big]$. Accounting for all trajectories, the density matrix is the sum of all individual trajectory density matrices multiplied by their respective weighting. Hence, the equality in the first line of Eq.(4.12). The second line follows from the fact that the subsystem $\mathbf{A}$ reduced density matrix is separable from the ancillae density matrix, as there is no operation introducing classical uncertainty between them. Therefore, their joint density matrix along each trajectory must be (unnormalised)

$$\check{\rho}_{\mathbf{A},M,\{x_t\}} = \check{\rho}_{A,\{x_t\}} \otimes \check{\rho}_{M,\{x_t\}} = \check{\rho}_{A,\{x_t\}} \otimes |\{x_t\}\rangle\langle\{x_t\}|,$$

with weighting $P(\{x_t\}) = \mathrm{Tr}\big[\check{\rho}_{M,\{x_t\}}\big]$, and the equality follows after accounting for all trajectories.

Eq.(4.11) shows that $S^{(\mathrm{cond})}_{2,\mathbf{A}}$ is related to the 2-nd Rényi entropy of the extended system (with the ancillae), albeit shifted by a normalisation factor. We note that the conditional purity $\overline{\overline{\mu}}_{2,\mathbf{A}}$ in Eq.(4.11) differs from the subsystem purity averaged over the measurement ensemble $\overline{\mu_{2,\mathbf{A}}}$, but is instead calculable as the $n = 2$-replica limit of the latter, i.e. $k, n = 2$ in Eq.(2.76). This amounts to averaging with a *distorted* probability distribution, now given by $P(\{x_t\})^2$ as shown in Eq.(4.11). Nonetheless, $\overline{\overline{\mu}}_{2,\mathbf{A}}$ corresponds to a physically well-defined quantity and captures the non-linear effect of monitoring, thus providing a valid figure of merit to identify the non-trivial effects of PPS on measurement-induced dynamics [219, 225].

Finally, we caution the reader that the conditional 2-nd Renyi entropy $S_{2,\mathbf{A}}^{(\mathrm{cond})}$, may scale quantitatively differently from the entanglement entropy, as shown for free fermions [80]. Hence the results of our theory cannot directly be extended to partial-post selected Renyi entropies.

4.3.2 Replica dynamics in PPS

In the case of continuous measurements we are considering here, the equivalent of Eq.(4.9) for the density matrix along the individual trajectory is given by the stochastic differential equation

$$\begin{aligned}\partial_t \rho = -i\Bigg[&\left(H + i\,(1-\zeta)\sum_j \hat{O}_j - \langle \hat{O}_j \rangle \right)\rho - \rho\left(H - i\,(1-\zeta)\sum_j \hat{O}_j - \langle \hat{O}_j \rangle \right) \Bigg] \\ &- \frac{\zeta}{2}\sum_j \left[\hat{O}_j, \left[\hat{O}_j, \rho\right]\right] + \sum_j dW_j \Big\{ \hat{O}_j - \langle \hat{O}_j \rangle, \rho \Big\}. \end{aligned} \tag{4.13}$$

Eq.(4.13) contains non-linear state-dependent terms. This can be circumvented using the replica trick by studying trajectory averages of the un-normalized density matrix [80]. For the class of measurement operators relevant to our problem so that $\hat{O}^2 \propto \hat{O}$ (equivalently $\hat{O}^2 \propto \mathbb{I}$), the problem reduces to an average over random non-Hermitian Gaussian noise. Explicitly, we can rewrite the quantum trajectories average of an operator $\hat{O}$ in (2.76) as

$$\int_{\mathcal{A}_j(t_l)} \prod_{l=1}^{M} \mu\left(\mathcal{A}_j(t_l)\right) \mathrm{Tr}[\hat{O}\check{\rho}^{\otimes n}_{\mathcal{A}_j(t_l)}] = \mathrm{Tr}\Big[\hat{O}\mathbb{E}_G[\check{\rho}^{\otimes n}_{\mathcal{A}_j(t_l)}]\Big] \tag{4.14}$$

and the notation $\mathbb{E}_G[\dots]$ indicates a Gaussian average over all random variables $\mathcal{A}_l$. In the monitored dynamics, the Gaussian measure $\mu(\mathcal{A}_j(t))$ has mean centred at $\mathbb{E}_G[\mathcal{A}_j(t)] = 0$ and variance $\mathbb{E}_G[\mathcal{A}_j(t)\mathcal{A}_{j'}(t')] = \gamma\delta(t-t')\delta_{j,j'}$ in the time continuum. The details of the derivation are summarised in Appendix B.2, where we follow the notation of Ref. [80], making an explicit link to the Kraus operator introduced in Eq.(4.4). The result is a random non-Hermitian Hamiltonian acting on the *un-normalised* density matrix, see Eq.(B.12). The generalization to more than one set of measurements is straightforward, and here we abuse the notation $\mathbb{E}_G[\dots]$ to denote the Gaussian average over all random variables from all measurement processes, each with its Gaussian measure.

This 'non-Hermitian noise' formalism can be applied to the post-selection procedure in Ch. 4.2, which is formulated in terms of Gaussian distributed measurement readouts. As shown in Eq.(4.6), the overall effect of PPS is to shift the centre of the Gaussian distribution of the measurement readouts by an amount $\delta\lambda = b\lambda$. When taking the continuum limit $dt \to 0$, the averages of the stochastic process in the PPS Schrödinger equation (4.9) are equivalently described in the 'non-Hermitian noise' formalism by a Gaussian distribution with a shifted mean of the measure $\mu\left(\mathcal{A}_j(t)\right)$ (see Appendix B.2 for the detailed derivation). In particular

$$\begin{aligned}
&\mathbb{E}_G^{(PPS)}[\mathcal{A}_j] = b\gamma = 1-\zeta, \\
&\mathbb{E}_G^{(PPS)}[\mathcal{A}_j\mathcal{A}_k] = \zeta\delta(t-t')\delta_{j,k} + (1-\zeta)^2,
\end{aligned} \tag{4.15}$$

where we adopt the convention in Eq.(4.10). This procedure can be further extended to deal with averages in the replica formalism. The fundamental object of interest in the replica dynamics (cf. Eq.(2.76)) is $\mathbb{E}_G[\check{\rho}^{\otimes n}]$. We will show in Ch. 4.5.1 that this will lead to an extra deterministic non-Hermitian term in the PPS dynamics.

As demonstrated in Appendix B.2, for the class of Gaussian-preserving measurement operators $O^2 \propto O$, the evolution of the unnormalized density matrix, Eq.(4.14), is governed by a time-dependent Hamiltonian of the form

$$H(t) = H_0 + i\sum_j \mathcal{A}_j(t)O_j. \tag{4.16}$$

H_0 represents the unitary part of the evolution and the non-unitary update from measurements is represented by the non-Hermitian contribution.

Under such mapping, the evolution of the un-normalised density matrix $\check{\rho}(t)$, is given by Eq.(2.75), which, in the time-continuous limit considered here reduces to

$$K(t) = \exp\left[-i\int_0^t dt' H(t')\right]$$
$$\check{\rho}_M(t) = K(t)\rho(0)K^\dagger(t),\ \ \rho_M(t) = \frac{\check{\rho}_M(t)}{\mathrm{Tr}[\check{\rho}_M(t)]}, \tag{4.17}$$

and we label the trajectory by M (previously $\{x_t\}$), representing the string of random measurement outcomes in a single run of the experiment (see Appendix B.2 for this time continuum process).

Operator-to-state —To proceed further, it is advantageous to employ the standard Choi–Jamiołkowski isomorphism to map operators into states, which we summarise in Appendix B.3 [235, 236]. In this formalism, we can express the n-replicated density matrix (an operator in n-replicated Hilbert space) as a state in a $2n$ duplicated Hilbert space. The evolution operator then acts as a superoperator on the duplicated Hilbert space.

$$\check{\rho}^{\otimes n}(t) \xrightarrow{Choi} |\check{\rho}^{\otimes n}(t)\rangle\rangle = \big(K(t)\otimes K^*(t)\big)^{\otimes n}|\rho^{\otimes n}(0)\rangle\rangle \tag{4.18}$$

where the object $|\ldots\rangle\rangle$ indicates that the state lives in the duplicated Hilbert space. The details of the isomorphism and the derivation of Eq.(4.18) are summarised in appendix B.3. In this operator-to-state formalism, the trajectory-averaged n-replicated un-normalised density matrix is given by

$$\mathbb{E}_G[|\check{\rho}^{\otimes n}(t)\rangle\rangle] \equiv |\check{\rho}^{(n)}(t)\rangle\rangle = \mathbb{E}_G[\big(K(t)\otimes K^*(t)\big)^{\otimes n}]|\rho^{(n)}(0)\rangle\rangle, \tag{4.19}$$

and we shorthand $|\check{\rho}^{(n)}(t)\rangle\rangle$ for the average un-normalised n-replicated density matrix in the duplicated Hilbert space. In particular, under the Choi–Jamiołkowski isomorphism, the trace operation in Eq.(2.76) becomes a transition amplitude

$$\lim_{n\to 1}\mathrm{Tr}\left[O^{\otimes k}\otimes\mathbb{I}^{\otimes n-k}\mathbb{E}_G[\check{\rho}^{\otimes n}(t)]\right] = \lim_{n\to 1}\langle\langle \mathcal{O}_k|\check{\rho}^{(n)}(t)\rangle\rangle, \tag{4.20}$$

where the boundary bra in the duplicated Hilbert space is

$$|\mathcal{O}_k\rangle\rangle = (O\otimes\mathbb{I})^{\otimes k}\otimes(\mathbb{I}\otimes\mathbb{I})^{\otimes n-k}\,|\mathbb{I}\rangle\rangle. \tag{4.21}$$

$|\mathbb{I}\rangle\rangle$ corresponds to the identity operator in the duplicated Hilbert space.

In the 2-replica analysis of interest, the relevant conditional 2nd Rényi entropy, under operator-to-state mapping, is written as

$$e^{-S_{2,\mathbf{A}}^{(cond)}} = \overline{\overline{\mu}}_{2,\mathbf{A}} = \frac{\langle\langle \mathcal{C}_{2,\mathbf{A}}|\check{\rho}^{(2)}(t)\rangle\rangle}{\langle\langle \mathbb{I}|\check{\rho}^{(2)}(t)\rangle\rangle}. \tag{4.22}$$

Eq.(4.20) shows that the averaged replicated dynamics is directly reflected by the state $|\check{\rho}^{(n)}(t)\rangle\rangle$, and in particular, its steady-state properties. Thus, the identification and characterization of MiPT is equivalent to the study of $|\check{\rho}^{(n)}(t)\rangle\rangle$ in the steady-state dynamics.

4.4 Monitored double-well

As a first application of the partial post-selected SSE introduced in Eq. (4.9), we consider a toy model consisting of a single particle in a double well potential, in which we monitor the occupation of one of the two sites. We model the system as a two-level system spanned by $|0,1\rangle$ and $|1,0\rangle$, where the first (second) index is the occupation of site 1 (2). The unitary dynamics is governed by a tunnelling Hamiltonian $H = -iJ|01\rangle\langle 10| + h.c.$ and we continuously monitor the difference in the occupation number $n_- = |01\rangle\langle 01| - |10\rangle\langle 10|$ [1]. Since the fermionic Hilbert space is 2-dimensional, we can equivalently write the dynamics in terms of a single spin 1/2 system. We identify $|0,1\rangle$ with $|\uparrow\rangle$ and $|1,0\rangle$ with $|\downarrow\rangle$, and the PPS SSE describing the dynamics is

$$d|\psi_t\rangle = -iJ\sigma_y dt + (1-\zeta)dt(\sigma_z - \langle\sigma_z\rangle)|\psi_t\rangle - \frac{\zeta dt}{2}(\sigma_z - \langle\sigma_z\rangle)^2|\psi_t\rangle + dW_t(\sigma_z - \langle\sigma_z\rangle)|\psi_t\rangle, \tag{4.23}$$

where $\overline{dW_t dW_{t'}} = \zeta\delta_{t,t'}dt$. In the absence of partial post-selection, the physics of the model is that of the Zeno effect for continuously monitored systems [8, 237–242]. While for the *average state*, the long-time stationary state is independent of the

[1] This is equivalent to continuously measuring $|01\rangle\langle 01|$ and/or $|10\rangle\langle 10|$ independently since the two operators are not independent as a single particle occupies the system.

measurement strength,it has been shown in different measurement models that the post-selected dynamics and the *probability distribution* of steady states show distinct features in the Zeno and non-Zeno regimes [8]. To capture the effect of partial post-selection on these features beyond the average dynamics, we analyze the distorted 2-nd partial purity in Eq. (4.11) for a single particle where the sub-region $\mathbf{A}$ consists of a single site:

$$\overline{\overline{\mu}}_{2,\mathbf{A}} = \frac{1}{2}\left(1 + \overline{\overline{\langle\sigma_z\rangle^2}}\right). \tag{4.24}$$

We can, therefore, use the formalism developed in Ch. 4.3. As pointed out in Ch. 4.3.2, the non-linear dynamics at hand can be reformulated into a simpler Gaussian averaging problem ($\sigma_z^2 = \mathbb{I}$). Under the Weiner-to-non-Hermitian mapping, the relevant Hamiltonian to our problem is

$$H(t) = J\sigma_y + iM_1(t)\sigma_z, \tag{4.25}$$

and $M(t)$ is a Gaussian stochastic variable whose mean and variance are (cf Eq.(4.15)): $\mathbb{E}_G[M_1(t)] = 1-\zeta, \mathbb{E}_G[M_1(t)M_1(t')] = \zeta\delta(t-t') - (1-\zeta)^2$. The Kraus operator governing the evolution of the density matrix follows directly from Eq.(4.17).

Utilising the operator-to-state mapping, we can compute $\overline{\overline{\mu}}_{2,\mathbf{A}}$ via Eq. (4.22) and Eq.(4.18) with $n = 2$, where the ket in the duplicated Hilbert space has dimension 16. The Gaussian average can be evaluated utilising a cumulant expansion up to the second order (see later part of Appendix B.3), resulting in the following *deterministic* effective Hamiltonian in the 2-replica dynamics:

$$\begin{aligned} &|\check{\rho}^{(2)}(t)\rangle\rangle = e^{-itH_{\text{eff}}}|\check{\rho}^{(2)}(0)\rangle\rangle \\ &H_{\text{eff}} = \sum_{\substack{\sigma=\pm\\ a=1,2}} \left[J\sigma_y^{(\sigma a)} + i(1-\zeta)\sigma_z^{(\sigma a)}\right] + i\zeta\left(\sum_{\substack{\sigma=\pm\\ a=1,2}} \sigma_z^{(\sigma a)}\right)^2. \end{aligned} \tag{4.26}$$

The choice of the initial state is unimportant, and $\lim_{t\to\infty}|\check{\rho}^{(2)}(t)\rangle\rangle$ evolves to a state with the largest imaginary eigenvalue.

In this 2-site model, the Choi representation of the distorted 2-purity, which can either be conditioned on site 1 or 2, is the boundary state

$$|\mathcal{C}_{2,\mathbf{A}}\rangle\rangle \equiv |\uparrow\uparrow\uparrow\uparrow\rangle\rangle + |\downarrow\downarrow\downarrow\downarrow\rangle\rangle. \tag{4.27}$$

Eq.(4.27) is written explicitly in the basis where the first entry is the first replica ket-like Choi branch, the second entry is the first replica bra-like Choi branch, and the remaining two entries are the duplicate elements in the second replica. Note that this representation is only valid in the restricted Hilbert space of a single particle in the double well.

From Eqs. (4.27) and (4.26), one can directly compute the matrix element in Eq. (4.22). Note that, when diagonalizing H_{eff} eigenstates of the eigenvalue with the largest imaginary part, it would yield degenerate eigenvalues. The degeneracy is due to the replica permutation and bra-ket exchange symmetries of H_{eff}. Only the eigenstates that are symmetric under the aforementioned symmetry operation contribute to $\overline{\overline{\mu}}_{2,\mathbf{A}}$. The results are reported in fig. 4.3.

To discuss the results, consider the post-selected case $\zeta = 0$ (cf Eq.(4.10)). In this case, we can alternatively solve Eq.(4.23) by noting that, modulo an overall gauge transformation, we can restrict to the states with real coefficients and parameterise it by $|\psi(t)\rangle = \cos\theta(t)|\uparrow\rangle + \sin\theta(t)|\downarrow\rangle$. This parameterization is equivalent to restricting to the $x-z$ plane of the Bloch sphere, where the North (South) Pole corresponds to $|\uparrow\rangle$ ($|\downarrow\rangle$). Inserting this expression into Eq.(4.23), we obtain an equation for the evolution of $\theta(t)$:

$$\frac{d\theta}{dt} = J - \sin 2\theta. \tag{4.28}$$

For $J < 1$, the equation admits a steady state $\theta = \arcsin(J)/2$, which drifts from the North pole to the equator with increasing J. Noting that, under the above state parameterization, the half-system purity takes the form $\mu_{2,\mathbf{A}} = \cos^4\theta + \sin^4\theta$, which can be directly computed from the steady state of Eq. (4.28). As a result, the entanglement increases (decreasing purity) with increasing J until it reaches a maximum at $J = 1$. We verified that Eq.(4.23) agrees with the results calculated

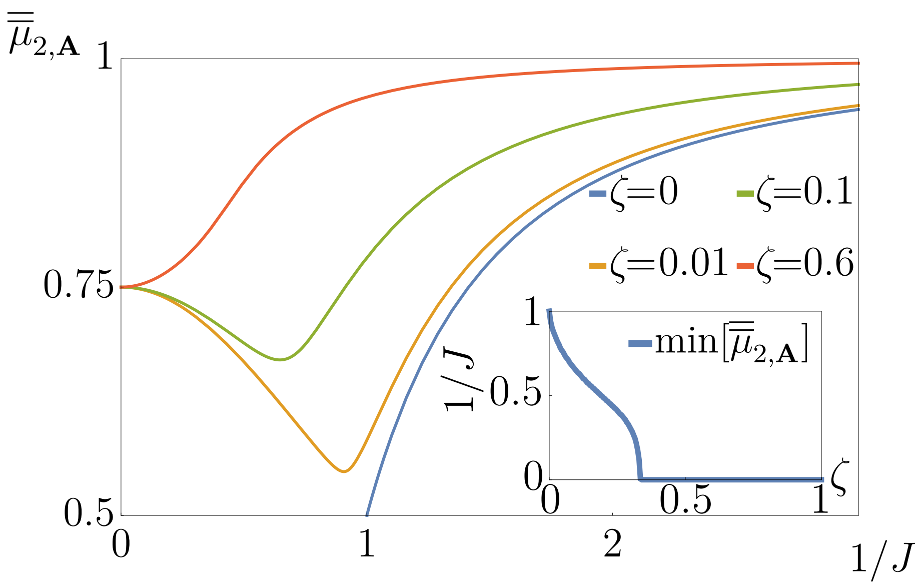

Figure 4.3: The steady-state average distorted 2-nd purity, $\overline{\overline{\mu}}_{2,\mathbf{A}}$ as a function of the inverse tunnelling strength in a double-well model for various degrees of partial post-selection ζ. Lower (higher) $\overline{\overline{\mu}}_{2,\mathbf{A}}$ corresponds to more (less) entanglement. For $\zeta > 0$, $\overline{\overline{\mu}}_{2,\mathbf{A}}$ is non monotonous. Inset: location of the minimum of $\overline{\overline{\mu}}_{2,\mathbf{A}}$ as a function of ζ. The minimum, hence the non-monotonicity, disappears for a weak degree of partial post-selection, i.e. large ζ.

via H_{eff} for $\overline{\overline{\mu}}_{2,\mathbf{A}}$. This is expected as there is one trajectory, and the distortion in Eq.(4.11) becomes exact.

For $J > 1$, Eq. (4.28) does not admit a steady state solution, and $|\psi(t)\rangle$ revolves periodically around the Bloch sphere [1]. For any finite ζ, however, a stated state distribution of states exists for the stochastic dynamics, with a well-defined trajectory-averaged $\overline{\overline{\mu}}_{2,\mathbf{A}}$. As we include more trajectories with $\zeta > 0$, although $\overline{\overline{\mu}}_{2,\mathbf{A}}$ no longer represents the true subsystem purity, it still serves as an entanglement measure, and it displays a minimum (i.e. maximum entanglement) at intermediate J. With increasing ζ, the minimum shifts to larger J (orange and green lines in Fig. 4.3) and its absolute value increases. The increment in the absolute value can be heuristically understood from the parameterization $|\psi(t)\rangle = \cos\theta(t)|\uparrow\rangle + \sin\theta(t)|\downarrow\rangle$, which, when inserted into Eq.(4.23), induces a θ dependence in the Weiner increments with larger weights towards the North Pole. Hence, the inclusion of more trajectories suppresses entanglement in this 2-site model. It should be noted that this behaviour is *not universal* but specific to this model.

4.5 Gaussian fermion model

We now apply the formalism of partial postselection to a specific model where the MiPT has been predicted [80]. The model, sketched in Fig. 4.1, consists of a chain of real Majorana fermions with unitary dynamics governed by random (Gaussian white noise) nearest-neighbour hopping and continuous weak measurement of odd and even bond parity. In the Weiner-to-non-Hermitian mapping introduced in Ch. 4.3.2 (cf. Appendix B.2), the dynamics of the model are governed by a non-Hermitian random

[1] For $\zeta = 0$ and $J > 1$ one can define a distorted 2-purity averaged over a time period. Such an average procedure would be immaterial if a steady-state solution exists.

Hamiltonian given by (see also Eq.(B.12) and (4.25))

$$H(t) = \sum_{j}^{L} \left[J_j(t) + iM_j(t)\right] i\chi_j\chi_{j+1} \tag{4.29}$$

and L (even) is the length of the chain, which is always even. $J_j(t)$ and $M_j(t)$ are Gaussian random variables in space and time with

$$\mathbb{E}_G[J_j(t)] = 0,\ \mathbb{E}_G[J_j(t)J_{j'}(t')] = J^2\delta(t-t')\delta_{j,j'}, \tag{4.30}$$

and the properties of the non-Hermitian Gaussian noise $M_j(t)$ follow from Eq.(4.15) to give

$$\begin{aligned}\mathbb{E}_G[M_j(t)] &= (1-\zeta)(1+(-1)^j\Delta),\\ \mathbb{E}_G[M_j(t)M_{j'}(t')] &= \zeta(1+(-1)^j\Delta)\delta(t-t')\delta_{j,j'}\\ &\quad + (1-\zeta)^2(1+(-1)^j\Delta)(1+(-1)^{j'}\Delta),\end{aligned} \tag{4.31}$$

where the partial post-selection, controlled by $1-\zeta$, determines the mean of the Gaussian measure. We have further specified the measurement/PPS strength dependence on the individual sites so that $-1 \leq \Delta \leq 1$ describes dimerisation in measurement/PPS strengths. This groups the measurement operators into two non-commuting (and competing) sets: the odd and even bond parity measurements, each with measurement strength $\zeta(1-\Delta)$ and $\zeta(1+\Delta)$, respectively.

This model has been investigated in the monitored limit $\zeta = 1$ in Ref. [80]. It was predicted to undergo MiPTs between area and log^2-scaling entanglement entropy as a result of the competition between unitary dynamics and measurement. The model's measurement-only limit, $J = 0$, consisting of two sets of competing measurements, coincides with the one investigated in Ref. [75]. This measurement-only MiPT shows a peculiar dynamical critical exponent in the full monitored limit, which differs from the projective counterpart (of a percolation universality class [108, 109] [1]) and the fully-post-selected limit (of Ising universality class [75]).

[1]Note that the percolation universality is specific of the model under consideration in the monitored projective limit

Following the description in Ch. 4.3.2, we can rewrite the n-replicated unnormalised density matrix (of n-replicated Majorana chains) as a state of $2n$ replicated Majorana chains. The average dynamics of this state follow Eq.(4.19), which, as shown in Ch. 4.4, leads to the study of an effective Hamiltonian.

4.5.1 Two-replica and effective spinful fermion model

Following Ch. 4.3, in the rest of the chapter, we will analyze the MiPT in the two-replica averaged dynamics. The quantity of interest is now the 2-replica *distorted* purity, Eq.(4.22).

From Eq.(4.19) with $n = 2$, the evolution of $|\check{\rho}^{(2)}(t)\rangle\rangle$ becomes

$$
\begin{aligned}
|\check{\rho}^{(2)}(t)\rangle\rangle &= \mathbb{E}_G[\big(K(t) \otimes K^*(t)\big)^{\otimes 2}]|\rho^{(2)}(0)\rangle\rangle \\
&= e^{-\mathcal{H}t}|\rho^{(2)}(0)\rangle\rangle.
\end{aligned} \tag{4.32}
$$

The effective Hamiltonian $\mathcal{H}$, obtained by Gaussian averaging (see Appendix B.3) is given by

$$
\begin{aligned}
\mathcal{H} = &\sum_j \frac{J^2}{2}\left(\sum_{\substack{s=\uparrow,\downarrow\\ a=1,2}} \mathcal{P}^{(sa)}_{i,i+1}\right)^2 - \sum_J \frac{\zeta_j}{2}\left(\sum_{\substack{s=\uparrow,\downarrow\\ a=1,2}} s\mathcal{P}^{(sa)}_{i,i+1}\right)^2 \\
&- \sum_{\substack{s=\uparrow,\downarrow\\ a=1,2}} \sum_j s(1-\zeta_j)\mathcal{P}^{(sa)}_{i,i+1},
\end{aligned} \tag{4.33}
$$

where $\mathcal{P}^{(sa)}_{i,i+1} = i\chi^{(sa)}_i \chi^{(sa)}_{i+1}$ is the parity operator of the pair of Majorana fermions $\chi^{(sa)}_j$ and $\chi^{(sa)}_{j+1}$ in the replicated space, $s = \uparrow (+), \downarrow (-)$ labels the ket and bra space, and $a = 1, 2$ labels the replica index. An **important** subtlety: the Majorana operators appearing in Eq.(4.33) do not follow the naive form

$$
\chi^{(\uparrow 1)}_j \neq \chi_j \otimes \mathbb{I} \otimes \mathbb{I} \otimes \mathbb{I},
$$

and similarly for other replicas, bra and ket indices. Such an expression is ill-defined: Majorana operators from different replicas commute with each other. To safely ensure proper **anti-commutation** relation, a set of newly defined Majorana operators $\{\chi_j^{(sa)'}\}$ are introduced, which differs from the original ones in (4.29) by a Klein factor, i.e.

$$\chi_j^{(sa)'} = \hat{\mathrm{N}}(sa)\chi_j^{(sa)}.$$

We have simply abused the notation by omitting the primes in Eq.(4.33). The details are reported in Appendix B.3, which follows the convention in Ref. [80, 225]. The operator $\hat{\mathrm{N}}(sa)$ is identically an additional 'Pauli string' across replicas (depending on the index sa), counting the total parity associated and maintains bilinear products of the same replica index $\chi_j^{(sa)'}\chi_k^{(sa)'} = \chi_j^{(sa)}\chi_k^{(sa)}$. With the newly-defined Majorana fermions, the state $|\mathcal{C}_{2,A}\rangle\rangle$ in Eq. (4.22) admits the form [225]

$$|\mathcal{C}_{2,\mathbf{A}}\rangle\rangle = \hat{\mathcal{C}}_{2,\mathbf{A}}|\mathbb{I}\rangle\rangle = e^{\frac{\pi}{4}\sum_{j\in\mathbf{A}}\chi_j^{(\downarrow 1)}\chi_j^{(\downarrow 2)}}|\mathbb{I}\rangle\rangle. \tag{4.34}$$

See Appendix B.6 for more detail. Eq.(4.34) indicates that the computation of $\overline{\overline{\mu}}_{2,\mathbf{A}}$ is associated with the parity of $\downarrow$ fermionic degrees of freedom in $\mathbf{A}$; this relation becomes apparent when expressed in terms of complex fermions; see below.

From Eq.(4.32), it can readily be seen that the average replica dynamics follow an imaginary time evolution, and thus $|\check{\rho}^{(2)}(t\to\infty)\rangle\rangle$ is determined by the low energy physics of $\mathcal{H}$, in particular by its ground state and gap properties.

To determine the low energy structure of $\mathcal{H}$ in Eq.(4.33), we note that $\mathcal{H}$ describes an interacting fermionic model with a global $O(2)\times O(2)$ symmetry. The two $O(2)$ symmetries are generated by the operators $\sum_j i\chi_j^{\uparrow 1}\chi_j^{\uparrow 2}$ and $\sum_j i\chi_j^{\downarrow 1}\chi_j^{\downarrow 2}$, and they correspond to rotation among n Majorana operators within the ket ($s=\uparrow$) and bra ($s=\downarrow$) sector. In the absence of PPS, $\zeta = 1$, the global symmetry is larger with $O(2)\times O(2)\rtimes\mathbb{Z}_2$, and is further enlarged for measurement-only or unitary-only cases [80, 225]. The two $O(2)$ symmetries indicate two conserved $U(1)$ charges. These in turn, can be interpreted as the conservation of fermion number of two distinct fermions species given by [225]

$$
\begin{aligned}
c_{j,\uparrow}^{\dagger} &= \frac{\chi_j^{(\uparrow 1)} + i\chi_j^{(\uparrow 2)}}{2}, \\
c_{j,\downarrow}^{\dagger} &= \frac{\chi_j^{(\downarrow 1)} - i\chi_j^{(\downarrow 2)}}{2}
\end{aligned} \tag{4.35}
$$

and the two conserved $U(1)$ charges appear explicitly as $\left[\sum_j c_{j,s}^{\dagger} c_{j,s}, \mathcal{H}\right] = 0$, with $s =\uparrow$ or $\downarrow$.

Expressing the Hamiltonian in eq. (4.33) in terms of these two fermion species, we arrive, after some algebraic manipulation, at the following spinful fermion Hamiltonian (detailed in appendix B.5)

$$
\begin{aligned}
\mathcal{H} =& H_{umk} + H_m + H_0 \\
H_{umk} =& \sum_j -4(\zeta_j + J^2) \sum_{s=\uparrow,\downarrow} (c_{j,s}^{\dagger} c_{j,s} - \frac{1}{2}) \times \\
& (c_{j+1,s}^{\dagger} c_{j+1,s} - \frac{1}{2}) \\
H_m =& \sum_j 4(\zeta_j - J^2)(c_{j,\uparrow}^{\dagger} c_{j+1,\uparrow} + c_{j+1,\uparrow}^{\dagger} c_{j,\uparrow}) \times \\
& (c_{j,\downarrow}^{\dagger} c_{j+1,\downarrow} + c_{j+1,\downarrow}^{\dagger} c_{j,\downarrow}) \\
H_0 =& -\sum_j 2(1 - \zeta_j) \sum_{s=\uparrow,\downarrow} (c_{j,s}^{\dagger} c_{j+1,s} + c_{j+1,s}^{\dagger} c_{j,s}).
\end{aligned} \tag{4.36}
$$

In the language of Eq.(4.35), the operator $\hat{\mathcal{C}}_{2,\mathbf{A}}$ in Eq.(4.34) admits a simple expression as

$$
\hat{\mathcal{C}}_{2,\mathbf{A}} |\mathbb{I}\rangle\rangle = e^{-i\frac{\pi}{2} \sum_{j\in\mathbf{A}} (c_{j,\downarrow}^{\dagger} c_{j,\downarrow} - \frac{1}{2})} |\mathbb{I}\rangle\rangle. \tag{4.37}
$$

Once again, the equivalent sign indicates that the operator representation is to be understood only when acting on the state $|\mathbb{I}\rangle\rangle$. Hereafter, we also assume the region $\mathbf{A}$ to be continuous for simplicity.

To address the ground-state properties and phases of $\mathcal{H}$, we note that $\mathcal{H}$ is number conserving in both spin-up and spin-down fermion species, and the long wavelength (low energy) physics of (4.36) depends on the particle number, or, more precisely, on the filling factor. The latter is determined by the initial state $|\mathbb{I}\rangle\rangle$, see (4.22), which is in the half-filling sector, as shown in Appendix B.5. We therefore analyse the half-filling ground state of $\mathcal{H}$.

Before proceeding, and for completeness, it is worthwhile to discuss the monitored limit $\zeta = 1$. $\mathcal{H}$ has an enlarged symmetry, since the total local parity across all replicas, $\mathcal{R}_j = \prod_{a=1}^{2} i\chi_j^{(\uparrow a)}\chi_j^{(\downarrow a)}$ is conserved. The Hamiltonian is invariant under an extra global $\mathbb{Z}_2$ symmetry in the Choi space: $\chi_j^{(\uparrow a)} \longleftrightarrow \chi_j^{(\downarrow a)}$ (this generalises to n replica as well [80]). In this case, the Hamiltonian can be expressed entirely as a function of local $SO(4)$ generators written in Majorana operators,

$$S_j^{\alpha,\beta} = \frac{i}{2}\left[\chi_j^{\alpha}, \chi_j^{\beta}\right], \tag{4.38}$$

and the states $|\mathbb{I}\rangle\rangle$ and $|\mathcal{C}_{2,\mathbf{A}}\rangle\rangle$ isolate the spin representation among different irreducible representations [80]. In Appendix B.4, we demonstrate an alternative way to obtain the exact solution where a mapping to an integrable model can be constructed via 2 different spin-1/2 operators analogous to the η, Σ spin from the Hubbard model [243]. In the monitored case, we show that Eq.(4.33) is equivalent to

$$\mathcal{H} \propto \sum_{\substack{\Theta=\Sigma,\eta \\ j=1}}^{L} \frac{1}{2}(1+\delta(-1)^j)\left[\Theta_j^+\Theta_{j+1}^- + \Theta_j^-\Theta_{j+1}^+\right] + J_{z,j}\Theta_j^z\Theta_{j+1}^z, \tag{4.39}$$

where $\delta = \frac{\Delta\gamma}{16(J^2+\gamma)}$, $J_{z,j} = \frac{J^2-\gamma_j}{J^2+\gamma_j}$. Eq.(4.39) corresponds to 2 decoupled XXZ spin-1/2 chains and its exact solution can be computed via standard means [182].

4.6 Strong PPS and bosonisation

An analytical solution of the ground state of Eq. (4.36) is not available. However, in the strong partial-post-selected limit, $1 \gg \zeta/(1-\zeta), J^2/(1-\zeta)$, and half-filling condition of interest here, the spectrum of excitation is approximately linear, and the problem can be treated within the standard abelian bosonization procedure [182].

This amounts to linearising the fermion operator around the Fermi surface

$$c_{j,s} \propto e^{-ik_F x_j}\tilde{\psi}_{\mathbf{R},s}(x_j) + e^{ik_F x_j}\tilde{\psi}_{\mathbf{L},s}(x_j), \tag{4.40}$$

and introducing the bosonic fields θ_s and ϕ_s via

$$\tilde{\psi}_{\mathbf{L},s}(x) \quad \propto e^{i(\phi_s(x)+\theta_s(x))},\ \tilde{\psi}_{\mathbf{R},s}(x) \quad \propto e^{-i(\phi_s(x)-\theta_s(x))}, \tag{4.41}$$

where $\tilde{\psi}_{\mathbf{L/R},s}(x)$ is the slowly varying part of left/right movers of the fermion [182], see Ch.2.2.1. The low energy properties of $\mathcal{H}$ are described by the linearised bosonic Hamiltonian.

The full bosonization procedure for $\mathcal{H}$ is reported in appendix B.5 which leads to the low energy effective Hamiltonian

$$\begin{aligned}\mathcal{H}_{\text{bos}} \approx \sum_{\epsilon=\sigma,\rho}\left[\frac{1}{2\pi}\int_x u_\epsilon K_\epsilon(\nabla\theta_\epsilon)^2 + \frac{u_\epsilon}{K_\epsilon}(\nabla\phi_\epsilon)^2\right] + \sum_{\epsilon=\sigma,\rho}\int_x \frac{2g_\epsilon}{(2\pi\alpha)^2}\cos\left(\sqrt{8}\phi_\epsilon\right)\\ + \frac{2g_2}{(2\pi\alpha)^2}\int_x \sin\left(\sqrt{2}\phi_\rho\right)\cos\left(\sqrt{2}\phi_\sigma\right),\end{aligned} \tag{4.42}$$

where $\phi_\rho = \frac{\phi_\uparrow+\phi_\downarrow}{\sqrt{2}}$ and $\phi_\sigma = \frac{\phi_\uparrow-\phi_\downarrow}{\sqrt{2}}$ are the charge and spin sectors fields. The coupling constants and Luttinger parameters are given by

$$\begin{aligned}&u_\rho K_\rho = u_\sigma K_\sigma \equiv v_F = 4(1-\zeta),\\ &\frac{u_\rho}{K_\rho} = v_F - \frac{32aJ^2}{\pi},\\ &\frac{u_\sigma}{K_\sigma} = v_F - \frac{32a\zeta}{\pi},\\ &g_\rho = -g_\sigma = -16(\zeta - J^2),\\ &g_2 = 16a\Delta((1-\zeta)\pi - \zeta),\end{aligned} \tag{4.43}$$

where Δ is the dimerization, v_F is the effective Fermi velocity in the non-interacting case (e.g. from H_0 in Eq. (4.36)), and a, the lattice constant, can be set to unity, $a = 1$. We keep only the most relevant operator in deriving Eq. (4.42). In particular, we discard highly irrelevant (in the RG sense) terms $\propto \cos(4\phi_{\uparrow,\downarrow})$ originating from the *umklapp* contributions in the Hamiltonian. We retain only the slow oscillating term with 0-k_F and 4-k_F components around the filling factor $k_F = \pi/2a$.

The expected validity of the bosonization treatment in the strong post-selected limit $1 \gg J^2/(1-\zeta), \zeta/(1-\zeta)$ is confirmed by Eq. (4.43). Indeed the charge and spin Luttinger parameters K_ρ, K_σ diverges at $J^2/(1-\zeta) \equiv \mathcal{J}^{*2} = \pi/8$ and $\zeta/(1-\zeta) \equiv \zeta^*/(1-\zeta^*) = \pi/8$ respectively. This also constrains other parameters in Eq.(4.43) so that the sign of g_2 is the same as Δ.

Although the divergence point ζ^* is beyond the regime of applicability of perturbation theory $\zeta \ll 1$, we expect that the physical picture it implies remains qualitatively correct. Indeed, a similar scenario arises when analysing the XXZ-spin 1/2 chain using bosonization[182]. For the XXZ chain, while the bosonization analysis fails to capture the value of the phase boundary (calculated using Bethe-ansatz), it does allow to characterize the properties of the different phases [1]. On this ground, the divergence of K_ρ or K_σ hints at the onset of a phase boundary, though we expect that the location of the phase boundaries to be generically different from ζ^* and $\mathcal{J}^{*2}$. The indication of a phase boundary from bosonisation is confirmed by numerical finite-size scaling results for measurement-only MiPTs reported in Ch. 4.7.

Within the bosonized theory in (4.42), the ground-state phases of $\mathcal{H}_{\text{bos}}$ are obtained by the RG flow of the parameters J^2 and ζ, which can be computed within standard methods [182, 244, 245], noting that Eq. (4.42) is the Hamiltonian of a Sine-Gordon model [182]. Here we follow the procedures in [182, 245] performing real space coarse-graining of the correlator of a pair of vertex operators i.e.$\langle \exp\left[-ia\phi(r_1)\right] \exp\left[-ia\phi(r_2)\right] \rangle_{\mathcal{H}}$. The details of the calculation are reported in Appendix B.7. In the analysis below, we will separate the no-dimerization case

[1] For a XXZ-spin 1/2 chain in the absence of magnetic field, bosonisation (without Bethe-ansatz) cannot capture the precise value of the phase boundary. Still, it distinguishes the XY phase from the anti-ferromagnetic/ferromagnetic Ising phase [182]. Here, bosonisation indicates a divergence of the Luttinger parameter at $J_z/J_{xy} = -\pi/4 > -1$, leading to the conclusion of a phase boundary separating the free Luttinger phase from a non-linear dispersing phase (in fact $\omega \sim k^2$). While the location of the phase boundary predicted from bosonisation differs from the known phase boundary at $J_z/J_{xy} = -1$, the physics of the phase boundary from perturbation theory is correct beyond its perturbative applicability.

$\Delta = 0$, from the general case. In the former, $g_2 = 0$ identically (cf. Eq.(4.43)), so that it cannot be simply obtained as a limit of the general case for $\Delta \to 0$. For no-dimerization, $\Delta = 0$, g_ρ and g_σ flows separately, and the perturbative RG flow up to second order in g_ϵ and K_ϵ gives

$$\begin{aligned}\partial_l K_\epsilon &= -\frac{y_\epsilon^2 K_\epsilon^2}{2}\\ \partial_l y_\epsilon &= (2-2K_\epsilon)y_\epsilon,\\ y_\epsilon &= \frac{g_\epsilon}{\pi u_\epsilon}\ ,\ \epsilon = \sigma, \rho\end{aligned} \tag{4.44}$$

where l is the logarithm of the RG time. In the most crude analysis in first order of g_ϵ, the coupling for $\cos\sqrt{8}\phi_\epsilon$ is irrelevant for the physically relevant scenario $K_\epsilon > 1$. However, accounting for the flow for K_ϵ can result in one of the modes being gapped but not both simultaneously, as we numerically evaluate the RG flows.

For $\Delta > 0$, the g_2 term is more relevant than the g_ϵ since the cosine of the former is with higher frequency, so we can safely discard the $\cos\left(\sqrt{8}\phi\right)$ terms in $\mathcal{H}_{\text{bos}}$. The RG flow equations, in this case, are derived in Appendix B.7 following a standard procedure, which leads to

$$\begin{aligned}\partial_l K_\rho &= -\frac{g_2^2 K_\rho^2}{16\pi^2 u_\rho^2}\frac{I(\mu_\rho, K_\sigma, \sqrt{2})}{2\pi},\\ \partial_l K_\sigma &= -\frac{g_2^2 K_\sigma^2}{16\pi^2 u_\sigma^2}\frac{I(\mu_\sigma, K_\rho, \sqrt{2})}{2\pi},\\ \partial_l g_2 &= \left(2 - \frac{1}{2}(K_\rho + K_\sigma)\right) g_2,\end{aligned} \tag{4.45}$$

where

$$\begin{aligned}\left(\frac{u_\sigma}{u_\rho}\right)^2 &= 1 + \mu_\rho,\\ \left(\frac{u_\rho}{u_\sigma}\right)^2 &= 1 + \mu_\sigma\\ I(\mu, K, \beta) &= \int_{-\pi}^{\pi} d\theta \left(\frac{1}{1+\mu\cos\theta}\right)^{\frac{\beta^2 K}{4}}.\end{aligned} \tag{4.46}$$

The RG flow in Eqs. (4.46,4.44) dictate the low energy physics of the model and are used in the next section to characterize the properties of the MiPT in the partial-post-selected model.

4.6.1 Conditional 2nd Rényi entropy

We are now able to determine the ground-state properties of the effective Hamiltonian in Eq.(4.42) from the RG flows, Eq.(4.45) and (4.44). As the ground state properties determine the entanglement scaling, we expect the entanglement to scale logarithmically in the critical phase and as an area law in the gapped phase. Below we confirm these expectations by calculating $S_{2,\mathbf{A}}^{(cond)}$. The calculation involves the action of $\hat{\mathcal{C}}_{2,\mathbf{A}}$ on the state $|\mathbb{I}\rangle\rangle$ (cf Eq.(4.34) and (4.37)), which can be mapped to a 2-point vertex correlation.

Under bosonisation, the operator $\hat{\mathcal{C}}_{2,\mathbf{A}}$ becomes a pair of vertex operators (excluding fast oscillating terms):

$$\hat{\mathcal{C}}_{2,\mathbf{A}} \equiv e^{i\frac{1}{2}(\phi_\downarrow(x_r)-\phi_\downarrow(x_l))}, \tag{4.47}$$

and the exponential of the conditional 2nd Renyi entropy (cf Eq.(4.11)) appears as

$$\begin{aligned} e^{-S_{2,\mathbf{A}}^{(cond)}} &= \langle\langle \mathcal{C}_{2,\mathbf{A}}|\rho^{(2)}(t\to\infty)\rangle\rangle \\ &= \lim_{t\to\infty}\langle\langle \mathbb{I}|e^{i\frac{1}{2}(\phi_\downarrow(x_r)-\phi_\downarrow(x_l))}e^{-t\mathcal{H}}|\mathbb{I}\rangle\rangle \\ &\sim \langle\langle \mathrm{GS}|e^{i\frac{1}{2}(\phi_\downarrow(x_r)-\phi_\downarrow(x_l))}|\mathrm{GS}\rangle\rangle \\ &= \langle\langle \mathrm{GS}|e^{i\frac{1}{2\sqrt{2}}[\phi_\rho(x_r)-\phi_\rho(x_l)]}e^{-i\frac{1}{2\sqrt{2}}[\phi_\sigma(x_r)-\phi_\sigma(x_l)]}|\mathrm{GS}\rangle\rangle. \end{aligned} \tag{4.48}$$

In the fourth line, we replace the boundary state $\langle\langle\mathbb{I}|$ by the ground state of $\mathcal{H}$, which is equivalent up to a length independent constant, see Appendix B.6.

From Eq.(4.48), we can readily extract the scaling of $S_{2,\mathbf{A}}^{(cond)}$. If both sectors are gapless, we have [182]

$$e^{-S_{2,\mathbf{A}}^{(cond)}} = \left(\frac{\alpha}{x_r - x_l}\right)^{\frac{K_\sigma+K_\rho}{16}}, \tag{4.49}$$

showing the logarithmic scaling of $S_{2,\mathbf{A}}^{(cond)}$. If both sectors are gapped (cosine potential is relevant), the field ϕ_σ and ϕ_ρ are locked in one of the minima of the potential. Hence, the configuration of ϕ fields is fixed, and the vertex correlation becomes a constant, giving an area law for $S_{2,\mathbf{A}}^{(cond)}$.

If only one of the sectors is gapped and the Hamiltonian remains separable, $S^{(cond)}_{2,\mathbf{A}}$ remains logarithmically scaling: while the gapped sector gives a constant in the vertex correlation (4.48), the gapless sector contributes a power law decay leading to logarithmic scaling of $S^{(cond)}_{2,\mathbf{A}}$.

4.7 Measurement-induced phases and their transitions

We are now in the position to analyse the Hamiltonians Eq.(4.39) and (4.42), along with the RG-flow equations Eq.(4.44, 4.45) to characterize the steady-state phases of partially post-selected dynamics of the Gaussian model in Eq.(4.29). We study both the measurement-only dynamics ($J = 0$) and unitary-measurement-induced phases ($J^2 > 0$), and we discuss them separately hereafter.

4.7.1 Measurement-only dynamics

In the absence of unitary dynamics, $J = 0$, the system is evolving entirely according to two competing sets of measurements: the set of odd and the set of even bond measurements. Notably, the $J = 0$ limit of the model (4.29) coincides with the measurement-only case studied in Refs. [75, 80] where monitored and post-selected limits follow very different behaviours. In particular, finite-size scaling reveals that the monitored system belongs to a different universality class from the fully post-selected model [75].

Post-selected limit— The fully post-selected dynamics are obtained by setting $\zeta = 0$ in Eq.(4.33), and the physics is entirely dictated by Δ. The effective Hamiltonian now reads:

$$\mathcal{H} = -\sum_{\substack{s=\uparrow,\downarrow \\ a=1,2}} \sum_j s(1 + \Delta(-1)^j) i\chi_j^{(sa)} \chi_{j+1}^{(sa)}, \tag{4.50}$$

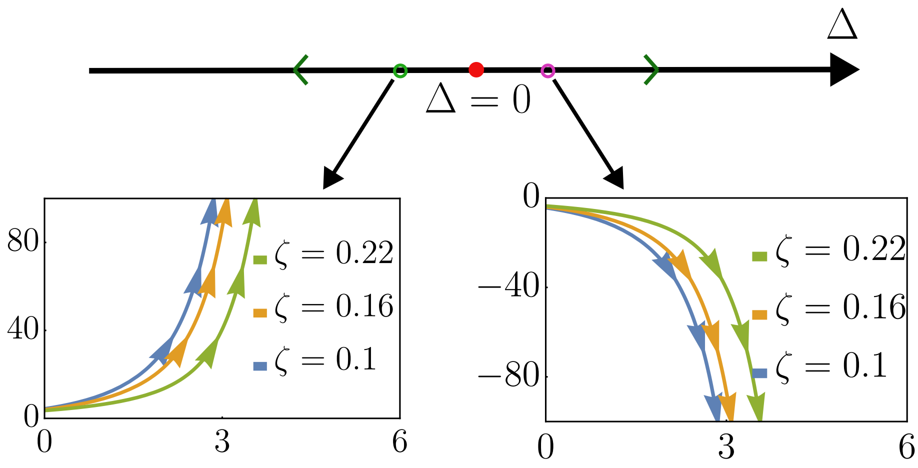

Figure 4.4: Schematic phase diagram for the measurement-only dynamics determined by the dimerization Δ. The arrows indicate the RG flow to the two distinct fixed points $\Delta = \pm 1$ with a critical point (red dot) at $\Delta = 0$. The plots show the RG flow of g_2 from Eq.(4.45) evaluated at different points (green and purple circles), indicating that the interaction is relevant in both cases, and it leads to area law of phases.

Using the usual Jordan-Wigner transformation, the imaginary time evolution is, therefore, equivalent to 2 decoupled $1D$ transverse field Ising models in either the bra ($s = \downarrow$) or ket ($s = \uparrow$) space.

The critical properties of the post-selected dynamics fall in the Ising universality class, and the critical exponent ν that determines the divergence of the correlation length $\xi \sim |\Delta|^{-\nu}$, is $\nu = 1$. Away from criticality for $\Delta > 0$, the even parities are measured more strongly, and this phase is characterised by a pair of entangled Majorana fermions residing at the edges of a finite-length chain. This phase is associated with a $\log_2$ topological entanglement entropy per replicated chain in the area-law phase.

On the other side $\Delta < 0$, the odd parities measurements are stronger, and it features all Majorana being measured in pairs. This, therefore, corresponds to a topologically trivial phase with vanishing topological entanglement entropy.

Strong post-selection — When $\zeta \neq 0$, the system no longer follows the deterministic dynamics from Eq.(4.50), but stochastic fluctuations inherent to the measurement process enter the system dynamics. With the partial post-selection introduced in Eq. (4.9), the parameter ζ controls the amount of fluctuations (i.e. the fraction of quantum trajectories) allowed in the system's dynamics. We can analyse the strong post-selected limit $\zeta \ll 1$ with the bosonized Hamiltonian (4.42). As argued in Ch. 4.6, the steady state of the system is governed by different equations for $\Delta = 0$ and $\Delta \neq 0$, so we address them separately.

For $|\Delta| > 0$, using the flow in Eq.(4.45), we observe that the cos operator corresponding to the g_2 coupling is in general relevant for $K_\rho + K_\sigma < 4$, which we confirm by evaluating Eq.(4.45) numerically. The results are shown in Fig. 4.4 for different values of ζ. The massive/gapped phase flow indicates an unbounded growth in the coupling g_2, which does not change sign along the RG flow. When reinterpreting the RG flowing parameters in terms of the original parameters of the model ξ, ζ and Δ via (4.43), this limit approaches the post-selected Hamiltonian (4.50) ($\zeta \to 0$). Indeed, Fig. 4.5 shows that the RG flow for $\zeta > 0$ channels into the post-selected RG flow $\zeta = 0$, for both Luttinger parameter K_ρ and K_σ, indicating that the strong-PPS low-energy phase flows to the same as the post-selected phase. This means that that the strong-PPS gapped phase at finite ζ with $\Delta > 0$ ($\Delta < 0$) is continuously connected to the gapped phase $\zeta = 0, \Delta > 0$ ($\zeta = 0, \Delta < 0$) of the post-selected model. The points $|\Delta| = 1$ are the two only stable fixed points in the measurement-only dynamics, as reported in the phase diagram in Fig. 4.4. We, therefore, expect that the universal properties of the strong-partial post-selected regime are inherited from Eq. (4.50), i.e. those of two uncorrelated copies of an Ising model.

This is the first main prediction of our theory: The MiPT remains in the same Ising-like university class for finite ζ as long as the bosonized approximation for the theory remains valid. Physically, this predicts the stability of the post-selected MiPT universal feature against (weak) fluctuations induced by the measurement's stochasticity.

For $\Delta = 0$, $J = 0$, Eq.(4.45), together with the definition of Luttinger parameters

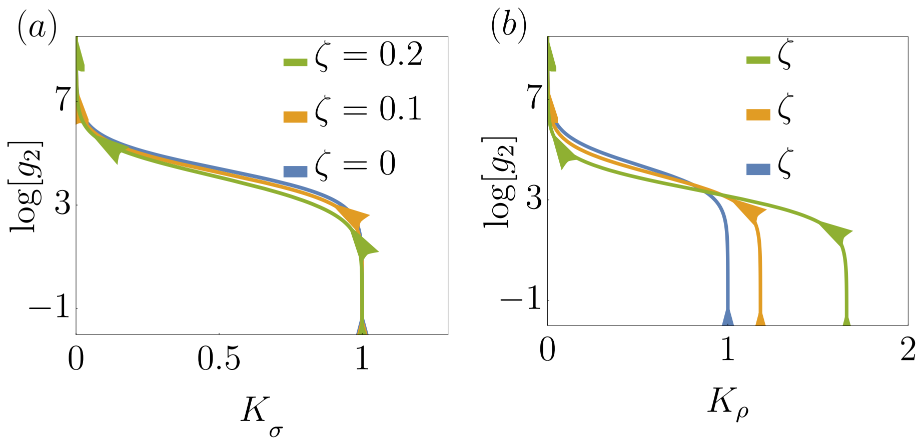

Figure 4.5: RG flow of the dimerised measurement-only dynamics (4.45) in the $g_2 - K_\sigma$ plane (a) and $g_2 - K_\rho$ plane (b) for $\Delta = 0.01 > 0$ and different degree of partial post-selection, ζ. Finite partial-post-selection flows (green and orange curves) channel into the no-post-selection one (blue curve). For $\Delta < 0$, the flow is reflected along the $g_2 = 0$ axis.

in Eq.(4.43), implies that the $g_2 = 0$, and that the σ- and ρ-modes decouple. The RG-flow is then standard [182], with the ρ-mode flowing to a massive phase ($g_\rho \to \infty$), while the σ-mode, following an expansion around $K_\sigma \to 1^+$, flows to $g_\sigma \to 0$, $K_\sigma > 1$. Correlations in the overall theory are thus dominated by the σ-mode, which is a Gaussian-free theory displaying free Luttinger liquid criticality. The scaling of $S^{(cond)}_{2,\mathbf{A}}$ follows from Eq.(4.49) which implies a logarithmic scaling with a pre-factor proportional to K_σ. We note that logarithmic scaling is observed numerically in entanglement entropy, which indicates that the robustness of Ising universality, as predicted by the analytics, applies to other entanglement measures.

From strong post-selection to monitored dynamics— In the post-selected limit, ($\zeta = 0$) the transition for the system's entanglement entropy follows an Ising universality similar to the conditional entropy. Our bosonized theory for the latter predicts that the Ising-like transition persists when moving away from the post-selected limit. Meanwhile, studies of the system entanglement entropy for the fully monitored case ($\zeta = 1$) show a measurement-only transition of a different nature [80] with a critical exponent of $\nu = 5/3$ [75]. Although our bosonised theory cannot access the full transition between the post-selected ($\zeta = 0$) and the monitored ($\zeta = 1$) dynamics due to the divergence of the Luttinger parameter at ζ^*(cf. Ch. 4.6), this divergence indicates a phase boundary separating the Ising-universality from a different universality [182] (as discussed in Ch. 4.6).

To further characterize the transition between the post-selected and fully monitored universality in other entanglement measures, we analyze the critical exponent $\nu : \xi \sim |\Delta|^{-\nu}$ of this measurement-only MiPT via numerical simulation of the free fermion model for generic ζ. To efficiently extract the critical exponent numerically, we employ techniques from free fermion simulation [72, 75] and perform finite size scaling analysis of the topological entanglement entropy S_{TEE} [75, 108, 114, 246, 247], as detailed in Appendix B.8. The results are presented in Fig. 4.6, showing that $\nu \approx 1$ for strong PPS before deviating abruptly in a narrow range around $\zeta \approx \zeta^*$ and approaching $\nu = 5/3$ when $\zeta \approx 1$. Surprisingly, numerical data shows that close to the transition, $\nu \approx 2.3 > 5/3$, before dropping back to $\nu = 5/3$ for larger ζ. The results suggest a consistent phase separation scenario for the entanglement entropy MiPTs. Indeed, the stability of the Ising value of the critical exponent $\nu = 1$ is similar to the region of validity of the bosonised theory, suggesting a common mechanism underpins both phenomena.

Monitored limit, $\zeta = 1$ — The monitored limit is given by Eq. (4.39), which, for the measurement-only case $J = 0$, reduces to an XXZ-Hamiltonian with a dimerisation in the hopping term, also known as the spin-Peierls model [182]. This model predicts a BKT transition at $\Delta = 0$ [182]. This differs from the Ising bosonized theory for the strong PPS. This difference is also consistent with the model's symmetry change in the two limits, as discussed in Sec 4.5.1.

Note that the BKT transition (hence the scaling of the distorted partial purity or entanglement entropy) predicted by Eq. (4.39) does not capture the correct universality class of the fully monitored dynamics. Indeed, in the limit $\zeta = 1$, it has been shown that the 2-replica model differs from the $n \to 1$ limit for which

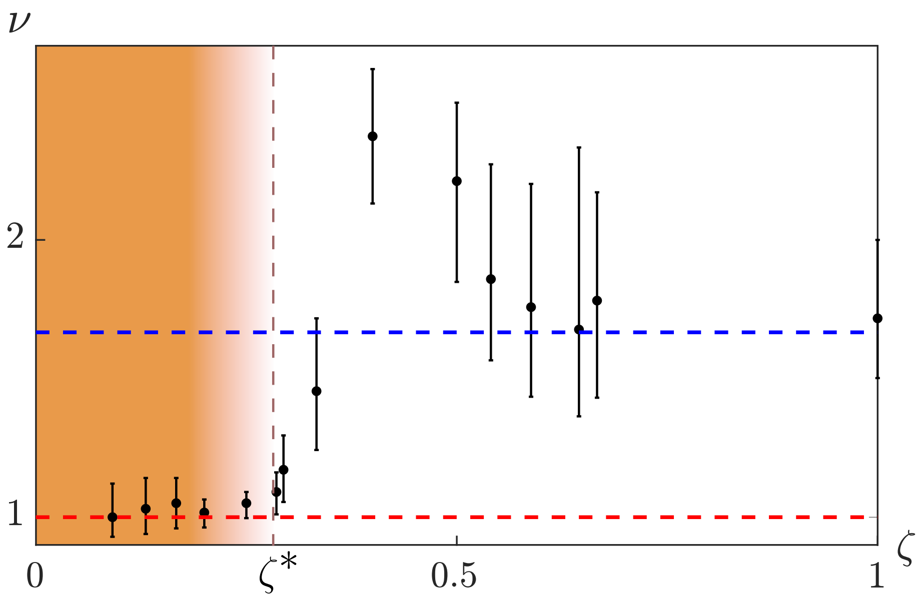

Figure 4.6: The critical exponent ν of the measurement only phase transition as a function of the degrees of PPS, ζ. The pink area marks the regime of validity of the bosonized theory. The dashed horizontal lines mark the known critical exponent for the post-selected model $\nu = 1$ (red) and monitored dynamics $\nu = 5/3$ (blue). The fully post-selected Ising critical exponent $\nu = 1$ is unchanged for a finite range of ζ above $\zeta = 0$. The abrupt deviation from $\nu = 1$ occurs in the proximity of the breakdown of the bosonized theory at $\zeta \approx \zeta^* = 0.28$ (end of the shaded region). The fully monitored critical exponent $\nu = 5/3$ is recovered for $\zeta \to 1$. The large error bars for increasing ζ are due to the large fluctuation from the increasing trajectory-to-trajectory fluctuations in this regime. The system sizes employed in the finite size scaling analysis are $L = \{32, 64, 96, 128, 160, 192\}$.

the phase transition in the measurement-only limit is not known [80]. However, since for strong PPS, the replicas completely decouple, the post-selected limit is independent of the replica number. We expect that the stability of the post-selected phase and its breakdown should be captured in the 2-replica case considered here.

4.7.2 Partial post-selected monitoring with unitary dynamics

No-dimerization case, $\Delta = 0$— To analyze the effect of unitary dynamics on the system, we start by considering the case where dimerization is absent, $\Delta = 0, J^2 > 0, \zeta > 0$. In this case, the RG flow in Eq. (4.45) keeps $g_2 = 0$, the ρ-mode and σ-mode decouple as indicated by H_{bos} and Eq. (4.44), and the Luttinger parameters K_ρ and K_ρ in Eq.(4.43) are both initially larger than unity. At the leading order, the RG flow signals that $\mathcal{H}_{\rm bos}$ is gapless for $K_\epsilon > 1$. Evaluating Eq.(4.44) numerically reveals that one of the sectors is always massless. Given the decoupling between the two sectors, $\lim_{t\to\infty} |\check{\rho}^{(2)}(t)\rangle\rangle$ will evolve to a tensor product of two ground states $|\mathrm{GS}_{\mathcal{H}_\rho}\rangle \otimes |\mathrm{GS}_{\mathcal{H}_\sigma}\rangle$. Thus, correlations w.r.t. $\mathcal{H}_{\rm bos}$ are dominated by the gapless sector ground state, which displays power-law decaying length-dependent, signalling a critical scaling of entanglement. More precisely, Eq.(4.48) directly signals a power decaying dependence for the exponential of $S^{(cond)}_{2,\mathbf{A}}$, contributed by the gapless sector vertex-pair correlator. This translates to a logarithmically scaling $S^{(cond)}_{2,\mathbf{A}}$. Therefore, we expect that the true entanglement entropy will be dominated by the critical sector and will show a critical entanglement scaling.

This result differs from the predicted $(\log L)^2$ in Ref. [80] for the fully monitored case. The absence of $(\log L)^2$ scaling in strong PPS where bosonisation remains valid could be traced back to the breaking of local parity $\mathcal{R}_j = \prod_a i\chi_j^{(+a)}\chi_j^{(-a)}$, $[\mathcal{R}_j, \mathcal{H}] \neq 0$, which prohibits one to express $\mathcal{H}$ solely as local SO(2N) generators. Consequently, $\mathcal{H}$ is no longer described by the non-linear sigma model in [80] that gives the $(\log L)^2$ scaling.

To confirm a change from $\log L$ to $(\log L)^2$ with increasing J^2 and increasing ζ, we numerically analyze the scaling of the entanglement entropy along the no-dimerization line. The results are shown in Fig. 4.7, and here we denote $S_{0,L}$ as the half-cut entanglement entropy of a system size L. For weak unitary $J^2 = 0.091$ and strong PPS $\zeta = 0.091$ marked in full green circle, the trajectory averaged half-cut entanglement entropy $\overline{S}_{0,L}$ follows a $\log_2 L$ dependence. This changes into a

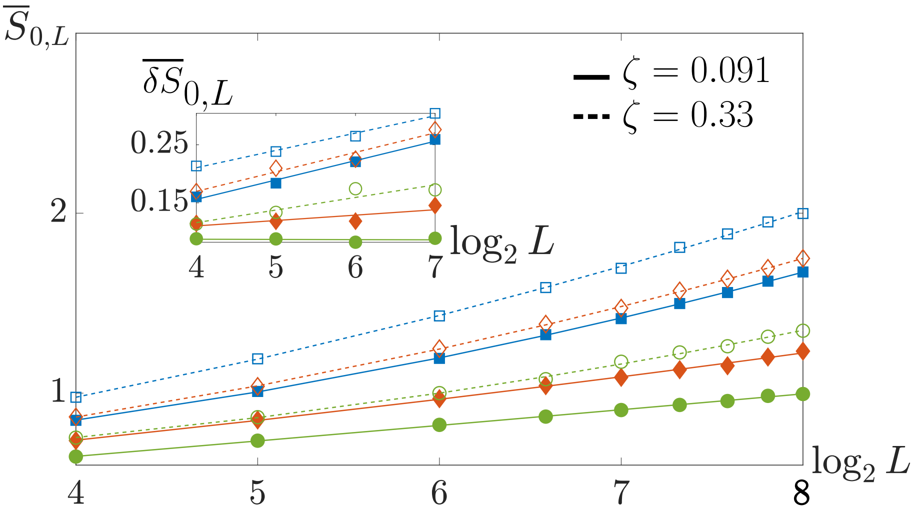

Figure 4.7: Trajectory averaged entanglement entropy from numerical simulation at zero dimerization $\Delta = 0$. The plot shows the scaling of average half-cut entanglement entropy $\overline{S}_{0,L}$ as a function of $\log_2 L$ (where L is the system size) for two degree of partial post-selection, $\zeta = 0.091$ (full markers/solid lines) and $\zeta = 0.33$ (hollow markers/dashed lines). Different colours correspond to different values of J^2 (divided by an implicit factor $\gamma + \gamma b = 1$), which are 0.091(green), 0.27(orange) and 0.45(blue) for full markers/solid lines, and 0.067(green), 0.2(orange) and 0.33(blue) for hollow markers/dashed lines. Lines are best fit with a second-order polynomial. Inset: average half-cut entanglement entropy difference $\overline{\delta S}_{0,L} \equiv \overline{S}_{0,2L} - \overline{S}_{0,L}$ for different values of J^2 and ζ as in the main plot. Here $\overline{S}_{0,L}$ follows a $\log_2 L$ dependence for small J^2 and ζ (green full circles), changing into a $(\log_2 L)^2$ dependence upon increasing J^2 (orange/blue markers) or upon increasing ζ (hollow markers). Error bars are within the marker sizes.

$(\log_2 L)^2$ dependence upon increasing J^2 (orange full diamond/blue full square) or upon increasing ζ (dashed line, hollow green circle). For $\zeta = 0.33$ (dashed lines), which is beyond the validity of our bosonized theory, all lines display a quadratic dependence. To further distinguish the log$L$-scaling from the $(\log L)^2$ one, we use as an indicator the difference in half-cut entanglement entropy $\delta S_{0,L} \equiv S_{0,2L} - S_{0,L}$ [80] — cf. Fig. 4.7 Inset. The two cases are then distinguished by a $\delta\overline{S}_{0,L} \sim$ log$L$ vs $\delta\overline{S}_{0,L} \sim$ const. dependence respectively (see Appendix B.8). This analysis demonstrates that increasing the degree of either unitary (J^2) or non-unitary (ζ) stochasticity leads to a qualitative change from a log-scaling to a (log)^2-scaling of the half-cut entanglement entropy.

The change in the scaling behaviour happens approximately at the point where bosonization is expected to break down ζ^* and $\mathcal{J}^{*2}$. This is consistent with the picture in the previous section, where the breakdown of bosonization at ζ^* signals a transition away from the university of the post-selected model towards the universality of the monitored model, which is captured by the non-linear sigma model in Ref. [80].

General monitored-unitary dynamics, $\Delta \neq 0$ — For generic strong PPS case with all $|\Delta| > 0$, $J^2 > 0$, and $\zeta > 0$, g_2 is the main parameter which controls the entanglement scaling. From a numerical solution of the RG flow Eq.(4.44), we see that for small initial values, g_2 either flows to irrelevant at large J^2 or grows indefinitely for sufficiently small values of J^2, (cf. Fig. 4.8). In the latter case, since the g_2 term is always more relevant than the g_ρ and g_ϕ terms, the physics is entirely governed by the g_2 term which opens a gap in the system leading to an area-law phase (cf Eq.(4.48)). When g_2 flows to zero at large J^2, the g_ϵ coupling term of $\cos\left(\sqrt{8}\phi\right)$ gaps at most one of the two sectors leaving at least one sector being gapless. This phase remains critical, as in the case of $\Delta = 0$, and it is continuously connected to the $\Delta = 0$ line. This suggests that there is a finite region of critical scaling separating the $\log^2 L$ phase from the area-law, which is different to the monitored

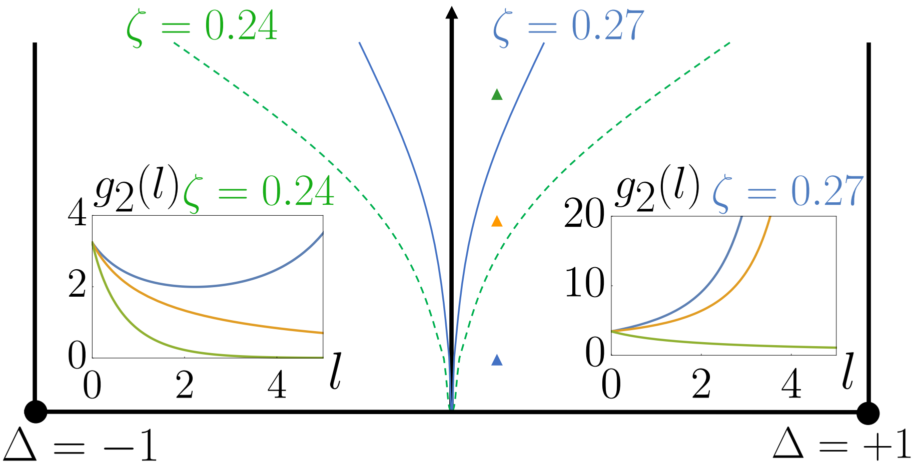

Figure 4.8: Schematic phase diagram obtained from the 2-replica approximation RG flow Eq.(4.45). A critical unitary strength J_c separating the gapped area-law scaling phase ($J^2 < J_c^2$) from the critical logarithmic phase ($J^2 > J_c^2$) as reported for $\zeta = 0.24$ (green dotted line) and $\zeta = 0.27$ (blue line). The left and right insets show the flow of g_2 under RG Eq.(4.45) for $\zeta = 0.24$ and $\zeta = 0.27$ respectively evaluated at $J^2 = 0.019$ (blue),$J^2 = 0.20$ (orange), and $J^2 = 0.38$ (green), with $\Delta = 0.1$ in all cases. The irrelevance of g_2 indicates a critical logarithmic scaling entanglement.

limit where the two phases are separated by a singular critical line [80] (see fig. 4.1 for a schematic sketch). We note that this phase transition from the area-law phase to the finite critical phase would be of BKT-universality [248].

The overall result for the phase diagram from the 2-replica approximation is schematically shown in Fig. 4.8. For a fixed partial post-selection $\zeta \neq 1$, and non-zero dimerization $\Delta \neq 0$, we find critical values of J^2 beyond which $|g_2|$ is irrelevant, corresponding to a critical-scaling phase. This phase expands when retaining a larger subset of quantum trajectories (i.e. increasing ζ). The results from the RG analysis of the 2-replica model are also confirmed by the numerical evaluation of the entanglement entropy scaling in appendix B.8, Fig. B.5. This expansion is understood as a result of the system exploring a larger region of the Hilbert space as more trajectories are retained. This imposes fewer constraints on the unitary dynamics in generating large-scale entanglement and is consistent with similar numerical findings with deterministic unitary dynamics [75].

4.8 Summary

In this work, we have analysed the steady-state out-of-equilibrium phases of a monitored many-body quantum system when only part of the measurement readouts is retained (partial post-selection). We first developed a general equation for the evolution of a quantum system under partial postselection of continuous Gaussian measurements, named Partial-Post-Selected Stochastic Schrödinger Equation (PPS-SSE) — cf. eq.(4.9), in which a parameter continuously bridges between the fully monitored and fully post-selected limits. Since the two limits are known to give rise to MiPT of different universality classes, we have studied such crossover for a specific model of free Gaussian real fermions with random unitary dynamics. We analyzed the MiPT in a 2-replica approximation which captures the simplest non-linearity in the system's state. Within the approximation, we derive the MiPT in terms of the low-energy long-wavelength properties of an associated bosonised Hamiltonian in a 2-replica-Choi-duplicated space in the limit of strong partial post-selection — cf. Eq.(4.42).

In the strong PPS limit, we predict that the model presents MiPTs from area laws (with distinct quantum order) to a critical phase. We show that for strong yet finite partial post-selection, the phase diagram displays the same universal features as the post-selected model. In particular, without unitary dynamics, the transition reduces to an Ising-like transition with a logarithmic critical scaling at the transition point. The entangling phase displays a log scaling instead of $\log^2$ in Ref. [80], with the only quantitative changes given by the expansion of the phase with critical scaling upon increasing the range of measurement outcomes retained — cf. Fig. 4.8. Notably, our theory predictions are limited by the validity of the bosonization, which breaks down at finite values of the partial post-selection, indicating a possible phase transition at that point. Numerical results corroborate this finding by showing an abrupt change in the universal scaling of the measurement-only transition at a similar value of partial post-selection — cf. Fig. 4.6.

Chapter 5

Entanglement in Non-Hermitian Su–Schrieffer–Heeger model

In this chapter, we explore the emergent non-Hermitian Hamiltonian from the post-selected dynamics of continuous measurements. We analyse a free fermion model; hence, the system is solvable. This chapter is based on unpublished results for a manuscript in preparation. The work is in collaboration with Rafael Soares, Youenn Le Gal and Marco Schirò from Collège de France.

5.1 Overview

In continuous measurements, the system constantly exchanges information with an external observer. Although the update is random, we know from a physical ground that quantum measurement favours the establishment of measurement eigenstates in the dynamics. Therefore, one might wonder if a simplified deterministic model can emerge from information-selection, describing these state-favouring dynamics: perhaps some non-Hermitian Hamiltonians with non-real eigenvalues describing amplification/damping? Indeed, in Ch. 2.1.3, a specific measurement outcome post-selecting scheme will lead to an emergent non-Hermitian Hamiltonian, whether it is the 'no-click' trajectory in quantum jump or fixing x_j to be some specific value. This has led to the use of non-Hermitian Hamiltonians as a proxy in the study of MiPTs, taking advantage of the deterministic evolution [75, 146–158]. Nonetheless, non-Hermitian Hamiltonians have been studied separately and extensively [249–251], and has been shown to display rich phenomena [147, 252–262].

As a proxy to study MiPTs, non-Hermitian Hamiltonians also display entanglement phase transitions [147, 252–256]. Most studies on this entanglement phase transition place emphasis on the spectrum, and associate the phase transition with the properties of the band [148]. Indeed, in Hermitian systems, this relation generically holds, as discussed in Ch. 2.3.2. Nevertheless, an associated question arises: how does the initial state affect the entanglement and the transition? Generally speaking, the entanglement phase transition is naively not expected to depend substantially on the initial state as most information is encoded in the spectrum. Indeed, in Hermitian physics, although entanglement scaling can depend on the initial states [197, 263], the structure of the transition in the dynamics remains unchanged, i.e. a phase transition into a gapped spectrum always leads to an area law. However, does this still hold for a non-Hermitian Hamiltonian?

In this chapter, we analyse and report an initial-state-dependent entanglement phase transition in a non-Hermitian Su–Schrieffer–Heeger (SSH) model. Contrary to generic non-Hermitian Hamiltonians, where the system 'forgets' about the initial state in the long-time dynamics due to amplification/dissipation isolating a subset of eigenstates, the non-Hermitian SSH Hamiltonian here retains some information in the long-time. This leads to a surprising, drastic change in the system's entanglement phase transition in the long-time steady dynamics, compared to the findings in Ref. [148]. Notably, certain initial states lead to a critical scaling in place of the original area law, significantly altering the entanglement/correlation properties of the system.

The rest of the chapter is organised as follows. In Ch. 5.2, we introduce the model, a non-Hermitian SSH chain. We first discuss the model's properties and spectrum, then briefly outline previous results in Ref. [148] on half-filling states

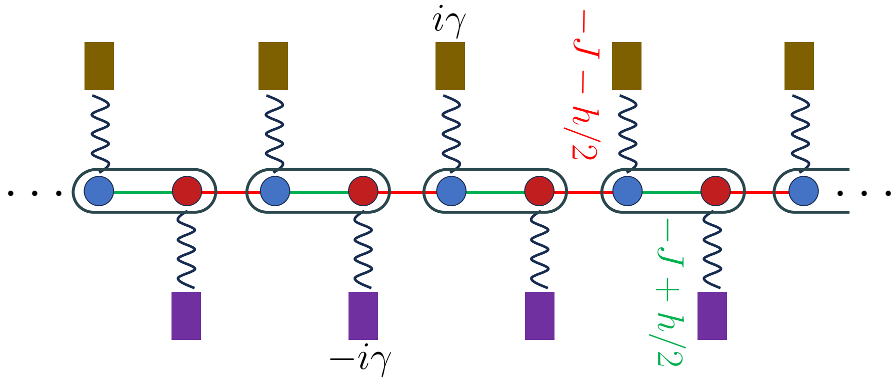

Figure 5.1: A schematic drawing of the non-Hermitian Su–Schrieffer–Heeger model in Eq.(5.1). The non-Hermiticity arises from the post-selection of the backaction from the detector. The red and blue dots are the A and B fermions, forming a unit cell.

when the number of particles is half the total number of available states. In Ch. 5.3, we analyse the model for non-half-filling states, first via numerical simulation, then analytics based on Toeplitz matrices and the low-energy continuum field theory. We present a generic phase diagram in Ch. 5.3.3 for initial states that conserve particle number. In Ch. 5.4, we summarise the analysis and findings.

5.2 The post-selected non-Hermitian SSH model

We consider a Su–Schrieffer–Heeger (SSH) chain

$$H = \sum_{j=1}^{j=L}(-J-\frac{h}{2})c^{\dagger}_{A,j}c_{B,j} + (-J+\frac{h}{2})c^{\dagger}_{B,j}c_{A,j+1} + h.c,$$

under the continuous measurements of $c^{\dagger}_{A,j}c_{A,j}$ and $1-c^{\dagger}_{B,j}c_{B,j}$. A periodic boundary condition applies, $c_{D,L+1} = c_{D,1}$ for $D = A$ or B, and we assume the lattice constant to be unity. Since there is freedom to choose the energy scale, we set $J = 1$ from now on. First, we post-select the measurement outcomes according to the discussion in Ch. 2.1.3: either the no-click limit in quantum jump or fixing $x_j = 0$ in the quantum state diffusion equation. Then, the post-selected dynamics evolve according to Eq.(2.38) (with the minus sign), which in the present model is the following non-Hermitian Hamiltonian

$$H = \sum_{j=1}^{j=L} \left[(-1 - \frac{h}{2}) c^\dagger_{A,j} c_{B,j} + (-1 + \frac{h}{2}) c^\dagger_{B,j} c_{A,j+1} + h.c \right] + i\gamma \sum_{j=1}^{j=L} \left[-c^\dagger_{A,j} c_{A,j} + c^\dagger_{B,j} c_{B,j} \right]. \tag{5.1}$$

Given a state $|\psi\rangle$, the evolution dictated by H is

$$|\psi(t)\rangle = \frac{e^{-iHt}|\psi\rangle}{\sqrt{||e^{-iHt}|\psi\rangle||}},$$

and the usual Schrödinger equation now includes additional terms accounting for normalisation

$$d|\psi\rangle = -iHdt|\psi\rangle - \frac{i}{2} dt \langle H^\dagger - H\rangle |\psi\rangle. \tag{5.2}$$

Utilising translational invariance of the unit cells (consisting of one A and one B fermion), we perform the following unitary Fourier transform on the operators

$$c_{D,j} = \frac{1}{\sqrt{L}} \sum_k e^{ikj} c_{D,k}, \tag{5.3}$$

where $k = \{-\pi + 2\pi/L, -\pi + 2 \cdot 2\pi/L, ..., \pi\}$. Inserting this into Eq.(5.1), we obtain

$$H = \sum_k \underline{\mathbf{c}}^\dagger H_k \underline{\mathbf{c}},\ H_k = \begin{pmatrix} -i\gamma & (-1+h/2)e^{-ik} - (1+h/2) \\ (-1+h/2)e^{ik} - (1+h/2) & i\gamma \end{pmatrix},$$

and $\underline{\mathbf{c}} = (c_{A,k}, c_{B,k})^T$. (5.4)

H_k can be diagonalised, giving the following eigenvalue spectrum

$$E_k = \pm\sqrt{h^2 - \gamma^2 + (4 - h^2)\cos^2(\frac{k}{2})}. \tag{5.5}$$

E_k can be classified in terms of parity-time($\mathcal{PT}$) symmetry; here, $\mathcal{P}$ stands for parity operation and $\mathcal{T}$ stands for time-reversal

$$\mathcal{P} c_{D,j} \mathcal{P} = c_{D,L-j+1},\ \mathcal{T} i \mathcal{T} = -i.$$

For $\gamma < h$, the spectrum is $\mathcal{PT}$ symmetric, and all the eigenvalues are real despite H being non-Hermitian [249]. For $\gamma > h$, although $\mathcal{PT}$-symmetry is broken and

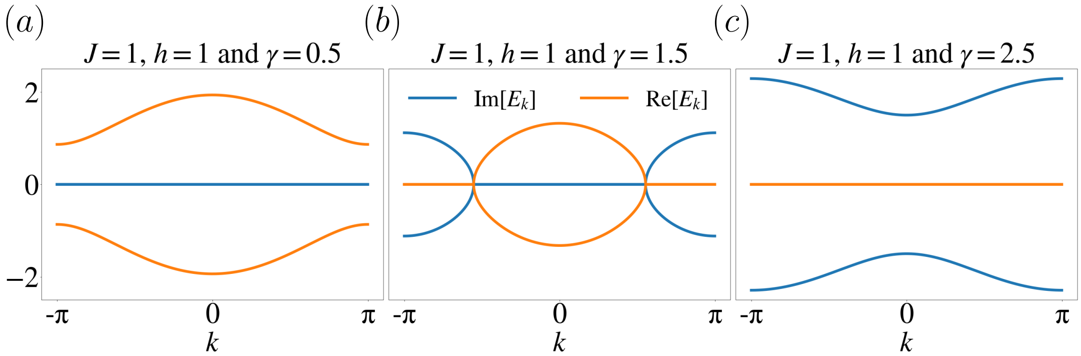

Figure 5.2: E_k the spectrum of H in Eq.(5.5). $h = 1$ and $J = 1$ are fixed across all figures, and the values of γ are $\gamma = 0.5$ (a), $\gamma = 1.5$ (b) and $\gamma = 2.5$ (c). As γ increases, H goes from $\mathcal{PT}$-symmetric (a), $\mathcal{PT}$-mixed (b), and $\mathcal{PT}$-absent (c) as indicated by the real/imaginary (orange/blue lines) mode in the spectrum.

eigenvalues can become imaginary, we can separate the system into two distinct phases: $\mathcal{PT}$-mixed phase where only some of the eigenvalues are imaginary and $\mathcal{PT}$-absent phase where all eigenvalues are imaginary. A graph displaying the spectrum is shown in Fig. 5.2.

An operator, O under the evolution of H, has the following equation of motion

$$\frac{d}{dt}\langle O\rangle = i\langle H^\dagger O - OH\rangle - i\langle H^\dagger - H\rangle\langle O\rangle\,. \tag{5.6}$$

This implies that for a non-Hermitian Hamiltonian, the eigenvalue of an operator can be only conserved in time if the initial state is an eigenstate of the operator

$$O|\psi(t=0)\rangle = o|\psi(t=0)\rangle,$$

which differs from the Hermitian counterpart $[H, O] = 0$. Defining the number operator to be

$$n_k = c^\dagger_{A,k}c_{A,k} + c^\dagger_{B,k}c_{B,k}, \qquad\qquad n_j = c^\dagger_{A,j}c_{A,j} + c^\dagger_{B,j}c_{B,j}, \tag{5.7}$$

the system's particle number is conserved (in time) if the initial state is an eigenstate of n_k $\forall k$, an eigenstate of n_j $\forall j$[1]. This observation will become handy later on.

[1]Indeed, the total particle number is $\sum_j n_j = \sum_k n_k$. This implies some initial states allow different k-mode to couple, but the total particle number is still conserved (and vice versa).

5.2.1 Entanglement scaling and transition at half-filling

The entanglement properties of the model in Eq.(5.1) have been studied in Ref. [148] starting from an initial state

$$|\mathrm{GS}\rangle = \prod_k d^\dagger_{-,k}|0\rangle,\ d^\dagger_{-,k} = \frac{1}{\sqrt{2}}(c^\dagger_{A,k} + e^{ik/2}c^\dagger_{B,k}), \tag{5.8}$$

where the product runs over all k. This state is translational invariant, is the ground state of $H(h=0,\gamma=0)$, and is an eigenstate of n_k; thus, the system is number-conserving. The particle number is $L/2$, and the system is half-filling. We briefly summarise the results of Ref. [148] here.

Under such dynamics, the system displays an entanglement phase transition from volume to area law. The phase diagram is depicted in Fig. 5.3, and one notices that the entanglement phase transition differs from the $\mathcal{PT}$-symmetry transition; it is entirely dictated by the presence /absence of real energy modes. There is a physical reasoning behind this: while the real modes correspond to infinite lifetime quasiparticle excitation, quasiparticles of purely imaginary modes have a finite lifetime. Thus, the real modes in the $\mathcal{PT}$-mixed phase spreads entanglement without bound, giving a volume law. On the other hand, when all modes are imaginary, all quasiparticles have a finite lifetime, and entanglement cannot spread in the system, giving an area law. This quasiparticle-lifetime-based argument extends to other initial half-filling states that conserve particle number, e.g. Néel states or single domain wall states, and numerical simulation has confirmed the validity of Fig. 5.3 for non-translationally invariant states (see Fig. 5.4 for domain wall state). It should be noted that this quasiparticle-lifetime-based argument implies that the prefactor of the volume law in the $\mathcal{PT}$-mixed phase is γ-dependent, as the number of real modes depends on γ; this is indeed the case as found in Ref [148].

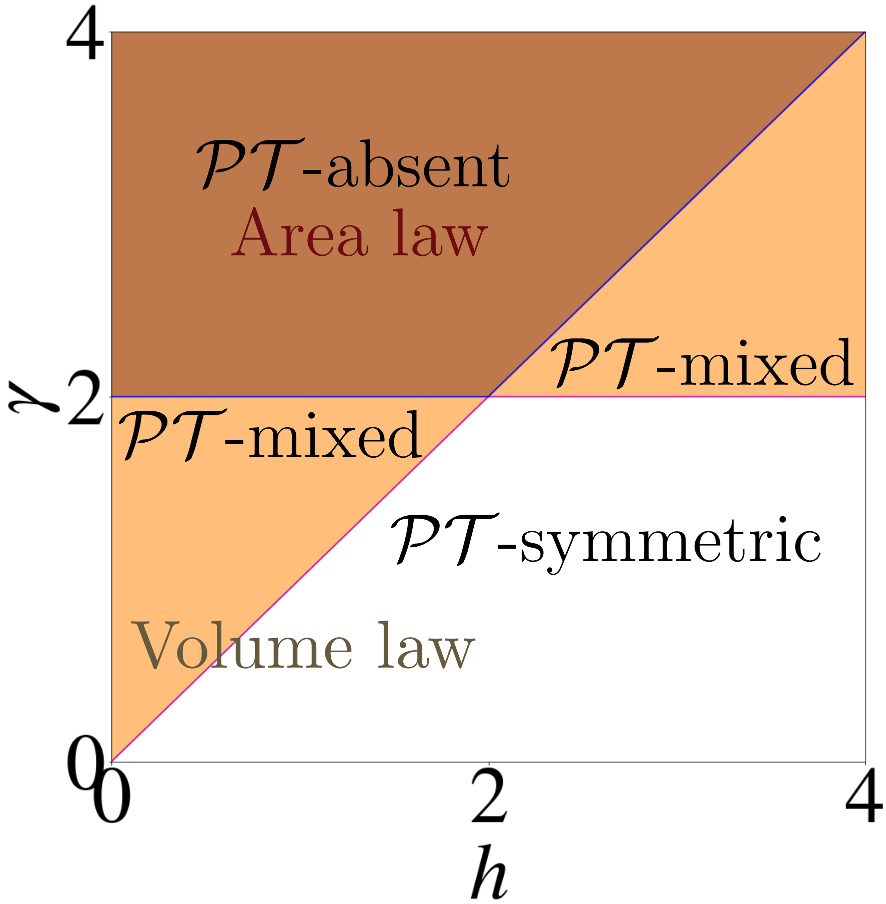

Figure 5.3: Phase diagram of H in Eq.(5.1) for a number-conserving half-filling initial state. The white ($\mathcal{PT} - symmetric$) and light orange regions ($\mathcal{PT} - mixed$) both have volume law scaling, while the brown region has area law scaling. $J = 1$ is fixed as an overall energy scale

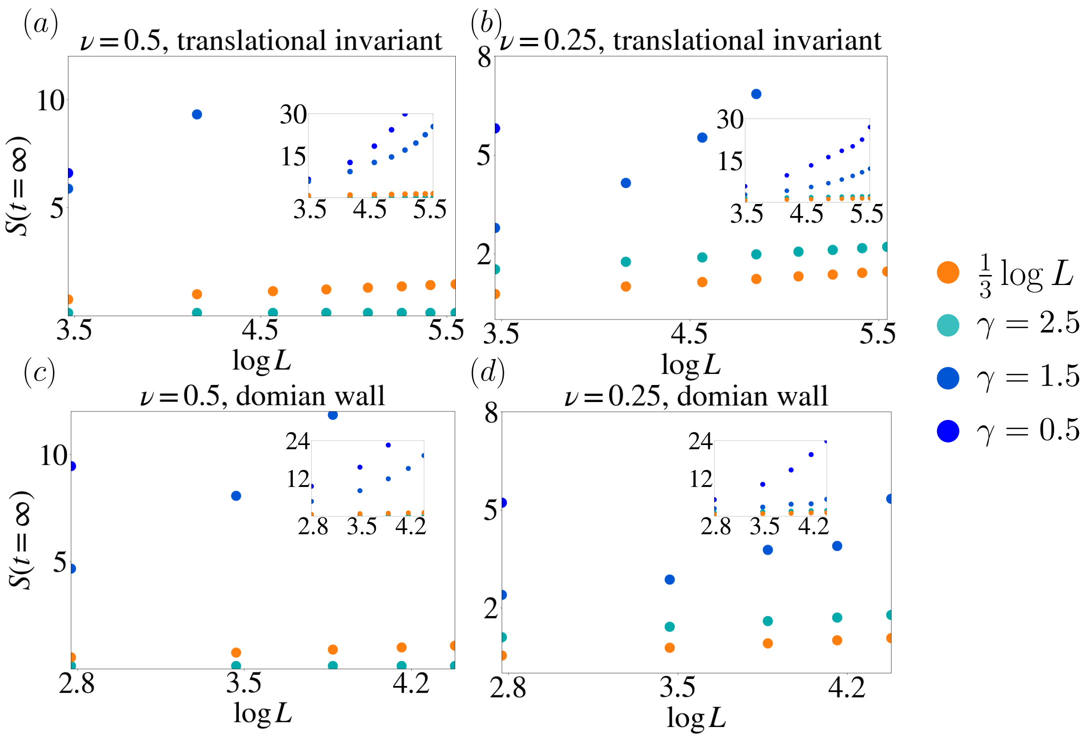

Figure 5.4: Steady state entanglement entropy scaling for different filling factor ν and different initial state structures. All the results are obtained via numerical simulation using QR-decomposition. Note that for translational invariant initial states [(a) and (b)], solving Eq.(5.11) numerically (the equation of motion for the 2-point correlator) yields the same steady-state entanglement features as in the QR-decomposition simulation. The legend on the left applies to all plots. Panel (a) and (b): Eq.(5.9) was used as the initial state with half-filling $\nu = 0.5$ on the left and quarter-filling $\nu = 0.25$ on the right. Panel (a) and (b) insets: zoomed-out plots to the main plots. The gradient of the light-blue-green line ($\gamma = 2.5$) is to be compared with 1/3 (orange line). (c) and (d): similar to (a) and (b), except that the initial state is a domain wall configuration. Note that due to the increasing duration needed to reach a steady state for large-L (domain wall melting), the system sizes displayed are smaller (x-axis). (c) and (d) insets: zoomed-out plots to the main plots.

5.3 Non-half-filling states

We now turn our attention to non-half-filling number-conserving states. Although one might expect this entanglement phase transition to be qualitatively generic for arbitrary states, due to number conservation, an intriguing phenomenon arises with no known Hermitian counterpart. Without loss of generality, we set $h = 1$ and vary γ; this way, we can still access all three categories of the spectrum. Furthermore, since there is a symmetry in the spectrum between hole and particle excitation, it is enough to consider *less than* half-filling only as the physics of more than half-filling readily follows from the symmetry.

For later convenience, we consider an extension of the translational invariant state in Eq.(5.8) as our non-half-filling initial state, We consider initial states of the form

$$|\psi\rangle = \prod_{|k|<2\nu\pi} d^{\dagger}_{-,k}|0\rangle, \tag{5.9}$$

where $0 \leq \nu \leq 1/2$ quantifies the filling of the system, with $\nu = 1/2$ the half-filling and $\nu = 0$ for no particles. We numerically simulate the dynamics via QR-decomposition [155] [in a similar fashion as reported in Appendix B.8]. The long-time steady-state results are shown in Fig 5.4(a), where we display the entanglement scaling for various γ for two different $\nu < 1/2$. A noticeable feature: the area law is no longer present. This significantly changes the entanglement phase transition, and the system displays a gapless critical feature. Anticipating an effective conformal scaling in a finite periodic system (zero temperature), we compare the logarithmic scaling of entanglement entropy with the following ansatz [204]

$$S_l \simeq \frac{c}{3}\log\left(\frac{L}{\pi}\sin\left(\frac{l\pi}{L}\right)\right) + A_1,$$

where l is the subsystem size. L is the length of the system, c is the (effective) central charge[1], and A_1 is a non-universal length-independent constant. Upon extracting

[1] In some non-Hermitian system, the central charge appearing does not correspond to any universal underlying conformal field [155].

from the numerics, it is found to be $c = 1$, indicating a free Dirac fermion or free boson field.

To demonstrate that the findings here are independent of the translational invariance of the initial state, we consider another set of number-conserving non-half-filling states: the domain wall configuration $|1\ldots100\ldots\rangle$. The results for these states are shown in Fig. 5.4(b). The same changes of entanglement scaling and phase transition in the steady-state can be seen[1]: volume-to-area for half-filling $\nu = 1/2$, and volume-to-log for less half-filling $\nu < 1/2$.

The initial state dependence found here is surprising since non-Hermitian Hamiltonians generally lose memory of the initial states. Although translation invariant initial states (Eq.(5.9)) conserve n_k and may retain some information, the initial state dependence in n_k-non-conserving states contrast with one's naive expectation. In the following, we will show that this is a consequence of particle number conservation.

5.3.1 2-point correlator function

To gain further insight into this initial-state-dependent entanglement transition, we turn our attention to the 2-point correlator function. Since H is quadratic, it preserves the Gaussianity of any Gaussian states; any quantities can be obtained from the 2-point correlator function via Wick's theorem. Specifically, utilising the decoupling of k modes in Eq.(5.4), we consider the following correlation matrix

$$G_k = \begin{pmatrix} \langle c^\dagger_{A,k} c_{A,k}\rangle & \langle c^\dagger_{A,k} c_{B,k}\rangle \\ \langle c^\dagger_{B,k} c_{A,k}\rangle & \langle c^\dagger_{B,k} c_{B,k}\rangle \end{pmatrix}, \tag{5.10}$$

along with initial states of the form Eq.(5.9). This guarantees that n_k is conserved and G_k is diagonal/decoupled in k ($G_{k,k'} = G_k \delta_{k,k'}$) at all time.

The evolution of G_k follows from Eq.(5.6), and its solution is initial state dependent. For unoccupied mode $|k| \geq 2\nu\pi$, $G_{k\geq 2\nu\pi}(t = 0) = 0$ gives a trivial

[1]As a small note, the early time behaviour is different due to the melting of domain wall and n_k is not conserved

solution

$$G_{k\geq 2\nu\pi}(t\to\infty)=0.$$

For occupied mode $|k|<2\nu\pi$, G_k takes on the solution [148]

$$G_k(t)=G_k(0)+\frac{1}{N_k(t)}\begin{pmatrix} B_k(t) & e^{ik/2}A_k(t)(-C_k+2JiD_k) \\ -e^{-ik/2}A_k(t)(C_k+2JiD_k) & -B_k(t)\end{pmatrix}, \tag{5.11}$$

where

$$\begin{aligned} G_k(0)&=\frac{1}{2}\begin{pmatrix} 1 & e^{ik/2} \\ e^{-ik/2} & 1\end{pmatrix},\ N_k(t)=1+(1+C_k)A_k(t), \\ A_k(t)&=\frac{\gamma^2-h^2\sin^2(k/2)}{2|E_k|^2}(1-\cos(2E_kt)),\ B_k(t)=\frac{\gamma-h\sin\big(k/2\big)}{2|E_k|}\sin(2E_kt), \\ C_k&=\frac{\gamma-h\sin\big(k/2\big)}{\gamma+h\sin\big(k/2\big)},\ D_k=\frac{\cos\big(k/2\big)}{\gamma+h\sin\big(k/2\big)}. \end{aligned} \tag{5.12}$$

To compute the entanglement entropy of a segment A of the chain (which can be disconnected), first, back Fourier transform

$$G_{m-n}(t)=\begin{pmatrix} \langle c^\dagger_{A,m}c_{A,n}\rangle & \langle c^\dagger_{A,m}c_{B,n}\rangle \\ \langle c^\dagger_{B,m}c_{A,n}\rangle & \langle c^\dagger_{B,m}c_{B,n}\rangle \end{pmatrix}=\frac{1}{L}\sum_k e^{-ik(m-n)}G_k(t), \tag{5.13}$$

to obtain the real space 2-point correlator[1]. Next, define a new matrix named $G^A(t)$, in which $G^A(t)$'s block elements are given by $G_{m,n}(t)$ [m (n) as the row (column) block index] and include only indices in region A. Diagonalise $G^A(t)$ to obtain the set of eigenvalues $\{\alpha_p\}$, and finally, the entanglement entropy of A is given by the formula [264, 265]

$$S_A=-\sum_{\{\alpha_p\}}\Big[\alpha_p\log\alpha_p+(1-\alpha_p)\log\big(1-\alpha_p\big)\Big]. \tag{5.14}$$

A quick numerical evaluation of Eq.(5.11) for the steady-state confirms that the half-cut entanglement entropy $S_{L/2}$ undergoes an entanglement phase transition, as

[1]Note that G only depends the distance $m-n$, as a result of translational invariance.

reported previously, from volume-to-log for non-half-filling states. The results are practically identical to the ones in Fig.5.4(a), as the QR-decomposition simulation is merely a restatement of Eq.(5.11).

5.3.1.1 Toeplitz matrix

Without loss of generality, we assume the segment to be continuous without a cut $A \equiv l$, and take the thermodynamic limit $L \to \infty$. To obtain an analytical expression of the steady-state entanglement dynamics, we note that the relevant matrix $G^l(t)$ is a **block Toeplitz** [266], that is

$$G^l(t) = \begin{pmatrix} G_0(t) & G_{-1}(t) & G_{-2}(t) & \dots \\ G_1(t) & G_0(t) & G_{-1}(t) & \dots \\ G_2(t) & G_1(t) & G_0(t) & \dots \\ \vdots & \vdots & \vdots & \ddots \end{pmatrix}, \tag{5.15}$$

where $G_g,\ g \in \{-l, -l+1, \dots, l\}$ is given in Eq.(5.13). Using this fact, we can follow the procedures in Ref. [197, 267, 268] to obtain the steady-state entanglement behaviour. First, let's rewrite Eq.(5.14) in a form where the matrix G^A appears explicitly. This can be done by using a trick such that each term in the sum in Eq.(5.14) appears as a simple pole of a complex function, and the sum is replaced by a complex contour integral. The result is

$$S_A = \frac{1}{2\pi i} \oint_{\mathcal{C}} d\lambda \mu(0^+, \lambda) \frac{d}{d\lambda} \ln \det \tilde{G}^l(\lambda), \tag{5.16}$$

where

$$\begin{aligned} &\tilde{G}_k(\lambda) = \lambda \mathbb{I}_2 - G_k(t \to \infty);\ \tilde{G}_g(\lambda) = \lambda \mathbb{I}_2 - G_g(t \to \infty) = \frac{1}{2\pi} \int_{-\pi}^{\pi} dk e^{-ikl} \tilde{G}_k(\lambda) \\ &\tilde{G}^l(\lambda) = \lambda \mathbb{I}_{2l} - G^l(t \to \infty) \\ &\mu(y, x) = -(y + x) \ln(y + x) - (1 + y - x) \ln(1 + y - x), \end{aligned} \tag{5.17}$$

and $\mathcal{C}$ is a contour that runs over a region of the complex plane covering all the eigenvalues of $\tilde{G}^l(\lambda)$[1], see Fig. C.1 in Appendix C.1. $G(t \to \infty)$ denotes the stationary value of the 2-point correlator in the long-time dynamics (for oscillating dynamics, it will be the average over one period). From this, we observe that $\tilde{G}_k(\lambda)$ is the generator of the Toeplitz matrix $\tilde{G}^l(\lambda)$. We can now obtain analytically the large-l behaviour by applying the generalised Szegő limit and the Fisher-Hartwig conjecture [267, 269, 270].

First note that there is a jump discontinuity of $G_k(t \to \infty)$ at $k = \pm 2\nu\pi$ and hence $\tilde{G}_k(\lambda)$. Next, the Szegő limit and the Fisher-Hartwig conjecture state that

$$\ln\det \tilde{G}^{l\gg 1}(\lambda) \simeq \frac{l}{2\pi}\int_{-\pi}^{\pi} dk \ln\det \tilde{G}_k(\lambda) + \frac{\log l}{4\pi^2}\sum_{r=1}^{2} \mathrm{Tr}\left[\log[\tilde{G}_{k_r^-}(\lambda)(\tilde{G}_{k_r^+}(\lambda))^{-1}]\right], \tag{5.18}$$

where the sum $\sum_{r=1}^{2}$ is over the number of discontinuities, $k_1 = -2\nu\pi$ and $k_2 = 2\nu\pi$, and

$$\tilde{G}_{k_r^-}(\lambda) \equiv \lim_{\substack{k\to k_r \\ k<k_r}} \tilde{G}_k(\lambda),$$

corresponds to approaching the jump from the negative side, with similar notation for k_r^+[2]. Before proceeding, it is convenient to calculate and note down the eigenvalues of $G_k(t \to \infty)$, $\{\alpha_+(k), \alpha_-(k)\}$. For an **unoccupied** mode, the eigenvalues are simply

$$\alpha_+(k) = 0,\ \alpha_-(k) = 0.$$

For an **occupied** real mode $\mathrm{Im}[E(k)] = 0$, and the eigenvalues are given by

$$\begin{aligned} \alpha_\pm(k) &= \frac{1 \pm \alpha_k}{2},\ \alpha_k = \sqrt{4\chi_k^2(C_k^2 + D_k^2) - 4\chi_k C_k + 1}, \\ \chi_k &= \frac{A_k(t\to\infty)}{N_k(t\to\infty)},\ A_k(t\to\infty) = \frac{\gamma^2 - h^2\sin^2(k/2)}{2|E_k|^2}, \end{aligned} \tag{5.19}$$

[1]Since all eigenvalues are real and in between the interval $[0, 1]$, the convention is a 'dumbbell' between 0 and 1

[2]As a side note, for a half-filling state $\nu = 1/2$, since there is no discontinuity in $\tilde{G}_k(\lambda)$, the second term proportional to $\log l$ diminishes. We recover the result in Ref. [148].

where C_k, D_k and $N_k(t)$ were defined in Eq.(5.12). Although a complicated expression, the eigenvalues are in between $0 < \{\alpha_+(k), \alpha_-(k)\} < 1$ and are real. For an **occupied** imaginary mode $\mathrm{Re}[E(k)] = 0$,

$$\alpha_+(k) = 1,\ \alpha_-(k) = 0.$$

Finally, following Eq.(5.16) and (5.18), the entanglement entropy admits the following form

$$S_l \simeq a_1 l + a_2 \log l, \tag{5.20}$$

where

$$\begin{aligned} a_1 &= \frac{1}{4\pi^2 i} \oint_{\mathcal{C}} \int_{-\pi}^{\pi} d\lambda dk \mu(0^+, \lambda) \frac{d}{d\lambda} \ln \det \tilde{G}_k(\lambda), \\ a_2 &= \frac{1}{8\pi^3 i} \oint_{\mathcal{C}} d\lambda \mu(0^+, \lambda) \frac{d}{d\lambda} \left\{ \sum_{r=1}^{2} \mathrm{Tr} \left[\ln^2 \left[\tilde{G}_{k_r^-}(\lambda) (\tilde{G}_{k_r^+}(\lambda))^{-1} \right] \right] \right\}. \end{aligned} \tag{5.21}$$

The evaluation of the integrals for a_1 follows from the eigenvalues $\{\alpha_+, \alpha_-\}$, and the details are reported in Appendix C.1. The final result for a_1 is

$$a_1 = \frac{1}{2\pi} \int_{-\pi}^{\pi} dk \Theta(E_k^2) \Theta(2\nu\pi - k) \left[\mu\left(0^+, \alpha_+(k)\right) + \mu\left(0^+, \alpha_-(k)\right) \right], \tag{5.22}$$

which is similar to that in Ref. [148]. This confirms that any non-zero occupation of the real modes contributes to a volume law $a_1 > 0$.

For a_2, the evaluation of the contour integral requires some trick as reported in Appendix C.1. Using Eq.(5.9) as the initial state, an informative form of a_2 is summarised below. In particular, in the $\mathcal{PT}$-mixed phase, a_2 heavily depends on the location of the cutoff wavenumber $2\nu\pi$, and k^*. k^*, defined as $\mathrm{Im}[E(|k^*|)] = \mathrm{Re}[E(|k^*|)] = 0$, is the wavenumber separating the real and imaginary mode, i.e. $k^* = 0$ for the $\mathcal{PT}$-broken phase. For the $\mathcal{PT}$-symmetric phase, and the $\mathcal{PT}$-mixed phase with the cutoff in the real modes $2\nu\pi < k^*$, it follows

$$a_2 = \frac{1}{2\pi^2} \sum_{k=\pm 2\nu\pi} \int_0^{\alpha_+(k)} d\lambda \ln\left(\frac{1-\lambda}{\lambda}\right) \ln \frac{\alpha_+(k) - \lambda}{\lambda} + \int_0^{\alpha_-(k)} d\lambda \ln\left(\frac{1-\lambda}{\lambda}\right) \ln \frac{\alpha_-(k) - \lambda}{\lambda}, \tag{5.23}$$

and $\alpha_\pm$ is given in Eq.(5.19). For $\mathcal{PT}$-absent phase, and $\mathcal{PT}$-mixed phase with the cutoff in the imaginary mode $2\nu\pi \geq k^*$

$$\begin{aligned} a_2 &= \frac{1}{2\pi^2}\sum_{k=\pm 2\nu\pi}\int_0^1 d\lambda \ln\left(\frac{1-\lambda}{\lambda}\right)\ln\frac{1-\lambda}{\lambda} + \int_0^0 d\lambda \ln\left(\frac{1-\lambda}{\lambda}\right)\ln\frac{\lambda}{\lambda} \\ &= \frac{1}{\pi^2}\int_0^1 d\lambda \ln\left(\frac{1-\lambda}{\lambda}\right)\ln\frac{1-\lambda}{\lambda} = \frac{1}{3}. \end{aligned} \tag{5.24}$$

From this, the central charge in the $\mathcal{PT}$-absent phase and $2\nu\pi \geq k^*$ $\mathcal{PT}$-mixed phase is analytically confirmed to be $c = 1$ via a large asymptotic Toeplitz matrix approach. This highly suggests the existence of an underlying conformal field theory description, which we will explore now.

5.3.2 Field theoretical description

To begin with, we first alleviate our assumption of a translational invariant initial state (cf Eq.(5.9)), allowing consideration of a domain wall state. Then, n_k is no longer conserved, but the total particle number $\sum_j n_j$ is. The system now relaxes into the least damped state: positive imaginary eigenvalues are filled first, with the most positive ones prioritised. We keep ν as the quantifier for filling, e.g. $\nu < 1/2$ for less than half-filling. To elucidate this description, we first consider the $\mathcal{PT}$-absent phase, where all eigenenergies are imaginary. For $\nu < 1/2$, the negative imaginary band is only filled in the interval $\pi(1-2\nu) < |k| < \pi$, with a shape cut in the distribution of n_k in the momentum space (see Fig.5.5(b)). Restricting to the 'low-energy limit' by linearising the band around the cutoff wavenumber $\pm k_\mathrm{F} \equiv \pi(1-2\nu)$, we have the following effective Hamiltonian (assuming $h < 2$)[1]

$$H \approx -i\left[-2\epsilon_0 - v_\mathrm{F}\sum_{\substack{k=-\infty \\ r=+,-}}^{k=\infty}(rk - k_\mathrm{F})c^\dagger_{k,\sigma}c_{k,\sigma}\right] \equiv -i(H_0), \tag{5.25}$$

[1]There is an implicit transformation on H such that it is transformed to an anti-Hermitian operator, with the left and right eigenket being adjoint to each other [271].

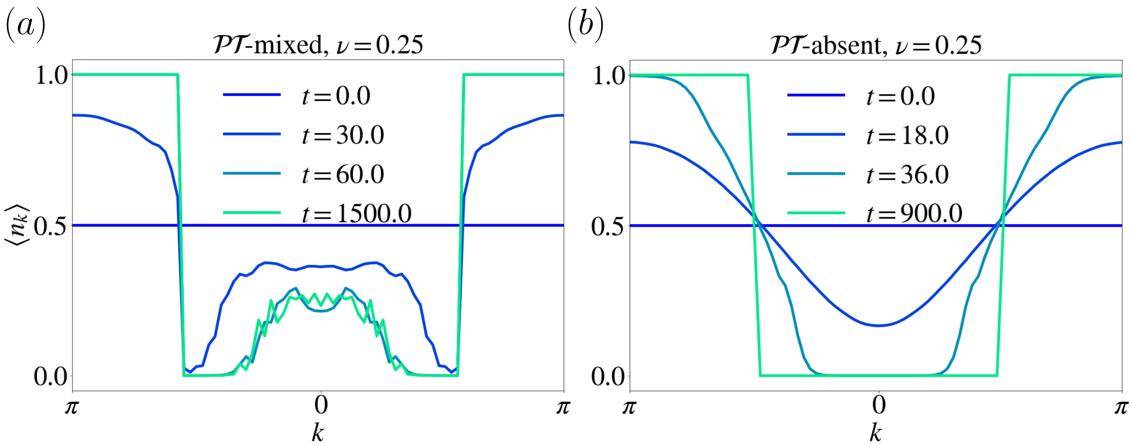

Figure 5.5: Distribution of $\langle n_k \rangle$ in momentum space for a domain wall initial state ($\langle n_k \rangle$-non-conserving). In both figures, the system is at $\nu = 0.25$ quarter filling. Time is measured in units of $1/J$. (a): $\mathcal{PT}$-mixed phase. The distribution is smooth, and a bump is visible in the real k-modes. (b): $\mathcal{PT}$-absent phase. The distribution has a sharp cutoff.

where

$$\begin{aligned} \epsilon_0 &= \sqrt{\gamma^2 - h^2 + (h^2-4)\cos^2(\frac{k_{\mathrm{F}}}{2})} > 0 \\ v_{\mathrm{F}} &= \frac{2(4-h^2)\cos\big(k_{\mathrm{F}}/2\big)\sin\big(k_{\mathrm{F}}/2\big)}{2\sqrt{\gamma^2 - h^2 + (h^2-4)\cos^2(\frac{k_{\mathrm{F}}}{2})}} > 0. \end{aligned} \tag{5.26}$$

Two species of fermions $c_{k,+}$ and $c_{k,-}$ are introduced for the two branches [left (-) and right (+) movers]. Inserting this Hamiltonian into the time evolution, the ket evolves as

$$|\tilde{\psi(t)}\rangle = e^{-iHt}|\psi(t=0)\rangle \approx e^{-H_0 t}|\psi(t=0)\rangle,$$

up to a normalisation (the tilde above). This is an imaginary time evolution of a *linear gapless* Luttinger Hamiltonian H_0, with its ground state describing a negative sea of fermions filled up to k_{F}. From bosonisation, we know this corresponds to a (1+1)d free boson CFT, giving $c = 1$ (it is also equivalent to a (1+1)d free Dirac fermions CFT). Using techniques from Ref. [203, 204, 272], the entanglement entropy is calculated to be

$$S_l \simeq \frac{c}{3}\log l, \tag{5.27}$$

which coincides with the findings in the Toeplitz matrix analysis. This, therefore, shows that the system is gapless with linear dispersion and $c = 1$.

The above argument readily extends to the $\mathcal{PT}$-mixed phase. For ν small enough such that no real mode is occupied, and the positive imaginary modes are partially filled (with a sharp cut in n_k in the steady-state), H_0 can be linearised in the same way above, yielding a low energy gapless Hamiltonian similar to Eq.(5.25). Then, the analysis proceeds likewise as above, yielding

$$S_l \simeq \frac{1}{3} \log l,$$

i.e. logarithmic contribution for the imaginary part.

For $\mathcal{PT}$-mixed and symmetric phase, a similar field theory argument has yet to exist. Still, it is worth pointing out that the occupation distribution takes an interesting form, as shown in Fig. 5.5(a). Instead of uniform distribution in the imaginary mode, the real modes prefer the higher energy mode, displaying a peak in the distribution as shown by the cyan line in Fig. 5.5(a).

5.3.3 Full phase diagram

To conclude the analysis, we present the entire phase diagram of the model under number conservation in Fig. 5.6. On the right panel in Fig. 5.6(a), the phase diagram is applicable only for translational invariant states of the form Eq.(5.9). These states are unique in that they conserve n_k, and the particle's initial (quasi-)momentum fixes the k-mode it can occupy. Furthermore, in Eq.(5.9), we demand that the addition/subtraction of particles (relative to the half-filling) starts at the edge of the Brillouin zone; hence, the real modes are always occupied if present. As discussed above, the volume law sustains whenever the real modes are filled. Therefore, the transition away from volume law only happens when the spectrum is $\mathcal{PT}$-absent, as indicated by a straight line at $\gamma = 2$ (remember $h = 1$ is set). This entanglement transition is generally a volume-to-log transition, except at $\nu = 1/2$, which is the limit that the spectrum cannot be linearised. As studied in Ref. [148], the transition

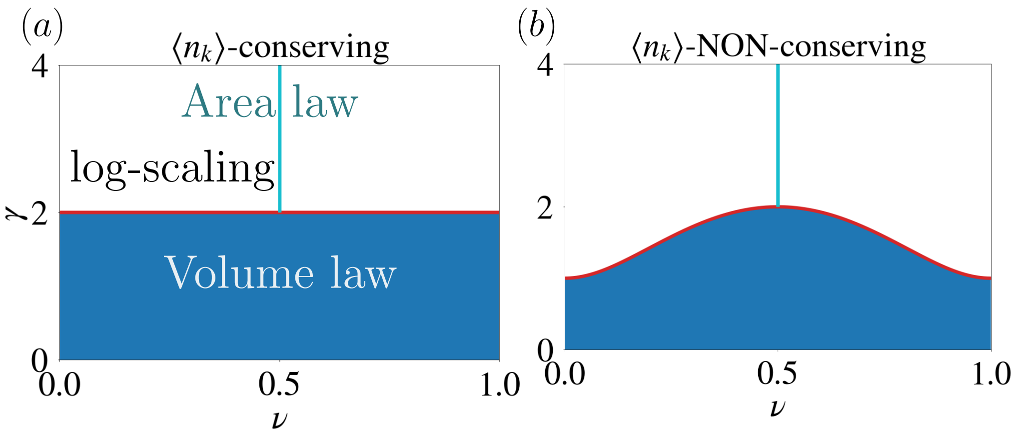

Figure 5.6: Phase diagrams in the filling space ν for $\langle n_k \rangle$-conserving (left) and $\langle n_k \rangle$-non-conserving initial states (right). The white regions are log-scaling phase, and the blue regions are volume scaling phases. The red line represents the boundary between volume law and non-volume law phases. Area law only exists at $\nu = 0.5$ (light-blue-green line). (a): the $\langle n_k \rangle$-conserving initial state is of the form Eq.(5.9). (b): the curve is obtained by solving Eq.(5.28).

follows a volume-to-area transition instead.

For generic number-conserving initial states that do not conserve n_k, the exact phase diagram is reported in Fig. 5.6(b), and we discuss it below. Starting from these states, the system relaxes to the least damped state given a fixed total particle number. This state is characterised by the prioritised filling of the most positive imaginary modes. Restricting to $\nu < 1/2$, the particles start occupying the real modes if the total particle number exceeds the number of positive imaginary modes. Should the real modes be occupied, they contribute a volume law scaling in entanglement. Therefore, the entanglement transition is no longer *independent* of ν, and its dependence is given by the solution to the following equation ($J = 1$ is fixed)

$$0 = h^2 - \gamma^2 + (4 - h^2)\cos^2((1 - 2\nu)\pi/2); \tag{5.28}$$

in other words, when $2\nu\pi = \pi - k^*$, the imaginary modes start to under/over-fill (k^* is the wavenumber separating real and imaginary modes). This phase transition boundary is displayed by the red lines in Fig. 5.6(b) and agrees with numerics. As a final note, the symmetry between $\nu < 1/2$ and $\nu > 1/2$ (particle and hole excitation) appears explicitly in Fig. 5.6(b), and Eq.(5.28) applies to $\nu > 1/2$.

5.4 Summary

In this chapter, we have analysed the steady-state phases of a post-selected monitored SSH chain. The post-selection distils an emergent non-Hermitian SSH Hamiltonian, which possesses a $\mathcal{PT}$-symmetric phase, a $\mathcal{PT}$-mixed phase and a $\mathcal{PT}$-absent phase. We extended the previous results in Ref [148] and analysed number-conserving non-half-filling states. First, we numerically found that the volume-to-area transition reported in half-filling states is fragile against any deviations from half-filling. These deviations change the transition to volume-to-log, and a gapless phase emerges. Next, with asymptotic Toeplitz matrix analysis, we confirm the presence of a logarithmic scaling with a central charge $c = 1$ when the imaginary mode is under/over-filled. Hinted by this finding, we argue that an underlying free boson CFT is responsible for the various observations. We show that the Toeplitz matrix results can be equivalently obtained via a low-energy limit analysis, and confirm an emergent CFT in this non-Hermitian model: linearising the Hamiltonian yields a free boson field, which is responsible for the $c = 1$ in the log-scaling.

As a final note, the interesting finding of the bump in $\langle n_k \rangle$ displayed in Fig. 5.5(a) is reminiscent of a finite temperature Fermi-Dirac distribution. Indeed, when imaginary modes are partially filled, a sharp cutoff in k-space occupation appears, see Fig. 5.5(b), reproducing the signature of a zero temperature Fermi-Dirac distribution. However, its implication in scenarios of partially filled real modes remains unclear, leaving an open question of its underlying physical mechanism.

Chapter 6

Conclusions and outlook

In this thesis, we analysed MiPTs in various scenarios with partial information available to the observer, either via explicit trajectory selection or inefficient measurement readouts. In the classical case of inefficient measurement readouts, classical uncertainties arise, and the density matrix becomes mixed. We explored this in Ch. 3 by numerically analysing a spin-1/2 spin chain under competing Hamiltonians, local continuous measurement and local random white noise, and computed various indicators of entanglement and operator correlation for MiPT. We first examined a 2-qubit model that shows an inconsistent response in the concurrence and half-system parity variance to inefficient measurements. Then, we promote this to a spatially extended model, which leads to the findings of separate entanglement and operator correlation MiPT. Our results there hint at a richer scenario for MiPTs in mixed states than that depicted by the entanglement phase transition alone. They further raise the question of the generality of the reported discrepancy between the entanglement scaling and operator correlations. On the one hand, the generality of the observed features beyond the model studied here is an exciting aspect to address, especially for other models where a mixed state transition has been identified [135]. This can be extended further and ask whether the discrepancy can be associated with some classical correlation components in the half-system parity variance, and whether non-classical correlations different from entanglement, like quantum discord, may play a role.

Seeing the intriguing findings in classical partial information, we move on and investigate the effect of partial information via trajectory selection, in Ch. 4. We formulated this problem by exploring the interpolation between non-Hermitian dynamics that arise from specific total trajectory selection and monitored dynamics of a perfect detector. We first developed a microscopic model describing the quantum process of partial post-selection (PPS), leading to a partially post-selected stochastic Schrödinger equation (PPS-SSE) in the time continuum limit. Next, we employed our PPS-SSE in a monitored free fermion model and show that the measurement-only MiPT's universality changes as a function of PPS strength. Notably, the non-Hermitian universality is robust against finite stochasticity from measurement. Finally, including a unitary component demonstrates the ability of PPS to alter the monitored free fermion phase diagram. Our theory and its prediction there shed new light on MiPT. First, the developed PPS-SSE is the first continuous stochastic equation that offers a novel analytical approach to study the relation between the critical phenomena observed in stochastic monitored dynamics and deterministic non-Hermitian evolution, as well as a means to analyse the transition between the two. It can be, therefore, employed to explore the role of multiple trajectories in a variety of MiPTs. Moreover, the underlying microscopic derivation can also be the basis for obtaining similar PPS for other measurement-induced dynamics, like quantum jumps [146, 149, 152, 159].

Furthermore, employing our newly developed tool in the MiPT of a Gaussian fermionic model reveals surprising physics: the post-selected measurement dynamics are robust against weak fluctuations induced by measurements. This strongly suggests that certain groups of trajectories behave identically to the post-selected dynamics, and sheds new light on the open question of the role of trajectories in MiPT. In particular, the behaviour of the critical exponent in trajectory selection greatly suggests that different trajectories possess different exponents and criticality, contributing different universal properties to the overall ensemble observed in MiPT.

Even more, it is interesting to explore the generality of this finding in other settings, such as projective measurements and random circuits, and the mechanism underpinning the transition from post-selected dynamics to monitored dynamics identified in this work. Finally, inspired by the feasibility of observing robust post-selected MiPTs by retaining a fraction of quantum trajectories, it suggests a possible alternative route to tackle the experimental post-selection problem by performing tomography of the average state of a fraction of trajectories as opposed to tracking the trajectory-by-trajectory entanglement entropy.

Motivated by the findings in Ch. 4 where non-Hermitian dynamics can emerge from a post-selection scheme different to the usual ones in Ch. 2.1.3, and the potential robustness and feasibility of observing post-selected dynamics MiPT, we studied a corresponding post-selected model from a measurement protocol in Ch. 4. More specifically, we analysed a non-Hermitian SSH model with $\mathcal{PT}$-symmetric, $\mathcal{PT}$-mixed and $\mathcal{PT}$-absent band structure. We find the entanglement dynamics at half-filling are not generic, and the system displays a different entanglement transition away from half-filling. We studied the dynamics analytically via Toeplitz matrix and a field theory approach. We argued from both results that an underlying CFT is responsible for some of the behaviours, with evidence supporting this argument. Our findings revealed subtle entanglement dynamics in a class of non-Hermitian Hamiltonians, whose eigenvalues can be grouped into purely real and purely imaginary in momentum space. The initial state has a surprisingly important role in the quantitative behaviour of entanglement scaling across an entanglement transition, with the appearance of gapless behaviour in place of gapped behaviour; this contrasts with the common expectation that non-Hermitian systems lose information about the initial state over time. With these enriched dynamics and dependence on initial states, it is natural to question how 'universal' universal behaviours are in non-Hermitian systems and how the remnant of initial state information changes the dynamics.

Overall, the results in this thesis paint a rich scenario of MiPT dependence on the information available to an observer. In fact, the results hint at a family of MiPTs signalled by entanglement and correlations from unitary to the Zeno limit, which is controlled by the available information. On the other hand, different paradigms of MiPTs appear when restricted to a subset of trajectories. Both scenarios are relevant to experimental developments in the field, either by addressing objective experimental limitations or pointing out a new experimental protocol. They further open more theoretical means to explore the peculiar physics brought about by the measurement-induced dynamics via the newly introduced techniques and ideas.

Appendix A

Background appendices

A.1 Joint unitary in two-level ancilla protocol

In this appendix, we write down the explicit form of the joint unitaries that give the stochastic Schrödinger equation in the main text in Ch. 2.1.2.2.

We start with the quantum diffusion equation. Consider the following joint Hamiltonian of a two-level ancilla and a two-level system

$$H = \frac{1}{dt}\left[\frac{\epsilon}{2} - \left(\frac{\epsilon}{2} - \frac{\pi}{4}\right)\sigma_s^z\right]\sigma_d^y + H_s, \tag{A.1}$$

where σ_s^α represents the α Pauli matrix acting on the system, and d for Pauli matrix acting on the ancilla/detector. H_s is the system's Hamiltonian, and there is no restriction on it. $\epsilon \propto \sqrt{dt}$ is a small number, and we have chosen the strength of the system-detector Hamiltonian to scale as $1/dt$, ensuring finite time continuum contribution. The joint unitary evolution on the joint state $|\psi\rangle$ can be trotterised

$$|\psi(t+dt)\rangle = M_{s-d}e^{-idtH_s}|\psi(t)\rangle, \tag{A.2}$$

where we define

$$\begin{aligned} M_{s-d} &= \exp\left\{-i\left[\frac{\epsilon}{2}\sigma_d^y - \left(\frac{\epsilon}{2} - \frac{\pi}{4}\right)\sigma_s^z\sigma_d^y\right]\right\} \\ &= \left(\cos\frac{\epsilon}{2} - i\sigma_d^y\sin\frac{\epsilon}{2}\right)\left(\cos\left[\frac{\epsilon}{2} - \frac{\pi}{4}\right] + i\sigma_s^z\sigma_d^y\sin\left[\frac{\epsilon}{2} - \frac{\pi}{4}\right]\right). \end{aligned} \tag{A.3}$$

Initialising the ancilla in the state $|0\rangle$, a projective measurement of $\sigma_d^z = |0\rangle\langle 0| - |1\rangle\langle 1|$ on the ancilla after an infinitesimal time step can yield either $+\,(1/2)$ or $-\,(1/2)$ as the measurement outcome. The backaction of each outcome is described by the following Kraus operators

$$\begin{aligned}
\langle 0|M_{s-d}|0\rangle = \hat{K}_+ &= \sqrt{\frac{1}{2}}\left[\cos\frac{\epsilon}{2}\left(\sin\frac{\epsilon}{2}+\cos\frac{\epsilon}{2}\right)+\sigma_s^z\sin\frac{\epsilon}{2}\left(\sin\frac{\epsilon}{2}-\cos\frac{\epsilon}{2}\right)\right], \\
\langle 0|M_{s-d}|0\rangle = \hat{K}_- &= \sqrt{\frac{1}{2}}\left[\sin\frac{\epsilon}{2}\left(\sin\frac{\epsilon}{2}+\cos\frac{\epsilon}{2}\right)-\sigma_s^z\cos\frac{\epsilon}{2}\left(\sin\frac{\epsilon}{2}-\cos\frac{\epsilon}{2}\right)\right],
\end{aligned} \tag{A.4}$$

which is equivalent to Eq. (2.28) up to $\mathcal{O}(\epsilon^2)$. To proceed with multiple measurement steps and produce the quantum state diffusion equation dynamics, one resets the ancilla to the state $|0\rangle$ after each infinitesimal unitary-measurement step.

For the quantum jump, the joint unitary appears as

$$H = \frac{\epsilon}{2dt}(\sigma_s^z - 1)\sigma_d^y, \tag{A.5}$$

and the procedure to derive the Kraus operators in Eq.(2.32) follows as above by setting $\epsilon \propto \sqrt{dt}$ and trotterise the evolution.

Appendix B

Appendices for partial post-selected free fermion

B.1 PPS, shifted Gaussian and their time continuum limit

Here, we demonstrate how the time continuum is taken, giving $\delta\lambda = b\lambda$. From Eq.(4.6), the shift in mean $\delta\lambda$ of P_{r_c} has the following r_c dependence

$$\delta\lambda = \Delta\sqrt{\frac{2}{\pi}}\frac{e^{-\frac{(-r_c+\lambda\langle\hat{O}_i\rangle)^2}{2\Delta^2}}}{1+\mathrm{Erf}\left[\frac{-r_c+\lambda\langle\hat{O}_i\rangle}{\sqrt{2}\Delta}\right]}. \tag{B.1}$$

Since λ scales as $\lambda \sim \sqrt{dt}$, we ask what dt-dependence we need to assign to r_c so that $\delta\lambda \sim \sqrt{dt}$, which matches the scaling of λ in the Kraus operator. In other words, we are solving

$$\frac{e^{-(-x+a\langle\hat{O}_j\rangle\sqrt{dt})^2}}{1+\mathrm{Erf}\left[-x+a\langle\hat{O}_j\rangle\sqrt{dt}\right]} = ba\sqrt{dt}, \tag{B.2}$$

where $x = \frac{r_c(dt)}{\sqrt{2}\Delta}$, $a = \frac{\sqrt{\gamma}}{\sqrt{2}\Delta}$. This choice of parameterising $\delta\lambda$ ensures that r_c depends negligibly on $\langle\hat{O}_j\rangle$ as $dt \to 0$, which is advantageous from an experimental point of view. The dependence of r_c on dt according to Eq.(B.2) is shown in Fig. B.1(a), and

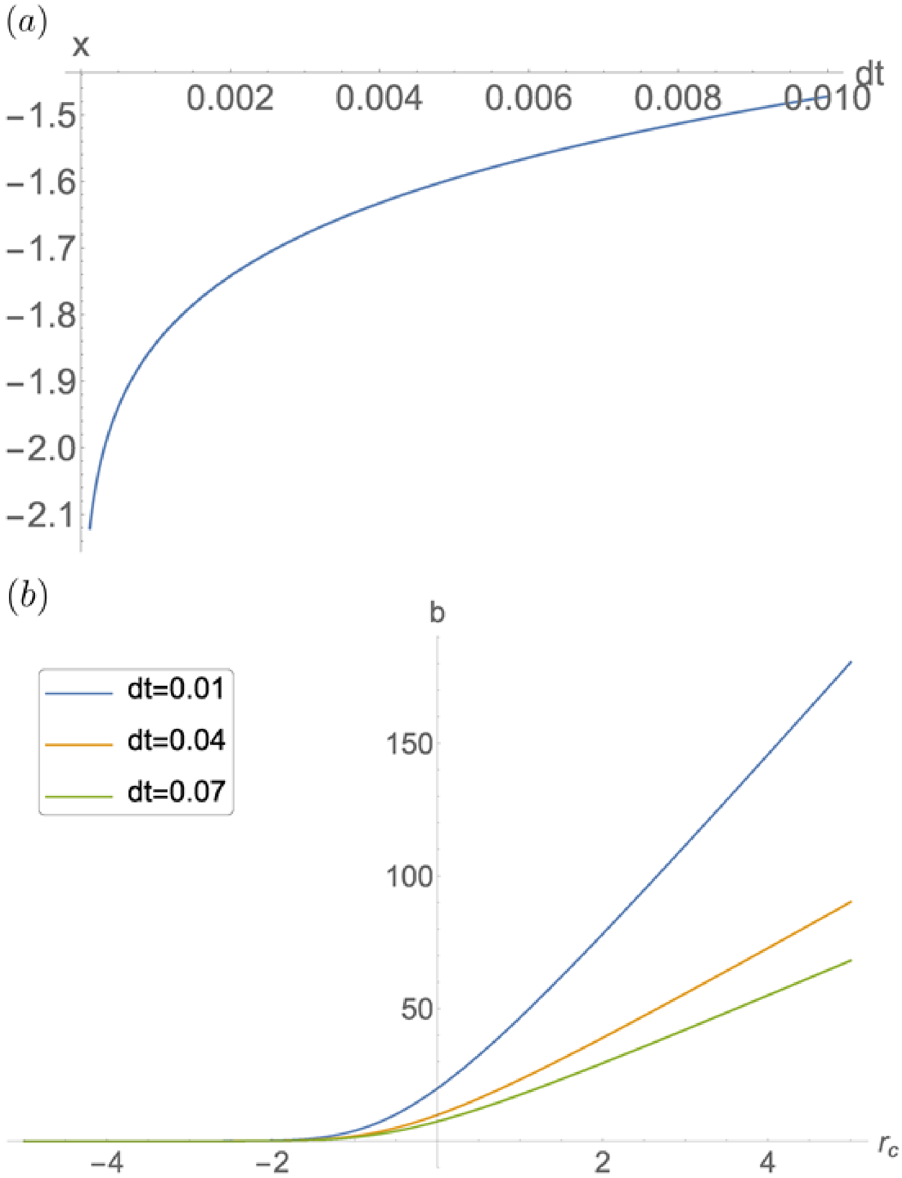

Figure B.1: (a): dependence of x, from Eq.(B.2), on dt, with $b = 1$ and $\langle \hat{O}_j \rangle = 0.1$. It can be seen that $r_c \sim x$ approaches $-\infty$ in the time continuum limit $dt \to 0$. (b): dependence of b, from Eq.(B.2), on r_c for various dt. As dt decreases, the same b corresponds to a r_c in the more negative direction.

it can be seen that $r_c \xrightarrow{dt\to 0} -\infty$. In the case of continuous measurement, γ is the parameter that captures measurement backaction in the limit $\lambda \xrightarrow{dt\to 0} 0$. Here, the time continuous PPS parameter is b. Its relation with the discrete PPS parameter r_c is given by Eq.(B.2), which is shown in Fig. B.1(b) for fixed dt. b is lower bounded by $b(r_c = -\infty) = 0$. Solving for Eq.(B.2), we arrive at Eq.(4.7).

Under this scaling, the correction to the variance scales like $\delta \sim \sqrt{dt}$. However unlike the unmodified mean λ which scales like $\lambda = \sqrt{\gamma dt}$, under this parametrization $\Delta = \mathcal{O}(dt^0)$ and hence we can safely set $\delta \to 0$.

In addition to the two-sample Kolmogorov-Smirnov test on the probability distribution in the main text, we have also verified numerically the shifted Gaussian approximation by considering a 2-qubit toy model. The toy model is described by the Hamiltonian $H = \sigma_1^+\sigma_2^- + \sigma_2^+\sigma_1^-$, and the 2 qubits are subject to measurement operators $(\mathbb{I} + (-1)^j\sigma_j^z)/2, j = 1, 2$. Firstly for fixed b in Eq.(4.7), two separate distributions of the steady state entanglement entropy is computed via 2 different ways: 1. the update of the state by the measurement operators is given by Eq.(4.2) with the probability distribution $P_{r_c}(x_j)$ given by the truncated Gaussian, 2. the update of the state is computed via Eq.(4.9). Then, the 2 distributions are compared using the Two-sample Kolmogorov-Smirnov test. This is repeated for different values of Δt, the time increment used. The results are shown in Fig. B.2.

For completeness, we also display numerically the samplings from the truncated and shifted Gaussian in Fig.(B.3), together with the associated p-values calculated. It displays statistical equivalence for $dt = 0.001$.

B.2 Continuous measurement as non-Hermitian noises and PPS on Gaussian average

The procedure we are using here is an extension to [80]. We make an explicit link to the discrete time description of continuous measurement in Eq.(4.2), and extend it to PPS. To begin with, we start from Eq.(4.2) and change some of the factors

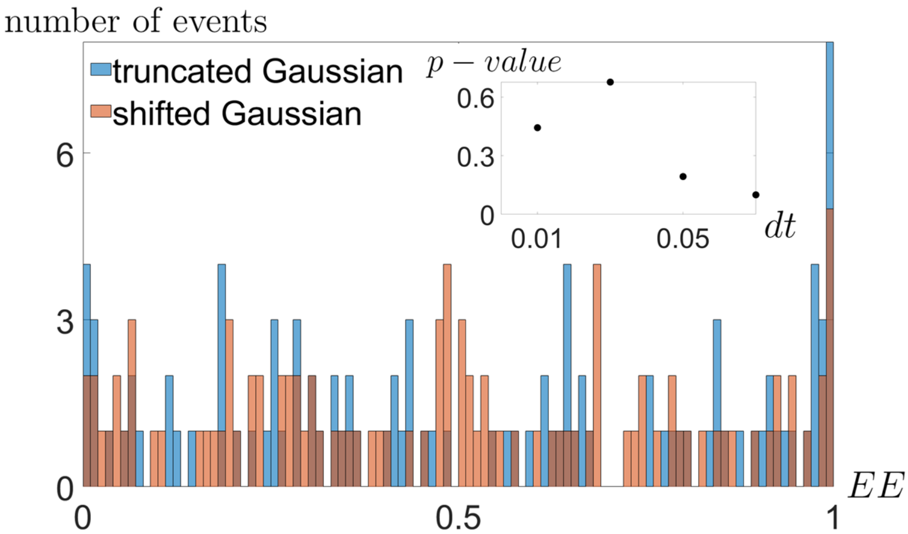

Figure B.2: Histogram of the steady state entanglement entropy distribution for various value of time increment in the numerics dt. Blue colour are data evolved using truncated Gaussian distribution at r_c, red colour uses Eq.(4.9). The parameters used for this histogram are $b = 0.2, \gamma = 0.5$ and $dt = 0.01$. The inset shows p-values calculated for various dt using the Two-sample Kolmogorov-Smirnov test, revealing an upward trend for decreasing dt implying more overlapping between the data. For the values of b and dt considered in the histogram, the null hypothesis cannot be rejected and the 2 different sets of data are statistically indistinguishable.

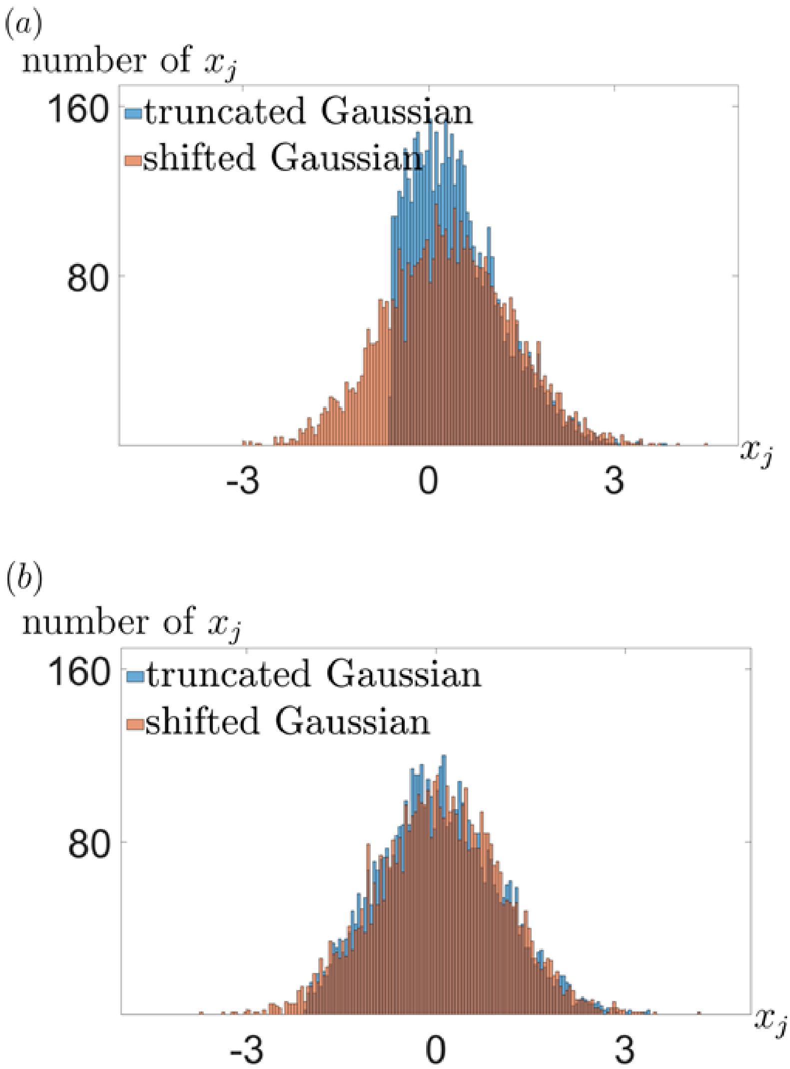

Figure B.3: Histograms of the truncated Gaussian $P_{r_c}(x_j)$ and shifted Gaussian $\underline{P}(x_j)$ in Eq.(4.6). (a): samplings drawn from the truncated Gaussian (blue) and the shifted Gaussian (red) for $dt = 0.05$ and the null hypothesis is rejected at a significance level of 0.05. The p-value from KS2 sample test is 0.00. (b): similar to (a) but samples generated with $dt = 0.001$. The p-value is 0.31 and the null hypothesis cannot be rejected, indicating the distribution is statistically indistinguishable. The values of the parameters used here are $\langle O_j \rangle = 1, b = 1$ and $\gamma = 0.5$ and we used 5000 samplings of the distributions.

slightly for later convenience:

$$\hat{k}_j(x,\lambda) = \mathcal{N}_j \exp\left(-\frac{(x-2\lambda\hat{O}_j)^2}{4\Delta^2}\right),$$
$$\hat{k}_j(x,\lambda)|\psi_t\rangle = \tilde{\mathcal{N}}_j \exp\left(-\frac{x^2}{4\Delta^2}\right)\exp\left(\frac{\lambda\hat{O}_j x}{\Delta^2}\right)|\psi_t\rangle. \tag{B.3}$$

An initial normalised density matrix ρ_0 is updated as

$$\frac{\hat{k}_j(x,\lambda)\rho_0\hat{k}_j^\dagger(x,\lambda)}{\mathrm{Tr}\left[\hat{k}_j(x,\lambda)\rho_0\hat{k}_j^\dagger(x,\lambda)\right]} = \frac{\check{\rho}_{x,\lambda}}{\mathrm{Tr}\left[\check{\rho}_{x,\lambda}\right]}. \tag{B.4}$$

The average density matrix $\overline{\rho}$ across all measurement outcomes at a particular time step is

$$\begin{aligned}\overline{\rho} &= \int_{-\infty}^{\infty} dx \frac{\check{\rho}_{x,\lambda}}{\mathrm{Tr}\left[\check{\rho}_{x,\lambda}\right]} P(x,\lambda)\\ &= \int_{-\infty}^{\infty} dx \hat{k}_j(x,\lambda)\rho_0\hat{k}_j^\dagger(x,\lambda)\\ &= \tilde{\mathcal{N}}_j^2 \int_{-\infty}^{\infty} dx \exp\left(-\frac{x^2}{2\Delta^2}\right)\exp\left(\frac{x\lambda\hat{O}_j}{\Delta^2}\right)\rho_0 \exp\left(\frac{x\lambda\hat{O}_j}{\Delta^2}\right),\end{aligned} \tag{B.5}$$

which implies

$$\int_{-\infty}^{\infty} dx \hat{k}_j^\dagger(x,\lambda)\hat{k}_j(x,\lambda) = \mathbb{I}$$
$$\tilde{\mathcal{N}}_j^2 \int_{-\infty}^{\infty} dx \exp\left(-\frac{x^2}{2\Delta^2}\right)\exp\left(\frac{x2\lambda\hat{O}_j}{\Delta^2}\right) = \mathbb{I}. \tag{B.6}$$

Rewriting

$$\Delta^2 = \Delta'^2\lambda/\delta t, x = M_j\Delta'^2 \text{and } \gamma = \lambda/\Delta'^2 = \lambda^2/\Delta^2\delta t, \tag{B.7}$$

Eq.(B.6) becomes

$$\tilde{\mathcal{N}}_j^2 \int_{-\infty}^{\infty} dM_j \exp\left(-\frac{M_j^2\delta t}{2\gamma}\right)\exp\left(2M_j\hat{O}_j\delta t\right) = \mathbb{I}, \tag{B.8}$$

and one can deduce that the Kraus operators are alternatively given by

$$\bar{\hat{k}}(M_j) = \exp\left(M_j\hat{O}_j\delta t\right), \tag{B.9}$$

normalised over the Gaussian measure $d\mu(M_j) \propto dM_j \exp\left(-\frac{M_j^2 \delta t}{2\gamma}\right)$

$$\int_{-\infty}^{\infty} d\mu(M_j) \bar{\hat{k}}^\dagger(M_j) \bar{\hat{k}}(M_j) = \mathbb{I}. \tag{B.10}$$

Equation(B.10) describes a Gaussian random variable M_j with mean $\mathbb{E}_G[M_j] = 0$ and variance $\mathbb{E}_G[M_j^2] = \gamma/\delta t$.

The readout of a continuous measurement is now represented by the variable M_j, and its backaction on the system is given by the Kraus operator in (B.9). To generalise it to a time process, we first give $M_j(t_l)$ a time index $t_l = l\delta t$. Then, an initial density matrix ρ_0 evolves from time $t_0 = 0$ to $t_N = T = N\delta t$ as

$$\check{\rho}_{\{M\}}(T) = \prod_{l=1}^{l=N} \bar{\hat{k}}(M_j(t_l))\rho(0)\bar{\hat{k}}^\dagger(M_j(t_l)), \tag{B.11}$$

where $\{M\}$ labels the quantum trajectory, and with a slight abuse of notation, we abbreviate it as M. In the time continuum limit, (B.11) becomes

$$\begin{aligned} &\check{\rho}_M = K(t)\rho(0)K^\dagger(t), \\ &K(t) = \exp\left[-i\int_0^T dt' H(t')\right] = \exp\left[-i\int_0^T dt' i M_j(t')\hat{O}_j\right], \end{aligned} \tag{B.12}$$

and $\mathbb{E}_G[M_j(t)] = 0$, $\mathbb{E}_G[M_j(t)M_j(t')] = \gamma\delta(t-t')$. From (B.12), we observe that the overall effect of a continuous measurement generates a random non-Hermitian Hamiltonian $H(t) = iM_j(t)\hat{O}_j$ in time. Generalisation to multiple measurements $j = 1 \ldots L$ and inclusion of another competing measurement set follows the same line: each process is independent of the others. We arrive at (4.29) in the main text.

In the case of PPS, we saw, in Appendix B.1, that PPS shifts the mean of the random variable x by $b\lambda$. We can interpret this as a shift in the mean of the measure. Using the relationship Eq.(B.7)

$$d\mu(M_j) \xrightarrow{PPS} dx \exp\left(-\frac{(x-b\lambda)^2}{2\Delta^2}\right) \propto dM_j \exp\left(-\frac{(M_j - b\gamma)^2\delta t}{2\gamma}\right), \tag{B.13}$$

we arrive at the final line where the mean of the Gaussian average is shifted $\mathbb{E}_G[M_j] = b\gamma = B$, as required from PPS. The generalisation to include multiple continuous measurements and the system's (random) unitary is straightforward, with different measurements corresponding to different non-Hermitian noises and taking the time continuum limit gives Eq.(4.17) (since noises from different measurements and white noises are independent from each other, cross product between different noise vanishes in time continuum limit).

B.3 operator-state correspondence and replica majorana Hamiltonian

In this appendix and below, we distinguish the ket or bra space in the Choi–Jamiołkowski isomorphism by $\sigma = \pm$ instead of $\uparrow$ and $\downarrow$ as used in the main text.

The Choi–Jamiołkowski isomorphism maps an operator to a duplicated Hilbert space:

$$\hat{O} = \sum_{i,j} O_{i,j} |i\rangle\langle j| \xrightarrow{Choi} \sum_{i,j} O_{i,j} |i\rangle \otimes |j\rangle = |\hat{O}\rangle. \tag{B.14}$$

Under the Choi–Jamiołkowski isomorphism, the trace operation between 2 operators becomes a transition amplitude:

$$\mathrm{Tr}[\hat{A}^\dagger \hat{B}] \xrightarrow{Choi} \langle \hat{A} | \hat{B} \rangle, \tag{B.15}$$

hence leading to, for example, Eq.(4.20). When dealing with a density matrix ρ, the action of an operator on the density matrix becomes an action on the Choi state:

$$\begin{aligned} \hat{A}\rho = \sum_{i,j,k} A_{i,j}\rho_{j,k} |i\rangle\langle k| &\xrightarrow{Choi} \sum_{i,j,k} A_{i,j}\rho_{j,k} |i\rangle|k\rangle = \hat{A} \otimes \mathbb{I}|\rho\rangle, \\ \rho\hat{A} \xrightarrow{Choi} \mathbb{I} \otimes \hat{A}^T |\rho\rangle, \qquad & \hat{B}\rho\hat{A} \xrightarrow{Choi} \hat{B} \otimes \hat{A}^T |\rho\rangle, \end{aligned} \tag{B.16}$$

and hence Eq.(4.18) is obtained. Writing out explicitly the average dynamics of the

n-replica described by Eq.(4.19):

$$\mathbb{E}_G^{(PPS)}[\big(K(t)\otimes K^*(t)\big)^{\otimes n}]|\rho^{(n)}(0)\rangle\rangle = \mathbb{E}_G^{(PPS)}\left[\exp\left(-i\int_0^t H_n(t')dt'\right)\right]|\rho^{(n)}(0)\rangle\rangle,$$

$$\text{where } H_n(t') = \sum_{\substack{\sigma=\pm\\ a=1\dots n}}\sum_j \left[J_j(t') + i\sigma M_j(t')\right] i\chi_j^{(\sigma a)}\chi_{j+1}^{(\sigma a)}. \tag{B.17}$$

σ distinguishes the ket/bra space, with a indexing the replica space: $\chi_j^{(\downarrow a)} = \mathbb{I}^{\otimes 2a+1}\otimes \chi_j^*\otimes\mathbb{I}^{\otimes 2a}$, $\chi_j^{(\uparrow a)} = \mathbb{I}^{\otimes 2a}\otimes\chi_j\otimes\mathbb{I}^{\otimes 2a+1}$. Up to this point, the Majorana operator $\chi_j^{(\sigma a)}$ is not well defined as it anti-commutes within the same branch and replica, while commuting with those in different branches or replicas. To resolve this, one should first map the fermionic Hilbert space to a spin-1/2 Hilbert space and then define new Majorana operators. The new operators differ from the one in Eq.(B.17) by a Klein factor, which is essentially a Pauli string in the replica space [80]. More precisely, let us first define a Pauli string across a single replica (for simplicity, we implicitly assume L to be a multiple of 4):

$$F^{(\sigma a)} = \prod_{j=1}^{j=L}\chi_j^{(\sigma a)}, \tag{B.18}$$

which is equivalent to the total parity of replica σa. Then, the following anti-commuting real fermionic operator can be constructed:

$$\begin{aligned}\chi_j'^{(\uparrow a)} &= \prod_{a'=1}^{a'<a}\left[F^{(\uparrow a')}F^{(\downarrow a')}\right]\chi_j^{(\uparrow a)},\\ \chi_j'^{(\downarrow a)} &= \prod_{a'=1}^{a'<a}\left[F^{(\uparrow a')}F^{(\downarrow a')}\right]F^{(\uparrow a)}\chi_j^{(\downarrow a)},\end{aligned} \tag{B.19}$$

with an additional Klein factor, $\hat{\mathrm{N}}(sa)$ in the main text. It can be checked that these newly defined Majorana operators anti-commute in the duplicated replica Hilbert space i.e. $\{\chi_j'^{(\sigma a)}, \chi_l'^{(\sigma' a')}\} = \delta_{j,l}\delta_{\sigma,\sigma'}\delta_{a,a'}$. Moreover, bilinear products of the form $\chi_j^{(\sigma a)}\chi_{j+1}^{(\sigma a)}$ is unchanged: $\chi_j^{(\sigma a)}\chi_{j+1}^{(\sigma a)} = \chi_j'^{(\sigma a)}\chi_{j+1}'^{(\sigma a)}$. To lighten the notation, we simply denote these proper replica Majorana operators as $\chi_j^{(\sigma a)}$, as we make no use of the original ill-behaved Majorana operators.

To evaluate Eq.(B.17), we expand it using the cumulant expansion up to 2nd order $\langle e^A\rangle \approx \exp\big[\langle A\rangle + 1/2(\langle A^2\rangle - \langle A\rangle^2)\big]$ and note that Gaussian measure is now centred at $(1-\zeta_j)$. With a slight abuse of notation, denoting the new anti-commuting Majorana as $\chi_j^{\prime(\sigma a)} \to \chi_j^{(\sigma a)}$ leads to Eq.(4.33) for $n=2$.

Finally, the boundary state $|\mathcal{C}_{2,\mathbf{A}}\rangle\rangle, |\mathbb{I}\rangle\rangle$ has the following properties with the Pauli matrices in the replica space $\sigma_{\alpha,j}^{(a)}$, $\alpha = x,y,z$ $a = 1,2$ [80]:

$$
\begin{aligned}
\sigma_{\alpha,j}^{(a)}\mathbb{I}\sigma_{\alpha,j}^{(a)} = \mathbb{I} &\xrightarrow{Choi} i\chi_j^{(+a)}\chi_j^{(-a)}|\mathbb{I}\rangle\rangle = |\mathbb{I}\rangle\rangle,\\
\sigma_{\alpha,j}^{(a)}\mathcal{C}_{2,\mathbf{A}}\sigma_{\alpha,j}^{(a)} = \mathcal{C}_{2,\mathbf{A}} &\xrightarrow{Choi} i\chi_j^{(+a)}\chi_j^{(-a)}|\mathcal{C}_{2,\mathbf{A}}\rangle\rangle = |\mathcal{C}_{2,\mathbf{A}}\rangle\rangle,\ j\notin\mathbf{A},\\
\sigma_{\alpha,j}^{(2)}\mathcal{C}_{2,\mathbf{A}}\sigma_{\alpha,j}^{(1)} = \mathcal{C}_{2,\mathbf{A}} &\xrightarrow{Choi} -i\chi_j^{(+2)}\chi_j^{(-1)}|\mathcal{C}_{2,\mathbf{A}}\rangle\rangle = |\mathcal{C}_{2,\mathbf{A}}\rangle\rangle,\ j\in\mathbf{A},\\
\sigma_{\alpha,j}^{(1)}\mathcal{C}_{2,\mathbf{A}}\sigma_{\alpha,j}^{(2)} = \mathcal{C}_{2,\mathbf{A}} &\xrightarrow{Choi} i\chi_j^{(+1)}\chi_j^{(-2)}|\mathcal{C}_{2,\mathbf{A}}\rangle\rangle = |\mathcal{C}_{2,\mathbf{A}}\rangle\rangle,\ j\in\mathbf{A}.
\end{aligned}
\tag{B.20}
$$

B.4 Solution for the 2-replica monitored case

Recall that the effective Hamiltonian without PPS reads

$$
\mathcal{H} = \frac{1}{2}\sum_j J^2\Big(\sum_{\substack{\sigma=\pm\\ a=1,2}} i\chi_j^{(\sigma a)}\chi_{j+1}^{(\sigma a)}\Big)^2 - \gamma_j\Big(\sum_{\substack{\sigma=\pm\\ a=1,2}} \sigma i\chi_j^{(\sigma a)}\chi_{j+1}^{(\sigma a)}\Big)^2. \tag{B.21}
$$

One can write it entirely as local SO(4) generators defined using Majorana operators:

$$
S_j^{\alpha,\beta} = \frac{i}{2}\Big[\chi_j^{\alpha}, \chi_j^{\beta}\Big], \tag{B.22}
$$

and for generic J^2, γ, only a subset of Eq.(B.22) commutes with $\mathcal{H}$ [80, 225]. An important set of local symmetries, which will become clear, are associated with the local on-site parity operators $\mathcal{R}_j = \prod_a i\gamma^{(+a)}\gamma^{(-a)}$ satisfying $\big[\mathcal{R}_j, \mathcal{H}\big] = 0$.

One can readily define the following spin-1/2 operators:

$$
\Sigma^{\mu} = \frac{1}{2}\underline{\mathbf{c}}_j^{\dagger}\sigma_{\mu}\underline{\mathbf{c}}_j, \tag{B.23}
$$

where σ_α , $\alpha = x, y, z$ are the usual Pauli matrices and $\underline{\mathbf{c}}_j = (c_{j,\uparrow}, c_{j,\downarrow})^T$. The other spin-1/2 generators are associated with the η spin in the Hubbard model, generated via the Shiba transformation [243, 273].

$$\eta^z_j = \frac{1}{2}\left(c^\dagger_{j,\uparrow}c_{j,\uparrow} + c^\dagger_{j,\downarrow}c_{j,\downarrow} - 1\right) \ , \ \eta^+_j = c^\dagger_{j,\uparrow}c^\dagger_{j,\downarrow}. \tag{B.24}$$

The two species of SU(2) generators Eq.(B.24) stem from the fact that SO(4)$\cong$ [SU(2)$\times$SU(2)]/$\mathbb{Z}_2$. The quotient by $\mathbb{Z}_2$ comes from the criterion that

$$\sum_j \left[\eta^z_j + \Sigma^z_j\right] = \sum_j c^\dagger_{j,\uparrow}c_{j,\uparrow} - \frac{L}{2} \ \in \mathbb{Z}, \tag{B.25}$$

and η^z_j, Σ^z_j can either be both integer or both half-integer (assuming L is even). Recalling that the local parity operator $\mathcal{R}_j = \pm 1$ commutes with $\mathcal{H}$, and constructing the projector $\Pi_{j,+} = \frac{1}{2}\left(1 + \mathcal{R}_j\right)$ we observe that

$$\Pi_{j,+}\Sigma^\mu_j\Pi_{j,+} = 0 \ , \text{ while } \ \Pi_{j,+}\eta^\mu_j\Pi_{j,+} = \eta^\mu_j. \tag{B.26}$$

Hence, the two different SU(2) Σ^μ, η^μ act on the $\mathcal{R}_j = \mp 1$ sector respectively. The choice of the initial state $|\rho(0)\rangle\rangle = |\mathbb{I}\rangle\rangle, \mathcal{R}_j|\mathbb{I}\rangle\rangle = +1|\mathbb{I}\rangle\rangle$ fixes the sector, and it should match the boundary state local parity sector. To complete the proof that η^μ (and hence Σ^μ) are spin-1/2 operators, we demonstrate that the total spin operator has eigenvalue:

$$\eta^{x2}_j + \eta^{y2}_j + \eta^{x2}_j|\mathbb{I}\rangle\rangle = \frac{4}{3}|\mathbb{I}\rangle\rangle = S(1+S)|\mathbb{I}\rangle\rangle, \tag{B.27}$$

where $S = 1/2$.

The SO(4) generators in Eq.(B.22) can be expressed in term of these two SU(2) generators i.e. $S^{(+1),(+2)} = 2(\Sigma^z + \eta^z)$. Writing Eq.(B.21) in terms of Eq.(B.24) and Eq.(B.23), we arrive at (4.39) and the physics can readily be extracted via usual means, i.e. Bethe Ansatz and bosonisation.

B.5 effective spin Hamiltonian and bosonisation details

As mentioned in the main text, there are two conserved charges $\left[\sum_j \gamma_j^{(\sigma 1)}\gamma_j^{(\sigma 2)}, \mathcal{H}\right]$, which suggest the following two complex fermions:

$$c^\dagger_{j,\uparrow} = \frac{\gamma_j^{(+1)} + i\gamma_j^{(+2)}}{2}\ ,\ c^\dagger_{j,\downarrow} = \frac{\gamma_j^{(-1)} - i\gamma_j^{(-2)}}{2}. \tag{B.28}$$

Written in terms of the complex fermions, it becomes $[\mathcal{H}, N_\sigma] = 0$, $N_\sigma = \sum_j c^\dagger_{j,\sigma}c_{j,\sigma}$, $\sigma =\uparrow,\downarrow$. These two conserved $U(1)$ charges will be the basis for abelian bosonisation later. Inserting this relationship and introducing the unitary transformation $c^\dagger_{j,\uparrow} \to (i)^j c^\dagger_{j,\uparrow}$, $c^\dagger_{j,\downarrow} \to (-i)^j c^\dagger_{j,\downarrow}$, the Majorana operators are transformed as:

$$\begin{aligned}
-i(\gamma_j^{(+1)}\gamma_{j+1}^{(+1)} + \gamma_j^{(+2)}\gamma_{j+1}^{(+2)}) &\to -2(c^\dagger_{j,\uparrow}c_{j+1,\uparrow} + c^\dagger_{j+1,\uparrow}c_{j,\uparrow}),\\
i(\gamma_j^{(-1)}\gamma_{j+1}^{(-1)} + \gamma_j^{(-2)}\gamma_{j+1}^{(-2)}) &\to -2(c^\dagger_{j,\downarrow}c_{j+1,\downarrow} + c^\dagger_{j+1,\downarrow}c_{j,\downarrow}).
\end{aligned} \tag{B.29}$$

Inserting these into Eq.(4.33), we arrive at Eq.(4.36).

We now proceed to bosonise Eq.(4.36) w.r.t. the basis $\sigma =\uparrow,\downarrow$. We first compute terms corresponding to no dimerisation, i.e. $\mathcal{O}(\Delta^0)$ terms. H_0, the kinetic part, gives the usual free Luttinger liquid Hamiltonian with $K = 1$:

$$H_0 = \frac{v_F}{2\pi}\sum_{\sigma=\uparrow,\downarrow}\int_x (\partial_x\theta_\sigma)^2 + (\partial_x\phi_\sigma)^2. \tag{B.30}$$

With bosonisation, we can investigate the strong PPS limit where $J^2, \gamma \ll B$. This is the limit at which the excitation is small compare to the Fermi energy and bosonisation remains valid. As bosonising a lattice model will inevitably generate term whose appearance depends directly on the filling fraction, the filling fraction is determined by utilising the properties in Eq.(B.20). This gives

$$\begin{aligned}\langle\langle\mathbb{I}|i\chi_j^{(+1)}\chi_j^{(-2)}|\mathbb{I}\rangle\rangle &= 0,\\ \langle\langle\mathbb{I}|-\chi_j^{(+1)}\chi_j^{(+2)}|\mathbb{I}\rangle\rangle &= 0,\\ \langle\langle\mathbb{I}|(c_{j,\uparrow}^\dagger + c_{j,\uparrow})(c_{j,\uparrow}^\dagger - c_{j,\uparrow})|\mathbb{I}\rangle\rangle &= 0,\\ \langle\langle\mathbb{I}|1-2c_{j,\uparrow}^\dagger c_{j,\uparrow})|\mathbb{I}\rangle\rangle &= 0.\end{aligned} \tag{B.31}$$

Similar results are obtained for $c_{j,\downarrow}^\dagger$ and the boundary state $|\mathcal{C}_{2,\mathbf{A}}\rangle\rangle$. Therefore, this specifies that we are dealing with half filling $k_F = \pi/2$ and terms that oscillate like e^{4ik_Fx} should be kept.

The term H_{umk} in Eq.(4.36) becomes

$$\begin{aligned}H_{umk} \propto \sum_{\substack{\sigma=\uparrow,\downarrow\\ j}} (c_{j,\sigma}^\dagger c_{j+1,\sigma} + c_{j+1,\sigma}^\dagger c_{j,\sigma})^2 &= -2\sum_{\substack{\sigma=\uparrow,\downarrow\\ j}} (c_{j,\sigma}^\dagger c_{j,\sigma} - \frac{1}{2})(c_{j+1,\sigma}^\dagger c_{j+1,\sigma} - \frac{1}{2})\\ \approx -2a\sum_{\sigma=\uparrow,\downarrow}\int_x \frac{2}{\pi^2}(\partial_x\phi_\sigma)^2 - \frac{2}{(2\pi\alpha)^2}cos4\phi_\sigma,\end{aligned} \tag{B.32}$$

while H_m gives

$$\begin{aligned}H_m \propto &\sum_j (c_{j,\uparrow}^\dagger c_{j+1,\uparrow} + h.c.)(c_{j,\downarrow}^\dagger c_{j+1,\downarrow} + h.c.)\\ \approx &a\int_x \left[\frac{4}{2\pi}\nabla\phi_\uparrow + \frac{e^{2ik_Fx}}{2\pi\alpha}2ie^{-i2\phi_\uparrow(x)} - \frac{e^{-2ik_Fx}}{2\pi\alpha}2ie^{i2\phi_\uparrow(x)}\right] \times \left[\uparrow\to\downarrow\right]\\ = &a\int_x \frac{4}{\pi^2}\nabla\phi_\uparrow\nabla\phi_\downarrow + \frac{8}{(2\pi\alpha)^2}cos[2(\phi_\uparrow - \phi_\downarrow)] - \frac{8}{(2\pi\alpha)^2}cos[2(\phi_\uparrow + \phi_\downarrow)].\end{aligned} \tag{B.33}$$

The $\cos 4\phi_\sigma$ term is highly irrelevant under RG compared to the cosines from Eq.(B.33) and therefore can be discarded without much concern.

We now move on to terms coming from dimerisation $\mathcal{O}(\Delta^1)$. This amounts to looking for e^{2ik_Fx} components from bosonisation as $(-1)^j = e^{2ik_Fx}$. Bosonising H_0 gives the following term

$$-2(1-\zeta)\Delta\sum_{\substack{j\\ \eta=\uparrow,\downarrow}}(-1)^j(c_{j+1,\eta}^\dagger c_{j,\eta} + h.c.) \approx \frac{16a(1-\zeta)\Delta\pi}{(2\pi\alpha)^2}\sum_{\eta=\uparrow,\downarrow}\int_x \sin 2\phi_\eta, \tag{B.34}$$

which is highly relevant. H_{umk} requires some attention, and bosonisation should be treated carefully within fermion normal ordering $:\psi(x)_R\psi^\dagger(x')_R := \left[2\pi(x-x')\right]^{-1}$, $:\psi(x)_L\psi^\dagger(x')_L := -\left[2\pi(x-x')\right]^{-1}$ [274]. In the end, this procedure gives H_{umk} the following term

$$-4\zeta\Delta \sum_{\substack{j\\ \eta=\uparrow,\downarrow}} (-1)^j (c^\dagger_{j,\eta}c_{j,\eta} - \frac{1}{2})(c^\dagger_{j+1,\eta}c_{j+1,\eta} - \frac{1}{2}) = \frac{-16a\zeta\Delta}{(2\pi\alpha)^2} \sum_{\eta=\uparrow,\downarrow} \int_x \sin 2\phi_\eta(x), \tag{B.35}$$

and a less relevant operator $(\partial_x\phi)^2 sin2\phi$ have been discarded. For H_m, the $2k_F$ component gives terms $\nabla\phi_\uparrow cos2\phi_\downarrow + \nabla\phi_\downarrow cos2\phi_\uparrow$ which are irrelevant in the current model: By power counting, it can be seen that its dimension is $1 + \frac{K_\rho + K_\sigma}{2}$. Since $K_\rho, K_\sigma \geq 1$ from Eq.(4.43), this term is simply irrelevant in the current setting.

Inserting these results, and performing a unitary rotation to the charge and spin degree of freedom $\phi_\rho = \frac{\phi_\uparrow+\phi_\downarrow}{\sqrt{2}}$, $\phi_\sigma = \frac{\phi_\uparrow-\phi_\downarrow}{\sqrt{2}}$, we arrive at Eq.(4.42).

B.6 Boundary state $|\mathcal{C}_{2,A}\rangle\rangle$

In this appendix, we discuss the state $|\mathcal{C}_{2,\mathbf{A}}\rangle\rangle$ (the fundamental object in the computation of $S^{(cond)}_{2,\mathbf{A}}$) and its expression in various bases. Our discussion is an extension to Ref. [225], which we contain here for self-consistency. For simplicity, we assume the region $\mathbf{A}$ to be continuous.

To begin with, we note that $|\mathcal{C}_{2,\mathbf{A}}\rangle\rangle$ belongs to the half-filling sector (cf appendix B.5), and there should exist some rotation between the two. More precisely, consider the identity operator before the Choi–Jamiolkowski isomorphism. In fermionic occupation basis, it can be expressed as:

$$\mathbb{I} = \frac{1}{2^{L/2}} \sum_{\vec{n}_1} |\vec{n}_1\rangle\langle\vec{n}_1|, \tag{B.36}$$

where $\vec{n}_p$ is a string of length $L/2$, consisting of either 0 or 1 i.e. $\{0 \text{ or } 1\}^{\otimes L/2}$. $|\vec{n}_1\rangle$ can also be expressed as $\prod_{j=1}^{j=L/2}(f^\dagger_j)^{n_{1,j}}|\text{vac}\rangle$, where $f^\dagger_j$ is a complex fermionic creation operator at site j, which can readily be defined from the Majorana operator in the model (cf Eq.(4.29)). In the duplicated 2-replica Hilbert space $\mathcal{H}\otimes\mathcal{H}^*\otimes\mathcal{H}\otimes\mathcal{H}^*$, the identity operator is mapped to a state $|\mathbb{I}\rangle\rangle$ which appears as:

$$\begin{aligned}
|\mathbb{I}\rangle\rangle &= \frac{1}{2^L}\sum_{\vec{n}_1,\vec{n}_2}|\vec{n}_1,\vec{n}_1\rangle\rangle\otimes|\vec{n}_2,\vec{n}_2\rangle\rangle \\
&= \frac{1}{2^L}\sum_{\vec{n}_1,\vec{n}_2}\prod_j(f_j^{\dagger(\uparrow 1)})^{n_{1,j}}\prod_j(f^{\dagger(\downarrow 1)})^{n_{1,j}}\prod_j(f^{\dagger(\uparrow 2)})^{n_{2,j}}\prod_j(f^{\dagger(\downarrow 2)})^{n_{2,j}}|\text{vac}\rangle\rangle \\
&= \frac{1}{2^L}\sum_{\vec{n}_1,\vec{n}_2}g(|\vec{n}_1|,|\vec{n}_2|)\prod_j(f_j^{\dagger(\uparrow 1)})^{n_{1,j}}(f^{\dagger(\downarrow 1)})^{n_{1,j}}(f^{\dagger(\uparrow 2)})^{n_{2,j}}(f^{\dagger(\downarrow 2)})^{n_{2,j}}|\text{vac}\rangle\rangle,
\end{aligned} \tag{B.37}$$

where

$$g(|\vec{n}_1|,|\vec{n}_2|) = (-1)^{\frac{|\vec{n}_1|}{2}(|\vec{n}_1|-1)+\frac{|\vec{n}_2|}{2}(|\vec{n}_2|-1)}, \text{ and } f_j^{\dagger(\sigma a)} = \frac{\chi_{2j-1}^{(\sigma a)}+i\chi_{2j}^{(\sigma a)}}{2}. \tag{B.38}$$

$g(|\vec{n}_1|,|\vec{n}_2|)$ is a factor accounting for the transformation from the replica-local basis (line 2) to site-local basis (line 3). Under the Choi–Jamiolkowski isomorphism mapping, the operator $\mathcal{C}_{2,\mathbf{A}}$ (cf Eq.(2.78)) is mapped to

$$\begin{aligned}
|\mathcal{C}_{2,\mathbf{A}}\rangle\rangle &= \frac{1}{2^L}\sum_{\vec{n}_1,\vec{n}_2}|\vec{n}_1\rangle\rangle|\vec{n}_{2,\mathbf{A}},\vec{n}_{1\overline{\mathbf{A}}}\rangle\rangle\otimes|\vec{n}_2\rangle\rangle|\vec{n}_{1\mathbf{A}},\vec{n}_{2\overline{\mathbf{A}}}\rangle\rangle \\
&= \frac{1}{2^L}\sum_{\vec{n_1},\vec{n_2}}g(|\vec{n_1}|,|\vec{n_2}|)\bigotimes_{j\in\mathbf{A}}|n_{1,j},n_{2,j}\rangle\rangle\otimes|n_{2,j},n_{1,j}\rangle\rangle\bigotimes_{j\in\overline{\mathbf{A}}}|n_{1,j},n_{1,j}\rangle\rangle\otimes|n_{2,j},n_{2,j}\rangle\rangle \\
&= \prod_{j\in\mathbf{A}}\hat{\mathcal{C}}_{2,j}|\mathbb{I}\rangle\rangle,
\end{aligned} \tag{B.39}$$

where $\vec{n}_{l,\mathbf{A}}$ denotes the string of $\vec{n}_l$ in region $\mathbf{A}$ (similarly for its compliment $\overline{\mathbf{A}}$). Expressed in site-local basis, one observes that $|\mathcal{C}_{2,\mathbf{A}}\rangle\rangle$ is merely a rotation on $|\mathbb{I}\rangle\rangle$ which can be implemented by a site-local operator

$$\hat{\mathcal{C}}_{2,j} = f_j^{\dagger(\downarrow 1)}f^{(\downarrow 2)} + f_j^{(\downarrow 1)}f_j^{\dagger(\downarrow 2)} + \frac{1}{2}(1+\Pi_{j,\downarrow 1}\Pi_{j,\downarrow 2}), \tag{B.40}$$

where $\Pi_{j,\sigma a} = 1-2f_j^{\dagger(\sigma a)}f_j^{(\sigma a)}$. Utilising

$$\begin{aligned}
\sum_{l=0,1}\left(c^\dagger_{2j+l,\downarrow}c_{2j+l,\downarrow}-\frac{1}{2}\right) &= i(f_j^{\dagger(\downarrow 1)}f_j^{(\downarrow 2)}+f_j^{(\downarrow 1)}f_j^{\dagger(\downarrow 2)}), \\
-\left[\sum_{l=0,1}\left(c^\dagger_{2j+l,\downarrow}c_{2j+l,\downarrow}-\frac{1}{2}\right)\right]^2 &= \frac{1}{2}(1+\Pi_{j,\downarrow 1}\Pi_{j,\downarrow 2})-1,
\end{aligned} \tag{B.41}$$

and after some manipulation, we arrive at (cf Eq.(4.37))

$$\begin{aligned} \hat{\mathcal{C}}_{2,j} &= e^{-i\frac{\pi}{2}\sum_{l=0,1}\left(c^\dagger_{2j+l,\downarrow}c_{2j+l,\downarrow}-\frac{1}{2}\right)}, \\ \prod_j \hat{\mathcal{C}}_{2,j} &= \exp\left[-i\frac{\pi}{2}\sum_{m=m_l}^{m=m_r}\left(c^\dagger_{m,\downarrow}c_{m,\downarrow}-\frac{1}{2}\right)\right]. \end{aligned} \tag{B.42}$$

In the last line, we denote the left (right) boundary of region **A** by $m = m_l$ ($m = m_r$). Note that there are $2L$ c-fermions and L f-fermions. Eq.(B.42) can readily be bosonised by keeping only the slowest oscillating terms and note that we are at half-filling (cf Eq.(B.31)). This leads to [182]

$$\begin{aligned} c^\dagger_{m,\downarrow}c_{m,\downarrow} &\approx -\frac{1}{\pi}\partial_x\phi_\downarrow(x_m)+\rho_0, \\ \prod_j \hat{\mathcal{C}}_{2,j} &\approx \exp\left[i\frac{1}{2}\left(\phi_\downarrow(x_r)-\phi_\downarrow(x_l)\right)\right], \end{aligned} \tag{B.43}$$

and Eq.(4.48) follows. To justify the replacement of the state $|\mathbb{I}\rangle\rangle$ by the ground state of $\mathcal{H}$, $|\mathrm{GS}\rangle\rangle$, we note that both the state $|\mathbb{I}\rangle\rangle$ and $|\mathrm{GS}\rangle\rangle$ belongs to the half-filling sector and therefore their overlap is finite. The state $|\mathbb{I}\rangle\rangle$ is $U(1)$ symmetry breaking in both $\uparrow$ and $\downarrow$ sector [225]. This amounts to picking out a θ field configuration in both sector in the bosonised language, while leaving the ϕ configuration unaffected. Since we are interested in the computation of the ϕ field correlation, such replacement only amounts to an unimportant constant proportional to the overlap $\langle\langle\mathbb{I}|\mathrm{GS}\rangle\rangle$, which is subsystem size independent. This concludes the prove of Eq.(4.48).

B.7 RG flow for Sine-Gordon Hamiltonian

The procedure here is a real space renormalisation group procedure that follows closely with Ref. [182, 245]. We will also demonstrate explicitly that the umklapp term H_{umk} in Eq.(4.36) is way less relevant. The form of Sine-Gordon Hamiltonian we encounter from Umklapp term and dimerisation has the following form

$$H = \sum_{i=1,2} \frac{1}{2\pi} \int dx\ u_i K_i (\partial_x \theta_i)^2 + \frac{u_i}{K_i} (\partial_x \phi_i)^2 + \frac{2g}{(2\pi\alpha)^2} \int dx\ cos(\beta\phi_1) cos(\beta\phi_2), \tag{B.44}$$

where K_i, u_i are the Luttinger parameter and velocity of two different bosonic field species ϕ_i, θ_i. β is the frequency and it is $\sqrt{8}$ for the umklapp term while $\sqrt{2}$ for dimerisaiton term. To begin with, consider the following correlation function

$$R(r_1 - r_2) = \langle e^{ia\sqrt{2}\phi_1(r_1)} e^{-ia\sqrt{2}\phi_1(r_2)} \rangle_H. \tag{B.45}$$

The average with respect to the free kinetic part of the Hamiltonian $H_0 = \sum_{i=1,2} \frac{1}{2\pi} \int dx\ u_i K_i (\partial_x \theta_i)^2 + \frac{u_i}{K_i} (\partial_x \phi_i)^2$ is

$$\begin{aligned} \langle e^{ia^2\sqrt{2}\phi_i(r_1)} e^{-ia^2\sqrt{2}\phi_i(r_2)} \rangle_{H_0} = e^{-a^2 K_i F_{1,i}(r_1 - r_2)} \simeq (\frac{\alpha}{r_1 - r_2})^{a^2 K_i}, \\ \langle [\phi(r_1) - \phi(r_2)]^2 \rangle_{H_0} = K_i F_{1,i}(r_1 - r_2)\ ,\ F_{1,i}(r) = \frac{1}{2} \log \left[\frac{x^2 + (u_i|\tau| + \alpha)^2}{\alpha^2} \right]. \end{aligned} \tag{B.46}$$

Since the Hamiltonian is separable in the kinetic part, averages w.r.t. to the free kinetic Hamiltonian can be performed separably $\langle f(\phi_1) g(\phi_2) \rangle_{H_0} = \langle f(\phi_1) \rangle_{H_{0,1}} \langle g(\phi_2) \rangle_{H_{0,2}}$. The full action reads

$$S = \overbrace{\sum_{i=1,2} \frac{1}{2\pi K_i} \int dx d\tau \frac{1}{u_i} (\partial_\tau \phi)^2 + u_i (\partial_x \phi)^2}^{S_{0,1} + S_{0,2}} + \frac{2g}{(2\pi\alpha)^2} \int dx d\tau\ cos(\beta\phi_1) cos(\beta\phi_2). \tag{B.47}$$

The θ contributions have been integrated out as they merely contribute a constant which cancels out in the expectation value. As $u_1 \neq u_2$, there is an extra non-trivial factor towards the end. If we expand in powers of g the first order is 0, and stopping at second order the partition function is

$$\begin{aligned}
Z =& \int \mathcal{D}\phi_1 \mathcal{D}\phi_2 e^{-S} \\
=& \int \mathcal{D}\phi_1 \mathcal{D}\phi_2 e^{-S_{0,1}-S_{0,2}} \Bigg[1 - 0 \\
&+ \frac{1}{32}\left(\frac{2g}{(2\pi\alpha)^2}\right)^2 \int d^2r' d^2r'' \prod_{i=1,2} \sum_{\epsilon_1,\epsilon_2=\pm} e^{i\epsilon_1\beta\phi_i(r')} e^{-i\epsilon_2\beta\phi_i(r')} \Bigg],
\end{aligned} \tag{B.48}$$

where $d^2r = dxd\tau$ is different from the conventional definition for now. Expanding (B.45) in g and stopping at 2nd order, we have

$$\begin{aligned}
&\langle e^{ia\sqrt{2}\phi_1(r_1)} e^{-ia\sqrt{2}\phi_1(r_2)} \rangle_H \\
\approx & e^{-a^2 K_1 F_{1,1}(r_1-r_2)} + \\
&\frac{1}{8}\left(\frac{g}{(2\pi\alpha)^2}\right)^2 \Bigg[\int d^2r' d^2r'' \langle e^{ia^2\sqrt{2}\phi_1(r_1)} e^{-ia^2\sqrt{2}\phi_1(r_2)} \prod_{i=1,2} \sum_{\epsilon_1,\epsilon_2=\pm} e^{i\epsilon_1\beta\phi_i(r')} e^{-i\epsilon_2\beta\phi_i(r')} \rangle_{H_0} - \\
&e^{-a^2 K_1 F_{1,1}(r_1-r_2)} \langle \prod_{i=1,2} \sum_{\epsilon_1,\epsilon_2=\pm} e^{i\epsilon_1\beta\phi_i(r')} e^{-i\epsilon_2\beta\phi_i(r')} \rangle_{H_0} \Bigg] \\
=& e^{-a^2 K_1 F_{1,1}(r_1-r_2)} \Bigg[1 + \frac{1}{8}\left(\frac{g}{(2\pi\alpha)^2 u_1}\right)^2 \int d^2r' d^2r'' e^{-\frac{\beta^2}{2}\left(K_1 F_{1,1}(r'-r'') + K_2 F_{1,2}(r'-r'')\right)} \\
\times & 2 \sum_{\epsilon=\pm} \left(e^{\frac{a\beta}{\sqrt{2}} K_1 \epsilon \left[F_{1,1}(r_1-r') - F_{1,1}(r_1-r'') + F_{1,1}(r_2-r'') - F_{1,1}(r_2-r')\right]} - 1 \right) \Bigg],
\end{aligned} \tag{B.49}$$

where $y = u_1\tau$. Due to the factor $e^{-\frac{\beta^2}{2}K_1F_{1,1}(r'-r'')} \sim (\frac{1}{r})^{\frac{\beta^2}{2}}$, which is a power law, small $r' - r''$ contributes the most. Introducing the following:

$$\begin{aligned}
R &= \frac{r'+r''}{2}, & r &= r' - r'', \\
r_1 - r' &= r_1 - R - \frac{1}{2}r, & r_1 - r'' &= r_1 - R + \frac{1}{2}r.
\end{aligned} \tag{B.50}$$

We can expand in r

$$\begin{aligned}
&\sum_{\epsilon=\pm} e^{\frac{a\beta}{\sqrt{2}} K_1 \epsilon \left[F_{1,1}(r_1-r') - F_{1,1}(r_1-r'') + F_{1,1}(r_2-r'') - F_{1,1}(r_2-r')\right]} - 1 \\
\approx & \frac{a^2\beta^2}{2} K_1^2 \left[\sum_{i,j=x,y} r_i \nabla_{R_j} \left(F_{1,1}(r_1 - R) - F_{1,1}(r_2 - R) \right) \right]^2 .
\end{aligned} \tag{B.51}$$

The integral is only non-zero for $i = j$ ($i \neq j$ odd function) and $\int d^2r x^2 = \int d^2r y^2 = \int d^2r \frac{r^2}{2}$. With integration by part, Eq.(B.49) becomes

$$= e^{-a^2K_1F_{1,1}(r_1-r_2)}\left[1 - \frac{1}{16}\left(\frac{g}{(2\pi\alpha)^2u_1}\right)^2 \int d^2r d^2R \; e^{-\frac{\beta^2}{2}\left(K_1F_{1,1}(r)+K_2F_{1,2}(r)\right)}\right.$$
$$\times a^2\beta^2K_1^2r^2\left[F_{1,1}(r_1-R) - F_{1,1}(r_2-R)\right]\left(\nabla_X^2 + \nabla_Y^2\right)\left[F_{1,1}(r_1-R) - F_{1,1}(r_2-R)\right]. \tag{B.52}$$

Since $F_{1,1}(r) \simeq \log(\frac{r}{\alpha})$ for $r > \alpha$, we can use the following identity

$$\left(\nabla_X^2 + \nabla_Y^2\right)\log(R) = 2\pi\delta(R), \tag{B.53}$$

and $\int d^2R\left[F_{1,1}(r_1-R) - F_{1,1}(r_2-R)\right]\left(\nabla_X^2 + \nabla_Y^2\right)\left[F_{1,1}(r_1-R) - F_{1,1}(r_2-R)\right] = -4\pi F_{1,1}(r_1-r_2)$. $F_{1,1}(0) = 0$ with regularisation. As a reminder,

$$F_{1,2}(r) = \log\left[\frac{\sqrt{x^2 + (\frac{u_2}{u_1}|y|+\alpha)^2}}{\alpha}\right] \simeq \log\left[\frac{\sqrt{x^2 + (\frac{u_2}{u_1}|y|)^2}}{\alpha}\right] = \log\left[\frac{r\sqrt{1+\epsilon_1 cos^2(\theta)}}{\alpha}\right], \tag{B.54}$$

where $\left(\frac{u_2}{u_1}\right)^2 = 1 + \epsilon_1$ and θ is the angle between the temporal and spatial variables. The above behaviour for $F_{1,2}$ approximately holds true provided $\epsilon > -1$ (regularisation can be appropriately ignored). Eq.(B.45) is thus

$$\begin{aligned}
R(r_1-r_2) \approx & e^{-a^2K_1F_{1,1}(r_1-r_2)}\left[1 + F_{1,1}(r_1-r_2)\frac{a^2\beta^2K_1^2\pi}{4}\left(\frac{g}{(2\pi\alpha)^2u_1}\right)^2 \times\right.\\
& \left.\int_{r>\alpha} d^2r e^{-\frac{\beta^2}{2}\left(K_1F_{1,1}(r)+K_2F_{1,2}(r)\right)}r^2\right]\\
= e^{-a^2K_1F_{1,1}(r_1-r_2)} & \left[1 + F_{1,1}(r_1-r_2)\frac{a^2\beta^2K_1^2}{2\pi}\frac{g^2}{32\pi^2\alpha^4u_1^2}\int_\alpha^\infty r^3dr\int_{-\pi}^{\pi}d\theta\;(\frac{\alpha}{r})^{\frac{\beta^2}{2}(K_1+K_2)}\right.\\
& \left.\times(\frac{1}{1+\epsilon_1 cos\theta})^{\frac{\beta^2K_2}{4}}\right]\\
= e^{-a^2K_1F_{1,1}(r_1-r_2)} & \left[1 + F_{1,1}(r_1-r_2)\frac{a^2\beta^2K_1^2}{32}\frac{\tilde{g}^2I(\epsilon_1,K_2,\beta)}{2\pi}\int_\alpha^\infty\left(\frac{\alpha}{r}\right)^{\frac{\beta^2}{2}(K_1+K_2)-3}\frac{dr}{\alpha}\right],
\end{aligned} \tag{B.55}$$

where $\tilde{g} = \frac{g}{\pi u_1}, I(\epsilon_1, K_2, \beta) = \int_{-\pi}^{\pi} d\theta (\frac{1}{1+\epsilon_1 cos\theta})^{\frac{\beta^2 K_2}{4}}$. The bracket can be re-exponentialised, giving

$$K_{1,eff}(\alpha) = K_1 - \frac{g(\alpha)^2 \beta^2 K_1^2}{32\pi^2 u_1^2} \frac{I(\epsilon_1, K_2, \beta)}{2\pi} \int_{\alpha}^{\infty} \left(\frac{\alpha}{r}\right)^{\frac{\beta^2}{2}(K_1+K_2)-3} \frac{dr}{\alpha}. \tag{B.56}$$

If we change the cutoff $\alpha = \alpha' + d\alpha$ and re-parametrise $\alpha = \alpha_0 e^l$, $K_{1,eff}$ and g has to change accordingly giving the renormalisation group flow shown below. The flow for K_2 can be worked out with the same procedure but replacing $\phi_1 \to \phi_2$ in the correlator $\langle e^{ia^2\sqrt{2}\phi_i(r_1)} e^{-ia^2\sqrt{2}\phi_i(r_2)} \rangle_{H_0}$. All in all, we have

$$\begin{aligned}
\partial_l K_1 &= -\frac{g^2 \beta^2 K_1^2}{32\pi^2 u_1^2} \frac{I(\epsilon_1, K_2, \beta)}{2\pi}, \\
\partial_l K_2 &= -\frac{g^2 \beta^2 K_2^2}{32\pi^2 u_2^2} \frac{I(\epsilon_2, K_1, \beta)}{2\pi}, \\
\partial_l g &= \left(2 - \frac{\beta^2}{4}(K_1 + K_2)\right) g,
\end{aligned} \tag{B.57}$$

where $\epsilon_2 = -\frac{\epsilon_1}{1+\epsilon_1}$. With this, we can immediately tell the Umklapp term $\beta = \sqrt{8}$ is simply less relevant, while for dimerisation $\beta = \sqrt{2}$ is highly relevant.

The RG flow for usual Sine-Gordon Hamiltonian of the form $H = \frac{1}{2\pi} \int dx\ uK(\partial_x \theta)^2 + \frac{u}{K}(\partial_x \phi)^2 + \frac{2g}{(2\pi\alpha)^2} \int dx\ cos(\beta\phi)$ can be worked out similarly and the extra factor $I(\epsilon_1, K_2, \beta)$ reduces to 1.

B.8 Details about numerics

The procedures for our numerics employed follow the steps described in Ref. [72], which is an extension of Ref. [72] to the generic particle non-conserving case. Across all simulations, the length of the associated complex fermion chain is set to a multiple of 4, and we employ an open boundary condition to compute a meaningful topological entanglement entropy. The discrete-time parameter δt has been chosen to be 0.05, and the number of trajectories for each set of parameters is typically above 600.

To simulate the PPS dynamics, we employ Eq.(4.9), assuming inhomogeneous measurement strength, and since the measurement operators $\hat{O}_j$'s square to $\mathbb{I}$, it reduces to

$$\begin{aligned} d|\psi_t\rangle = \frac{1}{N}\Big[(-iH - \sum_j \zeta_j \hat{O}_j \langle \hat{O}_j\rangle + \sum_j (1-\zeta_j)\hat{O}_j)dt \\ + \sum_j dW_j \hat{O}_j\Big]|\psi_t\rangle, \end{aligned} \tag{B.58}$$

where N is some normalisation, $dW_j dW_j' = \zeta_j dt \delta_{j,j'}$ is the Weiner process and we have absorbed any operator independent term into the normalisation. One can exponentialise this expression giving

$$\begin{aligned} |\psi_{t+dt}\rangle = \frac{1}{N_1}\exp\Big[- iHdt - dt\sum_j \gamma_j \hat{O}_j\langle\hat{O}_j\rangle + dt\sum_j B_j\hat{O}_j \\ + \sum_j dW_j\hat{O}_j\Big]|\psi_t\rangle. \end{aligned} \tag{B.59}$$

As H is a white noise with homogeneous strength, and shares the same set of operators $\hat{O}_j$ with the measurements, this is further modified to

$$\begin{aligned} |\psi_{t+dt}\rangle = \frac{1}{N_1}\exp\Big[- i\sum_j \hat{O}_j d\xi_j - dt\sum_j \gamma_j\hat{O}_j\langle\hat{O}_j\rangle \\ + dt\sum_j B_j\hat{O}_j + \sum_j dW_j\hat{O}_j\Big]|\psi_t\rangle, \end{aligned} \tag{B.60}$$

where $d\xi_j d\xi_{j'} = J^2\delta_{j,j'}dt, d\xi_j dW_j' = 0$ is another Weiner process. In the case of deterministic unitary, one can trotterise the update into the measurement and unitary evolution separately

$$|\psi_{t+\delta t}\rangle = e^{-iH\delta t}e^{-\delta t\sum_j \gamma_j\hat{O}_j\langle\hat{O}_j\rangle + \delta t\sum_j B_j\hat{O}_j + \sum_j \delta W_j\hat{O}_j}|\psi_t\rangle,$$

where δt is the discrete time interval and δW_j's are random variables with mean 0 and variance $\gamma\delta t$. In the lowest order of error, it is merely $\left[H\delta t, \delta W_j\hat{O}_j\right] \sim \mathcal{O}(\delta t^{3/2})$ which vanishes as δt is reduced. Eq.(B.60), however, includes the white noises as a unitary update, and the lowest order of error becomes $\mathcal{O}(\delta t)$. The error does not vanish in the time continuum limit. Therefore, the safest route is not to trotterise the update into the measurement and unitary evolution, and instead should retain them in a single exponential. We numerically checked that trotterising the measurement and unitary evolution resulted in a different simulation outcome than keeping them in a single exponential.

To simulate the Majorana chain, we implement the calculation in the Bogoliubov de Gennes (BdG) formalism, by first identifying 1 species of complex fermion to rewrite the chain: $c_j^\dagger = (\chi_{2j-1} + i\chi_{2j})/2$. The operators of interest, which are the odd and even bond parity, become the on-site and cross-site parity:

$$\begin{aligned} i\chi_{2j-1}\chi_{2j} &= (1 - 2c_j^\dagger c_j), \\ i\chi_{2j}\chi_{2j+1} &= (c_j^\dagger - c_j)(c_{j+1}^\dagger + c_{j+1}). \end{aligned} \tag{B.61}$$

As the model including the measurement is Gaussian preserving, starting from a Gaussian state, the evolution will remain in the space of Gaussian states. For a generic Gaussian state, one can express it as [72, 265]

$$|\psi\rangle = \left[\prod_{n=1}^{n=L} \sum_{k,n} V_{k,n}^* c_k^\dagger + U_{k,n}^* c_k\right] |0\rangle, \tag{B.62}$$

where V and U are $L \times L$ matrices which form a $2L \times 2L$ orthonormal matrix

$$W = \begin{pmatrix} U & V^* \\ V & U^* \end{pmatrix}, \tag{B.63}$$

and implies $U^\dagger U + V^\dagger V = \mathbb{I}, U^T V + V^T U = 0$. Any Gaussian state is fully characterised by the set of all two point correlators; All two point correlation can be calculated from directly from V and U as

$$\begin{aligned} C_{i,j} &= \langle c_i^\dagger c_j\rangle = V^* V^T, \\ F_{i,j} &= \langle c_i c_j\rangle = V^* U^T. \end{aligned} \tag{B.64}$$

Therefore, it is enough to evolve the matrices U and V alone. To achieve this, the white noise and measurement are written in the basis of complex fermion shown in

Eq.(B.61), giving 2 separate non-commuting sets of white noise and measurement. In the BdG formalism, each set of noise/measurement is represented by a matrix:

$$\sum_j (1 - 2c_j^\dagger c_j) \equiv \underline{c}^\dagger M_{2j-1} \underline{c},$$
$$\sum_j (c_j^\dagger - c_j)(c_{j+1}^\dagger + c_{j+1}) \equiv \underline{c}^\dagger M_{2j} \underline{c}, \tag{B.65}$$

where $\underline{c} = (c_1^\dagger, c_2^\dagger, \ldots, c_L^\dagger, c_1, \ldots, c_L)^T$, and the matrices are

$$M_{2j-1} = 2\mathbb{I}_{L\times L},$$
$$M_{2j} = \begin{pmatrix} -A & B^\dagger \\ B & A \end{pmatrix},$$
$$A = diag(1,1) + diag(1,-1), \qquad B = -diag(1,1) + diag(1,-1). \tag{B.66}$$

$diag(1, \pm 1)$ indicate 1 along the ± 1 off diagonal. Dimerisation implemented in the original Majorana chain corresponds to grouping the measurement strengths into two sets $\{\zeta_{2j-1}\} = \gamma$ and $\{\zeta_{2j}\} = \alpha$, and the corresponding PPS non-Hermitian strength $(1-\zeta_j)_\gamma$ and $(1-\zeta_j)_\alpha$. The ratio gives the dimerisation $\frac{1-\Delta}{1+\Delta} = \frac{\gamma}{\alpha}$. Denoting $(1 - 2c_j^\dagger c_j) = \hat{\Gamma}_j$ and $(c_j^\dagger - c_j)(c_{j+1}^\dagger + c_{j+1}) = \hat{A}_j$, Eq.(B.60) becomes

$$\frac{1}{N}\exp\Bigg[-i\sum_j \hat{\Gamma}_j d\xi_{1,j} - i\sum_j \hat{A}_j d\xi_{2,j} - \gamma dt \sum_j \hat{\Gamma}_j \langle \hat{\Gamma}_j \rangle - \alpha dt \sum_j \hat{A}_j \langle \hat{A}_j \rangle$$
$$+ B_\gamma dt \sum_j \hat{\Gamma}_j + B_\alpha \sum_j \hat{A}_j$$
$$+ \sum_j \hat{\Gamma}_j dW_{\gamma,j} + \sum_j \hat{A}_j dW_{\alpha,j} \Bigg], \tag{B.67}$$

where $d\xi_{k,j} d\xi_{l,j'} = J^2 dt \delta_{j,j'} \delta_{k,l}$, $dW_{\gamma,j} dW_{\gamma,j'} = \gamma dt \delta_{j,j'}$ and $dW_{\alpha,j} dW_{\alpha,j'} = \alpha dt \delta_{j,j'}$. The update of the matrices V and U can now be implemented in the BdG form, and in the first step, they are multiplied by:

$$\begin{pmatrix} \tilde{U}(t+\delta t) \\ \tilde{V}(t+\delta t) \end{pmatrix} = \exp[M] \begin{pmatrix} \tilde{U}(t) \\ \tilde{V}(t) \end{pmatrix}. \tag{B.68}$$

The matrix M is merely the exponential in Eq.(B.67) written in BdG form, and the operators are replaced by matrices of the form in Eq.(B.66) where entries are appropriately multiplied by the random variables $\delta\xi_{k,j}$, $\delta W_{\gamma,j}$ and $\delta W_{\alpha,j}$. The expectation values present can readily be computed from two-point correlators in Eq.(B.64). As $\tilde{U}$ and $\tilde{V}$ do not meet the criterion below Eq.(B.63), a final step involves a normalisation of the state to ensure W is orthonormal, which can be implemented via any orthonormalisation procedure of a matrix: the QR-decomposition, Gram-Schmidt or singular value decomposition. Here, we choose the QR-decomposition, and the final update is

$$QR = \begin{pmatrix} \tilde{U}(t+\delta t) \\ \tilde{V}(t+\delta t) \end{pmatrix}, \qquad \begin{pmatrix} U(t+\delta t) \\ V(t+\delta t) \end{pmatrix} = Q. \tag{B.69}$$

$U(t+\delta t)$ and $V(t+\delta t)$ are now properly normalised.

To compute the entanglement entropy, recall that the Nambu one-body Green's function matrix is

$$G = \begin{pmatrix} \mathbb{I}_{L\times L} - C^T & F \\ F^\dagger & C \end{pmatrix}. \tag{B.70}$$

The entanglement entropy of a subsystem $\mathbf{A}$ is calculated by reducing the Green's function to only fermionic operators in $\mathbf{A}$, $G_{\mathbf{A}}$, and is given by [263]

$$S_{1,\mathbf{A}} = -\sum_{\{\lambda_j\}}[\lambda_j \log_2 \lambda_j + (1-\lambda_j)\log_2 \lambda_j], \tag{B.71}$$

where $\{\lambda_j\}$ are the set of eigenvalues of $G_{\mathbf{A}}$. For completeness, higher order entropies are

$$S_{n,\mathbf{A}} = \frac{1}{1-n}\sum_{\{\lambda_j\}} \log_2\left[\left(\lambda_j\right)^n + \left(1-\lambda_j\right)^n\right]. \tag{B.72}$$

To extract the critical exponent ν in the measurement-only scenario, a finite-size scaling analysis on the topological entanglement entropy (S_{TEE}) is performed [72, 108, 114, 246]. In 1D systems, the computation of S_{TEE} was discussed Sec.2.3.1, and for convenience, we recap here that

$$S_{TEE} = S_{AB} + S_{BC} - S_B - S_{ABC}, \tag{B.73}$$

where the partitions A, B and C are pictured in Fig. 2.6(a). We fix the on-site parity measurement strength to some value $\gamma = \gamma_0$ for numerical convenience and vary α (equivalent to varying Δ).

As the choice of the parameter for finite-scaling analysis cannot be made arbitrarily, we justify it as follows: S_{TEE} (in log base 2) has a definite value of 0 (1), in the thermodynamic limit, in the topologically trivial (non-trivial) area-law phase i.e. it is a step function across the phase transition. This can be heuristically understood based on the fact that the two area law phases are characterised by the dominant measurements of Majorana odd or even bond parity, which destroy (odd) or retain (even) long-range entanglement between the 2 Majorana fermions at the opposite edges. With the properties discussed above, we note that S_{TEE} is a valid order parameter between the two different phases and displays singular behaviour at the phase transition in the thermodynamic limit. In a finite system, although the crossing (the singular behaviour of a step) is smeared out, the crossing point is scale-invariant: due to the emergent conformal invariance at the critical point, the length-dependence of the different terms in Eq.(B.73) cancels each other out. We can further elaborate on this and derive a suitable ansatz (the discussion here follows closely to that in Ref. [247]): using the fact that S_{TEE} is scale-invariant at the critical point (giving a crossing point across different system sizes) and it is dimensionless in length, an educated guess is

$$\begin{aligned} S_{TEE} &= G(\xi/L) = G((\alpha - \alpha_{crit})^{-\nu}/L) \\ &= F((\alpha - \alpha_{crit})L^{\frac{1}{\nu}}), \end{aligned} \tag{B.74}$$

where ξ, the correlation length, diverges at the critical point and $F(x)$ is some well-behaved function at $x = 0$. In the second equality, we use the fact that $\xi \sim (\alpha - \alpha_{crit})^{-\nu}$ in a quantum phase transition (where the parameter α plays the role of temperature in thermal transition). This justifies the use and the choice of S_{TEE}.

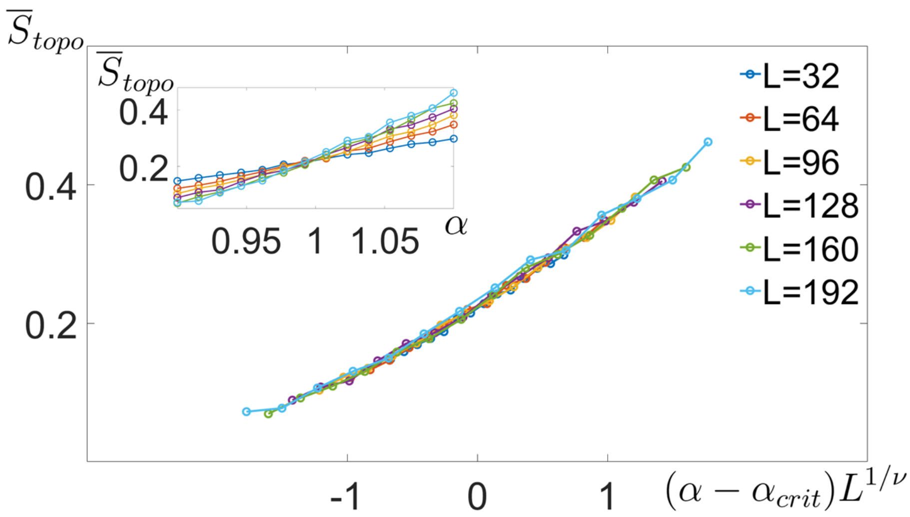

Figure B.4: Example of data collapse of the topological entanglement entropy using the scaling form in Eq. (B.74). The parameters used are $\gamma_0 = 1, \alpha_{crit} = 1, \gamma/B = 1.82$. The value $\nu = 1.83$ is obtained from the best-fit procedure. Inset: Raw data for the topological entanglement entropy against α, before finite size scaling collapse.

We note that it is also possible to use the connected 2-point correlation function to extract the exponent ν. However, in practice, this is not the optimal method since this quantity is heavily affected by the finite size effect and ξ often becomes larger than the system sizes one can access.

In the thermodynamic limit, the critical point is located at $\alpha_{crit} = \gamma_0$. S_{TEE} is computed for various system sizes L at a given ζ across an interval of α in the vicinity of $\alpha = \gamma_0$. Using the scaling form in Eq.(B.74) (F is some unknown function), S_{TEE} for various system sizes will collapse onto a single curve around the critical point (see Fig. B.4) for some suitable value of α_{crit} and ν [72, 109, 247]. The true critical point, α_{crit}, can be read off from the crossing point of S_{TEE} from different L's as shown in the inset of Fig. B.4, and is generally found to be $\gamma_0 \pm 2\%$ (it can be further located using the optimizing function below). One notable exception is $\zeta = 0.4$ which appears to deviate more than 2% from γ_0 ($\gamma_0 = 1,\ \alpha_{crit,\zeta=0.4} = 0.975$); however, it is still within the 5% error range.

For the data collapse, ν is used as a fitting parameter, and its value is determined by the 'best' data collapse, which is quantified by the following objective function [109]:

$$\epsilon(\nu) = \sum_{i=2}^{n-1} (y_i - \overline{y}_i)^2,$$
$$\text{where } \overline{y}_i = \frac{(x_{i+1} - x_i)y_{i-1} - (x_{i-1} - x_i)y_{i+1}}{x_{i+1} - x_{i-1}}. \tag{B.75}$$

x_i are defined to be $(\alpha_i - \alpha_{crit})L^{1/\nu}$ and $y_i = S_{TEE}(\alpha_i, L_i)$. i labels different data points and their ordering is sorted based on ascending order in $x_i's : x_1 < x_2 < \dots x_n$. The 'best' data collapse corresponds to the minimum of $\epsilon(\nu)$, at a given α_{crit}, and we follow the convention in [108, 109] to define the error as the range of ν which falls within 2 times the minimum $\epsilon(\nu) < 2\epsilon(\nu)_{min}$. In addition, α_{crit} is further narrowed down by locating the global minimum of $\epsilon(\nu)$, accounting for α_{crit} as well.

As a final point, to distinguish clearly numerically $(\log L)^2$ from $(\log L)$, one may employ the difference [80]

$$\delta S_{0,L} = S_{0,2L} - S_{0,L}, \tag{B.76}$$

where $S_{0,L}$ is the half-system entanglement entropy. The subleading term is, therefore, cancelled in $\delta S_{0,L}$, and the scaling is different:

$$\delta S_{0,L} \propto \begin{cases} \log_2 L, \text{ if } S_{0,L} \sim (\log\frac{L}{2})^2 \\ \text{constant, if } S_{0,L} \sim \log\frac{L}{2} \end{cases}. \tag{B.77}$$

Fig. B.5 reports the scaling of the half-cut entanglement entropy with system size. Increasing J^2 for fixed $\zeta = 0.091$ changes the scaling from area-law (full blue and orange squares) to system-size-dependent (full green squares). For $\zeta = 0.2$, the transition from the area-law (blue triangle) to size-dependent scaling (orange and green triangle) occurs at a smaller value of J^2. This is consistent with the theoretical finding from the bosonized theory in Fig. 4.8. Note that the exact value of the phase boundary is different from the one predicted within the 2-replica approximation, which is only expected to capture the qualitative behaviour, with a bias in favour of the area law phase [275].

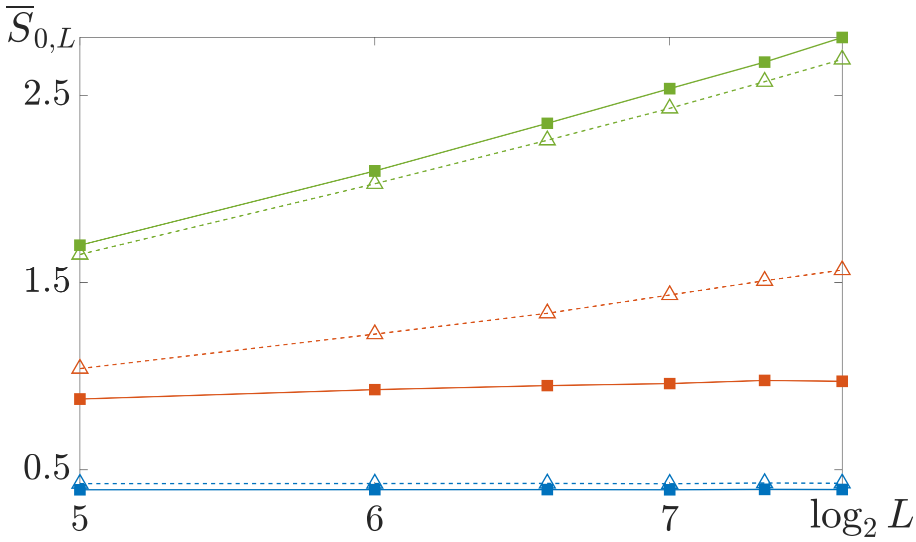

Figure B.5: Average half-cut entanglement entropy $\overline{S}_{0,L}$ from numerical simulations illustrating the area law (blue markers/orange squares) and system-size-dependent entanglement scaling (green markers/orange triangles) phases for non-zero dimerization. The two sets of lines are $\zeta = 0.091$ (filled squares/solid line) and $\zeta = 0.2$ (hollow triangles/dashed lines), and different colour schemes represent different J^2 values: $J^2 = 0.09$ (blue), $J^2 = 0.68$ (orange), and $J^2 = 1.25$ (green). It should be noted that although the line $\zeta = 0.091$, $J^2 = 0.68$ (filled orange/solid) appears to be increasing for small L; this is likely to be a finite size effect as it is trending to saturation for larger L.

Appendix C

Appendices for non-Hermitian SSH chain

C.1 Details of a_1 and a_2 in entanglement entropy

This appendix describes the details of evaluating a_1 and a_2 in Eq.(5.21). Let's begin with a_1. The key object is the logarithm of the determinant $\ln\det\tilde{G}_k(\lambda)$, and we note that in terms of the eigenvalues of $G_k(t\to\infty)$, α_+ and α_-, it appears as

$$\ln\det\tilde{G}_k(\lambda) = \ln[(\lambda-\alpha_+)(\lambda-\alpha_-)] = \ln(\lambda-\alpha_+) + \ln(\lambda-\alpha_-), \tag{C.1}$$

giving

$$a_1 = \frac{1}{4\pi^2 i}\int_{-\pi}^{\pi} dk \oint_{\mathcal{C}} d\lambda \mu(0^+,\lambda)\left[\frac{1}{\lambda-\alpha_+(k)} + \frac{1}{\lambda-\alpha_-(k)}\right]. \tag{C.2}$$

For occupied real k-modes $\mathrm{Im}[E(k)]=0$, using the residue theorem, the function $\mu(0^+,\lambda)$ evaluated at the poles $\mu(0^+,\alpha_\pm(k))>0$ is non-zero. For unoccupied modes $k<2\pi\nu$ or imaginary modes $\mathrm{Re}[E(k)]=0$, $\mu(0^+,\lambda)$ evaluated at the poles gives the null contribution $\mu(0^+,0)=\mu(0^+,1)=0$. Therefore, the final form is

$$a_1 = \frac{1}{2\pi}\int_{-\pi}^{\pi} dk\Theta(E_k^2)\Theta(2\nu\pi-k)\left[\mu\left(0^+,\alpha_+(k)\right) + \mu\left(0^+,\alpha_-(k)\right)\right], \tag{C.3}$$

which is the expression in Eq.(5.22).

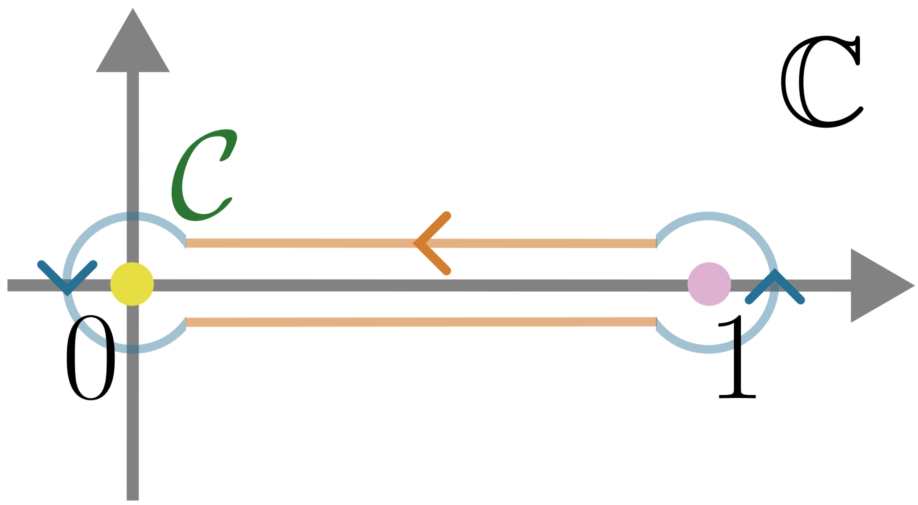

Figure C.1: The complex contour of the integration

For a_2, a little more effort is required. First, for ease of manipulation, one applies integration by parts to the integral in Eq.(5.21) [1]

$$a_2 = -\frac{1}{8\pi^3 i}\oint_{\mathcal{C}} d\lambda \frac{d}{d\lambda}\mu(0^+,\lambda)\sum_{r=1}^{2}\mathrm{Tr}\left[\ln^2\left[\tilde{G}_{k_r^-}(\lambda)(\tilde{G}_{k_r^+}(\lambda))^{-1}\right]\right], \tag{C.4}$$

and note that

$$\begin{aligned}\sum_{r=1}^{2}\mathrm{Tr}\left[\ln^2\left[\tilde{G}_{k_r^-}(\lambda)(\tilde{G}_{k_r^+}(\lambda))^{-1}\right]\right\} &= \sum_{\sigma=\pm}\ln^2\left[\frac{\lambda-0}{\lambda-\alpha_\sigma(2\nu\pi)}\right]+\ln^2\left[\frac{\lambda-\alpha_\sigma(2\nu\pi)}{\lambda-0}\right]\\ &= 2\sum_{\sigma=\pm}\ln^2\left[\frac{\lambda-0}{\lambda-\alpha_\sigma(2\nu\pi)}\right],\end{aligned} \tag{C.5}$$

where we have used $\alpha_\sigma(k>2\nu\pi)=0$. To proceed, we note that the integration contour $\mathcal{C}$ displayed in Fig. C.1 can be split into two contributions: the straight lines (orange lines) and the circular arcs (blue lines)

$$\oint_{\mathcal{C}} d\lambda = \oint_{\text{blue lines}} d\lambda + \oint_{\text{orange lines}} d\lambda.$$

It can be shown that the blue lines' contribution to the integral vanishes, and the

[1] Remember $\mathcal{C}$ is a closed contour, the boundary terms from this manipulation cancel

orange lines in the limit of vanishing blue lines' contribution reads [267]

$$\begin{aligned}a_2 =& -\frac{1}{8\pi^3 i}\oint_{\text{orange lines}} d\lambda \sum_{\sigma=\pm} 2\ln^2\left[\frac{\lambda-0}{\lambda-\alpha_\sigma(2\nu\pi)}\right] \\ =& -\frac{1}{4\pi^3 i}\sum_{\sigma=\pm}\left[\int_{\alpha_\sigma(2\nu\pi)+i0^+}^{0+i0^+} d\lambda + \int_{0+i0^-}^{\alpha_\sigma(2\nu\pi)+i0^-} d\lambda \frac{d}{d\lambda}\mu(0^+,\lambda)\ln^2\left[\frac{\lambda}{\lambda-\alpha_\sigma(2\nu\pi)}\right]\right].\end{aligned} \tag{C.6}$$

Next, note that the denominator in the logarithm is always negative in the integration limit; substituting $x = \lambda + i0^\pm$, we have [267]

$$\ln\frac{(x+i0^\pm)}{x+i0^\pm-\alpha_\sigma(2\nu\pi)} = \ln\left|\frac{x}{x-\alpha_\sigma(2\nu\pi)}\right| \mp (i\pi - i0^+), \tag{C.7}$$

for $x \in \big(0, \alpha_\sigma(2\nu\pi)\big)$. Substituting into the integral, it becomes

$$\begin{aligned}&\int_0^{\alpha_\sigma(2\nu\pi)} dx \frac{d}{dx}\mu(0^+,x)\times \\ &\left[-\left(\ln\left|\frac{x}{x-\alpha_\sigma(2\nu\pi)}\right| - (i\pi-i0^+)\right)^2 + \left(\ln\left|\frac{x}{x-\alpha_\sigma(2\nu\pi)}\right| + (i\pi-i0^+)\right)^2\right] \\ &= 4\pi i\sum_{\sigma=\pm}\int_0^{\alpha_\sigma(2\nu\pi)} dx\ln\left(\frac{1-x}{x}\right)\ln\left|\frac{x}{x-\alpha_\sigma(2\nu\pi)}\right|,\end{aligned} \tag{C.8}$$

and finally, we arrive at the

$$a_2 = \frac{1}{\pi^2}\sum_{\sigma=\pm}\int_0^{\alpha_\sigma(2\nu\pi)} dx\ln\left(\frac{1-x}{x}\right)\ln\left|\frac{x-\alpha_\sigma(2\nu\pi)}{x}\right|. \tag{C.9}$$

Equivalently, in a more concise form, it is

$$a_2 = \frac{1}{2\pi^2}\sum_{r=1}^{2}\sum_{\sigma=+,-}\int_{\alpha_\sigma(k_r^+)}^{\alpha_\sigma(k_r^-)} d\lambda\ln\left(\frac{1-\lambda}{\lambda}\right)\ln\left|\frac{\lambda-\alpha_\sigma(k_r^-)}{\lambda-\alpha_\sigma(k_r^+)}\right|. \tag{C.10}$$

References

[1] B. Misra and E. G. Sudarshan, "The zeno's paradox in quantum theory", Journal of Mathematical Physics **18**, 756–763 (1977).

[2] A. Peres, "Zeno paradox in quantum theory", American Journal of Physics **48**, 931–932 (1980).

[3] P. Facchi and S. Pascazio, "Quantum zeno subspaces", Physical review letters **89**, 080401 (2002).

[4] P. Facchi, A. Klein, S. Pascazio, and L. Schulman, "Berry phase from a quantum zeno effect", Physics Letters A **257**, 232–240 (1999).

[5] D. Burgarth, P. Facchi, V. Giovannetti, H. Nakazato, S. Pascazio, and K. Yuasa, "Non-abelian phases from quantum zeno dynamics", Physical Review A—Atomic, Molecular, and Optical Physics **88**, 042107 (2013).

[6] S. Gherardini, S. Gupta, F. S. Cataliotti, A. Smerzi, F. Caruso, and S. Ruffo, "Stochastic quantum zeno by large deviation theory", New Journal of Physics **18**, 013048 (2016).

[7] T. J. Elliott and V. Vedral, "Quantum quasi-zeno dynamics: transitions mediated by frequent projective measurements near the zeno regime", Physical Review A **94**, 012118 (2016).

[8] K. Snizhko, P. Kumar, and A. Romito, "Quantum zeno effect appears in stages", Phys. Rev. Res. **2**, 033512 (2020).

[9] L. Rosso, A. Biella, J. De Nardis, and L. Mazza, “Dynamical theory for one-dimensional fermions with strong two-body losses: universal non-hermitian zeno physics and spin-charge separation”, Phys. Rev. A **107**, 013303 (2023).

[10] P. Kumar, A. Romito, and K. Snizhko, “Quantum zeno effect with partial measurement and noisy dynamics”, Phys. Rev. Res. **2**, 043420 (2020).

[11] G. Mouloudakis and P. Lambropoulos, “Coalescence of non-markovian dissipation, quantum zeno effect, and non-hermitian physics in a simple realistic quantum system”, Phys. Rev. A **106**, 053709 (2022).

[12] S. M. Walls, J. M. Schachter, H. Qian, and I. J. Ford, “Stochastic quantum trajectories demonstrate the quantum zeno effect in an open spin system”, arXiv preprint arXiv:2209.10626 (2022).

[13] H. Chen and S. Pang, “Quantum control for the zeno effect with noise”, Phys. Rev. A **109**, 062414 (2024).

[14] P. M. Harrington, E. J. Mueller, and K. W. Murch, “Engineered dissipation for quantum information science”, Nature Reviews Physics **4**, 660–671 (2022).

[15] P. Lewalle, L. S. Martin, E. Flurin, S. Zhang, E. Blumenthal, S. Hacohen-Gourgy, D. Burgarth, and K. B. Whaley, “A Multi-Qubit Quantum Gate Using the Zeno Effect”, Quantum **7**, 1100 (2023).

[16] K. Kumari, G. Rajpoot, S. Joshi, and S. R. Jain, “Qubit control using quantum zeno effect: action principle approach”, Annals of Physics **450**, 169222 (2023).

[17] Y. Wang, K. Snizhko, A. Romito, Y. Gefen, and K. Murch, “Observing a topological transition in weak-measurement-induced geometric phases”, Phys. Rev. Res. **4**, 023179 (2022).

[18] M. F. Ferrer-Garcia, K. Snizhko, A. D’errico, A. Romito, Y. Gefen, and E. Karimi, “Topological transitions of the generalized pancharatnam-berry phase”, Science advances **9**, eadg6810 (2023).

[19] J. M. Dominy, G. A. Paz-Silva, A. Rezakhani, and D. A. Lidar, "Analysis of the quantum zeno effect for quantum control and computation", Journal of Physics A: Mathematical and Theoretical **46**, 075306 (2013).

[20] S. Hacohen-Gourgy, L. P. García-Pintos, L. S. Martin, J. Dressel, and I. Siddiqi, "Incoherent qubit control using the quantum zeno effect", Phys. Rev. Lett. **120**, 020505 (2018).

[21] X. Guo, C.-L. Zou, L. Jiang, and H. X. Tang, "All-optical control of linear and nonlinear energy transfer via the zeno effect", Phys. Rev. Lett. **120**, 203902 (2018).

[22] P. M. Harrington, J. T. Monroe, and K. W. Murch, "Quantum zeno effects from measurement controlled qubit-bath interactions", Phys. Rev. Lett. **118**, 240401 (2017).

[23] M. C. Fischer, B. Gutiérrez-Medina, and M. G. Raizen, "Observation of the quantum zeno and anti-zeno effects in an unstable system", Phys. Rev. Lett. **87**, 040402 (2001).

[24] S. Maniscalco, J. Piilo, and K.-A. Suominen, "Zeno and anti-zeno effects for quantum brownian motion", Phys. Rev. Lett. **97**, 130402 (2006).

[25] D. Segal and D. R. Reichman, "Zeno and anti-zeno effects in spin-bath models", Phys. Rev. A **76**, 012109 (2007).

[26] P. Facchi, D. A. Lidar, and S. Pascazio, "Unification of dynamical decoupling and the quantum zeno effect", Phys. Rev. A **69**, 032314 (2004).

[27] K. Jacobs, *Quantum measurement theory and its applications* (Cambridge University Press, 2014).

[28] V. S. Shchesnovich and V. V. Konotop, "Control of a bose-einstein condensate by dissipation: nonlinear zeno effect", Phys. Rev. A **81**, 053611 (2010).

[29] G. A. Paz-Silva, A. T. Rezakhani, J. M. Dominy, and D. A. Lidar, "Zeno effect for quantum computation and control", Phys. Rev. Lett. **108**, 080501 (2012).

[30] Y. Cao, Y.-H. Li, Z. Cao, J. Yin, Y.-A. Chen, H.-L. Yin, T.-Y. Chen, X. Ma, C.-Z. Peng, and J.-W. Pan, "Direct counterfactual communication via quantum zeno effect", Proceedings of the National Academy of Sciences **114**, 4920–4924 (2017).

[31] Y. Kondo, Y. Matsuzaki, K. Matsushima, and J. G. Filgueiras, "Using the quantum zeno effect for suppression of decoherence", New Journal of Physics **18**, 013033 (2016).

[32] P. Lewalle, Y. Zhang, and K. B. Whaley, "Optimal zeno dragging for quantum control: a shortcut to zeno with action-based scheduling optimization", PRX Quantum **5**, 020366 (2024).

[33] Q. Liu, W. Liu, K. Ziegler, and F. Chen, "Engineering of zeno dynamics in integrated photonics", Phys. Rev. Lett. **130**, 103801 (2023).

[34] J. Eisert, M. Friesdorf, and C. Gogolin, "Quantum many-body systems out of equilibrium", Nature Physics **11**, 124–130 (2015).

[35] L. M. Sieberer, M. Buchhold, J. Marino, and S. Diehl, "Universality in driven open quantum matter", arXiv preprint arXiv:2312.03073 (2023).

[36] M. P. Fisher, V. Khemani, A. Nahum, and S. Vijay, "Random quantum circuits", Annual Review of Condensed Matter Physics **14**, 335–379 (2023).

[37] T. Mori, "Floquet states in open quantum systems", Annual Review of Condensed Matter Physics **14**, 35–56 (2023).

[38] L. D'Alessio, Y. Kafri, A. Polkovnikov, and M. Rigol, "From quantum chaos and eigenstate thermalization to statistical mechanics and thermodynamics", Advances in Physics **65**, 239–362 (2016).

[39] P. Calabrese, F. H. Essler, and G. Mussardo, "Introduction to 'quantum integrability in out of equilibrium systems'", Journal of Statistical Mechanics: Theory and Experiment **2016**, 064001 (2016).

[40] P. Calabrese, "Entanglement spreading in non-equilibrium integrable systems", SciPost Physics Lecture Notes, 020 (2020).

[41] A. Bastianello, B. Bertini, B. Doyon, and R. Vasseur, "Introduction to the special issue on emergent hydrodynamics in integrable many-body systems", Journal of Statistical Mechanics: Theory and Experiment **2022**, 014001 (2022).

[42] L. Piroli, P. Calabrese, and F. Essler, "Quantum quenches to the attractive one-dimensional bose gas: exact results", SciPost Physics **1**, 001 (2016).

[43] A. Chan, A. De Luca, and J. T. Chalker, "Solution of a minimal model for many-body quantum chaos", Physical Review X **8**, 041019 (2018).

[44] B. Bertini, P. Kos, and T. Prosen, "Entanglement spreading in a minimal model of maximal many-body quantum chaos", Physical Review X **9**, 021033 (2019).

[45] H. Weimer, A. Kshetrimayum, and R. Orús, "Simulation methods for open quantum many-body systems", Reviews of Modern Physics **93**, 015008 (2021).

[46] M. Schiulaz, E. J. Torres-Herrera, F. Pérez-Bernal, and L. F. Santos, "Self-averaging in many-body quantum systems out of equilibrium: chaotic systems", Physical Review B **101**, 174312 (2020).

[47] J.-S. Caux, "The quench action", Journal of Statistical Mechanics: Theory and Experiment **2016**, 064006 (2016).

[48] V. Gritsev, P. Barmettler, and E. Demler, "Scaling approach to quantum non-equilibrium dynamics of many-body systems", New journal of Physics **12**, 113005 (2010).

[49] B. Bertini, M. Collura, J. De Nardis, and M. Fagotti, “Transport in out-of-equilibrium xxz chains: exact profiles of charges and currents”, Physical review letters **117**, 207201 (2016).

[50] L. Piroli, J. De Nardis, M. Collura, B. Bertini, and M. Fagotti, “Transport in out-of-equilibrium xxz chains: nonballistic behavior and correlation functions”, Physical Review B **96**, 115124 (2017).

[51] B. Bertini, E. Tartaglia, and P. Calabrese, “Quantum quench in the infinitely repulsive hubbard model: the stationary state”, Journal of Statistical Mechanics: Theory and Experiment **2017**, 103107 (2017).

[52] N. Defenu, A. Lerose, and S. Pappalardi, “Out-of-equilibrium dynamics of quantum many-body systems with long-range interactions”, Physics Reports **1074**, 1–92 (2024).

[53] R. Vasseur and J. E. Moore, “Nonequilibrium quantum dynamics and transport: from integrability to many-body localization”, Journal of Statistical Mechanics: Theory and Experiment **2016**, 064010 (2016).

[54] M. Rispoli, A. Lukin, R. Schittko, S. Kim, M. E. Tai, J. Léonard, and M. Greiner, “Quantum critical behaviour at the many-body localization transition”, Nature **573**, 385–389 (2019).

[55] I. Vakulchyk, I. Yusipov, M. Ivanchenko, S. Flach, and S. Denisov, “Signatures of many-body localization in steady states of open quantum systems”, Physical Review B **98**, 020202 (2018).

[56] J. Surace, M. Piani, and L. Tagliacozzo, “Simulating the out-of-equilibrium dynamics of local observables by trading entanglement for mixture”, Physical Review B **99**, 235115 (2019).

[57] M. L. Wall and M. L. Wall, “Out-of-equilibrium dynamics with matrix product states”, Quantum Many-Body Physics of Ultracold Molecules in Optical Lattices: Models and Simulation Methods, 177–222 (2015).

[58] A. Panda and S. Banerjee, "Entanglement in nonequilibrium steady states and many-body localization breakdown in a current-driven system", Physical Review B **101**, 184201 (2020).

[59] K. R. Hazzard, M. van den Worm, M. Foss-Feig, S. R. Manmana, E. G. Dalla Torre, T. Pfau, M. Kastner, and A. M. Rey, "Quantum correlations and entanglement in far-from-equilibrium spin systems", Physical Review A **90**, 063622 (2014).

[60] R. Ghosh, N. Dupuis, A. Sen, and K. Sengupta, "Entanglement measures and nonequilibrium dynamics of quantum many-body systems: a path integral approach", Physical Review B **101**, 245130 (2020).

[61] P. Reimann, "Typical fast thermalization processes in closed many-body systems", Nature communications **7**, 10821 (2016).

[62] Y. Ashida, K. Saito, and M. Ueda, "Thermalization and heating dynamics in open generic many-body systems", Physical review letters **121**, 170402 (2018).

[63] T. Shirai and T. Mori, "Thermalization in open many-body systems based on eigenstate thermalization hypothesis", Physical Review E **101**, 042116 (2020).

[64] B. Skinner, J. Ruhman, and A. Nahum, "Measurement-induced phase transitions in the dynamics of entanglement", Physical Review X **9**, 031009 (2019).

[65] A. Chan, R. M. Nandkishore, M. Pretko, and G. Smith, "Unitary-projective entanglement dynamics", Physical Review B **99**, 224307 (2019).

[66] Y. Li, X. Chen, and M. P. Fisher, "Quantum zeno effect and the many-body entanglement transition", Physical Review B **98**, 205136 (2018).

[67] M. Szyniszewski, A. Romito, and H. Schomerus, "Entanglement transition from variable-strength weak measurements", Physical Review B **100**, 064204 (2019).

[68] J. M. Koh, S.-N. Sun, M. Motta, and A. J. Minnich, "Measurement-induced entanglement phase transition on a superconducting quantum processor with mid-circuit readout", Nature Physics **19**, 1314–1319 (2023).

[69] Google Quantum AI and Collaborators, "Measurement-induced entanglement and teleportation on a noisy quantum processor", Nature **622**, 481–486 (2023).

[70] C. Noel, P. Niroula, D. Zhu, A. Risinger, L. Egan, D. Biswas, M. Cetina, A. V. Gorshkov, M. J. Gullans, D. A. Huse, et al., "Measurement-induced quantum phases realized in a trapped-ion quantum computer", Nature Physics **18**, 760–764 (2022).

[71] I. Poboiko, P. Pöpperl, I. V. Gornyi, and A. D. Mirlin, "Theory of free fermions under random projective measurements", arXiv preprint arXiv:2304.03138 (2023).

[72] X. Cao, A. Tilloy, and A. D. Luca, "Entanglement in a fermion chain under continuous monitoring", SciPost Phys. **7**, 024 (2019).

[73] C. Carisch, A. Romito, and O. Zilberberg, "Quantifying measurement-induced quantum-to-classical crossover using an open-system entanglement measure", arXiv preprint arXiv:2304.02965 (2023).

[74] M. Coppola, E. Tirrito, D. Karevski, and M. Collura, "Growth of entanglement entropy under local projective measurements", Physical Review B **105**, 094303 (2022).

[75] G. Kells, D. Meidan, and A. Romito, "Topological transitions in weakly monitored free fermions", SciPost Phys. **14**, 031 (2023).

[76] O. Alberton, M. Buchhold, and S. Diehl, "Entanglement transition in a monitored free-fermion chain: from extended criticality to area law", Physical Review Letters **126**, 170602 (2021).

[77] M. Buchhold, Y. Minoguchi, A. Altland, and S. Diehl, “Effective theory for the measurement-induced phase transition of dirac fermions”, Phys. Rev. X **11**, 041004 (2021).

[78] K. Yamamoto and R. Hamazaki, “Localization properties in disordered quantum many-body dynamics under continuous measurement”, Physical Review B **107**, L220201 (2023).

[79] M. Szyniszewski, O. Lunt, and A. Pal, “Disordered monitored free fermions”, arXiv preprint arXiv:2211.02534 (2022).

[80] M. Fava, L. Piroli, T. Swann, D. Bernard, and A. Nahum, “Nonlinear sigma models for monitored dynamics of free fermions”, Phys. Rev. X **13**, 041045 (2023).

[81] X. Turkeshi, L. Piroli, and M. Schiró, “Enhanced entanglement negativity in boundary-driven monitored fermionic chains”, Physical Review B **106**, 024304 (2022).

[82] K. Chahine and M. Buchhold, “Entanglement phases, localization and multifractality of monitored free fermions in two dimensions”, arXiv preprint arXiv:2309.12391 (2023).

[83] E. V. Doggen, Y. Gefen, I. V. Gornyi, A. D. Mirlin, and D. G. Polyakov, “Generalized quantum measurements with matrix product states: entanglement phase transition and clusterization”, Physical Review Research **4**, 023146 (2022).

[84] C.-M. Jian, H. Shapourian, B. Baue, and A. W. W. Ludwig, “Measurement-induced entanglement transitions in quantum circuits of non-interacting fermions: born-rule versus forced measurements”, arXiv preprint arXiv:2302.09094 (2023).

[85] B. Xing, X. Turkeshi, M. Schiró, R. Fazio, and D. Poletti, “Interactions and integrability in weakly monitored hamiltonian systems”, arXiv preprint arXiv:2308.09133 (2023).

[86] Q. Tang and W. Zhu, "Measurement-induced phase transition: a case study in the nonintegrable model by density-matrix renormalization group calculations", Physical Review Research **2**, 013022 (2020).

[87] M. Buchhold, T. Mueller, and S. Diehl, "Revealing measurement-induced phase transitions by pre-selection", arXiv preprint arXiv:2208.10506 (2022).

[88] B. Ladewig, S. Diehl, and M. Buchhold, "Monitored open fermion dynamics: exploring the interplay of measurement, decoherence, and free hamiltonian evolution", Physical Review Research **4**, 033001 (2022).

[89] Y. Minoguchi, P. Rabl, and M. Buchhold, "Continuous gaussian measurements of the free boson CFT: A model for exactly solvable and detectable measurement-induced dynamics", SciPost Phys. **12**, 009 (2022).

[90] T. Müller, S. Diehl, and M. Buchhold, "Measurement-induced dark state phase transitions in long-ranged fermion systems", Physical Review Letters **128**, 010605 (2022).

[91] T. Jin and D. G. Martin, "Measurement-induced phase transition in a single-body tight-binding model", arXiv preprint arXiv:2309.15034 (2023).

[92] C.-M. Jian, B. Bauer, A. Keselman, and A. W. W. Ludwig, "Criticality and entanglement in nonunitary quantum circuits and tensor networks of noninteracting fermions", Phys. Rev. B **106**, 134206 (2022).

[93] P. Zhang, C. Liu, S.-K. Jian, and X. Chen, "Universal Entanglement Transitions of Free Fermions with Long-range Non-unitary Dynamics", Quantum **6**, 723 (2022).

[94] T. Botzung, S. Diehl, and M. Müller, "Engineered dissipation induced entanglement transition in quantum spin chains: from logarithmic growth to area law", Physical Review B **104**, 184422 (2021).

[95] Q. Tang and W. Zhu, "Measurement-induced phase transition: a case study in the nonintegrable model by density-matrix renormalization group calculations", Phys. Rev. Res. **2**, 013022 (2020).

[96] A. Nahum and K. J. Wiese, “Renormalization group for measurement and entanglement phase transitions”, Phys. Rev. B **108**, 104203 (2023).

[97] T. Minato, K. Sugimoto, T. Kuwahara, and K. Saito, “Fate of measurement-induced phase transition in long-range interactions”, Phys. Rev. Lett. **128**, 010603 (2022).

[98] X. Turkeshi, “Measurement-induced criticality as a data-structure transition”, Physical Review B **106**, 144313 (2022).

[99] A. Zabalo, M. J. Gullans, J. H. Wilson, R. Vasseur, A. W. W. Ludwig, S. Gopalakrishnan, D. A. Huse, and J. H. Pixley, “Operator scaling dimensions and multifractality at measurement-induced transitions”, Phys. Rev. Lett. **128**, 050602 (2022).

[100] S.-K. Jian, C. Liu, X. Chen, B. Swingle, and P. Zhang, “Measurement-induced phase transition in the monitored sachdev-ye-kitaev model”, Phys. Rev. Lett. **127**, 140601 (2021).

[101] P. Sierant, M. Schirò, M. Lewenstein, and X. Turkeshi, “Measurement-induced phase transitions in $(d+1)$-dimensional stabilizer circuits”, Phys. Rev. B **106**, 214316 (2022).

[102] O. Lunt and A. Pal, “Measurement-induced entanglement transitions in many-body localized systems”, Phys. Rev. Res. **2**, 043072 (2020).

[103] I. Poboiko, I. V. Gornyi, and A. D. Mirlin, “Measurement-induced phase transition for free fermions above one dimension”, Phys. Rev. Lett. **132**, 110403 (2024).

[104] S. Choi, Y. Bao, X.-L. Qi, and E. Altman, “Quantum error correction in scrambling dynamics and measurement-induced phase transition”, Phys. Rev. Lett. **125**, 030505 (2020).

[105] X. Feng, B. Skinner, and A. Nahum, “Measurement-induced phase transitions on dynamical quantum trees”, PRX Quantum **4**, 030333 (2023).

[106] T. Kalsi, A. Romito, and H. Schomerus, “Three-fold way of entanglement dynamics in monitored quantum circuits”, Journal of Physics A: Mathematical and Theoretical **55**, 264009 (2022).

[107] H. Oshima and Y. Fuji, “Charge fluctuation and charge-resolved entanglement in a monitored quantum circuit with $U(1)$ symmetry”, Phys. Rev. B **107**, 014308 (2023).

[108] A. Lavasani, Y. Alavirad, and M. Barkeshli, “Measurement-induced topological entanglement transitions in symmetric random quantum circuits”, Nature Physics **17**, 342–347 (2021).

[109] A. Lavasani, Y. Alavirad, and M. Barkeshli, “Topological order and criticality in (2+ 1) d monitored random quantum circuits”, Physical review letters **127**, 235701 (2021).

[110] T. Orito, Y. Kuno, and I. Ichinose, “Measurement-only dynamical phase transition of topological and boundary order in toric code and gauge higgs models”, Phys. Rev. B **109**, 224306 (2024).

[111] Y. Kuno, T. Orito, and I. Ichinose, “Phase transition and evidence of fast-scrambling phase in measurement-only quantum circuits”, Phys. Rev. B **108**, 094104 (2023).

[112] D. Qian and J. Wang, “Steering-induced phase transition in measurement-only quantum circuits”, Phys. Rev. B **109**, 024301 (2024).

[113] K. Klocke and M. Buchhold, “Topological order and entanglement dynamics in the measurement-only xzzx quantum code”, Phys. Rev. B **106**, 104307 (2022).

[114] K. Klocke and M. Buchhold, “Majorana loop models for measurement-only quantum circuits”, Phys. Rev. X **13**, 041028 (2023).

[115] A. Sriram, T. Rakovszky, V. Khemani, and M. Ippoliti, “Topology, criticality, and dynamically generated qubits in a stochastic measurement-only kitaev model”, Phys. Rev. B **108**, 094304 (2023).

[116] S. Sang, Y. Li, T. Zhou, X. Chen, T. H. Hsieh, and M. P. Fisher, "Entanglement negativity at measurement-induced criticality", PRX Quantum **2**, 030313 (2021).

[117] B. Zeng, X. Chen, D.-L. Zhou, X.-G. Wen, et al., *Quantum information meets quantum matter* (Springer, 2019).

[118] M. Rangamani, T. Takayanagi, M. Rangamani, and T. Takayanagi, *Holographic entanglement entropy* (Springer, 2017).

[119] B. Bertini, P. Kos, and T. ž. Prosen, "Entanglement spreading in a minimal model of maximal many-body quantum chaos", Phys. Rev. X **9**, 021033 (2019).

[120] A. Nahum, J. Ruhman, S. Vijay, and J. Haah, "Quantum entanglement growth under random unitary dynamics", Physical Review X **7**, 031016 (2017).

[121] A. Nahum, S. Vijay, and J. Haah, "Operator spreading in random unitary circuits", Physical Review X **8**, 021014 (2018).

[122] A. Foligno and B. Bertini, "Growth of entanglement of generic states under dual-unitary dynamics", Physical Review B **107**, 174311 (2023).

[123] M. Szyniszewski, A. Romito, and H. Schomerus, "Universality of entanglement transitions from stroboscopic to continuous measurements", Physical review letters **125**, 210602 (2020).

[124] O. Lunt, M. Szyniszewski, and A. Pal, "Measurement-induced criticality and entanglement clusters: a study of one-dimensional and two-dimensional clifford circuits", Phys. Rev. B **104**, 155111 (2021).

[125] Y. Li, Y. Zou, P. Glorioso, E. Altman, and M. P. A. Fisher, "Cross entropy benchmark for measurement-induced phase transitions", Phys. Rev. Lett. **130**, 220404 (2023).

[126] S. Sharma, X. Turkeshi, R. Fazio, and M. Dalmonte, "Measurement-induced criticality in extended and long-range unitary circuits", SciPost Phys. Core **5**, 023 (2022).

[127] A. A. Akhtar, H.-Y. Hu, and Y.-Z. You, "Measurement-induced criticality is tomographically optimal", Phys. Rev. B **109**, 094209 (2024).

[128] C.-J. Lin, W. Ye, Y. Zou, S. Sang, and T. H. Hsieh, "Probing sign structure using measurement-induced entanglement", Quantum **7**, 910 (2023).

[129] E. Heinrich and X. Chen, "Measurement-induced phase transitions in quantum raise-and-peel models", Phys. Rev. B **110**, 064309 (2024).

[130] A. B. Watts, D. Gosset, Y. Liu, and M. Soleimanifar, "Quantum advantage from measurement-induced entanglement in random shallow circuits", arXiv preprint arXiv:2407.21203 (2024).

[131] A. Zabalo, M. J. Gullans, J. H. Wilson, S. Gopalakrishnan, D. A. Huse, and J. Pixley, "Critical properties of the measurement-induced transition in random quantum circuits", Physical Review B **101**, 060301 (2020).

[132] J. Iaconis, A. Lucas, and X. Chen, "Measurement-induced phase transitions in quantum automaton circuits", Phys. Rev. B **102**, 224311 (2020).

[133] Y. Li, R. Vasseur, M. P. A. Fisher, and A. W. W. Ludwig, "Statistical mechanics model for clifford random tensor networks and monitored quantum circuits", Phys. Rev. B **109**, 174307 (2024).

[134] Y. Yanay, B. Swingle, and C. Tahan, "Detecting measurement-induced entanglement transitions with unitary mirror circuits", Phys. Rev. Lett. **133**, 070601 (2024).

[135] B. Ladewig, S. Diehl, and M. Buchhold, "Monitored open fermion dynamics: exploring the interplay of measurement, decoherence, and free hamiltonian evolution", Phys. Rev. Res. **4**, 033001 (2022).

[136] Y. Minoguchi, P. Rabl, and M. Buchhold, "Continuous gaussian measurements of the free boson CFT: A model for exactly solvable and detectable measurement-induced dynamics", SciPost Phys. **12**, 009 (2022).

[137] C. Carisch, O. Zilberberg, and A. Romito, "Effect of the readout efficiency of quantum measurement on the system entanglement", Phys. Rev. A **110**, 022214 (2024).

[138] C. Carisch, A. Romito, and O. Zilberberg, "Quantifying measurement-induced quantum-to-classical crossover using an open-system entanglement measure", Phys. Rev. Res. **5**, L042031 (2023).

[139] S. J. Garratt and E. Altman, "Probing postmeasurement entanglement without postselection", PRX Quantum **5**, 030311 (2024).

[140] M. McGinley, "Postselection-free learning of measurement-induced quantum dynamics", PRX Quantum **5**, 020347 (2024).

[141] Y.-X. Wang, A. Seif, and A. A. Clerk, "Uncovering measurement-induced entanglement via directional adaptive dynamics and incomplete information", arXiv preprint arXiv:2310.01338 (2023).

[142] M. J. Gullans and D. A. Huse, "Scalable probes of measurement-induced criticality", Phys. Rev. Lett. **125**, 070606 (2020).

[143] H. Dehghani, A. Lavasani, M. Hafezi, and M. J. Gullans, "Neural-network decoders for measurement induced phase transitions", Nature Communications **14**, 2918 (2023).

[144] Y. Li and M. P. A. Fisher, "Decodable hybrid dynamics of open quantum systems with $\mathbb{Z}_2$ symmetry", Phys. Rev. B **108**, 214302 (2023).

[145] F. Barratt, U. Agrawal, A. C. Potter, S. Gopalakrishnan, and R. Vasseur, "Transitions in the learnability of global charges from local measurements", Phys. Rev. Lett. **129**, 200602 (2022).

[146] X. Turkeshi, A. Biella, R. Fazio, M. Dalmonte, and M. Schiró, "Measurement-induced entanglement transitions in the quantum ising chain: from infinite to zero clicks", Physical Review B **103**, 224210 (2021).

[147] X. Turkeshi and M. Schiró, "Entanglement and correlation spreading in non-hermitian spin chains", Physical Review B **107**, L020403 (2023).

[148] Y. Le Gal, X. Turkeshi, and M. Schirò, "Volume-to-area law entanglement transition in a non-hermitian free fermionic chain", SciPost Physics **14**, 138 (2023).

[149] C. Zerba and A. Silva, "Measurement phase transitions in the no-click limit as quantum phase transitions of a non-hermitean vacuum", arXiv preprint arXiv:2301.07383 (2023).

[150] M. Stefanini and J. Marino, "Orthogonality catastrophe beyond luttinger liquid from post-selection", arXiv preprint arXiv:2310.00039 (2023).

[151] A. Paviglianiti, X. Turkeshi, M. Schirò, and A. Silva, "Enhanced entanglement in the measurement-altered quantum ising chain", arXiv preprint arXiv:2310.02686 (2023).

[152] X. Turkeshi, M. Dalmonte, R. Fazio, and M. Schirò, "Entanglement transitions from stochastic resetting of non-hermitian quasiparticles", Physical Review B **105**, L241114 (2022).

[153] X. Feng, S. Liu, S. Chen, and W. Guo, "Absence of logarithmic and algebraic scaling entanglement phases due to the skin effect", Physical Review B **107**, 094309 (2023).

[154] L. Su, A. Clerk, and I. Martin, "Dynamics and phases of nonunitary floquet transverse-field ising model", arXiv preprint arXiv:2306.07428 (2023).

[155] X. Chen, Y. Li, M. P. Fisher, and A. Lucas, "Emergent conformal symmetry in nonunitary random dynamics of free fermions", Physical Review Research **2**, 033017 (2020).

[156] Q. Tang, X. Chen, and W. Zhu, “Quantum criticality in the nonunitary dynamics of (2+ 1)-dimensional free fermions”, Physical Review B **103**, 174303 (2021).

[157] S.-K. Jian, Z.-C. Yang, Z. Bi, and X. Chen, “Yang-lee edge singularity triggered entanglement transition”, Physical Review B **104**, L161107 (2021).

[158] J. Despres, L. Mazza, and M. Schirò, “Breakdown of linear spin-wave theory in a non-hermitian quantum spin chain”, arXiv preprint arXiv:2310.00985 (2023).

[159] Y. Le Gal, X. Turkeshi, and M. Schirò, “Entanglement dynamics in monitored systems and the role of quantum jumps”, PRX Quantum **5**, 030329 (2024).

[160] C. Carisch, O. Zilberberg, and A. Romito, “Does the system entanglement care about the readout efficiency of quantum measurement?”, arXiv preprint arXiv:2402.19412 (2024).

[161] H. M. Wiseman and G. J. Milburn, *Quantum measurement and control* (Cambridge university press, 2009).

[162] Z. K. Minev, S. O. Mundhada, S. Shankar, P. Reinhold, R. Gutiérrez-Jáuregui, R. J. Schoelkopf, M. Mirrahimi, H. J. Carmichael, and M. H. Devoret, “To catch and reverse a quantum jump mid-flight”, Nature **570**, 200–204 (2019).

[163] P. Sprent and N. C. Smeeton, *Applied nonparametric statistical methods* (CRC press, 2007).

[164] B. Øksendal and B. Øksendal, *Stochastic differential equations* (Springer, 2003).

[165] P. Rouchon, “A tutorial introduction to quantum stochastic master equations based on the qubit/photon system”, Annual Reviews in Control **54**, 252–261 (2022).

[166] D. Yang, C. Laflamme, D. V. Vasilyev, M. A. Baranov, and P. Zoller, "Theory of a quantum scanning microscope for cold atoms", Phys. Rev. Lett. **120**, 133601 (2018).

[167] S. N. M. Paladugu, T. Chen, F. A. An, B. Yan, and B. Gadway, "Injection spectroscopy of momentum state lattices", Communications Physics **7**, 39 (2024).

[168] Z.-H. Qian, J.-M. Cui, X.-W. Luo, Y.-X. Zheng, Y.-F. Huang, M.-Z. Ai, R. He, C.-F. Li, and G.-C. Guo, "Super-resolved imaging of a single cold atom on a nanosecond timescale", Phys. Rev. Lett. **127**, 263603 (2021).

[169] J. Zeiher, J. Wolf, J. A. Isaacs, J. Kohler, and D. M. Stamper-Kurn, "Tracking evaporative cooling of a mesoscopic atomic quantum gas in real time", Phys. Rev. X **11**, 041017 (2021).

[170] P. Facchi and S. Pascazio, "Quantum zeno subspaces", Phys. Rev. Lett. **89**, 080401 (2002).

[171] P. Facchi, A. Klein, S. Pascazio, and L. Schulman, "Berry phase from a quantum zeno effect", Physics Letters A **257**, 232–240 (1999).

[172] D. Burgarth, P. Facchi, V. Giovannetti, H. Nakazato, S. Pascazio, and K. Yuasa, "Non-abelian phases from quantum zeno dynamics", Phys. Rev. A **88**, 042107 (2013).

[173] T. J. Elliott and V. Vedral, "Quantum quasi-zeno dynamics: transitions mediated by frequent projective measurements near the zeno regime", Phys. Rev. A **94**, 012118 (2016).

[174] M. Majeed and A. Z. Chaudhry, "The quantum zeno and anti-zeno effects with non-selective projective measurements", Scientific reports **8**, 14887 (2018).

[175] P. G. Kwiat, A. G. White, J. R. Mitchell, O. Nairz, G. Weihs, H. Weinfurter, and A. Zeilinger, "High-efficiency quantum interrogation measurements via the quantum zeno effect", Phys. Rev. Lett. **83**, 4725–4728 (1999).

[176] J. Wolters, M. Strauß, R. S. Schoenfeld, and O. Benson, "Quantum zeno phenomenon on a single solid-state spin", Phys. Rev. A **88**, 020101 (2013).

[177] A. Signoles, A. Facon, D. Grosso, I. Dotsenko, S. Haroche, J.-M. Raimond, M. Brune, and S. Gleyzes, "Confined quantum zeno dynamics of a watched atomic arrow", Nature Physics **10**, 715–719 (2014).

[178] F. Schäfer, I. Herrera, S. Cherukattil, C. Lovecchio, F. S. Cataliotti, F. Caruso, and A. Smerzi, "Experimental realization of quantum zeno dynamics", Nature communications **5**, 3194 (2014).

[179] D. Layden, E. Martín-Martínez, and A. Kempf, "Perfect zeno-like effect through imperfect measurements at a finite frequency", Phys. Rev. A **91**, 022106 (2015).

[180] M. Zhang, C. Wu, Y. Xie, W. Wu, and P. Chen, "Quantum zeno effect by incomplete measurements", Quantum Information Processing **18**, 1–11 (2019).

[181] A. Chantasri, J. Dressel, and A. N. Jordan, "Action principle for continuous quantum measurement", Phys. Rev. A **88**, 042110 (2013).

[182] T. Giamarchi, *Quantum physics in one dimension*, Vol. 121 (Clarendon press, 2003).

[183] J. Von Delft and H. Schoeller, "Bosonization for beginners—refermionization for experts", Annalen der Physik **510**, 225–305 (1998).

[184] K. G. Wilson, "Renormalization group and critical phenomena. i. renormalization group and the kadanoff scaling picture", Physical review B **4**, 3174 (1971).

[185] J. Cardy, *Scaling and renormalization in statistical physics*, Vol. 5 (Cambridge university press, 1996).

[186] P. Francesco, P. Mathieu, and D. Sénéchal, *Conformal field theory* (Springer Science & Business Media, 2012).

[187] A. Altland and B. D. Simons, *Condensed matter field theory* (Cambridge university press, 2010).

[188] M. E. Peskin, *An introduction to quantum field theory* (CRC press, 2018).

[189] L. P. Kadanoff, "Built upon sand: theoretical ideas inspired by granular flows", Reviews of Modern Physics **71**, 435 (1999).

[190] K. G. Wilson and J. Kogut, "The renormalization group and the ϵ expansion", Physics reports **12**, 75–199 (1974).

[191] M. Levin and X.-G. Wen, "Detecting topological order in a ground state wave function", Physical review letters **96**, 110405 (2006).

[192] A. Kitaev and J. Preskill, "Topological entanglement entropy", Physical review letters **96**, 110404 (2006).

[193] J. Chen, Z. Ji, C.-K. Li, Y.-T. Poon, Y. Shen, N. Yu, B. Zeng, and D. Zhou, "Discontinuity of maximum entropy inference and quantum phase transitions", New Journal of Physics **17**, 083019 (2015).

[194] B. Zeng and X.-G. Wen, "Gapped quantum liquids and topological order, stochastic local transformations and emergence of unitarity", Physical Review B **91**, 125121 (2015).

[195] B. Zeng and D.-L. Zhou, "Topological and error-correcting properties for symmetry-protected topological order", Europhysics Letters **113**, 56001 (2016).

[196] Z.-C. Gu and X.-G. Wen, "Tensor-entanglement-filtering renormalization approach and symmetry-protected topological order", Phys. Rev. B **80**, 155131 (2009).

[197] P. Calabrese and J. Cardy, "Evolution of entanglement entropy in one-dimensional systems", Journal of Statistical Mechanics: Theory and Experiment **2005**, P04010 (2005).

[198] H. Kim and D. A. Huse, “Ballistic spreading of entanglement in a diffusive nonintegrable system”, Physical review letters **111**, 127205 (2013).

[199] H. Liu and S. J. Suh, “Entanglement tsunami: universal scaling in holographic thermalization”, Physical review letters **112**, 011601 (2014).

[200] A. M. Kaufman, M. E. Tai, A. Lukin, M. Rispoli, R. Schittko, P. M. Preiss, and M. Greiner, “Quantum thermalization through entanglement in an isolated many-body system”, Science **353**, 794–800 (2016).

[201] M. B. Hastings, “An area law for one-dimensional quantum systems”, Journal of statistical mechanics: theory and experiment **2007**, P08024 (2007).

[202] I. Arad, Z. Landau, and U. Vazirani, “Improved one-dimensional area law for frustration-free systems”, Physical Review B—Condensed Matter and Materials Physics **85**, 195145 (2012).

[203] P. Calabrese and J. Cardy, “Entanglement entropy and quantum field theory”, Journal of statistical mechanics: theory and experiment **2004**, P06002 (2004).

[204] P. Calabrese and J. Cardy, “Entanglement entropy and conformal field theory”, Journal of physics a: mathematical and theoretical **42**, 504005 (2009).

[205] P. Fromholz, G. Magnifico, V. Vitale, T. Mendes-Santos, and M. Dalmonte, “Entanglement topological invariants for one-dimensional topological superconductors”, Phys. Rev. B **101**, 085136 (2020).

[206] T. Micallo, V. Vitale, M. Dalmonte, and P. Fromholz, “Topological entanglement properties of disconnected partitions in the Su-Schrieffer-Heeger model”, SciPost Phys. Core **3**, 012 (2020).

[207] M. B. Hastings and T. Koma, “Spectral gap and exponential decay of correlations”, Communications in mathematical physics **265**, 781–804 (2006).

[208] M. B. Hastings, "Lieb-schultz-mattis in higher dimensions", Phys. Rev. B **69**, 104431 (2004).

[209] B. Nachtergaele and R. Sims, "Lieb-robinson bounds and the exponential clustering theorem", Communications in mathematical physics **265**, 119–130 (2006).

[210] M. B. Hastings, "Locality in quantum and markov dynamics on lattices and networks", Physical review letters **93**, 140402 (2004).

[211] D. Gosset and Y. Huang, "Correlation length versus gap in frustration-free systems", Physical review letters **116**, 097202 (2016).

[212] M. A. Nielsen and I. L. Chuang, *Quantum computation and quantum information* (Cambridge university press, 2010).

[213] G. Piccitto, D. Rossini, and A. Russomanno, "The impact of different unravelings in a monitored system of free fermions", The European Physical Journal B **97**, 90 (2024).

[214] M. Ippoliti and V. Khemani, "Learnability transitions in monitored quantum dynamics via eavesdropper's classical shadows", PRX Quantum **5**, 020304 (2024).

[215] J. Li, R. L. Jack, B. Bertini, and J. P. Garrahan, "Efficient post-selection in light-cone correlations of monitored quantum circuits", arXiv preprint arXiv:2408.13096 (2024).

[216] F. Evers and A. D. Mirlin, "Anderson transitions", Reviews of Modern Physics **80**, 1355 (2008).

[217] T. Guhr, A. Müller–Groeling, and H. A. Weidenmüller, "Random-matrix theories in quantum physics: common concepts", Physics Reports **299**, 189–425 (1998).

[218] C.-M. Jian, Y.-Z. You, R. Vasseur, and A. W. W. Ludwig, “Measurement-induced criticality in random quantum circuits”, Phys. Rev. B **101**, 104302 (2020).

[219] Y. Bao, S. Choi, and E. Altman, “Theory of the phase transition in random unitary circuits with measurements”, Physical Review B **101**, 104301 (2020).

[220] A. Nahum, S. Roy, B. Skinner, and J. Ruhman, “Measurement and entanglement phase transitions in all-to-all quantum circuits, on quantum trees, and in landau-ginsburg theory”, PRX Quantum **2**, 010352 (2021).

[221] C. Y. Leung and A. Romito, “Entanglement and operator correlation signatures of many-body quantum zeno phases in inefficiently monitored noisy systems”, arXiv preprint arXiv:2407.11723 (2024).

[222] M. Ippoliti and W. W. Ho, “Solvable model of deep thermalization with distinct design times”, Quantum **6**, 886 (2022).

[223] S. A. Hill and W. K. Wootters, “Entanglement of a pair of quantum bits”, Physical review letters **78**, 5022 (1997).

[224] M. B. Plenio, “Logarithmic negativity: a full entanglement monotone that is not convex”, Physical review letters **95**, 090503 (2005).

[225] Y. Bao, S. Choi, and E. Altman, “Symmetry enriched phases of quantum circuits”, Annals of Physics **435**, 168618 (2021).

[226] P. Rouchon and J. F. Ralph, “Efficient quantum filtering for quantum feedback control”, Phys. Rev. A **91**, 012118 (2015).

[227] Y. Li, X. Chen, and M. P. A. Fisher, “Quantum zeno effect and the many-body entanglement transition”, Phys. Rev. B **98**, 205136 (2018).

[228] A. Biella and M. Schiró, “Many-Body Quantum Zeno Effect and Measurement-Induced Subradiance Transition”, Quantum **5**, 528 (2021).

[229] P. Rungta, V. Bu žek, C. M. Caves, M. Hillery, and G. J. Milburn, "Universal state inversion and concurrence in arbitrary dimensions", Phys. Rev. A **64**, 042315 (2001).

[230] V. S. Bhaskara and P. K. Panigrahi, "Generalized concurrence measure for faithful quantification of multiparticle pure state entanglement using lagrange's identity and wedge product", Quantum Information Processing **16**, 1–15 (2017).

[231] M. Eissler, I. Lesanovsky, and F. Carollo, "Unraveling-induced entanglement phase transition in diffusive trajectories of continuously monitored noninteracting fermionic systems", arXiv preprint arXiv:2406.04869 (2024).

[232] T. Yu and J. Eberly, "Sudden death of entanglement", Science **323**, 598–601 (2009).

[233] A. Foligno, T. Zhou, and B. Bertini, "Temporal entanglement in chaotic quantum circuits", Physical Review X **13**, 041008 (2023).

[234] C. Y. Leung, D. Meidan, and A. Romito, "Theory of free fermions dynamics under partial post-selected monitoring", arXiv preprint arXiv:2312.14022 (2023).

[235] A. Jamiołkowski, "Linear transformations which preserve trace and positive semidefiniteness of operators", Reports on Mathematical Physics **3**, 275–278 (1972).

[236] M.-D. Choi, "Completely positive linear maps on complex matrices", Linear algebra and its applications **10**, 285–290 (1975).

[237] P. Kumar, A. Romito, and K. Snizhko, "Quantum zeno effect with partial measurement and noisy dynamics", Physical Review Research **2**, 043420 (2020).

[238] A. Chantasri, J. Dressel, and A. N. Jordan, "Action principle for continuous quantum measurement", Physical Review A—Atomic, Molecular, and Optical Physics **88**, 042110 (2013).

[239] K. Koshino and A. Shimizu, "Quantum zeno effect by general measurements", Physics reports **412**, 191–275 (2005).

[240] S. A. Gurvitz, L. Fedichkin, D. Mozyrsky, and G. P. Berman, "Relaxation and the zeno effect in qubit measurements", Physical review letters **91**, 066801 (2003).

[241] C. Presilla, R. Onofrio, and U. Tambini, "Measurement quantum mechanics and experiments on quantum zeno effect", annals of physics **248**, 95–121 (1996).

[242] F. Li, J. Ren, and N. A. Sinitsyn, "Quantum zeno effect as a topological phase transition in full counting statistics and spin noise spectroscopy", Europhysics Letters **105**, 27001 (2014).

[243] C. N. Yang and S. Zhang, "So 4 symmetry in a hubbard model", Modern Physics Letters B **4**, 759–766 (1990).

[244] D. Amit, Y. Goldschmidt, and S. Grinstein, "Renormalisation group analysis of the phase transition in the 2d coulomb gas, sine-gordon theory and xy-model", Journal of Physics A: Mathematical and General **13**, 585 (1980).

[245] J. V. José, L. P. Kadanoff, S. Kirkpatrick, and D. R. Nelson, "Renormalization, vortices, and symmetry-breaking perturbations in the two-dimensional planar model", Physical Review B **16**, 1217 (1977).

[246] K. Klocke and M. Buchhold, "Topological order and entanglement dynamics in the measurement-only xzzx quantum code", Physical Review B **106**, 104307 (2022).

[247] A. W. Sandvik, "Computational studies of quantum spin systems", in Aip conference proceedings, Vol. 1297, 1 (American Institute of Physics, 2010), pp. 135–338.

[248] D. B. Kaplan, J.-W. Lee, D. T. Son, and M. A. Stephanov, "Conformality lost", Physical Review D—Particles, Fields, Gravitation, and Cosmology **80**, 125005 (2009).

[249] C. M. Bender and S. Boettcher, “Real spectra in non-hermitian hamiltonians having p t symmetry”, Physical review letters **80**, 5243 (1998).

[250] Y. Ashida, Z. Gong, and M. Ueda, “Non-hermitian physics”, Advances in Physics **69**, 249–435 (2020).

[251] R. El-Ganainy, K. G. Makris, M. Khajavikhan, Z. H. Musslimani, S. Rotter, and D. N. Christodoulides, “Non-hermitian physics and pt symmetry”, Nature Physics **14**, 11–19 (2018).

[252] L. Li, C. H. Lee, S. Mu, and J. Gong, “Critical non-hermitian skin effect”, Nature communications **11**, 5491 (2020).

[253] K. Kawabata, T. Numasawa, and S. Ryu, “Entanglement phase transition induced by the non-hermitian skin effect”, Physical Review X **13**, 021007 (2023).

[254] S. Gopalakrishnan and M. J. Gullans, “Entanglement and purification transitions in non-hermitian quantum mechanics”, Physical review letters **126**, 170503 (2021).

[255] R. Hamazaki, K. Kawabata, and M. Ueda, “Non-hermitian many-body localization”, Physical review letters **123**, 090603 (2019).

[256] S. Mu, C. H. Lee, L. Li, and J. Gong, “Emergent fermi surface in a many-body non-hermitian fermionic chain”, Physical Review B **102**, 081115 (2020).

[257] H.-G. Zirnstein, G. Refael, and B. Rosenow, “Bulk-boundary correspondence for non-hermitian hamiltonians via green functions”, Physical review letters **126**, 216407 (2021).

[258] H.-G. Zirnstein and B. Rosenow, “Exponentially growing bulk green functions as signature of nontrivial non-hermitian winding number in one dimension”, Physical Review B **103**, 195157 (2021).

[259] S. Malzard, C. Poli, and H. Schomerus, "Topologically protected defect states in open photonic systems with non-hermitian charge-conjugation and parity-time symmetry", Physical review letters **115**, 200402 (2015).

[260] L. Herviou, N. Regnault, and J. H. Bardarson, "Entanglement spectrum and symmetries in non-hermitian fermionic non-interacting models", SciPost Physics **7**, 069 (2019).

[261] D. Leykam, K. Y. Bliokh, C. Huang, Y. D. Chong, and F. Nori, "Edge modes, degeneracies, and topological numbers in non-hermitian systems", Physical review letters **118**, 040401 (2017).

[262] S. Yao and Z. Wang, "Edge states and topological invariants of non-hermitian systems", Physical review letters **121**, 086803 (2018).

[263] V. Alba, M. Fagotti, and P. Calabrese, "Entanglement entropy of excited states", Journal of Statistical Mechanics: Theory and Experiment **2009**, P10020 (2009).

[264] J. Surace and L. Tagliacozzo, "Fermionic Gaussian states: an introduction to numerical approaches", SciPost Phys. Lect. Notes, 54 (2022).

[265] G. B. Mbeng, A. Russomanno, and G. E. Santoro, "The quantum ising chain for beginners", SciPost Physics Lecture Notes, 082 (2024).

[266] A. Böttcher and B. Silbermann, *Analysis of toeplitz operators* (Springer Science & Business Media, 2013).

[267] B.-Q. Jin and V. E. Korepin, "Quantum spin chain, toeplitz determinants and the fisher—hartwig conjecture", Journal of statistical physics **116**, 79–95 (2004).

[268] A. R. Its, B.-Q. Jin, and V. E. Korepin, "Entanglement in the xy spin chain", Journal of Physics A: Mathematical and General **38**, 2975 (2005).

[269] F. Ares, J. G. Esteve, F. Falceto, and A. R. De Queiroz, “Entanglement in fermionic chains with finite-range coupling and broken symmetries”, Physical Review A **92**, 042334 (2015).

[270] F. Ares, J. G. Esteve, F. Falceto, and A. R. de Queiroz, “Entanglement entropy in the long-range kitaev chain”, Physical Review A **97**, 062301 (2018).

[271] A. Mostafazadeh, “Pseudo-hermiticity versus pt symmetry: the necessary condition for the reality of the spectrum of a non-hermitian hamiltonian”, Journal of Mathematical Physics **43**, 205–214 (2002).

[272] H. Casini, C. Fosco, and M. Huerta, “Entanglement and alpha entropies for a massive dirac field in two dimensions”, Journal of Statistical Mechanics: Theory and Experiment **2005**, P07007 (2005).

[273] F. H. Essler, H. Frahm, F. Göhmann, A. Klümper, and V. E. Korepin, *The one-dimensional hubbard model* (Cambridge University Press, 2005).

[274] E. Orignac and T. Giamarchi, “Weakly disordered spin ladders”, Physical Review B **57**, 5812 (1998).

[275] B. Ferté and X. Cao, “Solvable model of quantum-darwinism-encoding transitions”, Physical Review Letters **132**, 110201 (2024).